Particle Ejection System

Target particle recovery using a transient water jet

By : Bruce John Peter Mortimer

Supervisor : A W D Jongens

Central Acoustics Laboratory
Electrical Engineering Department
University of Cape Town

A dissertation submitted to the University of Cape Town in fulfilment of the requirements of the degree of Master of Science in Engineering, Cape Town - April 1991.

The copyright of this thesis vests in the author. No quotation from it or information derived from it is to be published without full acknowledgement of the source. The thesis is to be used for private study or non-commercial research purposes only.

Published by the University of Cape Town (UCT) in terms of the non-exclusive license granted to UCT by the author.

University of Cape Town

OBJECTIVE

Desired particles are to be separated from undersired particles by means of a particle deflection system. This will entail the isolation of particles from the mainstream by an acoustically based system.

ABSTRACT

Industry often requires the sorting of one material from another. Although the detection of desired (or undesired) elements is well advanced, the mechanical ejection or removal of particles is fairly underdeveloped. Agriculture and mining applications have used air jets and water jets to eject particles ranging in weight from a few grams to several hundred. With the current trends in mechanization leading towards higher processing speeds, these traditional methods have been found to be unsuitable : they have slow turn-on and turn-off response times, leading to a high volume of material being ejected with the target. Higher processing speeds will lead to even greater amounts of waste material being ejected thus producing even lower yield concentrations. Thus the need for a quick response time, repetitive, impulse ejection mechanism in the sorting industry is apparent.

A kinematic analysis of the required ejection mechanism blast strength shows that the required force depends on the target mass, the required deflection angle the force application angle and the force duration. Acoustical techniques in air are unsuitable as ejection force mechanisms.

A water jet is proposed to meets these requirements. This water jet is caused by an electrical discharge in a liquid cavity. This produces a weak shock wave which is focused by the cavity to a nozzle where a slug of water is emitted. The cavity is a elliptical cavity of height h, with the electrodes mounted end on at the first focus and a reflecting cone and nozzle at the second focus.

The propagation of weak shock waves in the elliptical cavity is studied theoretically and numerically - using a finite difference simulation program. The reflected converging wave is shown to depend on the cavity eccentricity and the wall admittance. The resulting converging shock wave has an assymetrical pressure distribution. This analysis is used in the design of a prototype water jet generator.

The electrical discharge circuit used for the production of shock waves in the cavity is analysed and the physical discharge process of electrical to shock energy conversion reviewed. Conditions for the maximisation of this transfer correspond to large water gap resistances, high voltages and low circuit inductances.

Experiments on the prototype generator show that the transient water jet slug energy is relatively low. High speed photographic techniques reveal that the jet velocity is of the order

of 30 m/s. Published results **[15]** show much higher jets speeds are possible. The operation of the electrical discharge circuit is found to critically influence the water jet performance - electrical measurements show that the circuit is a sub-optimum, underdamped RLC circuit. The cone / nozzle operation is also shown to have a marked effect on performance. The nozzle in particular requires optimisation.

The prototype in its present form is not suitable for use in an ejection system. Although the pulse length, rise time and channel spread of the device are suitable, the blast strength is not sufficient for deflection of the heaviest range of particles. Optimisation of the electrical circuit and increased energies will increase the blast strength.

This thesis is dedicated to my parents
Dr. John and Jean Mortimer
for all their support in getting me here.

ACKNOWLEDGEMENTS

The author would like to thank Mr A. W. D. Jongens for his helpful and inspirational supervision. The financial support of the FRD is gratefully acknowledged. The DeBeers Diamond Research Laboratory is gratefully acknowledged for their financial assistance. Dr. J. O. Hansen and the staff of DRL are acknowledged for their many helpful comments and for making their facilities available for this thesis. Prof. B. Skews of the University of Witwatersrand, School of Mechanical Engineering is gratefully acknowledged for his help and advice as well as allowing the author access to his departments computing facilities. Mr S. Schrire is acknowledged for his advice on the trigger circuit. Mr. J. R. Green, Mr C. Dingley of UCT and Professor J. Reynders of WITS are thanked for their constructive comments on various aspects of the project. Mr. J. Hesselink is acknowledged for the loan of his air spark gap and the advice that he gave. Mr L. Watkins (ERI) and Mr. D. Kenyon (UCT) are thanked for their effort in constructing and machining some of the parts for the prototype. Thanks must go to those who proofed the document - Bruce Reeler (who's critical pencil was much appreciated) and Adrian Jongens (who read the document a number of times). My Condor 'Vector' is thanked for helping my spirits to soar. The author would also like to acknowledge the undergraduate and postgraduate staff of the Central Acoustics Laboratory, UCT, who offered advice, help and who all contributed to an enjoyable working environment.

TABLE OF CONTENTS

OBJECTIVE i

ABSTRACT ii

ACKNOWLEDGEMENTS iv

TABLE OF CONTENTS v

LIST OF FIGURES xi

NOMENCLATURE xiv

CHAPTER 1 : INTRODUCTION 1
- 1.1 Material sorting by target deflection 1
- 1.2 Analysis of the problem 1
  - 1.2.1 The Sorting System 1
  - 1.2.2 Requirements for efficient ejection 2
- 1.3 Air and water jets 6
  - 1.3.1 Properties of air jets 7
  - 1.3.2 Properties of water jets 8
- 1.4 Requirements of an acoustically based ejection system 8
- 1.5 Shock wave as a source of energy 8
  - 1.5.1 Lithotripsy 9
- 1.6 The elliptically focused water jet generator 11
  - 1.6.1 The water jet concept 11
  - 1.6.2 The elliptical shock generator application in an ejection system 13
  - 1.6.3 The prototype 13
- 1.7 Contents of Chapters 2 to 10 14

CHAPTER 2 : KINEMATICS OF THE EJECTION PROCESS 16
- 2.1 Assumptions 16
- 2.2 Definitions used in this analysis 17
  - 2.2.1 Definition of the angle of deflection ζ 17
  - 2.2.2 Definition of the external application force F_D 17
  - 2.2.3 Target particle initial conditions 17
- 2.3 Horizontal motion of ideal spheres ('billiard ball analysis') 17
- 2.4 Projectile analysis 18
  - 2.4.1 Momentum analysis 19
  - 2.4.2 Acceleration-mass projectile analysis 20
- 2.5 Numerical results 27
- 2.6 Discussion 29

CHAPTER 3 : PARTICLE DEFLECTION USING ACOUSTIC WAVES 30
3.1 Acoustics as a source of force 30
3.1.1 Momentum 30
3.1.2 Acoustic Radiation Force 30
3.1.3 Acoustic streaming 32
3.2 Applications using acoustic forces 33
3.2.1 Levitation 33
3.2.2 Intensity Measurement 34
3.3 Force on a target due to a shock wave in air 37
3.3.1 Finite amplitude waves 37
3.3.2 Shock wave force on a target sphere 38
3.3.3 Numerical results 38
3.3.4 Air shock wave application as an ejector 38
3.4 Conclusions 39

CHAPTER 4 : PARTICLE DEFLECTION USING AN ELECTRICAL DISCHARGE AND A WATER JET SLUG 40
4.1 Water jet systems 40
4.1.1 Water jet suitability as an ejector 40
4.1.2 Pulse water jets 41
4.1.3 Repetition rates of shock wave sources 42
4.1.4 Choice of a shock generation method 42
4.2 Shock wave production by an electrical discharge 43
4.2.1 Shocks from sparks 43
4.2.2 Energy storage for discharges 43
4.2.3 Electrical circuit 43
4.3 Analysis of the electrical circuit 44
4.3.1 Equivalent circuit 44
4.3.2 Charging circuit 45
4.3.3 Discharge circuit 46
4.3.4 Power release in the water gap resistance R_W 48
4.3.5 Oscillations 49
4.4 The discharge process 49
4.4.1 Establishment of the spark channel 49
4.4.2 Pressure from a spark discharge in water 50
4.5 Controllable parameters in the electrical circuit 53
4.6 Energy analysis 55
4.6.1 Required system efficiency 55
4.6.2 Efficiency of the discharge shock wave process 56
4.6.3 Efficiencies obtained 56
4.6.4 Acoustic efficiency 56
4.7 Conclusions 56

CHAPTER 5 : DESIGN OF AN ELLIPTICAL CAVITY 57
5.1 Elliptically focused water jet generator 57
5.1.1 Properties of ellipses 57
5.1.2 Applications using ellipses to focus a spark discharge 58
5.1.3 The water jet device 58

5.2 Wave propagation in elliptical cavities 59
5.2.1 Weak shock waves 60
5.2.2 Weak shock wave focusing 60
5.2.3 Angle of incidence vs. angle of reflection 61
5.2.4 Wave energy distribution in the wave front 61
5.3 Wave modes in the cavity wall 67
5.4 Ellipse cavity design 68
5.4.1 Eccentricity 68
5.4.2 Focal length of the ellipse (C) 69
5.4.3 Ellipse cavity height 70
5.5 Cone design 71
5.6 Nozzle design 72

CHAPTER 6 : CONSTRUCTION OF THE ELLIPTICAL CAVITY 74
6.1 The prototype system 74
6.2 The shock discharge 74
6.2.1 The electrodes 74
6.2.2 Insulator 75
6.2.3 Water spark gap 77
6.3 Elliptical Cavity 78
6.3.1 Eccentricity 78
6.3.2 Focal length, major and minor axes 78
6.3.3 Cavity height 78
6.3.4 Construction 79
6.4 Converging cone insert 80
6.4.1 Cone removal 80
6.4.2 Cone insert prototypes 81
6.5 The nozzle 81
6.5.1 Nozzle design 81
6.5.2 Nozzle removal 81
6.5.3 Nozzle prototypes 82
6.5.4 Cone nozzle combinations 82

CHAPTER 7 : THEORETICAL SIMULATIONS 83
7.1 Autodyne 83
7.2 Simulations 83
7.2.1 Units and dimensions 83
7.2.2 Limitations 83
7.2.3 Elliptical cavity 86
7.2.4 Cone Duct / nozzle interaction 86
7.3 Simulations using Autodyne 87
7.3.1 Rigid walled elliptical cavity simulations 88
7.3.2 Elliptical focusing with a compliant boundary 96
7.3.4 Cone nozzle interaction 98
7.4 Conclusions 109

CHAPTER 8 : TECHNIQUES FOR MEASUREMENT OF THE HIGH SPEED WATER JET 111
8.1 Measurement of experimental quantities 111
8.1.1 Pressure measurement within the cavity 111
8.1.2 Water jet velocity measurements 112
8.1.3 Water jet velocity accuracy 112
8.2 Pressure measurement within the cavity 113
8.2.1 Schlieren Systems 113
8.2.2 Interferometric approach 114
8.2.3 Pressure probes 114
8.2.4 Conclusions 115
8.3 Water jet measurement techniques 115
8.3.1 High speed photography 116
8.3.2 High speed photography using short duration light sources . . . 116
8.3.3 Electro-optical technique 119
8.3.4 The choice of a velocity measurement system 120
8.4 Water jet slug photography 120
8.4.1 Silhouette photography 120
8.4.2 Front lighting 121
8.4.3 Exposure calculations 121
8.4.4 Discussion 122
8.5 Water jet momentum and energy 122
8.6 Conclusions 123

CHAPTER 9 : EXPERIMENTAL RESULTS 124
9.1 Test Objectives 124
9.2 Testing of the prototype 124
9.2.1 Discharge circuit analysis 124
9.2.2 Water jet slug velocity 125
9.2.3 Water jet energy and momentum 125
9.3 Electrical discharge circuit measurement 125
9.3.1 Testing of circuit components 125
9.3.2 Measurement systems 126
9.4 Discharge without water gap 127
9.4.1 Measurement of the capacitor and circuit inductance 127
9.4.2 Measurement of the resistance of the leads 129
9.5 Discharge with a water gap 129
9.5.1 The water spark gap 130
9.5.2 Quiet discharges 132
9.5.3 Variation in the delay before water gap breakdown 133
9.6 Discharge in the prototype 134
9.6.1 Inductance of the prototype system 134
9.6.2 Resistance of the water gap 134
9.6.3 Circuit damping 136
9.6.4 Discharge circuit operation 136
9.7 Measurement of the water jet velocity 137
9.7.1 Water jet height measurements 137
9.7.2 Water jet high speed photography 137

9.7.3 Water jet slug propagation 138
9.8 Water jet energy and momentum measurements 142
9.8.1 Volume of water missing from the cavity 142
9.8.2 Water jet slug energy 142
9.9 Discussion 145
9.9.1 Electrical circuit operation 145
9.9.2 Water jet energy dependence on cone / nozzle combination . . . 145
9.9.3 Water jet velocities 146
9.9.4 Prototype performance 146

CHAPTER 10 : CONCLUSIONS AND RECOMMENDATIONS 147
10.1 Project summary 147
10.2 Prototype performance 149
10.2.1 Discharge circuit operation 149
10.2.2 Water jet performance 150
10.3 Water jet generator application in an ejection system 151
10.4 Recommendations 151

REFERENCES 153

LIST OF FIGURES

Figure 1 : Material handling by particle ejection 2
Figure 2 : Overlap between adjacent ejectors 4
Figure 3 :Cycle response time of a typical air ejector 7
Figure 4 : EMAS lithotripsy shock wave source 10
Figure 5 : Operation of the elliptically focused water jet generator 12
Figure 6 : Frictionless horizontal plane motion under the action of a time limited pulse 18
Figure 7 : Momentum vectors of undeflected particle, deflection force and resultant particle momentum vector 19
Figure 8 : Projectile motion before ejection 21
Figure 9 : Forces acting on the target particle during ejection 23
Figure 10 : Motion of the particle under the action of the ejection force 24
Figure 11 : Definition of the angle of deflection 26
Figure 12 : Particle motion after ejection 27
Fig 13 - Graph 1 : m = 50 g , s_E = 0.001 , t_D = 0.001 , $\zeta = 15^o$ and $\theta = 0^o$ . . 28
Figure 14 : Non-linearity of the equation of state produces a non-zero mean pressure - the Rayleigh radiation pressure 31
Figure 15 : Streaming 32
Figure 16 : Intensity measurement system 35
Figure 17 : Transient water jet production by a) the cumulation method, and b) the shock reflection method 42
Figure 18 : Itemised circuit for the production of a plasma discharge is water 44
Figure 19 : Equivalent discharge circuit 45
Figure 20 : Current responses in a series RLC circuit 47
Figure 21 : Power release in the circuit resistance as a function of the damping factor ξ 48
Figure 22 : Pressure and power release in a plasma channel 51
Figure 23 : Shock wave pulse shape 53
Figure 24 : Ellipse geometry as a means of focusing energy to a point. 58
Figure 25 : Elliptical cavity water jet in cross section 59
Figure 26 : Weak shock wave focusing in the ellipse at 3 different times 60
Figure 27 : Co-ordinate system used - polar co-ords 62
Figure 28 : Simplified spark discharge initial conditions 63
Figure 29 : Normalised calculated pressure of a cylindrical expansion or simplistic spark discharge at different times after discharge 64
Figure 30 : Pressure distribution of the focused wave plotted against angle θ 65
Figure 31 : Variation of normalised reflected pressure w.r.t. θ for different eccentricities a) y = 0 b) y = 0.03. 66
Figure 32 : Area of wave disruption due to the electrodes and the converging duct . 69
Figure 33 : Approximate cylindrical expansion from the spark channel will depend on the gap length λ_g and the cavity height h 70
Figure 34 : Disruption of the expanding wave by the convergent duct 72
Figure 35 : Electrode holders 75

Figure 36 : Electric field control of the outer electrode insulator 77
Figure 37 : Cavity support arrangement 80
Figure 38 : Nozzle insertion system 82
Figure 39 : Axial symmetric representation of the cone nozzle interaction 87
Figure 40 : Full ellipse focusing - 4 μ seconds after discharge 88
Figure 41 : Expanding wave undergoing reflection from the cavity wall - time 17 μ seconds 89
Figure 42 : Weak shock wave propagation in the ellipse - time 34 μ seconds 90
Figure 43 : Converging weak shock wave on the far focus of an elliptical cavity - time 60 μ seconds 91
Figure 44 : Shock wave convergence on the second focal point - time 68 μ seconds 92
Figure 45 : Post focusing of the weak shock wave - time 73 μ seconds 93
Figure 46 : Target locations for the measurement of the pressure time histories within the cavity 94
Figure 47 : Pressure amplitude vs. time recorded for the point locations shown in fig 47 95
Figure 48 : Ellipse weak shock wave focusing with a metal compliant boundary at 18 μ seconds after discharge 96
Figure 49 : Weak shock wave propagation in the cavity and cavity walls at time 36 μ seconds 97
Figure 50 : Weak shock wave convergence on the second focal point (with a metal compliant boundary) at time 70 μ seconds 98
Figure 51 : Axial symmetric representation of the cone nozzle interaction - velocity plot. The velocity boundary condition is shown. 99
Figure 52 : Pressure contour map resulting from boundary conditions - time 5.25 μ seconds 100
Figure 53 : Weak shock wave propagating as a plane axial symmetric shock converging on the cone duct - time 25 μ seconds 101
Figure 54 : Weak shock wave propagation axial symmetrically down the nozzle - 30 μ seconds after the start. 102
Figure 55 : Reflected wave and wave propagation down the nozzle - 36 μ seconds after the start. 103
Figure 56 : Target location points for the pressure history curves 104
Figure 57 : Pressure history curves corresponding to the target locations shown in fig 58 - combination small nozzle - regular cone. 105
Figure 58 : Weak shock wave in the nozzle of cone / nozzle combination medium nozzle - regular cone - of Chapter 6 (36 μ seconds after the start) 106
Figure 59 : Pressure combination plots for the medium nozzle - regular cone combination. 107
Figure 60 : Weak shock wave propagating down the nozzle for the low cone - small nozzle combination. 108
Figure 61 : Pressure combination plot for the small nozzle - low cone combination. 109
Figure 62 : Accuracy of water jet velocity 113
Figure 63 : Water jet velocity measurement by 100 Hz flash 117
Figure 64 : Velocity measurement by a single flash at a known delay 118
Figure 65 : Electro-optic water jet velocity measurement system 119
Figure 66 : Modified shadowgraph system using only 1 collimating mirror 121

Figure 67 : Water jet energy measurement system - using a ballistics approach . . . 122
Figure 68 : Voltage across air gaps during breakdown a) no jitter b) small amount of jitter at the start of switching. 126
Figure 69 : Discharge circuit schematic for the measurement of circuit inductance . 127
Figure 70 : Current vs. time for C = 0.08 μF, V = 15 kV i.e. 2 capacitors 128
Figure 71 : Experimental system for water gap discharges 130
Figure 72 : Voltage across a water spark gap during a discharge 131
Figure 73 : Voltage across water gap during discharge showing long delay before breakdown 131
Figure 74 : Current through and voltage across a water gap during discharge - C = 0.08 μF, V = 15 kV, breakdown length 3 mm 132
Figure 75 : Voltage and current during a quiet discharge 133
Figure 76 : Current through prototype generator water gap during discharge - V = 14kV, C = 0.08 μF and water gap length = 3 mm 134
Figure 77 : Propagation of a water jet slug (delay 1 ms) 139
Figure 78 : Water jet (delay 3 ms) 140
Figure 79 : Water jet at 5 ms. 141
Figure 80 : Target cone vertical displacement sequence. Photographs are 1 ms per frame (different events) 143

NOMENCLATURE

a	Major axis of ellipse
b	Minor axis of ellipse
c	Speed of sound of the medium
C	Focal length of ellipse
C	Capacitance of circuit
e	Eccentricity of ellipse
E	Point of ejection
E_E	Electrical stored energy ($0.5\ CV^2$)
E_F	Electric field strength between the discharge electrodes
F_a	Acoustic force on a target
F_D	External application force
F_S	Streaming force
h	Height of the elliptical cavity
h_E	Vertical distance to point of ejection E
I_W	Incident wave acoustic intensity
k	Wave number
L	Inductance of discharge circuit
m	Mass of target particle (to be deflected)
m_1	Gradient of the path of the undeflected particle at point E
m_2	Gradient of the path of the deflected particle at the instant F_D ceases
P_1	Momentum vector of undeflected particle
P_2	Momentum vector of deflection force system
P_C	Pressure at the plasma channel boundary (theoretical)
P_m	Maximum water pressure from an electrical discharge at a distance D from discharge
r	Polar radius from the first focus of ellipse
r'	Polar radius from the second focus of ellipse
R	Resistance
R_c	Resistance of leads and connections in the discharge circuit
R_s	Charging resistance
R_S	Radius of spherical target
R_W	Resistance of the water gap
s_E	Vertical distance to the point of ejection E
t_D	Application time (duration) of external application force on the target particle
t_E	Time to the ejection (to point E)
TIG	Tungsten inert gas
u	Initial velocity of target particle - velocity of conveyer belt
v	Velocity
V	Voltage (electrical context), Vollume (physical context)
x	Initial horizontal displacement of target particle undergoing projectile motion
x'	Horizontal displacement of target particle while undergoing deflection under action of deflection force
x_c	Deflecting cone base radius
y	Initial vertical displacement of target particle undergoing projectile motion
y'	Vertical displacement of target particle while undergoing deflection under action

of deflection force

Y_P Normalised acoustic radiation force function

γ Angle of application force (ccw from horizontal)

δ Polar angle from the first focus of ellipse

ζ Angle of deflection (defined in Appendix C)

Θ Initial angle of projection (conveyer belt ramp angle)

θ Polar angle from the second focal point of the elliptical cavity

λ_g Gap width between the discharge electrodes

ξ Damping factor of the discharge cicuit

τ Time constant of the circuit (charging circuit, and discharge circuit)

ϕ Velocity potential

CHAPTER 1 :

INTRODUCTION

1.1 Material sorting by target deflection

Industry often requires the separation of one material from another. It may seem surprising then, that until the 1950's, many industries relied on hand sorting combined with visual inspection as the principle means of quality control and material handling. The need to maximise the speed of the sorting process while simultaneously minimising the costs led to an automation of this process [1].

Agricultural quality control automation was spearheaded by the introduction of air jets to deflect unwanted items from a conveyer belt. This was achieved by firing the jets at the targets as they were falling through an inspection region [1]. The targets would then be separated from the mainstream, which would continue on its path unaffected. This technique is still widely used as the primary method for the separation of desired material from the mainstream.

Different industries have developed different detection methods. The detection system can either detect a desired item from a stream of waste, or as in quality control, detect an undesired item from a stream of product. Detection methods can be optical methods (fluorescence of target particle, the detection of an optically dark target particle or the use of image processing techniques), wave methods (using differences in microwave absorption to detect the target particle) and X-ray methods. Although these detection methods are relatively advanced, research into deflection methods has been widely neglected.

This project concentrates on an ejection system for the removal of desired particles. A novel method of ejection, using a transient water jet and an elliptical generator was investigated.

1.2 Analysis of the problem

1.2.1 The Sorting System

Particles, ranging in size from < 1 up to 30 mm in diameter (but probably in the range 3 to 8mm) are to be recovered from a 1 m wide, moving conveyer belt

(at 5 m/s or 18 km/h) which contains both the desired particles and waste material. The particles and waste material are assumed to be stationary relative to the belt. Optical or X-ray techniques are employed to fluoresce the particles and to determine their positions. These detection systems have practical range width limitations. Thus practical systems usually consist of several units in parallel covering a wide belt (with a width of up to 1 m).

The conveyer belt allows the particles to fall through an inspection region. While undergoing projectile motion, the desired particles can be sorted by removing them from the mainstream using some force mechanism. The waste material continues unaffected and is discarded. The ejection process is shown in **fig 1:**

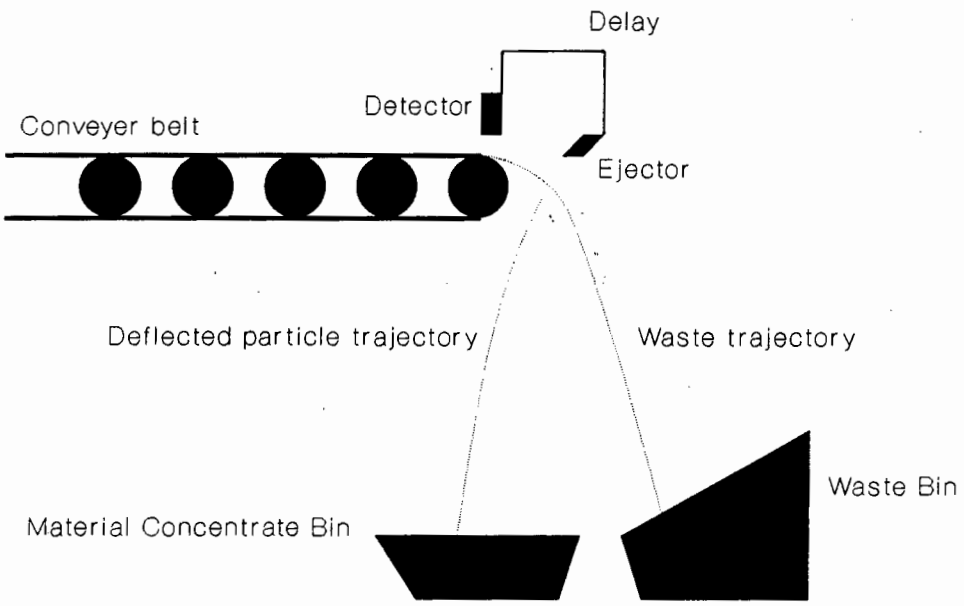

Figure 1 : *Material handling by particle ejection*

1.2.2 Requirements for efficient ejection

The specifications of the proposed ejection system are :

- **Deflection angle of the target particle**

The angle of deflection, ζ is defined as the angle between the tangents of the deflected and undeflected paths. The target particles must be deflected by a minimum deflection angle to ensure separation from the mainstream. Particles are required to be deflected by 15°.

- **Ejector blast strength**

The ejector energy must be efficiently concentrated towards the target particle. If the force from the ejectors is so large that the target achieves a high speed trajectory, over-ejection (the target is ejected out of the catchment system) or breakage of the target can occur.

Since there is a cost related need to have one ejection device that can be used to eject the full range of particles, the required ejection system must have sufficient force to deflect the largest expected particle.

The minimum force required to deflect the target particle is calculated in Chapter 2.

- **Distance of the ejector from the trajectory**

Typically systems have ejectors positioned 40 mm normal from the particle trajectory. The required ejection system must operate at similar distances from the particle stream.

- **Ejector blast width**

The width of the ejector blast in the direction normal to the movement of the conveyer belt, will mean that there is an unnecessary overlap between it and the adjacent ejector - this should be minimised. The ejector system seen normal to the conveyer belt propagation is shown in fig 2 :

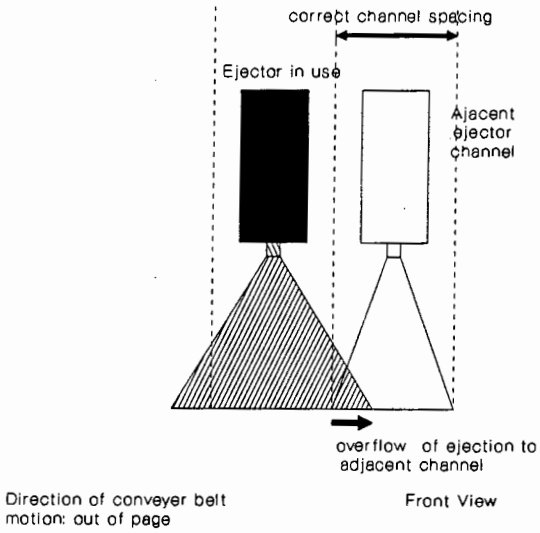

Figure 2: ***Overlap between adjacent ejectors***

The blast width should be larger than the mechanical size (width) of the ejector for multi-channel systems.

- **Particle speed**

An increase in the material handling rate will require an increase in the conveyer belt speed or an increase in the width of the conveyer belt. The latter is beyond the scope of this thesis. Conveyer belt speeds of 5 - 10 m/s are desired. Existing belt speeds are of the order of 2 m/s.

- **Particle size and mass**

The densities of the undesired particles and desired particles differ; they are respectively : 3.52 and 2.89 g/cc. Particles are sized to a 1:2 ratio. Thus the different streams will have the masses and sizes shown in the table (assuming spherical target particles):

Size Range	Volume	Mass	
diameter [mm]	[cm^3]	Undesired	Desired
2 - 4	0.0042	15 - 178 mg	12 - 96 mg
4 - 8		178 - 940 mg	96 - 800 mg
8 - 16		0.94 - 7.5 g	0.8 - 6 g
16 - 32	17.2	7.5 - 60 g	6 - 50 g

- **Blast duration**

Assuming that the particles are smaller than the ejector width and that the particles are spaced far apart, the pulse duration available for target ejection without overlap to those particles before and after the target is approximately given by :

$$Duration = \frac{Average\ particle\ size}{particle\ speed}$$

This representation is idealistic since real detector systems cannot at this stage detect individual targets accurately, and the trajectory of the particle will have some uncertainty associated with this. These factors can be represented by an increase in the size of the particle :

$$Duration = \frac{Ave.particlesize + detectorwindowsize + safetyfactor}{particle\ speed}$$

- **Response time of the ejector**

Since the material on the belt cannot be assumed to be stationary in real systems, there is an uncertainty as to what the target's actual trajectory will be. The response time between the electronic switch-on and the detection of the blast must be minimised to ensure that the target does not deviate from its trajectory in the time between detection and ejection. The possibility of collisions with other particles in flight will be minimised.

Real ejector systems may have a proportion of non-uniform, non-spherical targets. Some of these targets will have profiles with higher drag coefficients than ideal spheres - further introducing uncertainty into the particle trajectory.

The horizontal position of the ejector(s) from the conveyer belt can be approximately determined from :

$$Ejector\ spacing = particle\ speed \times Ejector\ response\ time$$

Thus the ejector response time should be minimised if the particle speed (or conveyer belt speed) is to be increased while simultaniously minimising the ejector spacing. The response time for the proposed ejector system should be less than 1 ms.

- **Certainty of desired particle recovery**

The repetition rate should allow multiple ejections if a 100 % recovery rate is required. The design of the ejector system's repetition rate has been excluded from development described in this work.

1.3 Air and water jets

The separation techniques used in the automation of material processing have centred on one of three techniques - mechanical interruption, water jets, and air jets. Water jet ejection was spearheaded by the mineral processing industry. Banks of water jets have been used to separate large particles (typically of the order 8 cm mean diameter).

Agriculture concentrated its reasearch on air jets. Typical repetition rates of air jets used to deflect small targets are in the region of 300 per second (this has been achieved in the rice sorting industry) [1].

Air jets have the advantage that they are the same medium as the operating medium (particles do not require drying after ejection). However, this fact means that the jets diffuse rapidly. The jet's momentum flux will decrease away from the nozzle. The target will then only be subjected to part of the jet profile - thus causing an innefficent energy transfer. Surrounding unwanted material will also be subjected to a component of this momentum flux consequently reducing the concentration of desired particles.

1.3.1 Properties of air jets

A typical cycle for an air ejector used in the mineral processing industry is shown in **Fig 3:**

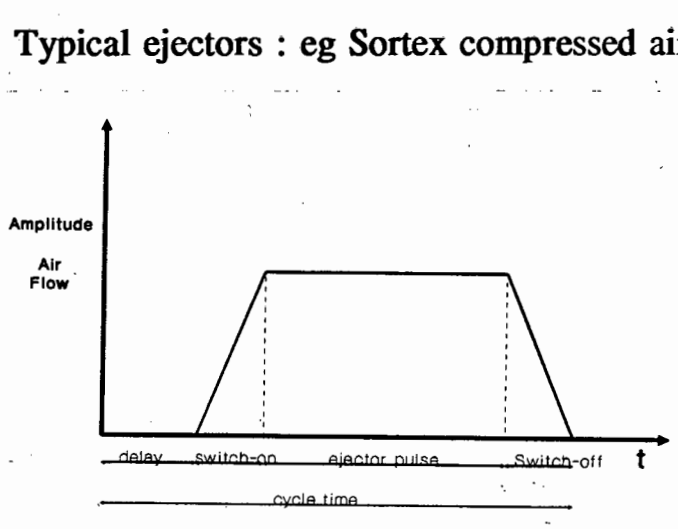

Figure 3 :*Cycle response time of a typical air ejector*

Typical ejectors used have the following response times :

Delay before switch-on (response time) : 15 milliseconds.
Switch-on time and Switch-off time : 5 milliseconds.
Ejector pulse length : 15 milliseconds.
Total cycle times : 40 milliseconds.

These values have restricted the speed of the conveyer belt to relatively low levels (typically in the order of 1 to 2 m/s).

The air jet cannot be concentrated to the extent that only the desired particle is deflected; inevitably some other, undesirable material will be deflected along with the particle. Typical air ejectors (for small diameter systems 1.6 mm) eject up to 500 particles per ejection.

1.3.2 Properties of water jets

In contrast to air jets, water jets do not suffer from the dispersion problems of air jets. Transient pulse water jets have largely been restricted to devices with moving parts and slow repetition frequencies. Typical water jet speeds range from about 17 m/s [2] in the common garden hosepipe to several km/s obtainable using high speed water cannons [3,4].

1.4 Requirements of an acoustically based ejection system

An acoustically based deflection system, possibly utilising high power ultrasonic devices was proposed as an alternative to the above deflection methods. The proposed ejection system was required to replace an existing air jet system. The performance requirements are summarised:

- It must have a fast response time ; less than 1 millisecond
- Be repetitive (have a short cycle time of under 10 milliseconds)
- have a sufficient momentum product to deflect targets of up to 50 grams by 15^{o}
- have a small momentum flux density (to ensure the target is deflected with minimal miss)
- have a low application time i.e. more impulsive than air jets.

In order to achieve the momentum transfer that is required to deflect the target particle, a projectile of sufficient velocity and mass (momentum) is required. The force obtained from acoustic waves in air will be shown to be very low in Chapter 3. Water jets have been shown to have low dispersion and better momentum transfer on collision with the target. Thus the energy transfer from medium to target will be much greater than that of air jets. Water jets are thus suitable mechanisms for ejection.

A transient, repetitive water jet generator forms the subject of this work. The device is reviewed, analyzed and tested for suitability in an ejection system.

1.5 Shock wave as a source of energy

Shock waves are in general highly destructive. However, a number of applications can make use of these destructive properties. Examples of these applications are:

Metal forming or shaping. Here thin metal plates can be formed to fit a mold by being placed in the vicinity of a spark discharge in water [5]. Metal forming systems have typical cycle times of 10 seconds to 30 seconds [5]. The energies used in these devices are very large : 3000 to 20 000 J. Large capacitors

(typically 10.5 μF at 30 kV) limit the charging times.

Crushing brittle materials [6,7].

In shock wave lithotripsy kidney stones are crushed in situ by focusing shock waves at them from an extracorporeal source [8,9].

Water jet cutting. High speed water jets can be used as an alternative to conventional drilling machinery [10]. The latter two applications are closely aligned to this work - these methods are discussed in some detail.

1.5.1 Lithotripsy

An application that uses water as a medium for the transmission of energy is shock wave lithotripsy (lithotripsy is Greek for stone grinding). This technique has revolutionised the treatment of kidney and gall stones since it allows them to be treated using extracorporeal techniques [8]. Lithotripsy has renewed interest in liquid shock wave research.

A shock wave is generated outside the body. This shock wave is then focused through a water coupling medium and the body to the target stone. The high pressures at the focal point and the relative mismatch in impedance between the stones and the surrounding medium, cause the stones to break into smaller components. These smaller components can then be passed normally with the patient's urine.

There are two types of shock wave sources ; point sources and finite amplitude piston transducer sources. The early lithotripters were of the first type, most notable being the system developed by Dornier.

Dornier System Lithotripters

Initial devices used an ellipsoidal cavity, with an electrode pair at one focal point, to focus a shock wave. Initial devices (manufactured by Dornier Systems) used low inductance circuit components with values of C = 90 nF, V = 20 kV. The circuit discharged at the first focus of an ellipsoid of rotation with values of 11 cm for the long axis, and 6.5 to 7.5 cm for the minor axis. Peak pressures that were obtained were in the region of 100 Bar (with rise times in the order of nanoseconds) [8,11,12].

In order to facilitate lithotripsy only half of the ellipsoidal cavity was used. This resulted in only about 10 % of the shock energy being unfocused.

Electromagnetic Shock Source (EMAS)

Recently, a second generation of lithotripters using an electromagnetic shock wave source (EMAS) and an acoustic lens (for focusing) has been developed by Siemens Medical Systems [13]. This technique uses a finite amplitude wave source as opposed to a point source discussed in the previous section.

A high voltage capacitor is discharged into a coil. This coil is mounted on an acoustically hard backing. A thin insulating film separates the coil from a metal disk. The coil / disk combination makes up a short-circuited transformer. The eddy currents induced in the disk cause it to be repelled (Lorentz forces) from the coil consequently emitting a high pressure plane pulse [14]. This is shown in fig 4:

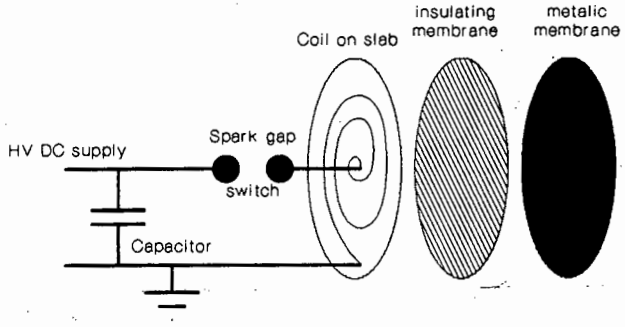

Figure 4 : *EMAS lithotripsy shock wave source*

The plane shock pulse can be focused in a number of ways : by acoustic lenses, by a spheroid shaped disk, by a paraboloid reflector, and by phasing a number of small EMAS units [8]. Siemens Lithostar and Lithostar Ultra systems use an acoustic lens typically of diameter 12 cm. This lens can be arranged such that the adjustment of the focal point of the source is done without having to continuously position the patient.

The peak pressure obtained at the focal point of this device is approximately : P_M = 50 kPa (50 Bar) [8].

Conclusions

High pressure amplitudes in water can be created using existing technologies. Lithotripters produce focused shock pressures in the region of 50 Bar. The technology described can be used as the foundation for the formation of a water shock for the production of a water jet (described in section 1.4.2).

1.6 The elliptically focused water jet generator

1.6.1 The water jet concept

Water jets can be created in a number of ways. A positive displacement piston can be used to emit a slug of high speed liquid. Bowden and Brunton used this technique in high speed water droplet erosion of solids experiments [40].

This technique has also been used in water jet cutting applications. Some of these systems are even in commercial use (eg. mining, parking meter cutter [10]). The difficulty with this method is that the mechanical inertia of the piston limits the repetition frequency.

An alternative method for the production a water slug has been proposed - the shock reflection method [17]. A shock wave is impinged onto a liquid-air boundary.

A pulsed water jet for the cutting and cleaning of metals has been proposed in Gustafsson (1987) [15,16,17]. In this work he motivates the need for a water jet that has a high repetition rate. He proposes an elliptically focused shock wave reflection water jet for this purpose. Since the system is not mechanical, its repetition frequency is not affected by the mechanical inertias of the operating parts of a conventional mechanical transducer.

An electrical discharge is used to create a shock at one of the foci of a cylindrically symmetric water filled elliptical cavity. The shock is then focused to the far focus by the elliptical container. The shock is then transferred down a converging duct to a nozzle. At the end of the shock wave impinges on a liquid - air free surface nozzle to produce a jet of liquid. The schematic operation of the water jet is shown in fig 5:

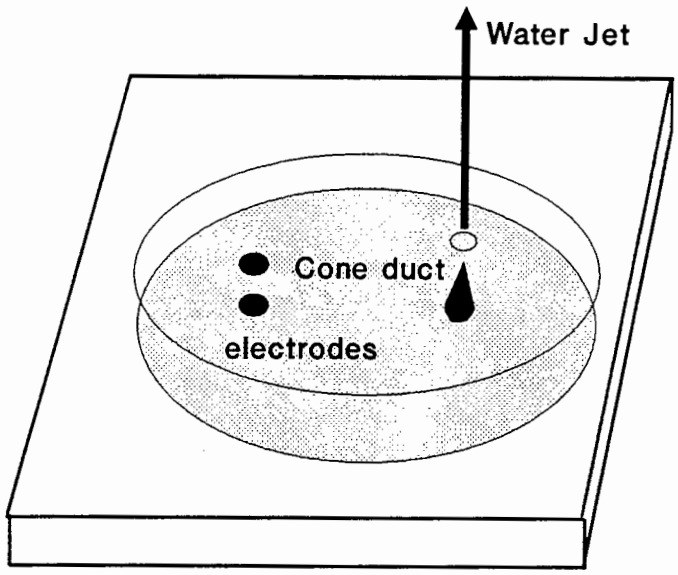

Figure 5 : ***Operation of the elliptically focused water jet generator***

The weak shock generated by the discharge will travel at close to the speed of sound of the liquid (1500 m/s). Electrical discharges can generate significant energies (at least 100 J). The way in which this energy is released can be controlled.

Experimental verification of the elliptical water jet generator has in part been performed by Gustafsson **[15,17]**. In a nonoptimised device, he obtained water jet speeds of the order of 100 m/s. No measurements of the momentum (or mass of the water slugs) have been reported **[18]**.

Gustafsson also used a Schlieren system to observe the shock wave reflection process within the cavity **[15,17]**. An elliptical cavity with two glass cover plates was used (reference **[15]** is shown in **Appendix L**). These photographs showed shock reflection and focusing to the second focal point. However, they also showed a series of other shocks (one in front of the leading shock and a number behind the wave) which were quite consistent over different experiments. Gustafsson attributed these shocks to firstly the wave mode in the cavity wall, and secondly to the electrical circuit.

A detailed theoretical analysis of the energy in the focusing wave-front and the influence of eccentricity (of the cavity) was derived **[16]**. Using these results the effect of the physical design factors of the elliptical cavity can be seen.

1.6.2 The elliptical shock generator application in an ejection system

The performance of the elliptically focused shock wave water jet generator has not been published [74]. This thesis examines the electrical discharge process, the design and simulation of the focusing cavity and experimentally investigates the performance of the device.

Initial indications [16,17,18] are that the generator is suitable for the production of a high speed transient water jet slug. The momentum transfer available in water jet-target collisions are higher than that of air - target interactions. The momentum product of the water jet can be varied by altering the electrical discharge energy and the modification of physical cavity parameters (size, reflecting cone and nozzle).

The repetition rate of the device is determined by the electrical circuit charging time. This is analyzed in Chapter 4. This factor is not for the purposes of this thesis considered a limiting factor. Instead this thesis uses the energy produced by the water jet, the water jet dispersion, and pulse lengths as the sole criteria for ejection system suitability.

1.6.3 The prototype

A prototype elliptical cavity was constructed. The ellipse eccentricity was $e = 0.5$, the major half axis length a, was 50 mm and the minor half axis length b, was 43.33 mm (see **Appendix G** for the definition of an ellipse and **Appendix H** for the technical drawing of the prototype). The focal points are thus located 50 mm apart. The cylindrical cavity was 5 mm in height.

The electrical discharge circuit consisted of : a 0 to 30 kV Brandenburg high voltage DC source - at 1 mA. A 27 MΩ charging resistance was constructed using twenty seven, 1 MΩ resistors in series. These resistors were mounted on a polythene rod and immersed in a PVC tube (diameter 100 mm) filled with silicone liquid (viscosity : cP 100). The PVC tube and end fittings were standard plumbing fittings. Four, 0.04 μF, 60 kV capacitors could be arranged in parallel to form a capacitor bank. An air gap switch of diameter 12.6 mm was used for HV switching. A review of HV switching techniques is performed in **Appendix F**. The calibration of the sphere gaps (gap length vs. breakdown voltage) is shown in **Appendix N**.

1.7 Contents of Chapters 2 to 10

Some of the work presented in Chapters 2 and 3 has been presented at the SAAI Acoustics Today conference held in Durban in September 1989.

Chapter 2 covers the kinematics of the ejection process. The minimum force and momentum required to achieve ejection of the target particle are calculated. Two approaches are considered; firstly using the momentum required to change the momentum vector of the undeflected particle, and secondly using a kinematic approach (integral calculus). Both analyses were found to give similar results.

Chapter 3 attempts to solve the ejection problem by means of a weak acoustic wave in air. This chapter reviews the physical phenomena associated with forces in linear acoustics and calculates the magnitude of these forces. These forces were found to be an order of magnitude less than the required force for ejection (calculated in the previous Chapter). Shock waves in air are also considered as a means of producing the required force. The forces on a sphere due to shocks of different magnitudes are presented.

Chapter 4 discusses methods for the production of transient water jets. The mechanism by which shocks are generated in water as a result of an expanding plasma channel is presented. The HV electrical circuit is analyzed and the factors effecting the circuit efficiency are identified. Shock wave pressures from discharges in liquids are reviewed and calculated.

Chapter 5 covers the design of the elliptical cavity. The principle variables are the ellipse eccentricity and focal length. The effect of these factors on the focused shock wave are examined.

Chapter 6 details the construction of the elliptical cavity. The choice of cavity parameters using the design compromises identified in the previous Chapter are presented. Construction materials and construction techniques used are discussed.

Chapter 7 covers the theoretical simulation of various aspects of the shock wave focusing process in the cavity. Elliptical cavity focal point to focal point focusing was simulated. Comparisons between the theoretical development of Chapter 5 are made. The cone nozzle interaction was also simulated (approximately). Using the results of these simulations, the experimental performance of the different combinations is predicted.

Chapter 8 discusses the techniques used to quantify the water jet.

Pressure measurement and high speed photography techniques are reviewed for the verification of the theory of Chapter 5, and the measurement of the jet velocity respectively.

Chapter 9 discusses the testing of the prototype system. Electrical measurements during the discharge are described - calculations using these quantities show the operation of the circuit. The water jet velocity and energy are measured for a number of physical and electrical configurations. Conclusions regarding the most efficient system are reached.

The conclusion and the recommendations of this thesis are covered in Chapter 10.

CHAPTER 2 :

KINEMATICS OF THE EJECTION PROCESS

The process of material handling by particle ejection requires a knowledge of the trajectories of the particles - while they are in the inspection region and while they are undergoing projectile motion under the action of the external deflection force. This chapter deals with a kinematic analysis of the amount of force that is required for the deflection of a target particle.

Initially, simplified kinematic motion in a two dimensional frictionless system is considered. The effect of gravity is neglected in this analysis. This calculation is referred to as the 'billiard ball analysis' and is covered in section 2.3.1.

The force required to deflect the particle is calculated (to a first approximation) in section 2.4.1 using a momentum vector analysis. This gives the minimum momentum product required by the force deflection mechanism for deflection of a target particle.

A full projectile motion analysis of the trajectories of the particle before, during and after ejection is covered in section 2.4.2 and in **Appendix B**. This analysis relates the deflection force to the deflection angle. The deflection force application angle and duration can be varied. The conveyer belt can have a ramp angle and the position of ejectors can be set in this analysis. Finally, the results of the projectile motion are analyzed and calculated for different physical systems.

2.1 Assumptions

This chapter assumes :

- the target can be regarded as being a particle (i.e. its dimensions are small in comparison to the radius of curvature of its path, and the motion can be treated as the motion of a point) **[19]**.
- the motion of the particle is in a single plane.
- that air resistance can be neglected.

- that particles do not interact (collide).
- the force is time limited and acts on the particle as a point with a constant direction and amplitude.
- that the energy transfer between force and particle is ideal (lossless).

2.2 Definitions used in this analysis

2.2.1 Definition of the angle of deflection ζ

The angle of deflection of the target particle is defined as the angle between the trajectory of the deflected particle and the trajectory of the particle if were not deflected.

2.2.2 Definition of the external application force F_D

The force is assumed to be a pulse with duration t_D seconds. The analysis can be expanded to include a general function of force $F_D(t)$. In section **2.3** ('Billiard ball analysis'), the external force is assumed to act only in the X-direction (i.e. $\gamma = 0^o$).

In section **2.4.1** the external force is shown as the momentum vector p_2. This vector is assumed to be at right angles to the particle's momentum vector p_1.

The kinematic analysis of section **2.4.2** allows an external force F_D, to act on the particle with a variable angle, γ. This angle is measured from the horizontal in an anticlockwise direction.

2.2.3 Target particle initial conditions

The target has a mass **m**. The particle is projected from a conveyer belt into an inspection region. The initial velocity **u** of the particle is the same as the conveyer belt velocity.

The kinematic analysis of section **2.4.2** allows the particle to be projected at an initial angle θ. This angle is measured from the horizontal in an anticlockwise direction.

2.3 Horizontal motion of ideal spheres ('billiard ball analysis')

Motion is assumed to be on a frictionless horizontal plane. The particle travels at an initial velocity u. At point A, it is acted upon by a force F_D, for a time

t_D. This is shown in fig 6:

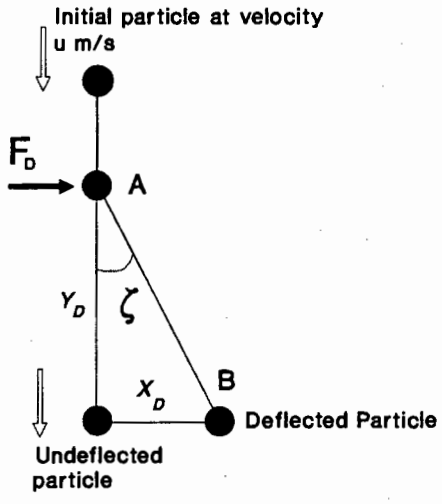

Figure 6 ***:Frictionless horizontal plane motion under the action of a time limited pulse***

The angle of deflection ζ is defined as the angle between the vertical plane and the line joining point A to point B. ζ is then defined as :

$$\tan(\zeta) = \frac{X_D}{Y_D}$$

From the kinematic analysis derived in **Appendix A**, we get :

$$\zeta = \arctan\left(\frac{F_D t_D}{2mu}\right)$$

This equation shows that the shorter the pulse (t_D), the larger will be the required applied force F_D to achieve a given deflection.

For ejection, we require a 50 g (maximum) mass to be deflected by 15°. If the initial velocity u is 5 m/s, the force for different application times is given in the following table :

t_D [s]	F_D [N]
0.00001	13 400
0.0001	1340
0.001	134
0.01	13.4
0.1	1.3
1	0.134

2.4 Projectile analysis

2.4.1 Momentum analysis

The force required to deflect a target particle can, to a first approximation, be found by a simple momentum analysis. The momentum vectors of the undeflected particle and deflection force vector together with their resultant is shown in **fig 7:**

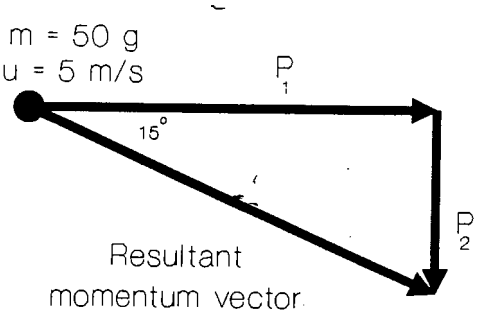

Figure 7 :*Momentum vectors of undeflected particle, deflection force and resultant particle momentum vector*

The momentum vectors are given by :

$$P_1 = m.u$$
$$P_2 = P_1 \tan 15^o$$

Substituting target = 50 g, then :

u = 5 m/s P_2 = 0.067 Kg m/s
u = 10 m/s P_2 = 0.134 Kg m/s

Thus the force required for deflection (for an application time of 1 ms) will be:

u = 5 m/s F_D = 67 N
u = 10 m/s F_D = 135 N

2.4.2 Acceleration-mass projectile analysis

This section covers an analysis of the target particle projectile motion under the influence of gravity, initial conditions, and an external time-limited deflection force. An integral analysis in rectangular co-ordinates is performed using Newtonian kinematics. This section describes the equations of motion of the projectile and of the deflection process. A complete derivation of this analysis can be found in **Appendix B**.

Three stages of analysis

The particle ejection problem can be seen in three parts. Firstly, the motion of a projectile due to some initial velocity **u**, at an initial angle of projection θ. This stage is a common 'shot put' or projectile motion problem. Secondly, the motion of the particle under the action of an external force F_D, starting at point E, acting on the particle with an application angle γ, for an application time of t_D seconds. Finally the particle motion can be described by simple projectile motion under the action of gravity with initial conditions given by the previous conditions. These conditions are shown in **fig 8 , fig 9 and fig 10.**

a) Particle motion before ejection

The motion of a particle projectile with an initial velocity **u** is shown in **fig 8:**

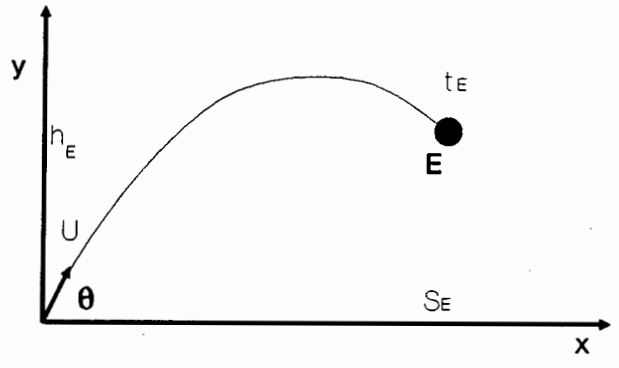

Figure 8 : ***Projectile motion before ejection***

E is the point of ejection - where the deflection force F_D will start to act. This analysis covers the motion of the particle up to point E.

The equations of motion of the projectile are described by (see Appendix **B** for the derivation) :

$$x = u.t\cos(\theta)$$
$$y = u.t.\sin(\theta) - \frac{1}{2}.g.t^2$$

and :

$$V_x = u.\cos(\theta)$$
$$V_y = u.\sin(\theta) - g.t$$

The slope of the path (gradient) at any point is given by :

$$M_1 = \frac{dy}{dx} = \tan(\theta) - \frac{g.x}{u^2}.\sec^2(\theta) \qquad (1)$$

At point E (the point of ejection) the following equations hold :

$$X_{t_E} = S_E = u.t_E.\cos(\theta)$$

$$X_{t_E} = S_E = u.t_E \cos(\theta)$$
$$Y_{t_E} = h_E = u.t_E.\cos(\theta) - \frac{1}{2}g.t_E^2$$

and

$$t_E = \frac{S_E}{u.\cos(\theta)}$$

Where : t_E = time to ejection
S_E = horizontal distance travelled before ejection
h_E = height above (or below) launch point

b) Particle motion under the action of F_D

Forces acting on the particle

The diagram of the forces acting on the target particle is shown in **fig 9** :

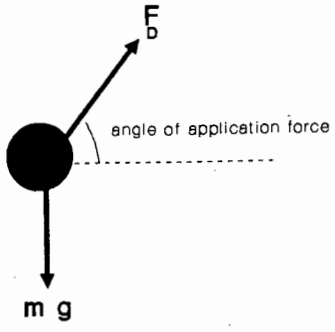

Figure 9 :*Forces acting on the target particle during ejection*

The forces acting on the particle are (By Newton II) :

$$F_X = F_D\cos(\gamma) = ma_X$$
$$F_Y = F_D\cos(\gamma) - mg = ma_Y$$

Thus

$$a_X = \frac{F_D\cos(\gamma)}{m}$$
$$a_Y = \frac{F_D\sin(\gamma) - mg}{m}$$

Motion of the target under the action of F_D

The co-ordinates from the previous section are trasformed to the point E. The initial conditions are obtained from section **2.4.2.a)** - the conditions at point E. The motion of the projectile under the action of F_D is shown in **fig 10** :

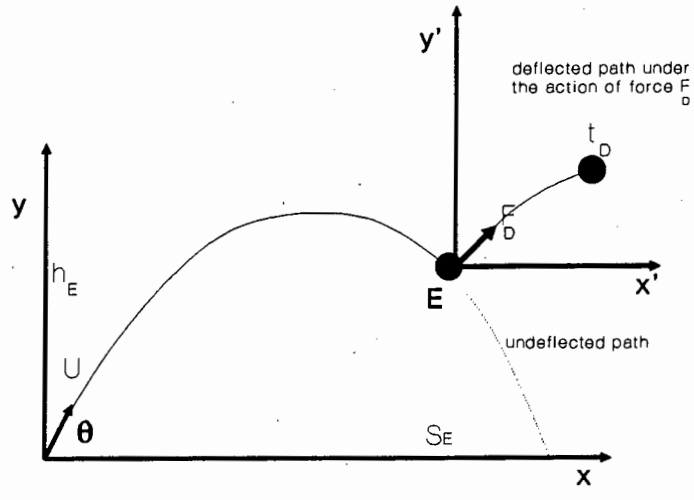

Figure 10 : *Motion of the particle under the action of the ejection force*

The velocity and displacement of the target particle is given by (derived in **Appendix B**) :

$$V_Y' = \frac{F_D.\sin(\gamma) - mg}{m}.t' + u.\sin(\theta) - g.t_E$$

$$V_X' = \frac{F_D.t'.\cos(\gamma)}{m} + u.\cos(\theta)$$

$$x' = u.t'.\cos(\theta) + \frac{F_D.t^2.\cos(\gamma)}{2.m}$$

$$y' = \frac{F_D.\sin(\gamma) - m.gt^2}{2.m} - g.t_E.t' + u.t'.\sin(\theta)$$

The tangent of the deflected path

The gradient of the deflected path can be described by :

$$M_2 = \frac{dy'}{dx'} = \frac{\frac{dy'}{dt'}}{\frac{dx'}{dt'}} = \frac{V_y'}{V_x'}$$

The tangent of the deflected path is then :

$$M_2 = \frac{\frac{F_D.\sin(\gamma) - m.g}{m}.t' + u.\sin(\theta) - g.t_E}{\frac{F_D.t_D.\cos(\gamma)}{m} + u.\cos(\theta)} \qquad (2)$$

Redefinition of deflection angle ζ

The deflection angle has been defined to be the angle between the tangents of the deflected and undeflected paths (M_2 and M_1). In this analysis, the tangent of the undeflected path is defined to be at the point of ejection t_E, and the tangent of the deflected path is defined to be at the point of ejection after the application force has ceased i.e. $t = t_D + t_E$.
Fig 11 shows the generalised deflection of a particle projectile.

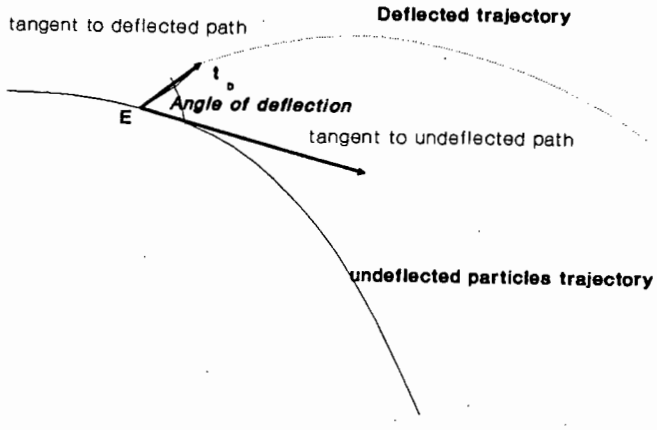

Figure 11 : ***definition of the angle of deflection***

Using the geometric analysis presented in **Appendix C**, the deflection angle in terms of the tangents of the deflected and undeflected paths is given by :

$$\tan(\zeta) = \frac{M_2 - M_1}{1 + M_2.M_1} \qquad (3)$$

Where M_1 and M_2 are obtained from equations (1) and (2).

Deflection force in terms of variables

The deflection force is a function of several variables. Equation (3) relates these variables. The deflection force is a function of :

$$F_D = \mathcal{F}(\zeta, \theta, \gamma, m, u, t_D, t_E)$$

i.e. force variables (application angle γ and application time t_D), system variables (time to ejection t_E and ramp angle θ), and fixed constants (angle of deflection ζ, mass of target m and the initial velocity u). Instead of solving (3) w.r.t. F_D directly, numerical results can be obtained using a numerical methods

equation solver. The results of these calculations are shown in section 2.5.

c) Particle motion after the ejection process

The motion of the particle after the ejection force has ceased will be projectile motion with initial velocity conditions given by the section **2.4.2 b)**. The co-ordinates are transformed to the final point of the deflected trajectory under the - action of F_D. The path of the projectile is shown in **fig 12** :

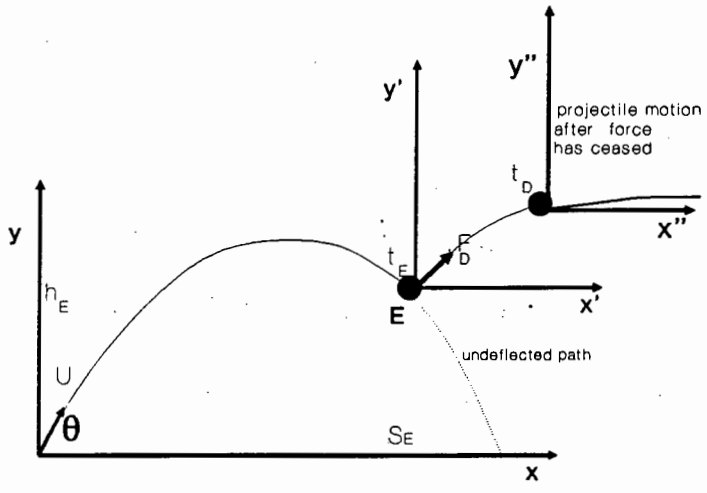

Figure 12: *Particle motion after ejection*

The equations describing target particle projectile motion after the deflection force has ceased are described in **Appendix B.**

2.5 Numerical results

Using the results of section **2.4**, the force required to deflect a particle of mass 50 g with an initial velocity of 5 m/s and a force application time of 1 millisecond, by 15° is :

- By the momentum analysis (**2.4.1**)

$F_D = 67$ N

- By the kinematic analysis (**2.4.2**) :

$F_D = 67$ N

Where $\theta = 0^o$, and the distance to deflection $s_E = 0.001$ m and the angle of application normal to the path of the undeflected particle.

Variation of F_D with angle γ

The variation in the application force required for the deflection of a target particle (m = 50 g) by 15^o is shown in **graph 1** :

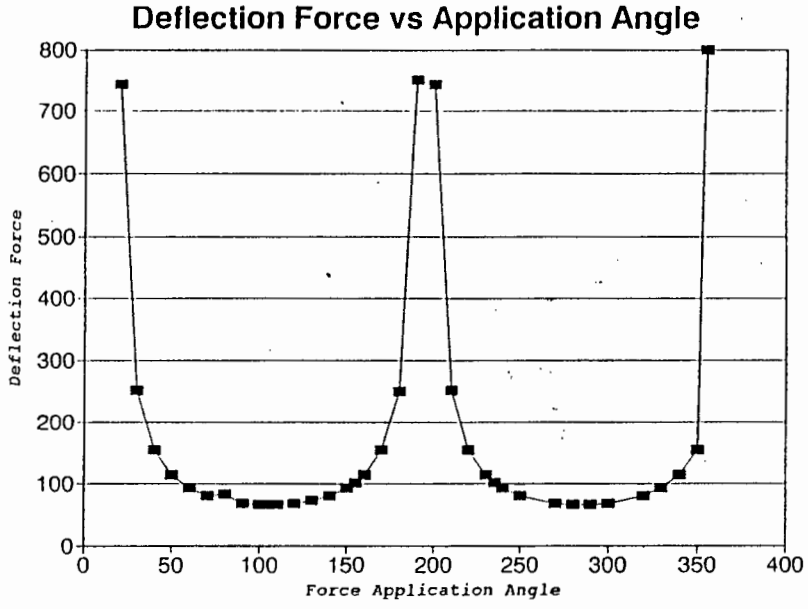

Fig 13 - Graph 1 : m = 50 g , s_E = 0.001 , t_D = 0.001 , $\zeta = 15^o$ and $\theta = 0^o$

The graph shows two minimums : for the case of the ejection force acting from below the particle trajectory and for the case of the ejection force acting from above the trajectory. The force required for deflections in both cases is approximately the same.

The required deflection force is relatively constant for several angles over the minimum.

Analysis of the solutions

The force required for deflection calculated using the two solutions are shown to correlate for force or momentum normal to the path of the undeflected particle. A slightly lower force is required if the application force is acting either upwards and slightly back from the normal to the undeflected trajectory, or acting downwards and slightly forward of the normal.

2.6 Discussion

This chapter has derived expressions for the force and momentum required to move a target particle for a number of different conditions. It was found that in order to achieve the deflection of a target, impulsive forces required either high amplitudes or long action times. The latter is not desirable since we want to minimise the recovery window. Thus we require large force amplitude - pulse source force systems.

Nature of the applied impulse forces

Practical ejectors (air ejectors) have a deflection force of only 2 Newtons. However, these systems have force duration times of the order 15 ms. The force required to deflect particles with short (1 ms or less) application pulses will require considerably stronger application forces. This force has been calculated to be approximately 70 N.

A kinematic analysis of a generalised ejection system has been performed. This analysis has defined the particle motion before and after ejection. The force required for the deflection of the target particles has been calculated in terms of the force and system variables.

CHAPTER 3 :

PARTICLE DEFLECTION USING ACOUSTIC WAVES

Acoustic forces are responsible for a number of physical phenomena such as acoustic levitation and the water fountain (where a water fountain is produced at the surface of a bath of water, in which a high power ultrasonic transducer has been placed, facing the water surface) [20].

This chapter investigates the nature and magnitude of acoustic forces. Applications using acoustic forces are reviewed and the feasibility of using these technologies as a source of force for ejection purposes is discussed.

3.1 Acoustics as a source of force

This section covers the theoretical background to acoustic wave forces.

3.1.1 Momentum

Energy and momentum are transported by acoustic waves [21,22]. Momentum is a vector quantity, thus it has magnitude and direction. The magnitude of the vector is proportional to the sound intensity and the direction of the vector is parallel to that of the wave vector of sound [21]. An external force is required whenever the direction or the magnitude of the momentum vector is to be changed. Thus when some area of a medium is absorbing or generating a sound wave, this area will experience a force acting on it. In addition, when sound passes from one medium to another, the wave will be reflected and refracted. This will cause a change in the momentum vector of the wave. Thus the boundary will experience a net force on it. These forces have been historically termed the Langevin 'radiation pressure'.

3.1.2 Acoustic Radiation Force

The momentum analysis of the preceding section can be used as a basis for the understanding of acoustic radiation force. Two acoustic radiation forces are possible depending on the boundary condition of the system :

The Langevin acoustic radiation force

This force is due to a change in direction or length of the momentum vector. For plane waves, the Langevin radiation pressure is given as twice the kinetic acoustic energy density 2T, or by the total acoustic energy density E_c = incident wave intensity / speed of sound of the medium (I_w/c). The force on the target (F_a) is equal to the surface integral of the radiation pressure [23].

The Rayleigh acoustic radiation pressure

If the sound wave is confined to a rigid tube, the tube will prevent any mass exchange between the sound field and the surrounding medium. The non--linearity of the equation of state p = p(ρ) of the sound conducting medium will cause the average pressure of the tube to be slightly higher than the equilibrium value of pressure P_o without the sound field being present [22]. This is shown in fig 14. The pressure increase from the mean is the Rayleigh radiation pressure.

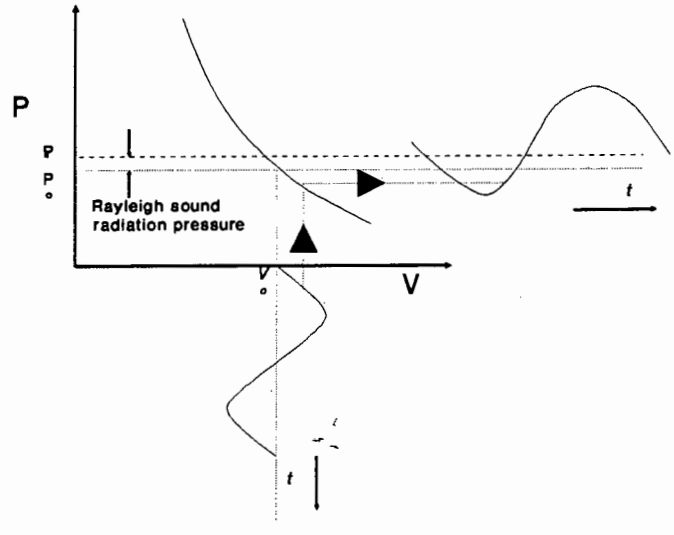

Figure 14 :*Non-linearity of the equation of state produces a non-zero mean pressure - the Rayleigh radiation pressure*

This figure shows the P-V equation of state together with two superimposed time variation graphs. The lower graph is a sinusoidal volume vs. time variation. This compression and expansion causes a resultant pressure vs. time variation constructed from the equation of state. The resultant extrapolated curve is shown to the right of the equation of state.

The boundary conditions for this force are not encountered in ejection systems. Thus this force in not considered further.

3.1.3 Acoustic streaming

The term streaming is given to the bulk flow that results whenever a sound is present in a fluid **[24]**. This effect is shown in **fig 15** :

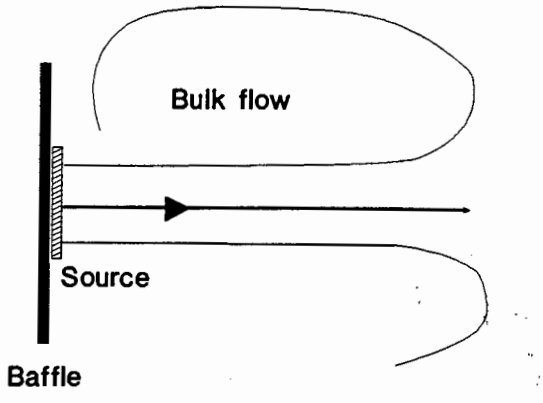

Figure 15 : ***Streaming***

Streaming can be explained by considering the action of the transducer. For the first cycle, the face of the piston or transducer is moving outward. The fluid particles in the vicinity of the transducer are forced predominantly in a direction normal to the surface. After a half-period the surface of the transducer will move inward. It will now suck the fluid back in. However, not all the particles that were forced out earlier are drawn back in; some new particles from the sides flow in. The result is that a net volume flow in the forward direction normal to the transducer will occur.

Force on a target due to acoustic streaming

This force on the target is a result of target drag. It depends on the streaming velocity. Typical streaming velocities in water are about 212 cm/s (for an acoustic pressure amplitude of 0.2×10^6 to 1.2×10^6 N/m^2) **[24]**. The magnitude of this force on a spherical target is given (to a first approximation) by Stoke's formula **[25]**:

$$F_S = 6\pi\eta R_S u$$

Where R_S is the radius of the sphere, u is the mean streaming velocity and η is the fluid viscosity. In water (η = 1.005 cP) the streaming force on a sphere of radius 16 mm in a stream of velocity 0.12 m/s, is approximately 3.6×10^{-5} N. Thus this force is too small to be of practical interest.

3.2 Applications using acoustic forces

A number of applications use acoustic radiation forces. These technologies are reviewed with attention to the magnitude of the maximum force produced by these mechanisms.

3.2.1 Levitation

Acoustic techniques have been employed to levitate objects and liquid drops in space and on earth [26].

Levitation facilitates containerless processing thus avoiding the contaminating influence of the solid crucible. This facilitates the manufacture of near-perfect semiconductors, glass that has a high transparency in the infrared region, and metal foams. It has also been used to study physical phenomena such as : liquid drop physics, bubble dynamics, cavitation and has been used in a number of biological experiments [26,27].

King [28] showed that a standing wave will produce a significantly larger pressure field than a propagating wave with the same energy density. Thus the resonant modes of a cavity are usually the preferred method for the generation of high pressure fields for acoustic levitation [29]. Levitated objects will converge on areas of minimum acoustic potential energy. This corresponds to regions of minimum sound pressure in the standing wave. The particles will remain in these positions (freely suspended) provided that the acoustic forces are strong enough. The force at these positions will be given by [30] :

$$F = \pi R_S^2 (KR)\, \rho\, v_o\, \mathcal{F}\left(\frac{\rho_b}{\rho}, \frac{C_b}{C}\right)$$

Where : R_S = radius of the sphere target

$k = 2\pi/\lambda$ for a gas atmosphere
ρ = density of the gas
v_o = acoustic particle velocity

and where :

$$\mathcal{F}\left(\frac{\rho_b}{\rho}, \frac{C_b}{C}\right) = \frac{5}{6}$$

for liquids or solids levitated in a gas.

Forces in levitation

Using the above equation a solid sphere of 0.4 cm radius would experience a radiation force of approximately 1.3×10^{-3} N, when placed at a velocity antinode in a 20 kHz plane standing wave in which the radiated sound intensity of the source was 1 W/cm^2 (160 dB sound pressure level) and the standing wave gain was threefold.

Higher intensity sources than the one quoted above are available **[30]** and concave reflectors and driver elements can be used (this increases the radiation force by up to 6 times that produced by conventional flat source and reflector systems) **[31]**

3.2.2 Intensity Measurement

The radiation force method has become an important tool for the measurement of ultrasonic power outputs **[32]**. This technique uses the fact that any body that is insonified with a beam of sound will experience a force whose magnitude and direction will depend on the intensity of the field as well as the size and shape of the material of the body. Thus if the force on a target can be measured, and the properties of the target are known, the intensity of the incident radiation can be derived.

Spherical targets have also been widely used in radiation measurements **[33]**. Wave scattering effects must be considered. In addition, some of the sound will be absorbed by the target, thus intrinsic excitation of the sphere itself is possible - affecting the scattering and the radiation force.

Force measurement systems

The most common measurement system is the pendulum set-up. This system uses a spherical target and a telescope micrometer to measure the deflection. This is shown in **fig 16:**

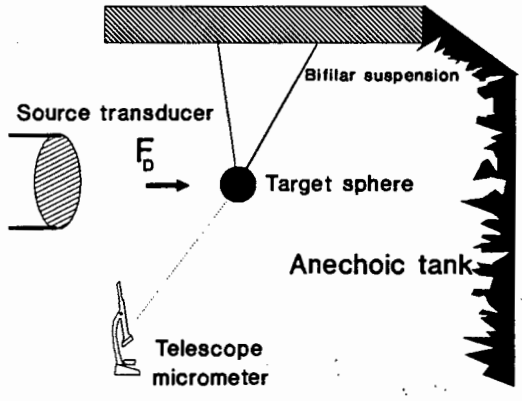

Figure 16 : ***Intensity measurement system***

The radiation force is related to the energy density of the wave (E) by the relation :

$$F = \pi a^2 E Y_p \qquad (4)$$

Where Y_P is the normalised frequency and material dependent, radiation force function (F/cross sectional area/unit energy density). This factor takes into account the scattering and the internal resonance effects of the sphere. Hasegawa **[34]** and Anson and Chivers **[35]** have calculated Y_P for different source and target configurations for a wide range of materials.

Although Y_P has not been calculated for the case of a solid target in air in these references **[34,35]** (it has been presented for the case of a solid in water), the exact magnitude of Y_P is not required for a first approximation of the radiation force. Since the scattering effects will dominate for the case of the target being in air (i.e. ignore the targets compressibility) Y_P will vary between 0 and 3. An average value for a well behaved solid spherical target with a kR (wave no.,

radius of sphere product) greater than 3, is 0.8 . The maximum value for a rigid sphere in a focused transducer is 4 **[90]**.

Expansion of the average energy density term

The mean energy density term, E, in equation (4) can also be written as :

$$E = 0.5 \rho k^2 A^2$$

Where ρ is the density, A is the pressure amplitude normalised to the specific impedance of the medium, and k is the wave number.

If the wave is a plane wave, the average energy density simplifies to :

$$E = \frac{I}{c}$$

since:

$$I = \frac{P_{RMS}^2}{\rho c}$$

Substituting :

$$E = \frac{P_{RMS}^2}{\rho c^2} \qquad (5)$$

The differences between water and air as a host medium can be seen from equasion (5). Although high pressure amplitudes are possible in water (up to 10^6 Pa) the magnitude of the energy density is limited by the speed of sound squared in the denominator. Thus although air has much lower acoustic pressures, it has a lower sound speed, and a lower density than water, the energy density of air will not be considerably smaller than that of water (the intensities of waves in air are much smaller than waves in water).

Numerical results

The acoustic radiation force on a spherical target with the following parameters:

$Y_P = 0.8$

$R_S = 16$ mm

is given by :

- For Air as a medium :

Note : SPL (dB) values are Re 1 μPa.

SPL (dB)	P (Pa)	I (W/m^2)	Force (N)
96	1.26	0.0061	7×10^{-9}
120	20	0.0096	1.8×10^{-6}
160	2000	0.017	0.018
200		0.027	180

The sound pressure level of 200 dB's (SPL) is hypothetical since no practical transducer can produce levels of this magnitude.

- For Water as the medium :

P (Pa)	Force (N)
1.2×10^{6}	0.4

3.3 Force on a target due to a shock wave in air

3.3.1 Finite amplitude waves

When the sound field quantities (sound pressure, varying density, and particle velocities) are no longer small in comparison to their static or mean values, deviations from linear acoustic theory become apparent. The above mentioned acoustic radiation pressure is a result of these non-linearities. Another important nonlinear effect is the formation of shock waves **[36]**.

3.3.2 Shock wave force on a target sphere

Lyakhov and Potapov [37] have calculated the force acting on a sphere due to a shock wave. The shock wave was assumed to be a plane shock wave. The shock wave impinging on a sphere produces two forces - a compressive force and a force in the direction of the plane wave. It is the latter force that is of interest for ejection purposes. The calculation method is given in **Appendix D.**

3.3.3 Numerical results

The force on a 16mm (radius) sphere is calculated for different shock strengths in **Appendix D.** The results are shown in the following table :

M_S	P_{21}	F_a (N)
1.02	1.05	5
1.2	1.5	48
1.65	3	240
2.95	10	1600

Here M_s is the shock wave Mach number (defined in **Appendix D**) and P_{21} is the normalised shock pressure (ratio of shock to ambient pressures).

3.3.4 Air shock wave application as an ejector

Shock waves with Mach numbers greater than 1.6 will produce forces in the range required for deflection. This corresponds to moderate to strong shock strengths **[61]**. The non-linearities in the medium will dominate the shock wave propagation.

Shock wave focusing in air has been studied by a number of researchers **[93,93,94,95,96]**. Most of these studies have concentrated on experimental or numerical simulations. Analytical studies of shock wave propagation is restricted to approximate methods **[95,96,61]**. Non-linearities introduce a number of effects which differ strongly from linear geometric process - self focusing and shortening of the focal length, cusps and arêtes can occur. The fluid flow in the medium is non-zero and can (for Mach numbers > 2.068) be supersonic **[96]**. Reflection and diffraction of shocks around boundaries is complex, depending on the shock wave history, wall geometry, shock amplitudes and angle of incidence **[97]**.

The production of shock waves in the laboratory environment is usually accomplished using a shock tube - a tube with two sections separated by a diaphragm, with one compartment pressurised. The diaphragm is burst and a plane shock wave propagates down the tube. Shock strengths of Mach 3 can be generated using these systems. Micro-explosions can also used to produce air shocks. However, these methods are not repetitive. Spherical shocks can be generated using an air spark. Shock amplitudes are restricted to small Mach numbers (M_S = 1.01, E_{spark} = 0.05 J) **[44,45,98]**.

The containment of shock waves is also complicated by the non-linear effects of shock reflection and diffraction **[96,99]**.

3.4 Conclusions

Acoustic forces are in general very low. The forces are only significant when the source is a finite amplitude source (greater than 160 dB). There is no marked advantage (other than the possible generation of high pressure amplitudes) of locating the system in water. The force obtained from conventional acoustic sources is too low to be used in a particle ejector application.

Strong plane shock waves can give forces in the range required. However, shock waves are difficult to contain, focus and produce in air and are therefore unsuitable for ejector application.

CHAPTER 4 :

PARTICLE DEFLECTION USING AN ELECTRICAL DISCHARGE AND A WATER JET SLUG

The previous chapter reviewed acoustic force mechanisms for the production of a deflection force. Chapter 2 has calculated that for particle ejection, the ejection force should be greater than 70 N if the force was to be a pulse force of duration 1 millisecond. Acoustic forces were found to be an order of magnitude lower. An alternative form of deflection force generation and energy transfer was thus required. A water jet slug impinging on the target particle was proposed to meet the ejection system requirement.

4.1 Water jet systems

Water jets have been used in a number of applications - eg. the cleaning and cutting of materials [10,17,38,39]. In general water jets are either pulsed (transient) systems or continuous jets. The former emits a single slug of water while the latter emits a continuous stream.

4.1.1 Water jet suitability as an ejector

The requirements for the ejection system (given in the introduction) are :

- To separate desired particles from a moving conveyer belt containing both desired and undesired material.
- To achieve an optimum concentration of separated material.
- To be a repetitive system.
- To have minimal dispersion and deflection of material around the target i.e. be impulsive and restricted in width.

The requirement that the ejection force be a time limited impulse force indicates that continuous water jet systems are unsuitable. Continuous systems can be designed to produce pulsed water jets. These systems use a mechanism to interrupt the flow - usually a mechanical obstacle [17,10].

The slug of water will have a mass (equal to the density of water multiplied by the volume of the slug). Transient water jets can attain high speeds, thus

relatively high momentum products (p = m.v) can (in theory) be obtained. If the momentum is greater than 0.067 kg.m/s, a particle of mass 50 g at velocity of 5 m/s will be deflected by 15° or more (Chapter 2).

Thus a 1 ml water drop impinging on a 50 g target, will cause ejection if the slug has a velocity greater than 67 m/s (assuming an ideal lossless transfer of energy during the collision).

The momentum product can also be used to enhance the impulse nature of the ejection system. The length of the slug can be made short and the velocity large - while still achieving the same momentum. The dispersion of the deflection force energy is then minimised.

4.1.2 Pulse water jets

Pulsed water jets can be produced by either **[17]**: A piston impinging on a slug of water in a chamber. This slug is then forced into an initially empty nozzle, where it is accelerated to produce a jet speed (of up to several kilometres per second **[10]**). This method is termed the cumulation method **[17]**. Or secondly, the shock reflection method, where a shock wave is sent through a chamber that is completely filled with liquid **[40]**. When the shock wave reaches the free surface of the liquid at the front end of the nozzle, a jet is emitted.

These cumulation method and the shock reflection method are illustrated in **fig 17:**

relatively high momentum products (p = m.v) can (in theory) be obtained. If the momentum is greater than 0.067 kg.m/s, a particle of mass 50 g at velocity of 5 m/s will be deflected by 15° or more (Chapter 2).

Thus a 1 ml water drop impinging on a 50 g target, will cause ejection if the slug has a velocity greater than 67 m/s (assuming an ideal lossless transfer of energy during the collision).

The momentum product can also be used to enhance the impulse nature of the ejection system. The length of the slug can be made short and the velocity large - while still achieving the same momentum. The dispersion of the deflection forces energy is then minimised.

4.1.2 Pulse water jets

Pulsed water jets can be produced by either **[17]**: A piston impinging on a slug of water in a chamber. This slug is then forced into an initially empty nozzle, where it is accelerated to produce a jet speed (of up to several kilometres per second **[10]**). This method is termed the cumulation method **[17]**. Or secondly, the shock reflection method, where a shock wave is sent through a chamber that is completely filled with liquid **[40]**. When the shock wave reaches the free surface of the liquid at the front end of the nozzle, a jet is emitted.

These cumulation method and the shock reflection method are illustrated in **fig 17:**

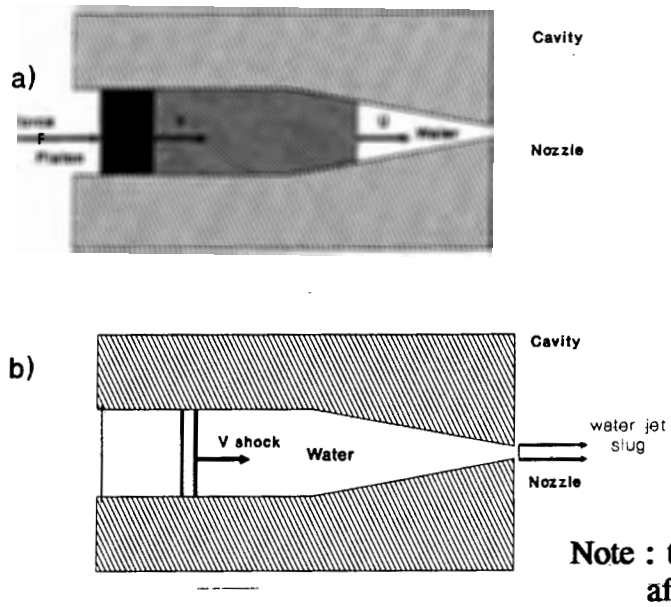

Note : the slug is only emitted after the shock reaches the nozzle exit.

Figure 17: ***Transient water jet production by a) the cumulation method, and b) the shock reflection method***

University of Cape Town

4.1.3 Repetition rates of shock wave sources

Pulsed water jet systems are suitable for ejection purposes. However, repetition rates in the case of cumulation devices [3] are limited by the mechanical inertias of the moving parts required to accelerate the water jet [17]. These moving parts are usually pistons of high mass accelerated to impact an initially stationary slug of water (as shown in fig 17).

In the shock reflection method, the operation frequency is not limited in the same way as in the cumulation method. The shock can be generated using alternate methods such as micro-explosions (lead azide beads) [41], laser pulses [42] and electrical discharges [5,6,7,8,17,43]. These techniques can be designed such that there are no moving mechanical parts and the limitations in operating frequency are set by the technique used.

4.1.4 Choice of a shock generation method

Alternate sources

Laser sources can be used to produce strong pressure shock waves in water [42]. However, the cost of a pulsed laser system is prohibitively expensive for a project of this nature. Micro-explosions [41] are not repetitive, thus they are not suitable.

Electrical discharge source

Electrical discharges are an experimentally convenient energy source for the production of shock waves. Their repetition rate is determined by the time taken to charge the high voltage circuit. A number of electrical parameters can be varied - giving the designer control over the total energy released in the water discharge as well as control over the way it is released (the energy release w.r.t. time).

4.2 Shock wave production by an electrical discharge

4.2.1 Shocks from sparks

Transient shock waves can be produced by short duration discharges between electrodes. These discharges have been used to generate shocks in air **[45,46]** and in water **[43]**. The high voltage discharge across the electrodes must create an electric field strength in excess of that required for breakdown of the medium. Water requires a field strength of between 10 - 100 kV/cm **[46,62]**, while air requires breakdown strengths of the order 11 kV/cm. The resulting plasma channel formed between the electrodes will expand rapidly, introducing a shock wave into the surrounding medium.

4.2.2 Energy storage for discharges

Capacitors can release their energy relatively quickly (in the order of μS). The energy is stored over a long period by a source of low power. Other storage systems (inductive, mechanical) are in general temporary storage mechanisms and have slow discharge times (of the order ms to seconds)**[46,47]**.

4.2.3 Electrical circuit

A discharge circuit suitable for the production of shock waves in water **[7]** is shown in **fig 18 :**

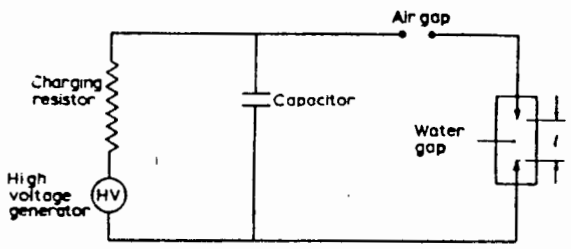

Figure 18: *Itemised circuit for the production of a plasma discharge is water*

This circuit consists of a high voltage DC source, a capacitor bank, charging resistor, water gap discharge electrodes and a switch (usually an air gap). The source charges the capacitor bank to a voltage greater than the breakdown voltage of the water gap discharge electrodes. The charging current is limited by the charging resistor. If the high speed switch is closed, the gap will break down and the capacitor energy will be discharged through the water gap.

4.3 Analysis of the electrical circuit

The itemised discharge circuit is analyzed in two stages : the charging circuit and the RLC discharge circuit. The first analysis is used to determine the charging time for the circuit, and hence the possible repetition rate for the system. The second analysis shows what factors influence the power release in the water gap. Conditions for maximising this transfer can then be obtained.

4.3.1 Equivalent circuit

The equivalent circuit charging and discharge circuit is shown in **fig 19:**

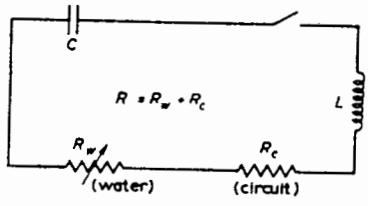

Figure 19: ***Equivalent discharge circuit***

The circuit components of the itemised circuit shown in **fig 18** are shown as their circuit equivalents. The air gap is represented as a high speed switch, the water gap as a resistance, and an inductance L is included. This represents the inductance of the circuit leads and components. The water gap resistance varies throughout the discharge process **[6,7]**. However, as a first approximate, it can be assumed to be constant **[48]**[1].

The circuit shown in **fig 17** can be seen as two separate circuits. Firstly a RC charging circuit $t<0$ (before the switch or air gap is closed) and secondly a series RLC circuit $t\geq 0$.

4.3.2 Charging circuit

If the HV source could supply the capacitor bank with a constant current, the charging time would be given by :

[1] The order of resistance of the water spark gap is significantly higher than that obtained with spark gaps in air. The magnitude of a typical spark gap resistance is calculated in **Appendix F.**

$$i = C \frac{dV}{dt}$$

$$V = \frac{1}{C} \int_0^t i\,dt$$

$$= \frac{it}{C}$$

$$t = \frac{VC}{i}$$

Thus if the charging current was 1 mA, the charging voltage 20 kV, and the capacitor bank 0.1 μF, the charging time would be :

t = 2 seconds

However, in general the HV charging circuit will not supply a constant current. The charging circuit will be a RC series circuit with a constant voltage source (R_S is the charging resistor). In this circuit the charging current will decrease as the capacitor starts to attain its final potential. This circuit is analyzed in **Appendix E.** The charging time is determined from the time constant of the circuit. This is given by :

$$\tau = R_S C$$

4τ corresponds to 98 % of the final charge and 96 % of the final energy having been transferred to the capacitor. If the charging resistor R is 30 MΩ and the capacitance 0.1 μF, 4τ corresponds to a time of 12 seconds.

The maximum efficiency of a current limiting resistor - HV DC source system is shown in **Appendix E** to be 50 % Circuits with better charging efficiencies and faster charge times can be designed **[47,48]**. However, this aspect of the project is beyond the scope of this thesis.

4.3.3 Discharge circuit

The discharge circuit is analyzed in detail in **Appendix E.** For a series RLC circuit (with the capacitor at some initial charge) the current response will be given by three solutions to a second order differential equation. These three

solutions are illustrated in fig 20:

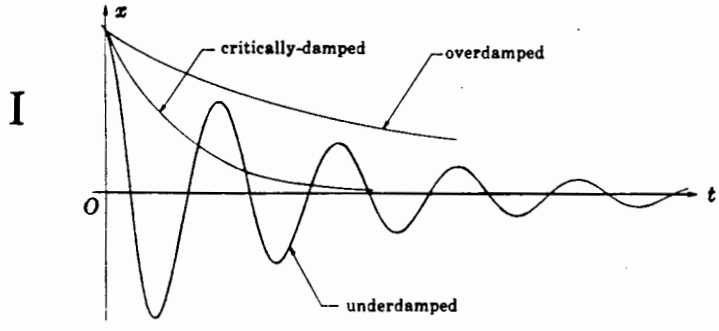

Figure 20: ***Current responses in a series RLC circuit***

The anticipated value of resistance (circuit leads and the water gap R_W : $R = R_W + R_{circuit}$) will be relatively small. Thus :

$$\frac{1}{LC} > \frac{R^2}{2L}$$

This corresponds to the underdamped solution. Some oscillation in the current will be expected. Critical damping (no oscillation) will be achieved if :

$$\xi = \frac{1}{2} R \sqrt{\frac{C}{L}}$$
$$= 1$$

The required circuit resistance for critical damping is then :

$$R = 2\sqrt{\frac{L}{C}}$$

In addition, the current pulse duration of a critically damped circuit is approximately given by :

$$T_{critdamp} \approx 3\sqrt{\frac{L}{C}}$$

4.3.4 Power release in the water gap resistance R_W

The way in which power is released in the circuit resistance varies with different values of the circuit damping factor ξ is shown in **fig 21** (after Carley **[48]**) :

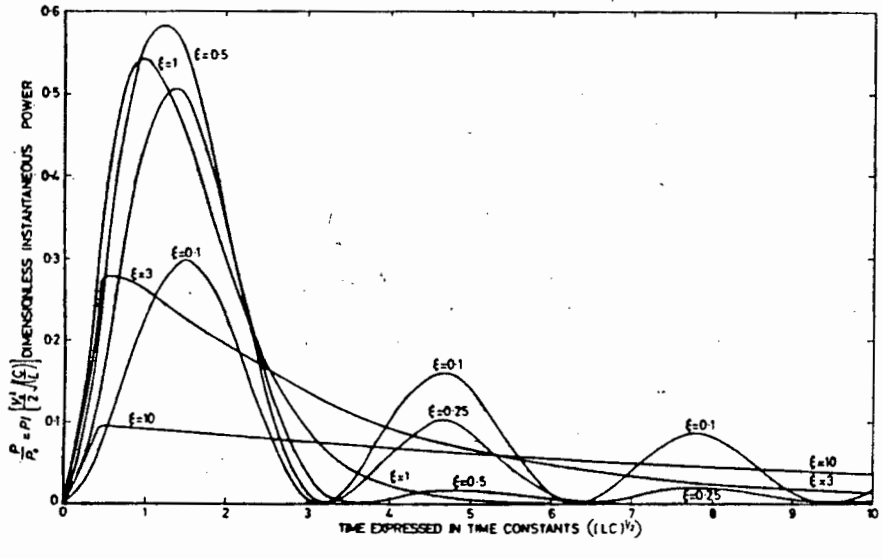

Figure 21: *Power release in the circuit resistance as a function of the damping factor ξ*

The most concentrated power release in the initial peak occurs for values of ξ in the range 0.5 to 1.

4.3.5 Oscillations

The current oscillation associated with a RLC underdamped circuit will spread the energy of the discharge over several cycles. **Fig 21** shows that circuits with $\xi < 1$ will be oscillatory. Multiple oscillations are thought to form several smaller shocks in addition to the initial peak due to the initial current rise. Shock wave propagation or focusing could be obstructed by multiple shock waves **[17]**.

4.4 The discharge process

4.4.1 Establishment of the spark channel

Breakdown in the water gap has a number of physical effects which influence circuit operation.

Ionic discharges

After switching of the primary circuit, the voltage across the water spark gap will rise to the capacitor voltage in a fraction of a microsecond. There is a variable delay before one or both of the electrodes emit streamers and a weak current conducts between the electrodes **[6]**. This weak current is an ionic current. It represents an energy loss in the circuit since it does not contribute to the formation or development of the plasma channel.

The ionic current conduction lowers the voltage across the water gap. The mean rate at which sparks can form and the rate at which the voltage across the electrode falls **[48]** are in competition. If the delay before the breakdown is so long that the ionic conduction lowers the voltage below the breakdown strength of the water, a 'quiet' discharge will occur **[6,48,49]**. This is discussed further in the experimental results of chapter 9.

The electric field between the electrodes depends on the applied voltage, the gap spacing, and the shape of the electrodes and surrounding cavity. The higher the electric field strength, the shorter this delay, and the less likelihood of quiet discharges. Typical values of the delay are from a few to 100 microseconds **[48]**.

Channel formation

After the streamers have provided the conducting path between the electrodes, the voltage across the gap will decrease rapidly. At the same time a

considerable rise in current takes place [50]. A rapid transfer of energy to the initially small volume (initially a high resistance) of the spark channel will occur if the current rise time is short. The channel temperature rises rapidly and produces an expansion in the surrounding fluid.
The mechanical inertia of the surrounding fluid tends to resist the channel expansion. This results in high pressures and shock waves development.

Higher energy sparks ($>>$ 100 J) can introduce complex expansion rings in the liquid around the discharge [43]. This ring oscillates for several microseconds after the discharge has occurred. Lithotripter research has also reported [8] the occurrence of a pressure pulse due to the collapse of the plasma bubble approximately 1 millisecond after discharge (ie. after the shock has reached the second focus). These factors are not expected to influence this thesis and are not discussed further.

Alpha torque forces

New research [51] has postulated that spark discharges (plasmas) will produce pressure shock amplitudes far in excess of equivalent energy thermally driven expansion systems. This is as a result of the so called 'alpha torque forces'. The pressure in the fluid surrounding a discharge is thought to be the result of 'alpha torque forces' between the plasma channel and the fluid. The work has not been fully verified and is assumed to be beyond the scope of this thesis.

Initiating wire to ensure rapid breakdown

The variable delay before breakdown can be minimised by the inclusion of an initiating metal wire between the water gap electrodes [43]. This thin (typically 1mm) wire will cause the gap to breakdown almost immediately. The reliability of discharges is increased since the streamers and channel paths are repeatable. Although this technique has seen application in some physical experimental systems [49], it is not suitable for repetitive discharges.

4.4.2 Pressure from a spark discharge in water

Zimmerman [52] calculated the pressure at the spark channel boundary of a discharge in water. To do this, he assumed that the power release in the gap could be approximated by a triangle. This is shown in fig 22 together with the calculated form of pressure release. As a comparison, the power release of a circuit that is nearly damped (obtained from fig 21) is superimposed on the ideal, triangular form.

If a nearly damped discharge is chosen [48]:

$$\theta \approx 1.2\sqrt{LC}$$
$$T \approx 3\sqrt{LC}$$

Substituting these values into equation (4) we get:

$$P_c = 0.82 \frac{V}{\sqrt{Ll}}$$

Where : L is the circuit inductance (μH).

This equation shows that high pressures will be achieved if the circuit inductance is minimised, high voltages are used and if the water gap lengths are large.

If the circuit values are V = 20 kV, l = 3 mm , L = 1 μH and C = 0.1 μF, the calculated pressure at the channel boundary is approximately ≈ 30 kiloBar.

Validity of calculated pressure

Zimmerman[52] predicts the pressure to be constant for a time. It has been experimentally measured to decrease after the start of the discharge. The difference can be attributed to the postulated triangular pulse being an approximation of the actual power release and the resistance of the spark channel varying throughout the discharge.

Other calculations [53] give results 4 times less optimistic than Zimmerman. Bjorno [10] derived an approximate empirical expression for the pressure due to a shock wave :

$$P_m = \frac{6\ (lV^2)^{\frac{1}{3}}}{D}$$

Where D is the distance from the spark source.

Substituting the values V = 20 kV, the gap length l = 3 mm, and the distance from the channel to be 2 cm, the calculated pressure is 64 kBar. Extension of (5) to small values of D (channel boundary) is inaccurate - small values of D were not measured due to electromagnetic interference from the spark.

Shock wave pulse and propagation

The energy from the discharge in the channel will cause a shock or pressure discontinuity which will have the form shown in **fig 23:**

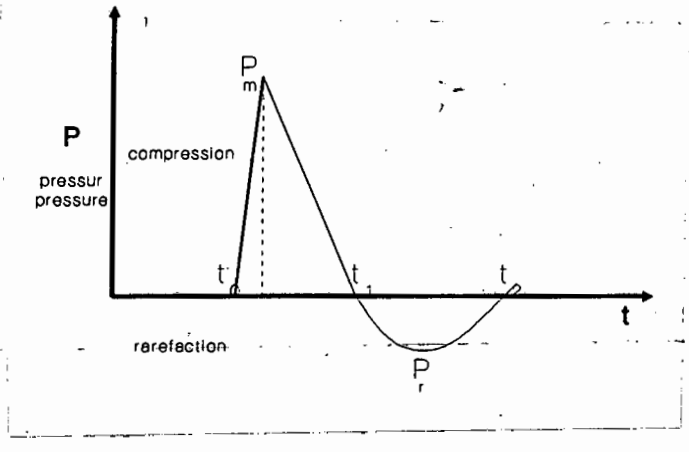

Figure 23: ***Shock wave pulse shape***

This figure shows a vertical shock front, behind which the compressive stress falls off approximately exponentially. The pulse can be approximated by a triangular form. The shock wave will expand as a spherical or cylindrical front depending on the geometry of the system. Weak shock waves will decay to their acoustic limits **[48].**

The shock wave pulse duration is related to the discharge time T. Using **fig 21,** the pulse duration is shown to increase with increasing ξ.

4.5 Controllable parameters in the electrical circuit

Electrical water gap discharge circuits have a number of controllable parameters. These parameters facilitate the control of the water sparks intensity, risetime and duration and thus control of the pressure shock in the water.

- **Electrical energy**

V and C give the stored electrical energy = ½ CV^2

- **Water gap resistance**

The longer the plasma channel or the smaller the channel width, the greater the resistance of the water gap - and the greater the energy dissipated in the gap.

- **Rate of current increase**

The risetime of the current will depend on the circuit damping (as shown in **fig 21**).

- **Current pulse duration**

The duration of the current pulse is given by the time constant $\tau = (LC)^{½}$. If the circuit is underdamped the duration of the first current pulse is $\approx 4\tau$.

- **Circuit inductance**

The energy requirement sets the capacitance. The rate of current increase and discharge duration conditions require small values of circuit inductance (see below). All components will have some value of self inductance. Minimisation of this quantity is discussed in **Appendix S**.

Optimum circuit configuration

There are two considerations : firstly the shock wave pressure and secondly the shock wave profile. The electrical energy must be transferred to the shock efficiently. As high as possible shock pressures are required. Shock durations are to be small since shock waves decay and increase in pulse length as they expand. For an impulsive water jet, the initiating shock duration should be as small as possible so as to produce a water jet slug that contains less fluid but at a higher velocity.

The energy of the electrical circuit must be transferred to the water gap when the spark channel is smallest - i.e. when the spark channel resistance is highest. This means that the rate of current rise must be as high as possible. The risetime depends on the damping of the circuit. The highest risetimes are for ξ in the range 0.5 to 1.

The energy of the electrical circuit is determined from the capacitance and the

voltage. It is proportional to the square of the voltage. The pulse duration of the discharge is proportional to the root of LC. Thus it is evident that capacitance and inductance are to be small. The energy requirement (see efficiency section 4.6) will fix the value of circuit capacitance. High voltages are advantageous for high pressures (equation (4)). Low circuit inductances are required for small pulse durations and high shock pressures.

The circuit should be slightly underdamped or critically damped for maximum power transfer to the water gap, and for maximum current risetimes. The circuit damping can be set by altering the length of the spark gap thereby changing the water gap resistance. A high value of gap length is advantageous for large shock pressures.

4.6 Energy analysis

In order to see what efficiencies are required for the ejection system, an energy balance is performed on the electrical and kinematic processes.

4.6.1 Required system efficiency

Electrical Energy in : $E = 0.5\ C\ V^2$
$= 18\ J$

($V_{max} = 15$ kV, $C_{max} = 0.16\ \mu F$)

Kinematic energy required :

The required change in momentum is

$p = 0.067$ kg m/s
$= m\ v$

Thus : $v = p/m$

$E_K = 0.5\ m\ v^2$
$= 0.5\ p^2/m$
$= 0.05$ J

Thus the minimum kinetic energy that is required is approximately 0.1 J for the ejection process (ie. for a mass of m = 50 g to be deflected by 15°).

Thus the minimum efficiency that is required is approximately : 1%

4.6.2 Efficiency of the discharge shock wave process

The energy released by the electrical circuit is not all converted into mechanical (shock) energy [49]. Instead the electrical energy is converted into :

- mechanical work to generate the water shock wave [48,52]
- thermal radiation [49]
- ionic discharge in the pre-discharge phase [48]
- thermal conduction to the surrounding fluid [49]
- RF radiation
- Light / UV radiation [49]

4.6.3 Efficiencies obtained

Frungel [54,55] describes experiments on the efficiency of plasma arc discharges. The experiment used an annular and rod electrodes and discharged a small mass vertically. Using different discharge energies and different projectile masses they calculated the electrical to mechanical efficiency of the system to be in the region of 1 %.

4.6.4 Acoustic efficiency

This is defined to be the ratio of the available energy in the positive pulse of the shock wave to the total input energy. This was measured by Bjorno [6] to be approximately 4 % for a 15 kV, 1 μF, subcritically damped circuit.

4.7 Conclusions

The transient water jet has been identified as a suitable force mechanism for ejection. The shock wave reflection technique for the production of water jets is repetitive. An electrical discharge has been investigated as a suitable energy source for the shock wave.

An analysis of the electrical discharge circuit has been performed. Factors influencing the conversion of electrical energy to shock wave energy have been identified. An optimum circuit configuration has been proposed.

The system efficiency is required to be greater than 2.5 % for ejection to occur. Published efficiencies give electrical to pressure efficiencies of the order of 4 % and electrical to kinetic efficiencies of the order of 1 %.

CHAPTER 5 :

DESIGN OF AN ELLIPTICAL CAVITY

A device for the production a transient water jet using the shock reflection method (described in Chapter 4) and an electrical discharge has been proposed [15,16,17].

The previous chapter proposed an electrical discharge as the source of energy for the production of a weak shock wave in a liquid. The shock wave from an electrical discharge is not plane - the wave can be spherical or approximately cylindrical depending on the geometry of the cavity and electrode arrangement.

In general, the shock wave arriving at the surface of the nozzle from an arbitrary cavity, will not necessarily be coherent - but rather a succession of shocks, thereby reducing the energy available for the production of the jet. To optimally utilise the discharge energy, the cavity has to be designed in such a way that the shock is focused at the nozzle.

An elliptical cavity described in this chapter is one solution to the focusing problem. Weak shock wave focusing within the cavity is analyzed. The results of this analysis are used for the design of an elliptical cavity prototype.

5.1 Elliptically focused water jet generator

5.1.1 Properties of ellipses

From Huygen's principle [56], it can be seen that rays from one focal point of ellipse and ellipsoid geometries converge and focus to the second focal point. This is proved geometrically [57] in Appendix F. This principle assumes that the wavelength is small with respect to boundary (i.e. high frequency waves) and that the reflection process is geometric.

A spark discharge will produce a spherical or cylindrical shock wave depending on the boundary conditions. One way of focusing the electrical energy from the discharge to another point (the nozzle) is to use the focusing property of ellipses. An ellipsoid or elliptical cylindrical cavity with the discharge at one focus will focus spherical and cylindrical waves to the second focus respectively.
The way in which ellipse geometries focus energy from one focal point to the

other is shown in **fig 24** :

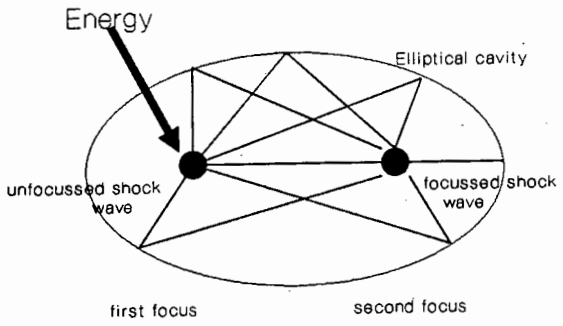

Note : lines show the trajectories of an element on the shock wave

Figure 24: ***Ellipse geometry as a means of focusing energy to a point.***

The parameters describing ellipse properties are given in **Appendix F.**

5.1.2 Applications using ellipses to focus a spark discharge

Lithotripsy technology has been reviewed in **Chapter 1.** Dornier system lithotripters use ellipsoidal cavities to focus the water shock from an electrode pair at one focus to the kidney stone at the other.

Ellipsoidal cavities (for spherical point source focusing) are difficult to construct. They require a number of rings to be accurately machined - these rings are slotted together such that their interior makes a three dimensional ellipsoidal cavity **[58].** In the water jet application, it is useful instead to make use of the cylindrical properties of a spark discharge arrangement.

5.1.3 The water jet device

The elliptically focused weak shock water jet generator proposed by Gustafsson **[16,17]** is shown in cross-section in **fig 25** :

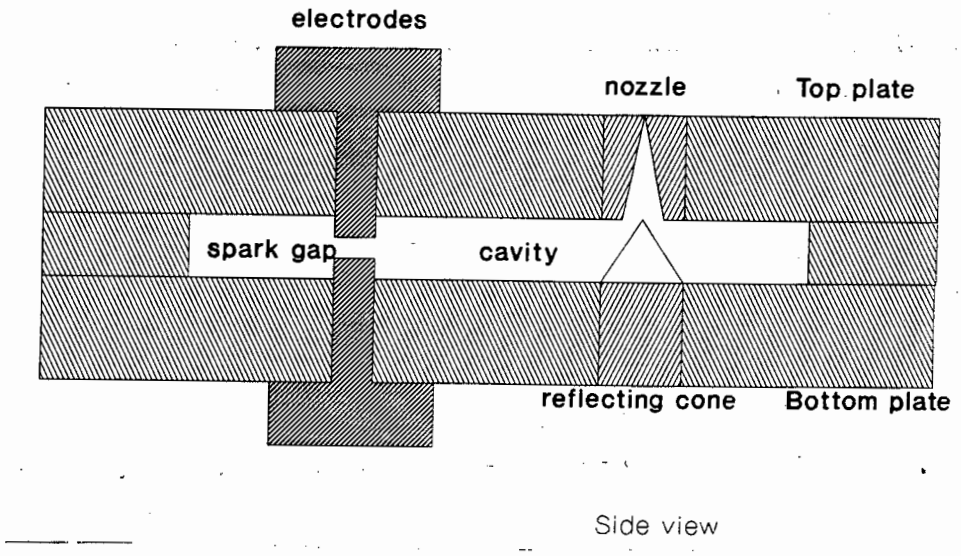

Figure 25: ***Elliptical cavity water jet in cross section***

The cavity is planar with an elliptical shape. The electrodes of the electrical discharge circuit are situated at the first focus of the ellipse. They are mounted end on, perpendicular to the ellipse. The shock wave generated by the electrical discharge will expand cylindrically until it comes into contact with the cavity walls. There the wave will undergo a reflection; part of the incident energy will be reflected and part will be transmitted into the cavity wall.

The reflected shock wave will converge towards the second focus of the ellipse. In order to efficiently utilize the initial shock expansion wave from the discharge, as much shock energy as possible must be focused to the second foci. At the far focus the converging shock wave is approximately reflected by a right angled cone possitioned normal towards the nozzle. This cone changes the direction of shock wave propagation of a portion of the incident wave through 90°. The resultant reflected shock wave in the nozzle will produce a water jet slug (vertically).

5.2 Wave propagation in elliptical cavities

Gustafsson **[16,17]** has published, using two separate methods, derivations of weak shock wave focusing and pressure distributions in an elliptical cavity. The pressure distribution in and behind the converging weak shock was derived. He showed that this distribution is dependant on the eccentricity of the ellipse as well as the wall admittance. The calculated pressure distribution in the cavity was found to be asymmetric.

This section describes the calculation procedure that was used in this analysis. Results pertinent to the design of practical elliptical water jet devices are presented.

5.2.1 Weak shock waves

Nonlinear effects are negligible for pressures up to the order of several kBar [16]. This means that the sound speed of the weak shock wave will be close to the acoustic sound speed of 1500 m/s. Wave propagation can therefore be described by linear acoustic techniques. Shock waves fitting these requirements are termed weak shock waves.

5.2.2 Weak shock wave focusing

General shock wave propagation within a elliptical cavity is shown in fig 26:

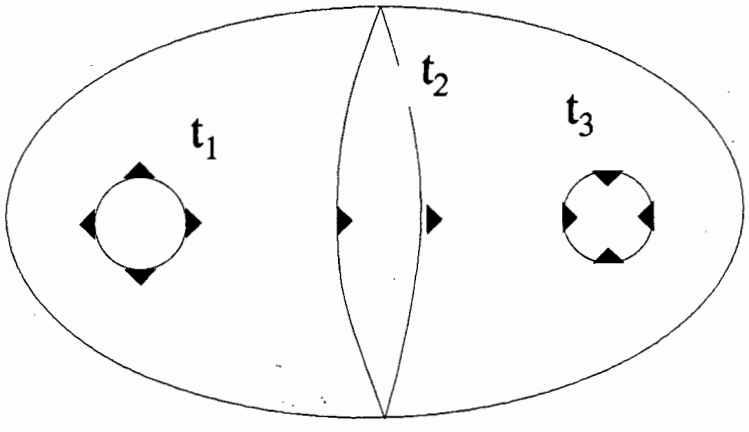

Figure 26: ***Weak shock wave focusing in the ellipse at 3 different times***

This diagram shows the shock wave expanding cylindrically until it is reflected by the cavity walls. At time t_2 the weak shock wave has two components : a concave converging component and a convex expanding component. The latter will pass through the second focus before it is reflected from the rear cavity wall. The final focused wave will be a circular symmetric, cylindrical wave converging on the second focus.

5.2.3 Angle of incidence vs. angle of reflection

The focusing process shown in **fig 24** assumes that the weak shock wave reflection process is regular and that the angle of incidence equals the angle of reflection. If the wave strength is such that the non-linearities of the medium are no longer small (shock wave), the reflection will be a complex process depending on the shock strength and incident angle (**Chapter 3**).

Gustafsson **[15]**, using Schlieren techniques (described in section 8.2.1) showed that reflection in the cavity was regular for a 8 kV, 0.6 μF (E = 19.2 J) spark induced shock wave. Reference **[15]** is included in **Appendix L.**

5.2.4 Wave energy distribution in the wave front

The procedure for the calculation of the pressure in the converging wave of elliptical cavities is as follows **[17]** :

Initial expanding weak shock wave :

The linear (non-convective) form of the wave equation is **[59]**:

$$c\,\nabla^2\phi = \frac{\partial^2\phi}{\partial t^2}$$

Where c is a constant and ϕ is the velocity potential.

The co-ordinate system employed in the analysis of the ellipse is shown in **fig** 27 (after Gustafsson **[16,17]**:

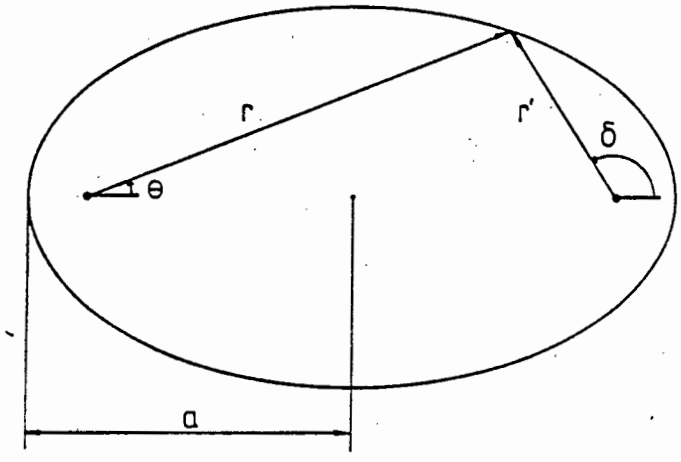

Figure 27: *Co-ordinate system used - polar co-ords*

Two cylindrical co-ordinate systems - centred on the two focal points - are used. The shock wave originates at the focal point on the right and is described by r' and the angle δ. It converges to the second focus where it is described by r and the angle θ. The form of the wave equation using cylindrical co-ordinates for the converging wave is then **[60]**:

$$\frac{\partial^2\phi}{\partial r^2} + \frac{1}{r}\frac{\partial\phi}{\partial r} = \frac{\partial^2\phi}{\partial t^2}$$

The diverging wave is described by the same form of equation, but uses r' in place of r.

The pressure and velocity of the expanding weak shock waves are related by :

$$u = \nabla\phi$$
$$P = -\frac{\partial\phi}{\partial t}$$

The shock wave from the discharge is assumed to be predominantly a cylinder of high pressure between the electrodes, that is released instantaneously **[17]**.

This is shown in fig 28:

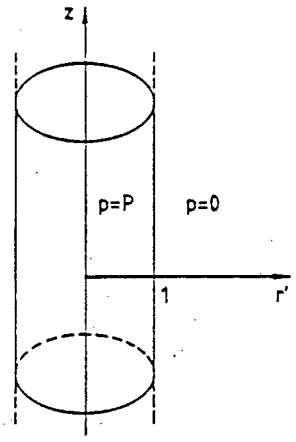

Figure 28: ***Simplified spark discharge initial conditions***

The boundary conditions that meet this physical assumption are :

$$\frac{\partial \phi}{\partial t}(r,0) = \begin{cases} -P & r \leq 1 \\ 0 & r > 1 \end{cases}$$

Substituting the boundary conditions and solving by Laplace transforming [17], the expanding wave will be described by the function ϕ. The velocity and the pressure functions of the expanding wave can then be obtained from the velocity potential ϕ.

The normalised calculated pressure function of the expanding weak shock wave from an electrical discharge is shown in fig 29 after Gustafsson [17]:

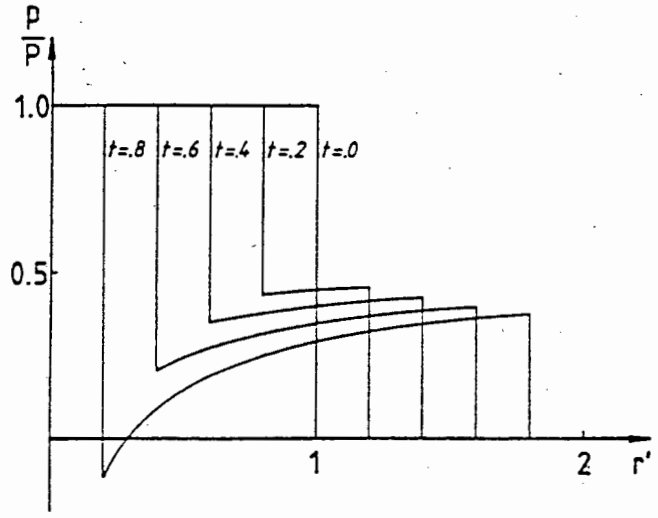

Figure 29: ***Normalised calculated pressure of a cylindrical expansion or simplistic spark discharge at different times after discharge***

Reflection of the weak shock wave

Although shock reflection is assumed to be regular, the wall cannot be assumed to be rigid. The admittance or distensibility of the wall will effect the reflection process and the thus the reflected converging wave. Part of the initial wave will be transmitted into wall and part of the wave will be reflected. The transmission of wave energy into the wall depends on the wall material and θ - the angle at which reflection occurs.

The wall parameters are introduced as a boundary condition. The reflection process is assumed to be singular - i.e. the boundary can be differentiated into separate regular reflections all occurring at individual points on the cavity wall. This is represented by the boundary condition **[17]**:

$$u \cdot \bar{n} = yP$$

where $\bar{n}$ = the unit normal vector to the wall, and y is the wall admittance.

The above boundary condition is a point-wise approximation to real reflection. This is valid provided that there are no additional wave modes in the cavity wall at the point of focus **[16,17,38]**. The condition for this not to occur is discussed

in section 5.3.

This condition implies that the velocity of the wave normal to the wall will have maximum velocity transmission at angles of incidence normal to the wall.

Reflected shock wave

The complex expanding wave and boundary conditions to the system, complicate the analysis of the reflected shock wave. Gustafsson used two approaches to the problem **[16,17]**. The first approach perturbed the solution of a reflection from a cylindrical cavity to include cavities with small eccentricity. This method is only valid for small eccentricities. The second approach used a geometrical acoustics approach **[61]**. This solution although not limited to small eccentricities, is approximate in its description of the pressure profile behind the wavefront.

Fig 30 (simplified from fig B7 e-f **[17]** Gustafsson) shows a plot of the normalised pressure for different angles in the cavity. These curves were calculated using the small eccentricity solution. θ is the angle from the second focal point, thus $\theta = 0^o$ corresponds to the focal line C between the two foci.

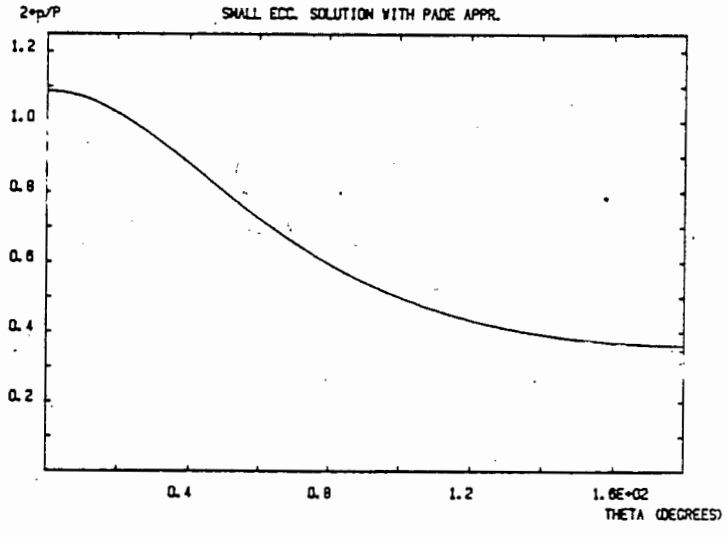

Figure 30: ***Pressure distribution of the focused wave plotted against angle θ***

This curve shows a non-uniform pressure distribution with θ.

The normalised reflected pressure, plotted as a function of θ for different

eccentricities is shown in fig 31 (after Gustafsson [17]).

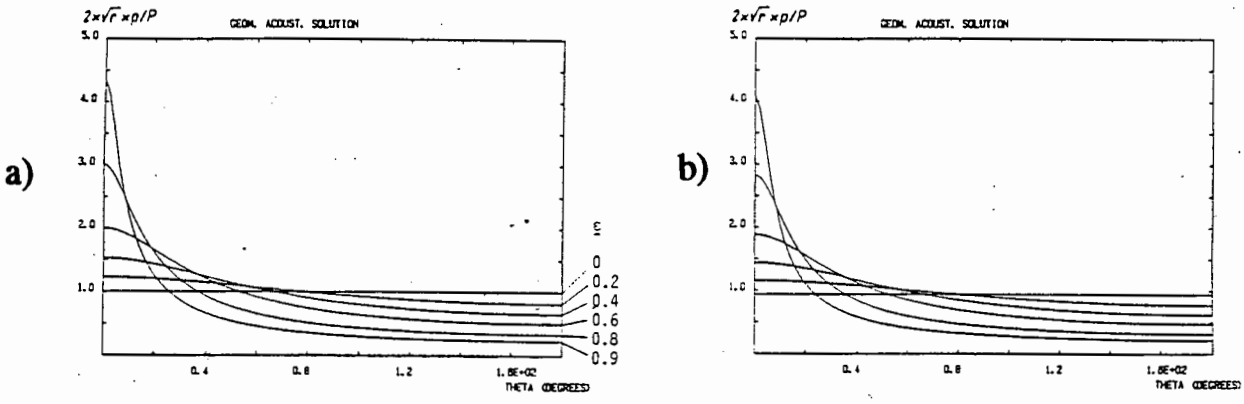

Figure 31: *Variation of normalised reflected pressure w.r.t. θ for different eccentricities a) y = 0 b) y = 0.03.*

Eccentricity zero corresponds to the trivial case of a circle - the pressure in the reflected wave is constant w.r.t. θ. The pressure increases for small angles and decreases for large ones with increasing eccentricity. The energy is concentrated at small angles for even small or moderate eccentricities. The pressure amplitude is seen to vary with wall admittance (y).

Variation of pressure with eccentricity

The pressure variation with angle can be understood by considering the reflection process. If the wall is rigid, the pressure in the reflected wave will equal the pressure in the incident wave. Large angles correspond to weaker incident waves since they have had large propagation distances from the source. Thus reflected waves at large angles will correspond to weaker waves. Small angles have short distances to reflection resulting in relatively strong reflected waves. In addition, these reflected waves have long distances to the second focal point - after reflection they converge and strengthen.

The second effect shown in fig 31 is that of wall admittance. This effect is more pronounced for small angles than large angles. This is as a result of small angles corresponding to near normal reflection (and maximum transmission) to the cavity wall.

Energy lost on reflection

The energy lost on reflection with a non-rigid wall has been shown to be proportional to [17]:

$$1-(\frac{1-y}{1+y})^2 \approx 4y$$

For rigid walls : y = 0, i.e. no-loss. If the boundary is a steel / water interface : y = 0.03, this corresponds to a loss of ≈ 10 % of the incident wave energy.

5.3 Wave modes in the cavity wall

The wave mode in the cavity wall depends on the admittance and the speed of sound in the wall. This wave will disrupt the reflection process if it travels at the same speed as the contact point (pointwise-reflection can no longer then be assumed). If the wall wave travels ahead of the contact point, it can introduce an additional shock wave into the cavity - the lateral wave. The lateral wave will arrive at the second focus before the reflected wave and thus might obstruct the focusing process. This was verified experimentally by Gustafsson [15,17 (**Appendix L**)].

The condition for the avoidance of the lateral wave has been derived to be [17]:

$$ec \leq 1 \qquad (5)$$

Where e is the eccentricity of the ellipse and c is the ratio of the highest wave mode in the wall to the speed of sound of the weak shock wave in the liquid. Thus if the product of the eccentricity and the normalised wall mode velocity is less than 1, the contact point (of reflection) will always move at least as fast as the highest wave mode in the wall.

The above analysis introduces a dilemma in the choice of ellipse cavity materials. For the reflection to be as lossless as possible, the wall material should be rigid. However, the ratio of wave modes in the wall to the liquid sound speed increases with increasing rigidity [62]. Thus ellipses of small eccentricity and compliant materials have to be used if the lateral wave is to be

eliminated entirely.

5.4 Ellipse cavity design

There are a number of physical parameters and design tradeoffs in the design of the cavity. The design objective is to maximise the energy transfer from the energy release at the electrodes to the nozzle. The ellipse cavity height, focal length, major and minor axes, eccentricity, and construction materials must be chosen.

5.4.1 Eccentricity

The reflected wave pressure distribution has shown that for even moderate values of eccentricity, the pressure distribution is asymmetrical w.r.t. θ. The total energy / unit volume in the wavefront was found by Gustafsson [17] to be invariant to a first order in eccentricity. However, the energy in the wave is concentrated at small angles θ. This concentration increased with eccentricity.

The presence of the electrode holders and the cone converging duct disrupts the focusing of the cavity. The effect of this disruption can be minimised if the area causing the disruption (diameter of the cone or the electrode holder) is small when compared to the total area of the wave front[2]. In each case this condition can be met if the ellipse has a fairly small eccentricity (i.e. the shape of the ellipse is tending towards that of a circle) and / or the dimensions of the diffracting obstacles (cone duct, electrodes and electrode holders) are small. This effect is shown in **fig 32** :

[2] The wave front at the point of disruption is in fact approximately equal to the Latus Rectum chord of the ellipse - this is shown in **Appendix G** and fig 32

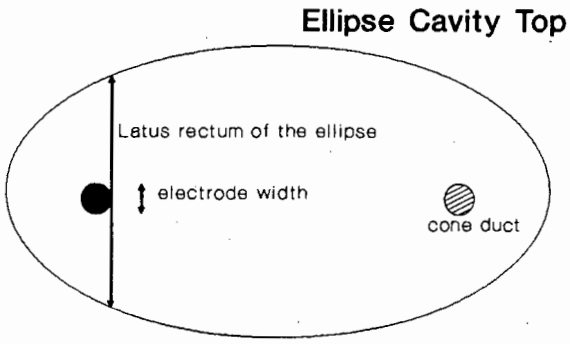

Figure 32: ***Area of wave disruption due to the electrodes and the converging duct***

The cavity eccentricity must also be chosen so as to elliminate lateral waves (5.3). The lateral wave has been shown to be insignificant if the product of the normalised wave mode speed c and the eccentricity is less than 1. This limits the eccentricity value. The value of normalised wave mode speed c, for a water steel combination is approximately 4, limiting e to values less than 0.25.
The above requirements show that small eccentricities should be used. However, small eccentricities correspond to short focal lengths C. The following discussion shows that C must be considered when choosing a value of eccentricity.

5.4.2 Focal length of the ellipse (C)

The eccentricity is the ratio of the major axis a, to the focal length C. If the focal length is chosen, the major and minor axes will then be set by :

$$C^2 = a^2 - b^2 \qquad (6)$$

The focal length can be used to set the propagation distance to focusing. If this distance is too long, the weak shock wave will dissipate and decay. This is will initially be at a rate higher than the acoustic decay rate (for cylindrical waves) of $r^{-1/2}$. Ultimately all shocks will dissipate at this acoustic rate **[24,48]**.

The minimum focal length is determined from the maximum wave disruption permissable on the initial pass. The wave disruption due to the cone duct will be greater if the electrodes and cone are located in close proximity i.e. small eccentricities. This is discussed further in section 5.5.

5.4.3 Ellipse cavity height

Cyllindrical waves

The analysis assumes that weak shock waves from the discharge are cylindrically symmetric. This corresponds to the physical condition : the spark gap width λ_g must be comparable to the height of the cavity h. This is shown in **fig 33:**

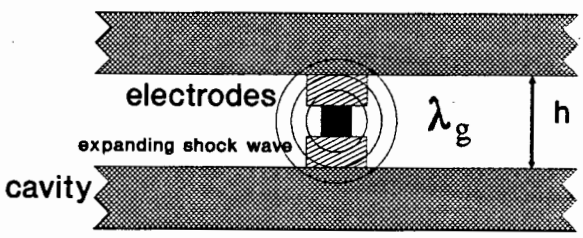

Figure 33: *Approximate cylindrical expansion from the spark channel will depend on the gap length λ_g and the cavity height h*

The spark gaps should ideally be flush mounted with the upper and lower plates of the ellipse. This will produce a cylindrical wave and the system will not obstruct the reflected shock as it converges to the second focus.

In order to initiate breakdown within the water gap, the electric field strength between the electrodes must be higher than that of the water. If the applied voltage is set, the distances between plane electrodes must be such that an electric field strength E_f given by :

$$E = \frac{V}{\lambda_g}$$

Where : V is the application voltage and λ_g the electrode gap.

The previous chapter has shown that the electric field should be as high as possible. This together with stress points (in the electric field) will minimise the delay before breakdown leaders form. Electrodes that are pointed or mounted away from the wall will increase the field stress points.

Wave disruption

The electrodes themselves also form an obstacle to the path of the focusing wave. The weak shock will expand towards the first wall and be reflected such that part of the wave front will pass through the electrode holders on the way to the second focus. It can be seen from **fig 31** that part of the wave strength ($\theta=0^o$) is strongest. Thus in order to reduce the perturbing and obstructing influence of the electrodes and electrode holders, they should be designed to be as small as possible.

5.5 Cone design

As has been shown a section of the expanding weak shock wave will be obstructed by the cone before it reflects off the back wall. **Fig 31** shows that this is the weakest portion of the focused wave. The perturbation in the expanding wave could disrupt the focusing process. That section of obstructed wave will depend on the dimensions of the convergent duct relative to the dimensions of the cavity. This is given by the ratio of the cone base to the latus rectum of the ellipse. This ratio will depend on the eccentricity. Ellipses with low eccentricities will have small ratios (for a given cone radius). However, the electrodes will be positioned closer to the cone duct. Thus the obstructed wave will be stronger. High eccentricities (long thin ellipses) indicate that the cone dimensions will be significant.

This is shown in **fig 34** :

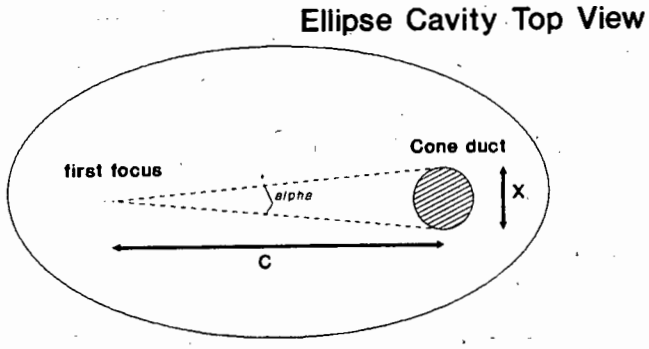

Figure 34: *Disruption of the expanding wave by the convergent duct*

The disruption is given by :

$$\begin{aligned} \tan\alpha &\approx \frac{X}{C} \\ \%_{lost} &\approx \frac{\alpha}{2\pi} \\ &\approx \frac{\arctan\frac{X}{C}}{2\pi} \end{aligned} \qquad (7)$$

Thus the focal length should be long and the ratio of the cone diameter to the latus rectum small to minimise the disruption.

5.6 Nozzle design

The design of a nozzle for a pulsed water jet is an extremely complex task. This thesis does not attempt to address this problem. A PhD on the subject of pulsed nozzle design by R. Lövgren has been quoted [17] but he has not published any results. Access to this work has not been possible.

For simplicity a uniformly tapered nozzle arrangement has been chosen. The dimensions of this nozzle are discussed in the next chapter. Some discussion on

the factors effecting water jet slug momentums and jets speeds is given in **Appendix O.**

CHAPTER 6 :

CONSTRUCTION OF THE ELLIPTICAL CAVITY

The previous chapter has analyzed the elliptical cavity. This chapter uses parameters identified in this analysis for the design of a prototype water jet generator.

6.1 The prototype system

The technical drawing of the prototype water jet generator is shown in **Appendix H**. The cavity has been designed to have an eccentricity of 0.5, a major axis length of 50 mm and a height of 5 mm.

The cone / nozzle interaction has not been theoretically analyzed. It is desirable to experimentally investigate the effect of these two cavity parameters on the water jet performance. This was achieved by designing the cone reflecting duct and the nozzle as removable (interchangeable) elements. This is discussed further in sections 6.4 and 6.5.

The analysis of the electrical circuit (**Chapter** 4) has shown that the water gap length determines water gap resistance. The circuit damping increases with increasing resistance. The optimisation of the electrical circuit therefore requires the water gap resistance and hence gap length to be varied. This was achieved using the system outlined in 6.2.2

6.2 The shock discharge

Chapter 4 described the process of shock wave production in a liquid due to an electrical discharge. This section details the construction of the electrodes, electrode holders, insulators and cavity plates for the production of an electrical discharge at the first focus of the cavity.

6.2.1 The electrodes

The electrodes used were flat ended cylindrical Tungsten Inert Gas electrodes.

Their diameter was 2.5 mm. The TIG metal is hard[3] and resists corrosion and spark pitting.

The electrodes were connected to the circuit using the electrode holder system shown in fig 35:

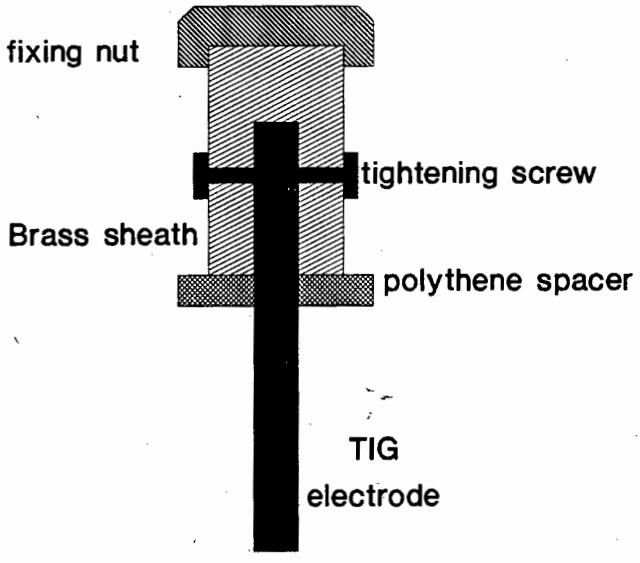

Figure 35: ***Electrode holders***

This figure shows a brass sleeve which fits over the TIG electrodes. Two tightening screws hold the electrode in place. The brass sleeve exterior is tapped to fit a standard nut gauge. This system was required since the TIG electrodes cannot be tooled (tapped) directly.

6.2.2 Insulator

Insulators are required between the electrodes and the cavity plate. The top insulator prevents flash over between the HV terminal and the top cavity plate. The lower plate bushing insulates the circuit from the cavity walls[4].

---

[3] The TIG electrodes were cut to length using a sintered diamond cutter. Other cutting materials were ineffective against thie hard TIG

[4] The lower electrode is almost at ground potential. The current shunt probe (described in Chapter 9) was inserted between the lower electrode and earth. The cavity walls must be earthed - safety and sheilding considerations. Thus the lower electrode cannot be in electrical contact with the cavity walls.

Insulator materials

Two insulator materials were considered ; PVC and high density Polythene. They have breakdown strengths of 33 and 40 kV/mm respectively **[62]**. Polythene was chosen for its higher breakdown strength and its availability. Thus the minimum insulator thickness for a voltage of 40 kV is 1 mm. A 2 mm thickness was chosen giving a safety factor of twice the insulator rating.

The formation of airgaps between the insulator and electrode rods was prevented by placing silicone sealant on the electrodes during their insertion into the insulators. The insulators were constructed to fit tightly into the holes in the covering plates at the first focus of the cavity (shown in **Appendix H**).

Electrode spacers

A number of polythene ring washers were inserted as spacers over the electrodes to ensure that the electrode holder was mounted against the outer sleeve of the plate insulator. The electrode gap length could thus be varied by varying the number of spacers. These spacers are shown for the cavity top plate insulator combination in **fig 35**.

Electric field control

In order to ensure that the electric field around the electrode holders was gradual, with no stress points (due to sharp corners), the outer surface of the electrodes and electrode holders were covered with a cone of silicon. This is shown in **fig 36** :

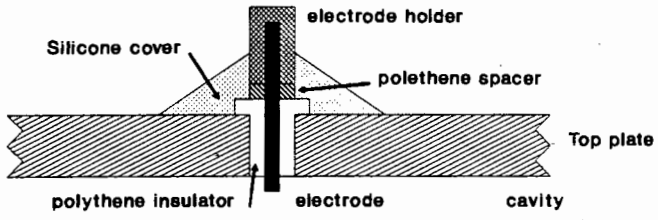

Figure 36: *Electric field control of the outer electrode insulator*

6.2.3 Water spark gap

Breakdown distances

The breakdown strength of water is between 10 and 100 kV/cm **[5,6]** for a uniform electric field. This corresponds to a maximum spark gap of 1 mm for a 10 kV DC discharge to occur. The electric field stress around the electrodes is increased if the electrodes are not plane but pointed.

Cavity height and electrode spacing

The height of the cavity has been chosen (in section 6.3.3) to be 5 mm. **Chapter 5** showed that for the production of cylindrical waves the electrodes must have a gap length comparable to the cavity height. This gap has been chosen to be approximately 2 to 3 mm.

Electric field control in the cavity

The electrodes protrude from the polythene insulator. In order to make the field distribution around this insulator gradual, a small amount of silicone sealant was placed around the insulator to form a cut-off cone. The base of this cone was approximately 7 mm and the height 1.5 mm. This sealant also had the advantageous effect of preventing water leaks around the electrodes and insulators.

6.3 Elliptical Cavity

6.3.1 Eccentricity

Chapter 5 has shown that there are a number of factors that must be considered when choosing the cavity eccentricity. The eccentricity must be chosen such that the lateral wave is avoided and that the disruption due to the electrodes and cone is small.

The lateral wave can be prevented by choosing eccentricities less than the inverse of the ratio of maximum sound speed in the cavity wall to the sound speed in the liquid (equation (5) **Chapter 5**). Eccentricities below 0.25 are required for the elimination of lateral waves for steel / water cavities. Low eccentricity ellipses correspond to large latus rectum chords. Thus the proportion of area perturbed by the electrode holders is small in relation to the total chord (latus rectum) of the ellipse. However, the focal length decreases with eccentricity. The smaller the focal length, the greater the area of wave disrupted by the cones. Thus the eccentricity and focal length must be chosen together.

The elliptical cavity was designed with an eccentricity of 0.5. The focal length was chosen to be 50 mm. This meant that the percentage of the expanding wave disrupted by the cone (from equation (7) **Chapter 5**) was < 5 % (for the cones described in section 6.4.2).

6.3.2 Focal length, major and minor axes

These parameters are related (see **Appendix G**). If the eccentricity and focal length are chosen, the major and minor axes are given by :

$$a = \frac{c}{e}$$

$$c^2 = a^2 - b^2$$

Substituting the chosen values of eccentricity and focal length; the major axis is 50 mm and the corresponding minor axis is 43.3 mm.

6.3.3 Cavity height

The cavity height was chosen to ensure that the weak shock wave propagating from the spark gap was approximately cylindrical. The spark gap distance is approximately 2 mm (set by breakdown requirements - maximum voltage that could be generated).

The height of the ellipse was chosen to be 5 mm. It is of the same order as the spark gap distance and it corresponds to a standard gauge-plate[5] dimension.

6.3.4 Construction

The outer covering plates were chosen to be rectangular 10 mm gauge-plate tool steel plates with outer dimensions of 150 and 160 mm. The ellipse was cut out of the centre plate (5 mm) using a computer controlled milling machine (see **Appendix H**).

The plates were held together by eight, 5 mm bolts mounted through the plates. These were arranged equi-distanced along each side.

The cavity was supported by 4 L-plates which acted as 'legs' for the system. It was arranged to be planar with the nozzle facing upwards. The L-plates were connected to the centre bolt and nut combination of each side of the cavity. This is shown in **fig 37:**

[5] Gauge-plates are pre-finished tool steel plates. They have smooth parallel front faces. Thus they require no further milling or tooling before construction.

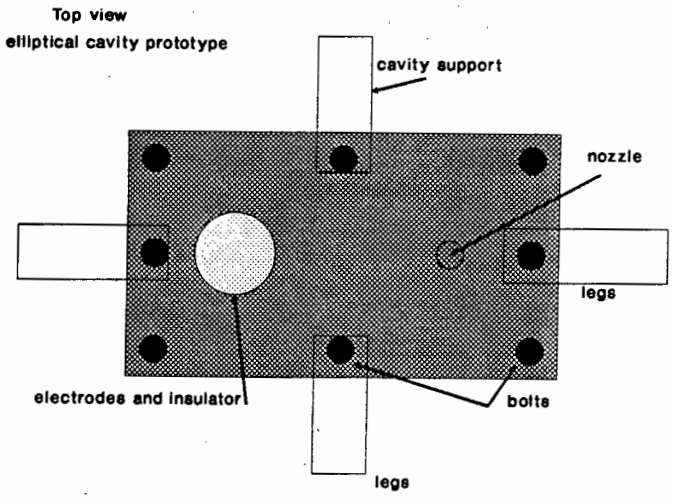

Figure 37: *Cavity support arrangement*

In order to facilitate rapid assembly and disassembly of the device, the lower plate and the cavity centre plate were fixed together by a thin silicone gasket.

6.4 Converging cone insert

The cone reflects the incident focused weak shock wave towards the nozzle. Chapter 5 has shown that the incident wave is not symmetric (w.r.t. θ) in pressure amplitude about the second focal point. It has shown that the energy is concentrated around the focal chord[6]. The interaction of the converging weak shock wave with the cone is a complex 3-D problem. No attempt has been made to analytically study this area.

For constructional simplicity, only symmetric cones were used in the prototype.

6.4.1 Cone removal

The fitting facilitates the removal of the cone. The cone insert is inserted from the interior of the cavity were it rests on a flange to position it flush with the floor of the cavity. It is held in place by a locking screw and washer that is tapped into the rear of the cone insert from the outside of the plate. This is shown in the technical drawing of the complete elliptical cavity prototype shown

[6] It is proposed [17] that the cone might then not need to be circular symmetric for the reflection of a large proportion of the incident wave energy.

in **Appendix H.**

6.4.2 Cone insert prototypes

Three different cones of different shapes and sizes were constructed. These are shown in the following table :

Base radius	Cone height	Combination
4 mm	4 mm	regular cone
7.5 mm	4 mm	low cone
4.75 mm	0 mm	flat insert

The last cone in the table corresponds to a flat insert i.e. the cavity without a reflecting cone. The regular cone is a 45^{o} reflector - optimum for geometric reflection.

6.5 The nozzle

6.5.1 Nozzle design

The design of high speed water jet nozzles has been discussed in **Chapter 5** and **Appendix O.** This was shown to be a difficult task. For simplicity, the nozzles were designed to be convergent ducts with lengths of 10 mm (the height of the top cover plate). They were made with a specially constructed DBit cutter.

6.5.2 Nozzle removal

The nozzle was constructed to be removable. Thus different nozzle shapes and dimensions could be tested. The nozzle insertion system is shown in **fig 38 :**

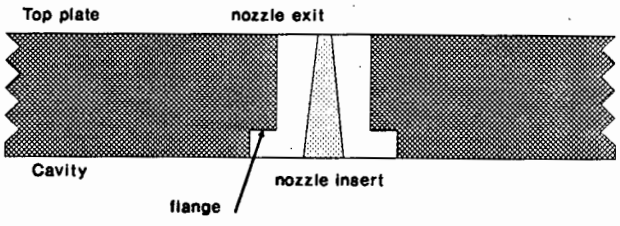

Figure 38: ***Nozzle insertion system***

6.5.3 Nozzle prototypes

Three nozzles were constructed. These are shown in the following table :

Inner diameter	Exit diameter	Nozzle length	Nozzle
3 mm	1 mm	10 mm	small nozzle
6.3 mm	2.1 mm	10 mm	medium nozzle
8 mm	3 mm	10 mm	large nozzle

6.5.4 Cone nozzle combinations

Nine cone-nozzle combinations are possible. The response of the system to the various nozzle and cone combinations are compared in the theoretical simulations of **Chapter 7** and the testing of the prototype system covered in **Chapter 9.**

CHAPTER 7 :

THEORETICAL SIMULATIONS

This chapter describes theoretical simulations performed on the elliptical cavity. These simulations were aimed at optimizing some of the physical parameters and confirming the analysis of **Chapter 5**.

Two aspects of the elliptically focused shock wave water jet generator were simulated. Firstly, the focusing process within the ellipse (from focal point to focal point) was simulated. This was done with a rigid boundary and a metal compliant boundary. Secondly, the cone duct / nozzle interaction was simulated.

7.1 Autodyne

The package used was a two dimensional fluid dynamic finite difference system - Autodyne II. Simulations were performed on WITS Mechanical Engineering School's Sun work-stations.

Autodyne allows any of three different calculation methods (Euler, Lagrange and ALE) **[63]** to be used on a fluid, solid or gas, with user defined boundary conditions, initial conditions and calculation grids. A Lagrange calculation subspace for each material in the prototype was chosen. The subspaces were designed to be grids with shapes corresponding to all or part of the simulation system. The material would then be defined to completely fill the Lagrange subgrid.

7.2 Simulations

7.2.1 Units and dimensions

Simulations are in the units of gram, mm, microsecond. The dimensions of the various simulated systems correspond to the physical dimensions of the prototype system.

7.2.2 Limitations

Autodyne is a useful tool for the qualitative analysis of fluid weak shock

interactions. However, the package has a number of limitations which effect the analysis process.

2D package

The package is a two dimensional system. The weak shock wave focusing process and cone / nozzle interaction in the prototype system is three dimensional. Thus the cavity cannot be simulated as a complete system. Instead, two dimensional simplifications of the system were simulated individually.

Mesh size

The mesh size used in the calculation determines the numerical accuracy of the simulation[7]. There were computer run-time limitations and memory limitations to the maximum size of grid that could be used. The grids used for each of the simulations are given in **Appendix I and J.**

Shock wave source

The initial weak shock wave was initiated by a transient boundary condition on a free surface at the first focal point (ellipse simulations) or at the channel boundary (cone-nozzle interactions). This boundary condition is an approximation to actual shock wave initiation. A triangular wave with a steep rise time and high peak pressure was introduced on a free surface boundary condition to represent the shock.

Chapter 4 has shown that the pressure release from a spark channel can ideally be expected to be in the form shown in **fig 22. Chapter 5** has used a unit step cylindrical pressure expansion (**fig 28**).

Chapter 4 calculated the theoretical pressure peak at the plasma channel boundary from spark discharge in water. Using the anticipated electrical parameters for the experimental RLC discharge circuit and a literature survey of published pressure magnitudes, the peak pressure was expected to be of the order 30 - 60 KBar.

---

[7] One method of overcoming part of this grid accuracy limitation is to define high density grids over places of interest. These areas (for example the focal areas of the elliptical cavity) are then calculated with a greater resolution and numerical accuracy than with a uniform grid. This technique was not attempted in these simulations.

Run-time errors reulted when the initial shock pressures were above a few kilobar. Thus the simulations described in this chapter all used initial pressures an order of magnitude below the expected values. Quantitative results are therefore unobtainable, but qualitative results showing general geometric focusing trends and comparisons between systems are valid.

The weak shock wave used in the case of the cone nozzle combination was introduced by a unit step velocity boundary condition. This representation is an approximation to the converging shock wave (discussed in **Chapter 5**). The analysis is only valid for times much less than that required for fluid flow out of the nozzle to occur : The channel length used was 40 mm. The velocity boundary condition was 5 m/s. Thus the time for this condition to reach the end of the channel is 8 ms.

Axial symmetry

The package allows axial symmetry (about the X-axis). The accuracy of the package under axial symmetric conditions has not been verified.

Equation of state of water

All simulations used the linear equation of state for water. Towards the focal region, the pressure magnitudes increase significantly. Non-linear effects can no-longer be ignored **[66]**. A different equation of state must then be used. A common one cited in the literature is the modified Tate equation **[66,67]**. Simulations using this equation were not attempted during this thesis.

Viscosity

The package does not explicitly handle viscosity. Gustafsson **[17]** showed that the effect of viscosity is negligible in the elliptical cavity. Finite difference packages introduce numerical dispersion and diffusion **[65]**. It is noted **[64]** that these numerical errors are very similar to the effect of wave smearing due to viscosity.

Numerical oscillations

Behind the simulated weak shock waves a number of perturbations or oscillations in the pressure contour were observed. Some of these are due to the approximate weak shock wave source. However, some are also due to an effect in finite difference systems termed numerical oscillations, which occur behind discontinuities **[65]**.

7.2.3 Elliptical cavity

The elliptical cavity focusing from the first focal point to the second focal point was simulated. The walls of the cavity were entered in coordinate form using the same coordinates used by the computer controlled milling machine (**Chapter 6**).

Two types of elliptical focusing problems were simulated. The first simulated the focusing process with rigid walls (section **7.3.1**). The second investigated focusing with a metal water boundary (i.e. compliant boundary) (section **7.3.2**). The ellipse was simulated using the full ellipse co-ordinates - four quadrants of the ellipse, and also using only the top half of the ellipse - two quadrants (**Appendix I**). The latter simulation is possible since the focusing process is symmetric about the focal chord.

7.2.4 Cone Duct / nozzle interaction

The operation of the device (as described in **Chapter 1** and **Chapter 5**) requires the converging shock to be reflected through 90°. This was achieved by the placement of a right-hand cone at the second focus. The converging shock is then approximately reflected off this cone and down a converging duct (or nozzle) to a free surface or water-air boundary.

The cone / nozzle interaction was simulated using an axial symmetric approach. The focused weak shock pressure in the cavity has been shown to be asymmetrical about the cone (**Chapter 5**).

Simulation of the shock wave convergence is restricted by a boundary condition limitation and a dimensional limitation. Autodyne only allows 2D problems where the cone and nozzle arrangement is a 3D one. The non-uniform pressure distribution cannot be readily simulated. The package does not allow sources to vary effectively over the boundary that they are defined. Individual mesh boundary conditions would be a crude approximation and are limited by the mesh limitation of the package.

As a first approximation, the converging shock wave pressure is assumed to be symmetric. This assumption allows the simulation to be represented in the form shown in **fig 39** :

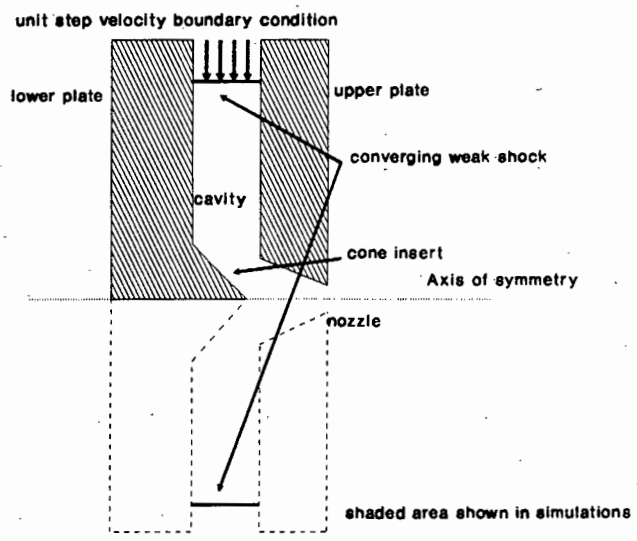

Figure 39: ***Axial symmetric representation of the cone nozzle interaction***

A plane wave (from a unit step velocity boundary condition) initiated at the free surface (water) at the top of the channel, propagates downwards towards the deflecting cone. After reflection from this cone it propagates at right angles to the original path down the nozzle.

The plane wave propagating down the duct is equivalent to a converging spherical symmetric cylindrical wave due to the axial symmetry about the X-axis. This analysis views only part of the device and is rotated through 90° to facilitate the necessary symmetry.

All simulations performed using this configuration assume rigid boundaries. Thus the steel water interaction is assumed non-compliant[8].

7.3 Simulations using Autodyne

For continuity, only representative simulations are shown in this chapter. The remaining simulation results are shown in **Appendix I and J.**

[8] Chapter 5 has shown that if the boundary can be represented by a pointwise boundary condition, the wave transmission into the cavity wall will be a function of incident angle and wall admittance. This will be minimum for incident angles close to 90°. Thus very little wave energy will be lost to the cavity wall and floor. Some energy will be lost to the cone (45° incidence). However, this is neglected in this analysis.

Three simulations are shown : full ellipse focusing, half ellipse focusing with a metal compliant boundary, and cone / nozzle interactions for various cone / nozzle combinations.

7.3.1 Rigid walled elliptical cavity simulations

Full rigid ellipse focusing was simulated. These results show the focal point to focal point focusing in the elliptical cavity.

The simulation used a triangular pressure pulse as the shock source. The start of the pulse was a time 0, peak at 2 and tail at 4 microseconds. The peak pulse amplitude was 1 kBar.

Rigid boundary conditions were imposed on the walls of the ellipse grid.

The following photographs show the pressure contours resulting from full ellipse focusing. There are six figures all taken at times after the initial shock wave has occurred.

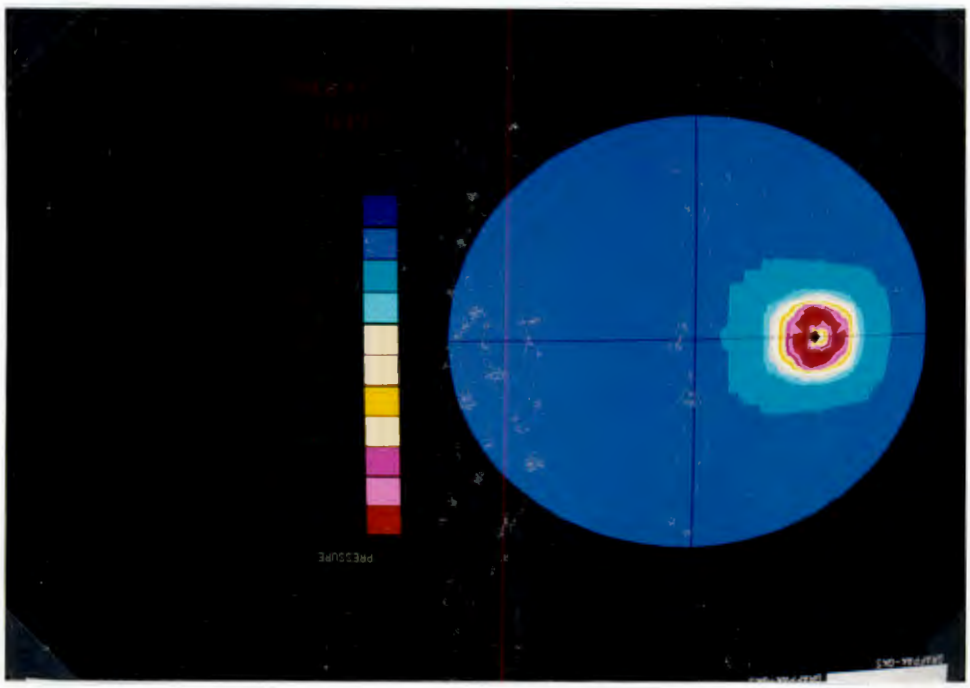

Figure 40: ***Full ellipse focusing - 4 μ seconds after discharge***

Fig 40 shows the initial shock wave (peak amplitude 1 kBar) expanding from the first focus of the ellipse. The colour contours (pressure distribution in the expanding wave) indicate that as predicted in **Chapter 5**, the pressure wave is initially symmetric with angle about the first focus. The photograph shows the weak shock wave before any wall reflection has occurred.

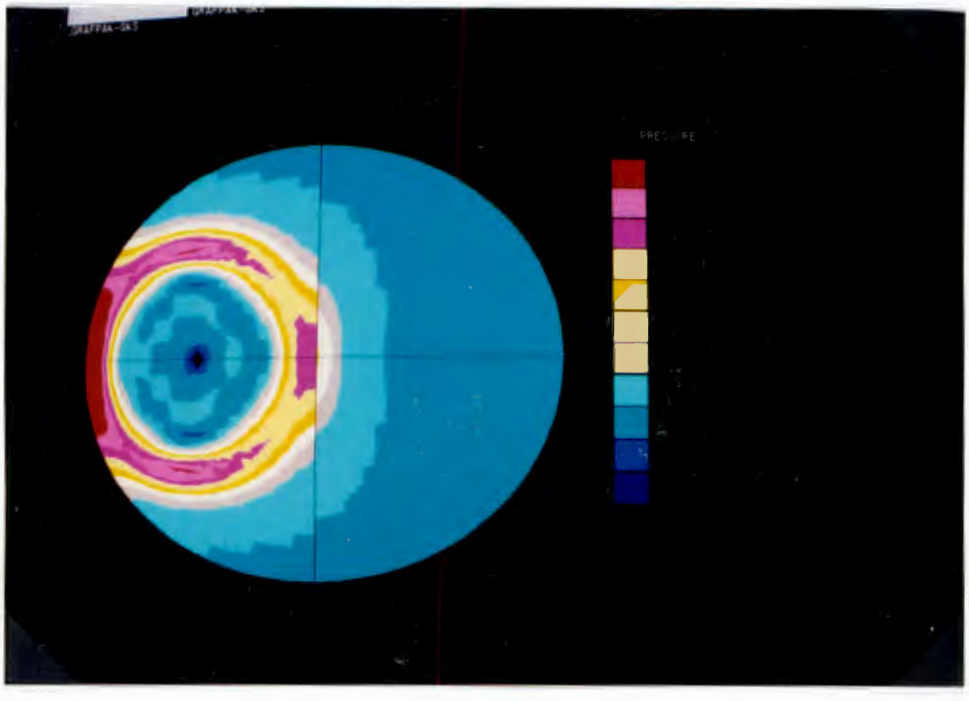

Figure 41: ***Expanding wave undergoing reflection from the cavity wall - time 17 μ seconds***

Fig 41 shows the expanding weak shock wave at the point where it is starting to reflect from the cavity wall. The pressure distribution is no longer uniform, but is instead more concentrated around the area where reflection is occurring. Acoustic theory predicts that the wave near the cavity wall will have an amplitude of twice the incident wave pressure amplitude (if the walls are assumed to be rigid). Autodyne chooses the colour combinations and scales for the pressure contour display. The other sections of the expanding shock wave are decreasing in amplitude (dissipating) as they expand from the first focus.

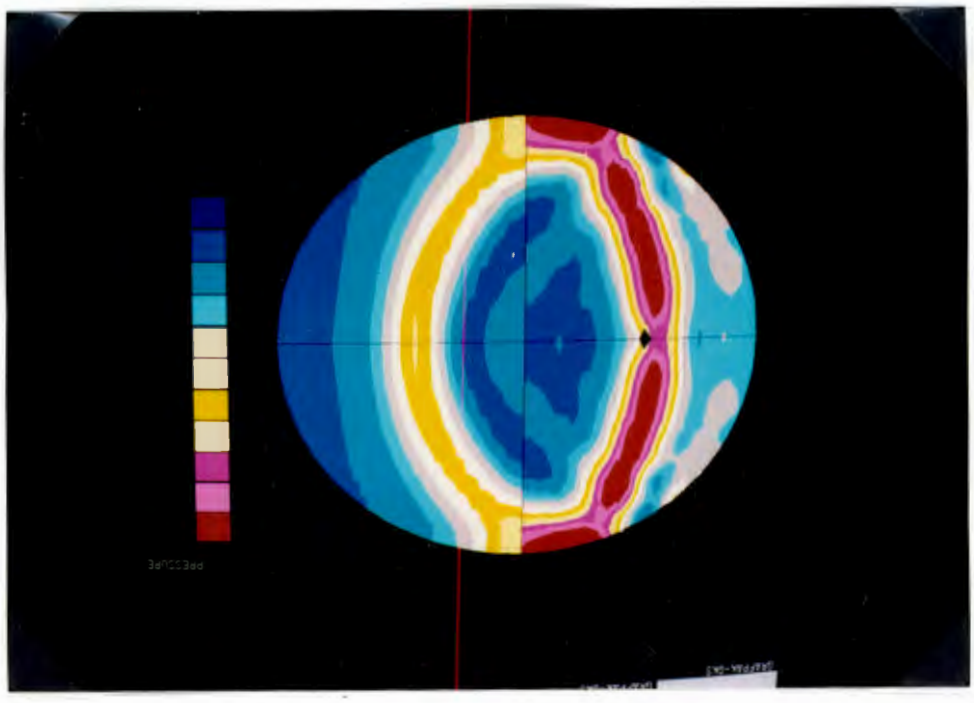

Figure 42: ***Weak shock wave propagation in the ellipse - time 34 μ seconds***

Fig 42 shows the weak shock wave propagating in the elliptical cavity. This shows the same form as that predicted in **fig 26**. It shows two wavefronts : a concave wavefront that is strengthening as it focuses and converges on the second focus, and a convex wavefront that is dissipating as it expands. The contact point with the cavity wall is seen to be at the top and bottom of the cavity. **Chapter 5** has shown that the speed of this contact point relative to the speed of the highest wave mode in the wall will determine whether lateral (interference) waves will occur.

The concave wavefront is about to cross the first focus. It is at this point that the electrodes are situated in the prototype system. As predicted in **Chapter 5**, this part of the wave is much stronger than the expanding concvex wave which is also about to intersect with the second focal point. The second focal point corresponds to the point where the cone duct is situated in the prototype system. Since the two parts of the converging and expanding weak shock waves within the cavity will be perturbed by these obstructions, the dimensions of the electrode holders and electrodes must be minimised (as discussed in **Chapters 5** and **6**). The concave wavefront pressure contour shows some pertubation - this is due to the free-surface grid used to initiate the shock wave at the first focus.

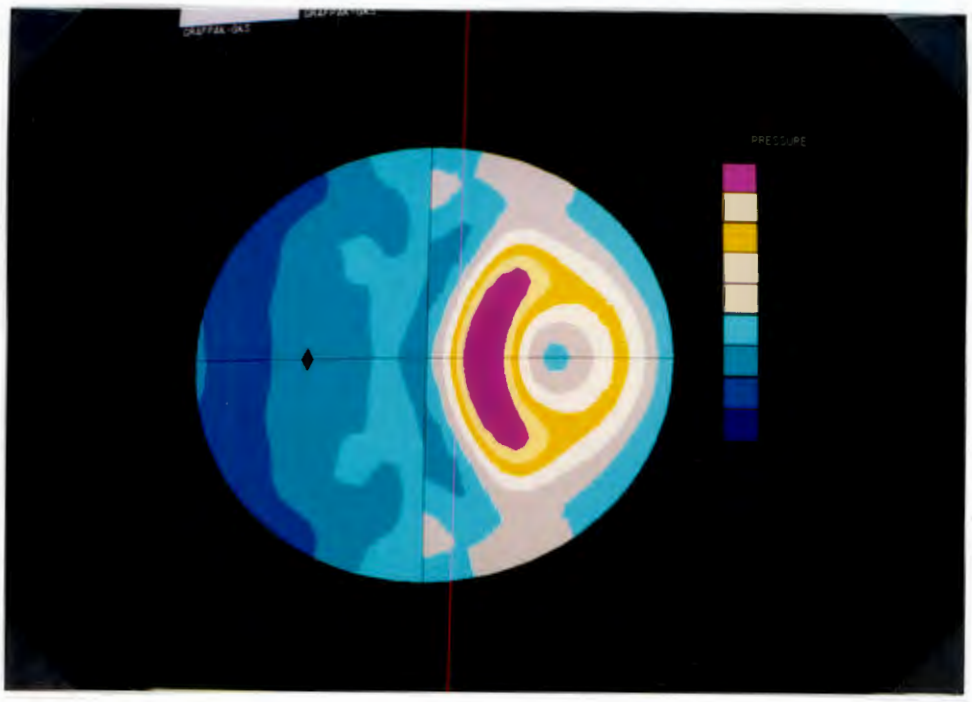

Figure 43: *Converging weak shock wave on the far focus of an elliptical cavity - time 60 μ seconds*

Fig 43 shows the converging weak shock wave that has been focused to the second focus of the cavity. The pressure distribution is not uniform. It has in fact a maximum pressure along the axis of the ellipse. This corresponds to the angle $\theta=0^{o}$ predicted in **Chapter 5**. The weak shock wave that has reflected off the rear cavity wall will now converge and strengthen to the second focus. This wave pressure is significantly lower than the concave wavefront. Rarefaction and compression waves are shown to be forming behind the converging waves. These are as a result of the boundary conditions used to produce the weak shock wave, cumulative numerical errors on the finite difference grid, and numerical oscillations behind the wavefront.

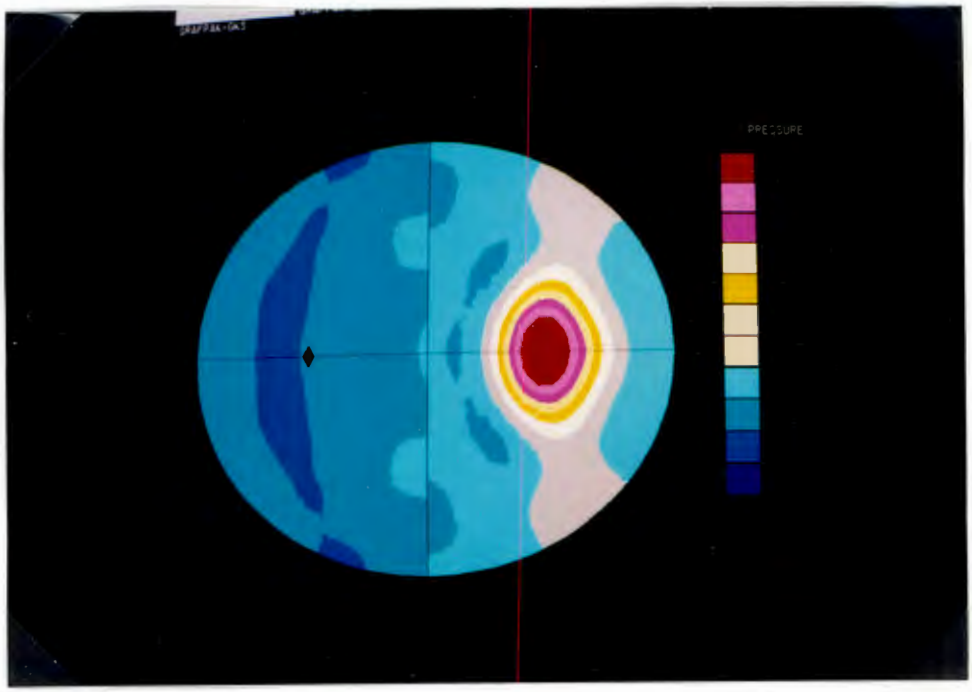

Figure 44: *Shock wave convergence on the second focal point - time 68 μ seconds*

Fig 44 shows the weak shock wave that has converged to the second focal point. At this stage the wave would be reflected by the cone towards the nozzle which would be positioned facing upwards in this figure. The pressure contour diagram also shows that the non-uniformity of the pressure wave that was shown in the previous **fig 43** is not apparent. This can be attributed to the source being imaged to the second focal point. This imaging is not ideal (the target focal pressure is not a perfect circle but is rather more oblong). This can be attributed to numerical errors and to the fundamental approximation in introducing the weak shock perturbation at the first focus : the wave is introduced by a pressure boundary condition on a free surface. This surface is not spherical but rather made up of two grid block surfaces per hemisphere. Thus the source is not spherical but rather a polygon. The grid used in this analysis is shown in **Appendix I.**

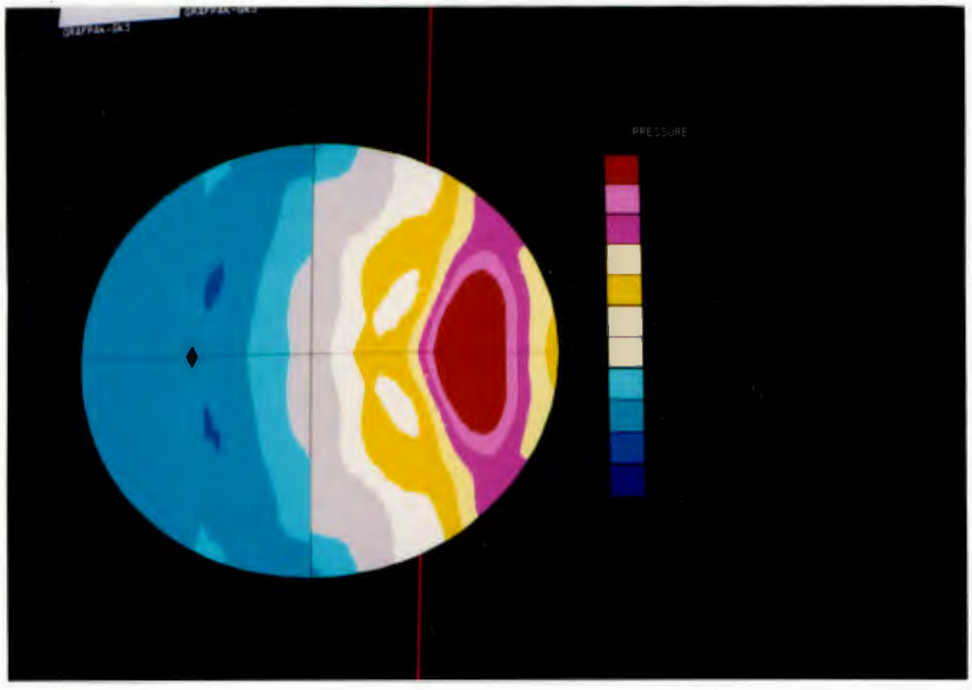

Figure 45: *Post focusing of the weak shock wave - time 73 μ seconds*

Fig 45 shows the pressure contours at 73 μ seconds after focusing. The weak shock wave is expanding non-linearly. The pressure maximum is considerably less than that obtained during the focusing.

Non-linear effects which disrupt the focusing process close to the focal region cannot be observed in this simulation **[66]**. The peak pressure used was 1 kBar which is regarded as being within the linear range of water. In addition the linear equation of state was used. If the modified Tate equation and higher initial pressures were used, **[67]** results indicate that the actual focal point would be between the rear wall and the second focus.

The pressure history target locations (for the measurement of the pressure amplitude of a point with respect to time) are shown in **fig 46:**

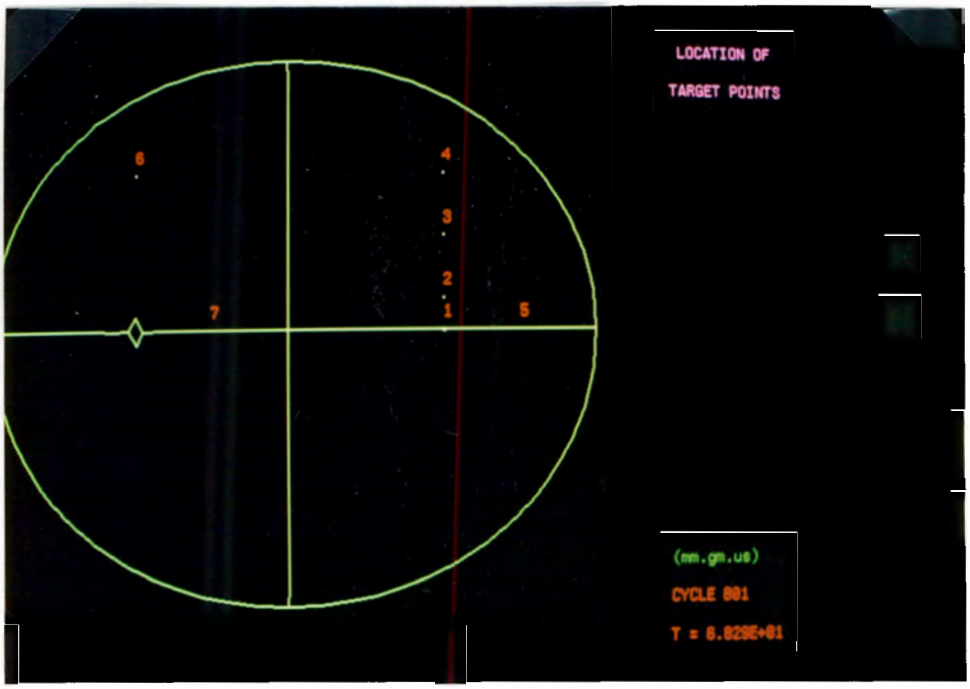

Figure 46: *Target locations for the measurement of the pressure time histories within the cavity*

The pressure histories recorded at these target locations are shown in **fig 47 :**

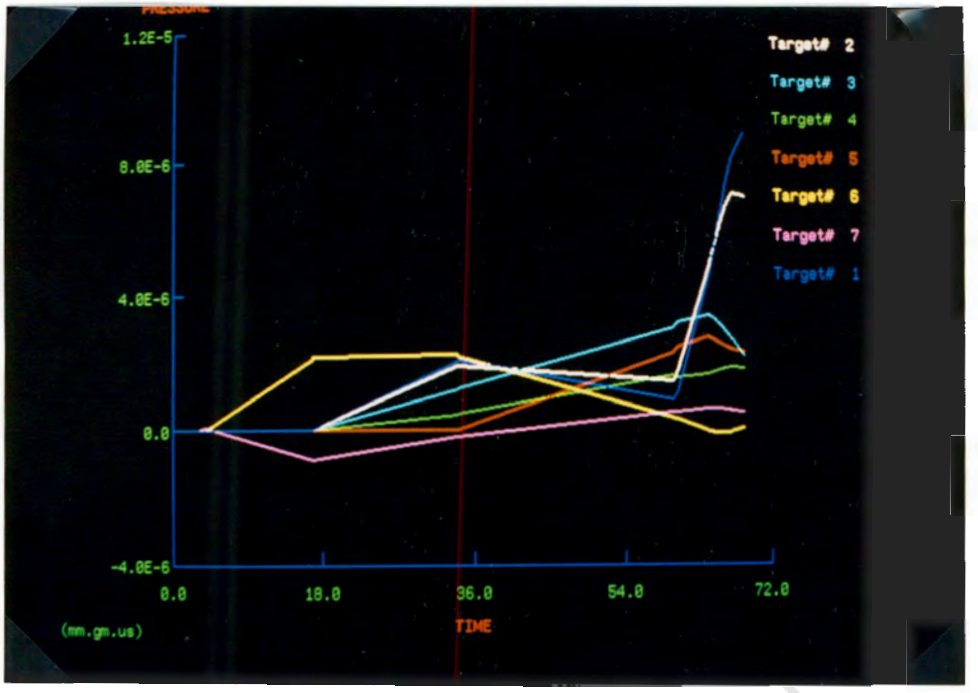

Figure 47: *Pressure amplitude vs. time recorded for the point locations shown in fig 47*

These curves show the relative pressure magnitude at different points in the cavity. The pressure maximum at the second focal point (target 1) is at time 67 μseconds. The distance travelled by a wave to reach the focus is 75 mm. Thus the wave is travelling at the approximate acoustic velocity of water (1500 m/s).

Target 1 also records the first pass of the expanding shock wave at 33 μseconds. The relative pressure magnitude increase after focusing is approximately 3. Thus the elliptical cavity has a magnification factor of 3. Magnification factors obtained experimentally **[66]** with three dimensional shallow ellipsoidal cavities and spark sources give magnification factors of the order of 100.

The shock wave focusing process is further illustrated in **Appendix I** - half ellipse focusing.

University of Cape Town

7.3.2 Elliptical focusing with a compliant boundary

In order to see the effects of the metal on the reflection process, the boundary of the ellipse was defined to be a water steel interface. The material and calculation grid used in this analysis is shown in **Appendix I.**

The peak pressure used in this analysis was 2×10^{-4} MBar. Only the top two quadrants of the ellipse were used. The lower surface (or focal chord) of this ellipse was defined such that flow could not cross the boundary.

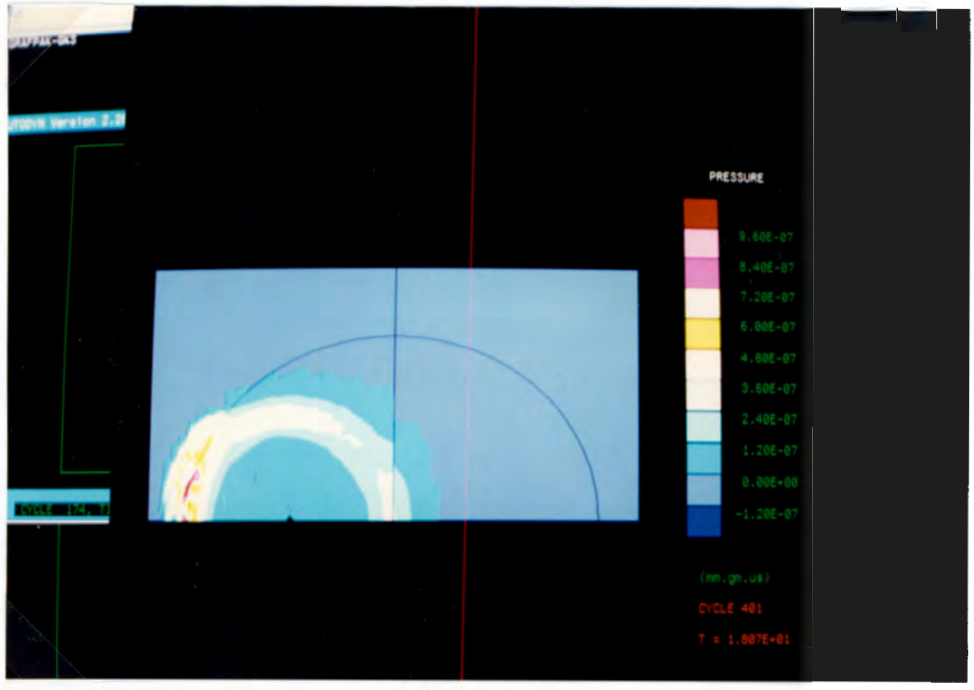

Figure 48 : ***Ellipse weak shock wave focusing with a metal compliant boundary at 18 μ seconds after discharge***

Fig 48 shows weak shock wave focusing in the elliptical cavity with a water steel interface. The wave is seen to expand cylindrically until it reflects from the cavity wall. Here it is partially reflected and partially transmitted into the metal wall. The initial pressure amplitude used in this simulation is relatively small so the behaviour of the wave is expected to be acoustic.

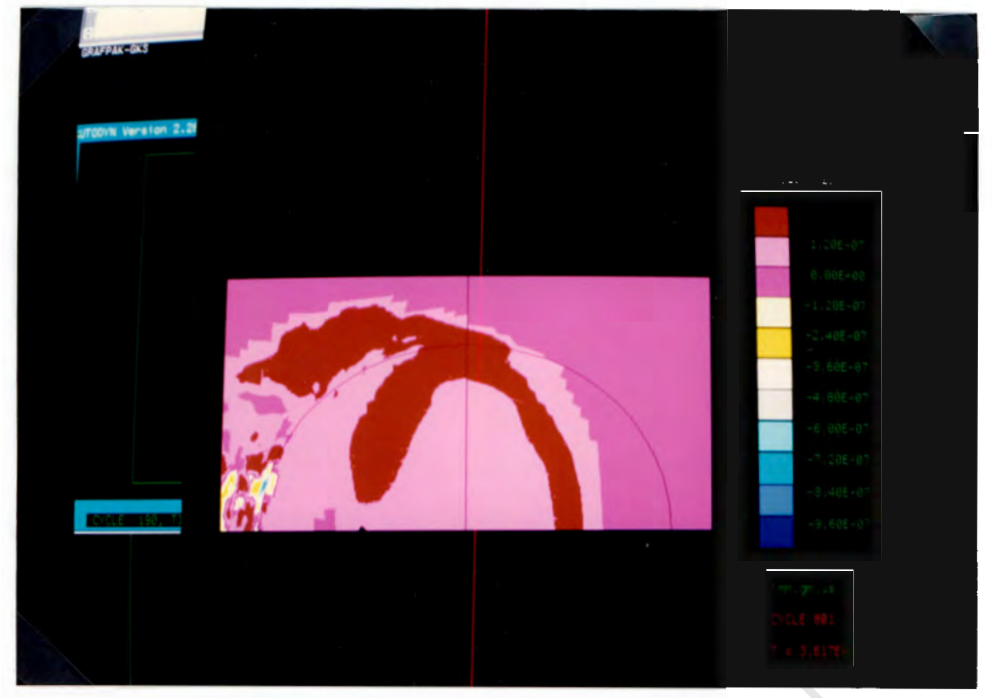

Figure 49: ***Weak shock wave propagation in the cavity and cavity walls at time 36 μ seconds***

Fig 49 shows the weak shock wave propagation in the cavity (liquid) and the cavity wall (steel). Autodyne does not allow the user to set the scale and colours used in this analysis. There are no modes in the cavity wall ahead of the contact point - the point of reflection between the water shock and wall (i.e. lateral waves will not occur).

The focusing of the weak shock wave to the second focal point is shown in **fig 50 :**

University of Cape Town

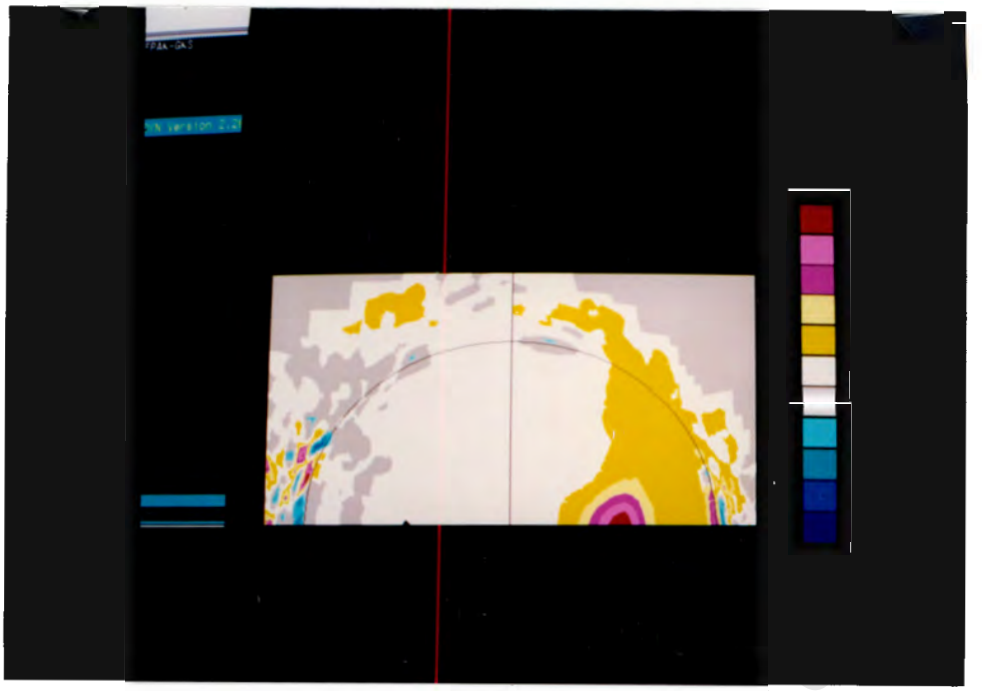

Figure 50 : *Weak shock wave convergence on the second focal point (with a metal compliant boundary) at time 70 μ seconds*

These figures have shown lateral waves have not formed and that the focusing process occurs in the same manner as has been simulated with rigid boundaries in section 7.3.1.

7.3.4 Cone nozzle interaction

The cone-nozzle interaction for various experimental configurations[9] are shown next. In this case the weak shock wave was introduced by a velocity boundary condition on the liquid. The two plates correspond to the lower cavity plate (floor) on the left and the top plate on the right. The vertical height of the channel is 40 mm. The material systems used are described in **Appendix J**.

The velocity boundary condition introduced to produce an axial symmetric converging shock wave is shown in the particle velocity plot (just after the unit step has occured) **fig 51 :**

[9] Simulations of all possible experimental configurations were not possible

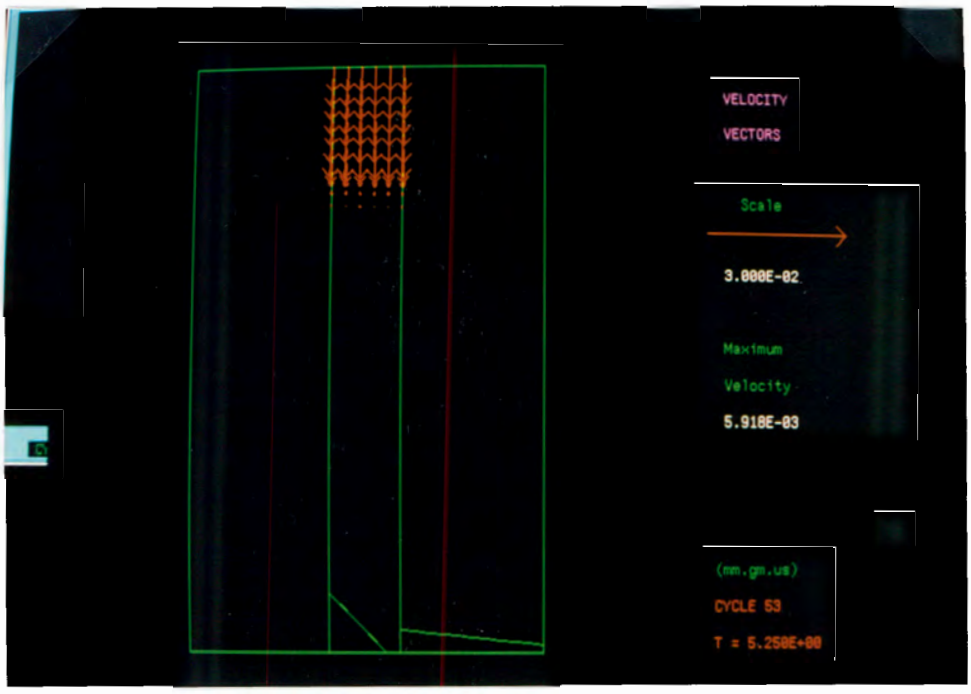

Figure 51: *Axial symmetric representation of the cone nozzle interaction - velocity plot. The velocity boundary condition is shown.*

The pressure contour map resulting from this boundary condition is shown in **fig 52:**

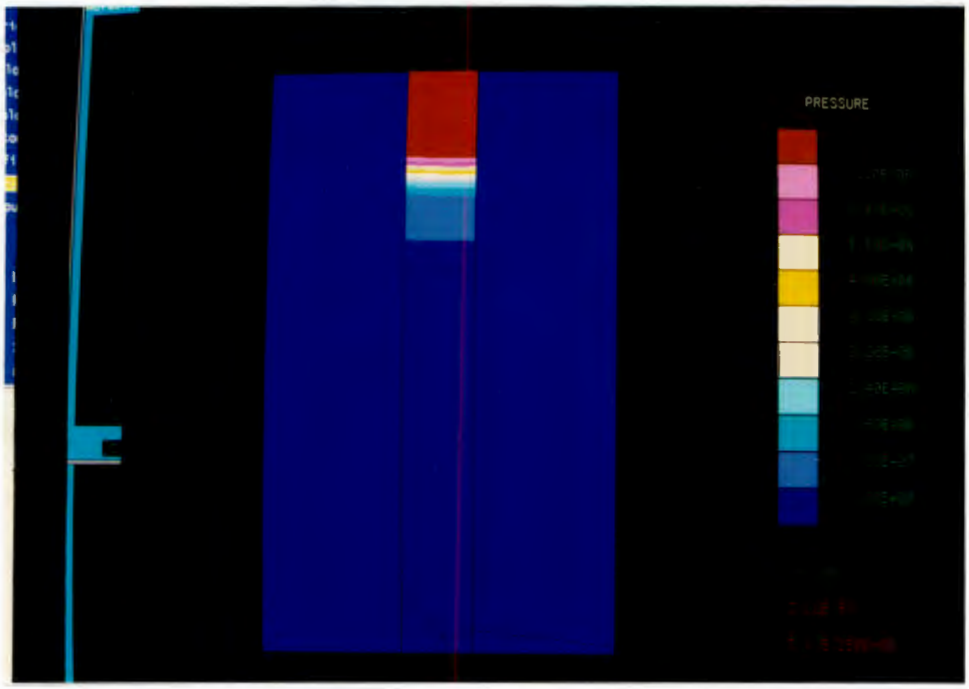

Figure 52: *Pressure contour map resulting from boundary conditions - time 5.25 μ seconds*

The weak shock wave propagates as a weak plane wave down the channel until it meets the cone duct. At this point the wave is reflected. In reality (if the boundary conditions were not rigid) some of the wave energy would also be transmitted into the metal cone. The wave propagation is shown in **fig 53:**

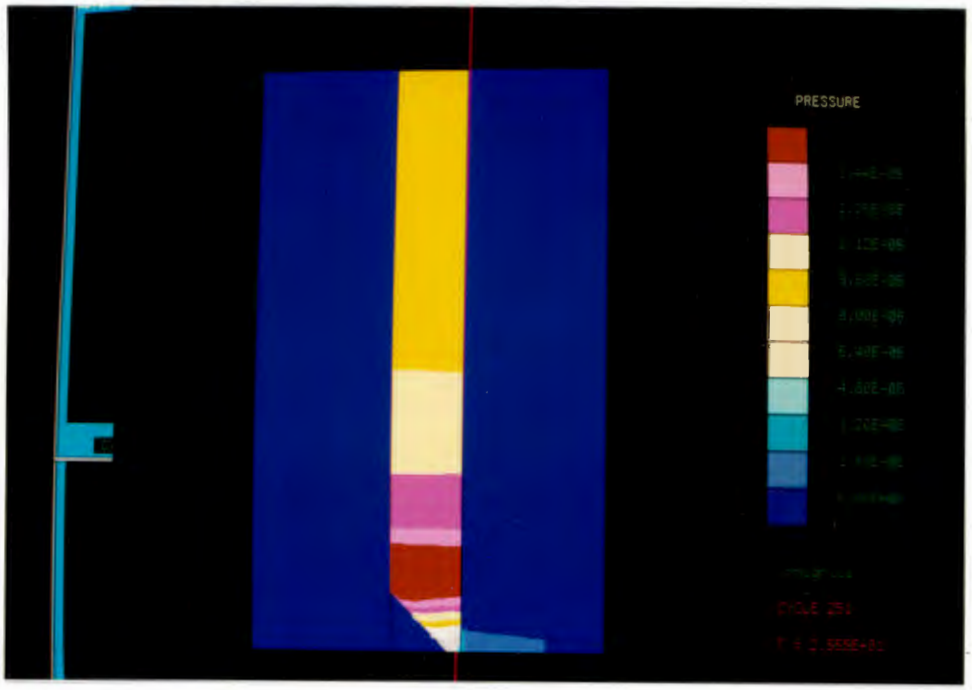

Figure 53: *Weak shock wave propagating as a plane axial symmetric shock converging on the cone duct - time 25 μ seconds*

The wave is reflected from the cone duct down a convergent nozzle. In this case the nozzle has an inner diameter of 3mm and an outer diameter of 1 mm (corresponding to combination small nozzle - regular cone of **Chapter 6**). Some of the weak shock energy is also reflected back up the channel i.e. axially symmetric expansion. This is shown in the pressure contour photograph of **fig 54:**

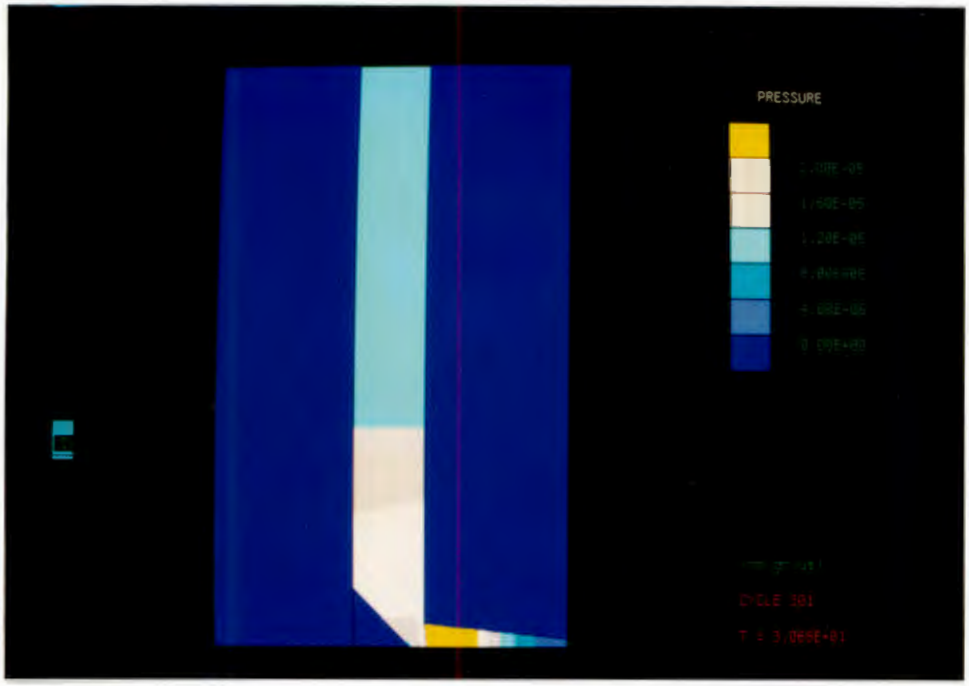

Figure 54: *Weak shock wave propagation axial symmetrically down the nozzle - 30 μ seconds after the start.*

The reflected wave back towards the source is also shown in fig 55. This photograph also shows the back pressure in the nozzle. It is this back pressure that is assumed to give rise to the emitted water jet (discussed in **Appendix O**).

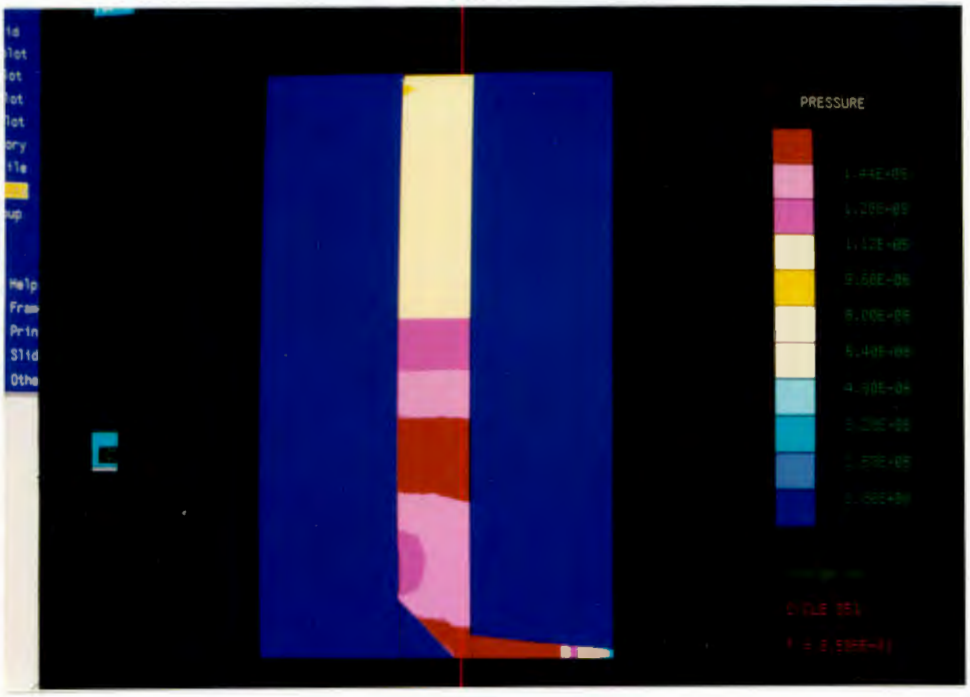

Figure 55: *Reflected wave and wave propagation down the nozzle - 36 μ seconds after the start.*

The target locations for pressure history points in the system are shown in fig 56 :

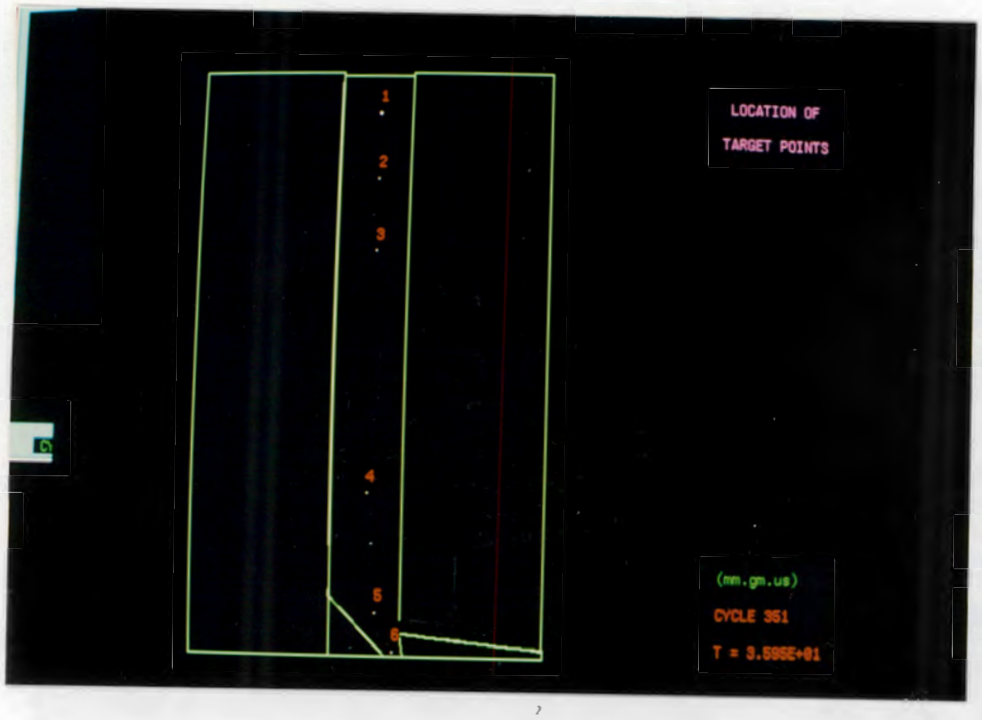

Figure 56: ***Target location points for the pressure history curves***

The pressure histories curves (w.r.t. time) of the target point locations shown in **fig 56** are shown in **fig 57**. These pressures show that the pressure at the start of the nozzle (location 6) is about 1.5×10^{-5} MBar.

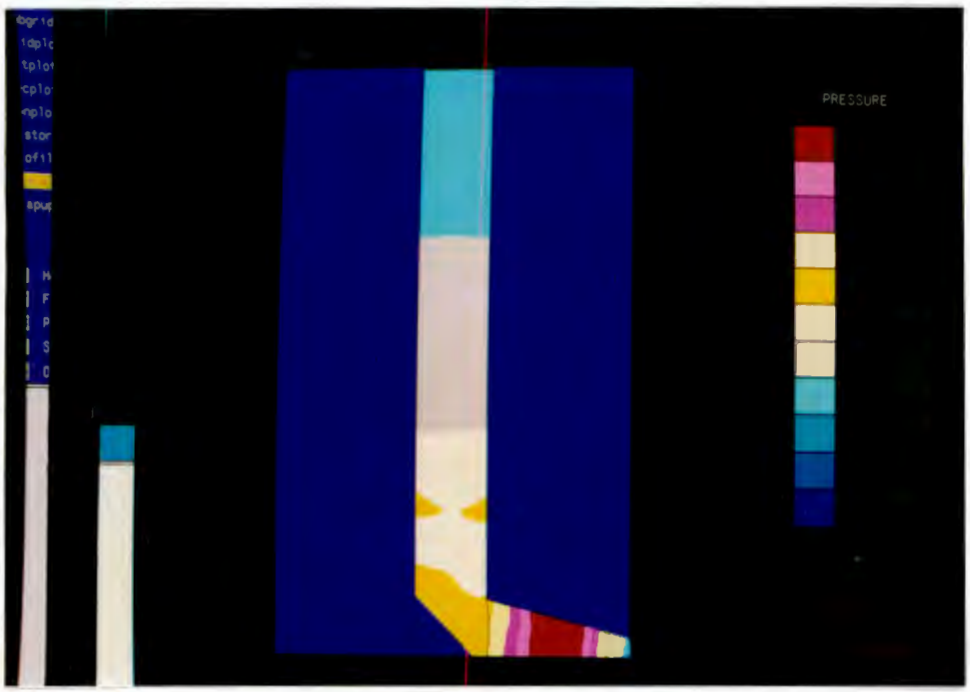

Figure 58: *Weak shock wave in the nozzle of cone / nozzle combination medium nozzle - regular cone - of Chapter 6 (36 μ seconds after the start)*

The pressure combination plot (target locations are the same as **fig 56**) is shown in **fig 59**. Target location 7 is not shown in **fig 56**. It is located midway down the nozzle. The pressure at the start of the nozzle is about 4×10^{-5} MBar. This combination has a higher back pressure than the previous combination. Thus this combination will produce a jet with a greater energy. This is experimentally verified in **Chapter 9**.

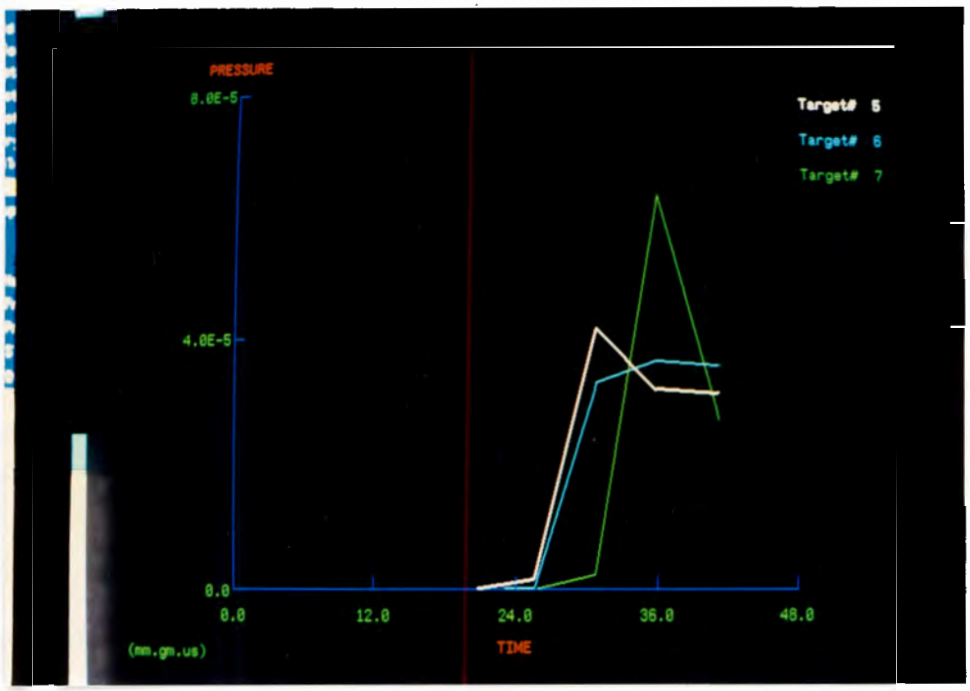

Figure 59: *Pressure combination plots for the medium nozzle - regular cone combination.*

The combination small nozzle - low cone (described in Chapter 6) is simulated next.

The pressure contour photograph of the weak shock wave in the nozzle is shown in **fig 60:**

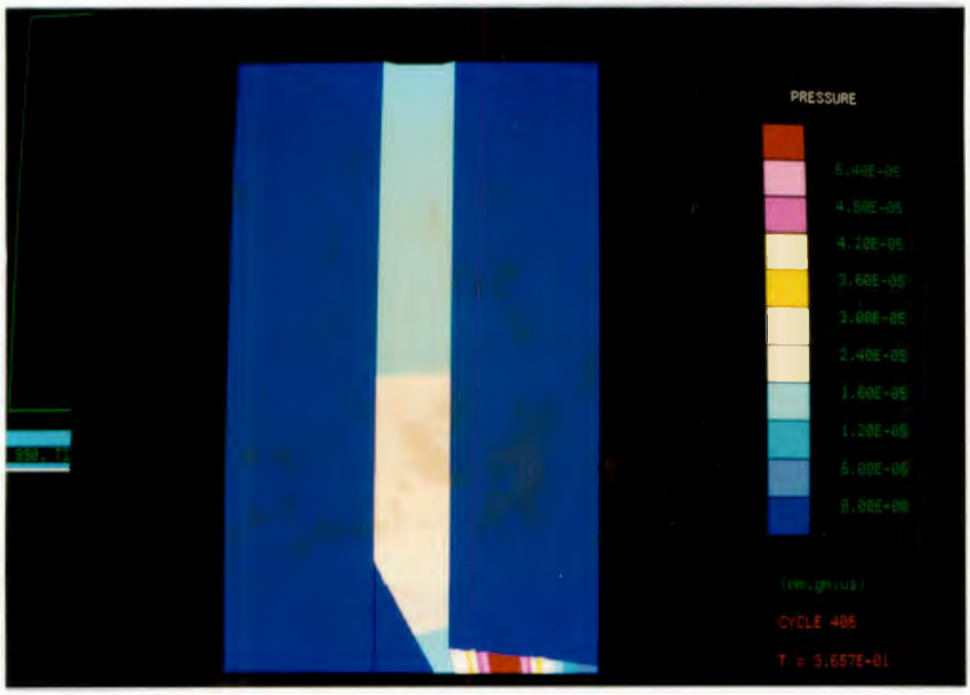

Figure 60: *Weak shock wave propagating down the nozzle for the low cone - small nozzle combination.*

The pressure time histories are shown in fig 61. The target locations are the same as those given in fig 56.

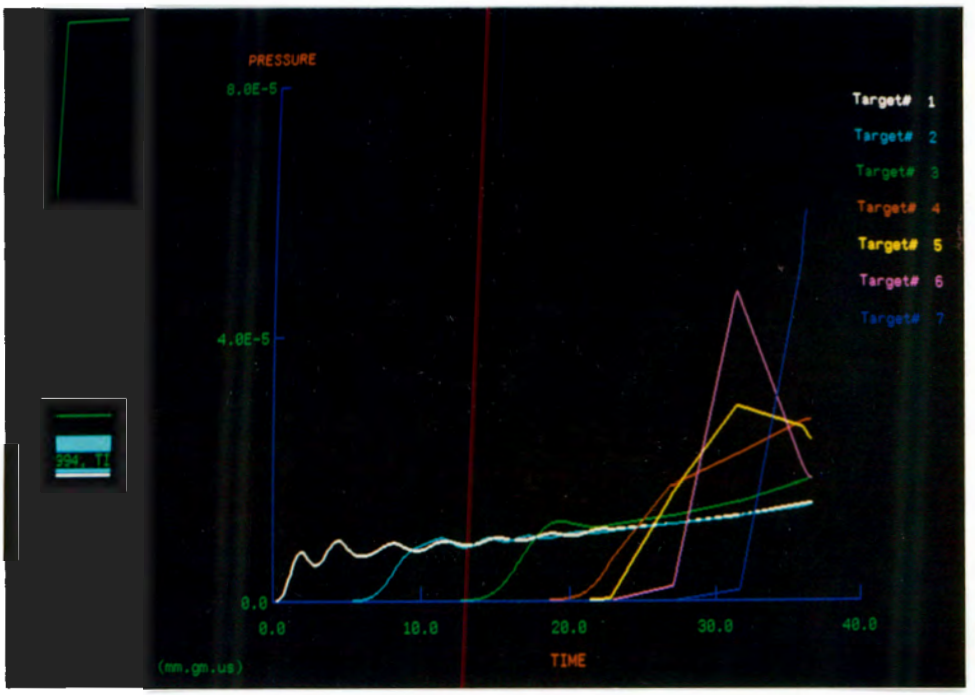

Figure 61: *Pressure combination plot for the small nozzle - low cone combination.*

The pressure recorded at target location 6 is similar to that obtained in the medium nozzle - regular cone simulation. However, the pulse duration in this case is very short - it is less than 10 μ seconds and triangular in shape. The pressure in the previous combination shows no sign of decaying over the measurement period. Consequently the medium nozzle - regular cone combination is expected to have the best jet performance.

7.4 Conclusions

Results show that ellipses focus from the minor focal point to the major focal point. This does not change significantly when the boundaries are no longer ridged but are compliant. This is in agreement with the Schlieren results published by Gustafsson **[15,17]** (**Appendix L**). Wave modes in the wall are seen to be traveling at a speed less than the contact point of reflection. Thus no lateral waves were produced in these simulations.

The analysis performed in **Chapter 5** shows that the shape of the converging weak shock wave is symmetric but that the pressure distribution varies strongly with angle θ about the second focal point. This is shown in **fig 43** of the

simulation. This is also in agreement with the pressure profiles predicted in the analysis of **Chapter 5**.

No non-linear focusing processes were observed in the simulations. The waves are approximately linear acoustic. The second focal point corresponds with the geometrical focal point (as predicted by Huygens principle).

The method of initiating the weak shock is an approximation of the actual spark discharge - pressure process. Thus the pressure magnitudes as the pressure time variation used in the simulation do not correspond to the pressures and profiles presented in **Chapter 4**. In spite of this simplification, good qualitative results showing the nature of the weak shock wave process were obtained.

The cone / nozzle interaction has been simulated using an approximate axial symmetric approach. Pressure histories for three cone / nozzle combinations have been recorded. These results show that the peak pressure amplitude, and pulse duration at the target at the nozzle vary strongly between configurations. This shows the importance of nozzle cone system design.

Simulations showed that the medium nozzle - regular cone would have the highest and longest back pressure (pressure at the nozzle). The small nozzle - low cone combination had similar pressures but was of impulse duration. The small nozzle - regular cone had comparatively low pressures. The discussion of **Appendix O** showed that the higher the back pressure and the higher the pressure pulse duration, the more energy available in the jet. Thus the medium nozzle - regular cone is expected to have the highest energy jet (out of these combinations). Experimental verification of this is presented in **Chapter 9**.

CHAPTER 8 :

TECHNIQUES FOR MEASUREMENT OF THE HIGH SPEED WATER JET

The water jet prototype is expected to produce a transient, water jet slug (with a velocity of the order of 100 m/s) [17]. There are a large number of parameters that effect the production of this water jet. Some of these factors have been analysed and simulated in **Chapters 4, 5** and 7. An experimental (and theoretical) investigation into all of these parameters is beyond the scope of this thesis. The primary objective of this work is to determine whether the water jet is suitable for use in an ejection system. **Chapter** 1 has covered general requirements for ejection systems and **Chapter** 2 has calculated the force required for ejection of a target particle.

The proposed water jet generator's suitability as an ejector force mechanism depends on the energy, speed and dispersion of the jet. This chapter reviews methods for the measurement of these quantities. Practical limitations restrict the number and the type of tests that can be performed on the system.

8.1 Measurement of experimental quantities

8.1.1 Pressure measurement within the cavity

Shock wave focusing in the cavity has been shown to be a complex process (**Chapters** 5 and 7). Gustafsson [15,17] has published qualitative Schlieren results (Schlieren methods are described in section 8.2.1)[10]. Verification of the theoretical development presented in **Chapters** 5 and 7 requires a knowledge of the pressure distribution within the cavity.

Experimental methods for the quantitive measurement of pressure are presented in section 8.2.

---

[10] Schlieren results allow the focusing process to be visualised - i.e. the wave front position can be determined. Quantitive measurements of the pressure in the wavefront are not possible **[68]**.

8.1.2 Water jet velocity measurements

The effect of some design parameters on the performance of the jet requires the water jet velocity, energy (momentum) and profile to be measured. Techniques for the measurement of these qualities are presented in section 8.3.

8.1.3 Water jet velocity accuracy

The jet velocity is expected to be in the range : 10 m/s to 1000 m/s **[17,18]**. Velocity measurement usually involves the measurement of distance over time. There are two sources of error in this process (assuming that the jet is not decelerating): time inaccuracy due to start or finish uncertainties and uncertainty in the distance measurement. These errors are cumulative and given by the expression :

$$v = \frac{d}{t}$$
$$\frac{\partial v}{v} = \pm\left(\frac{\partial d}{d} + \frac{\partial t}{t}\right)\times 100\% \qquad (8)$$

Where : $\partial v/v$ is resultant error in the velocity measurement[11], and $\partial t/t$ and $\partial d/d$ are the error in the time and displacement of the water jet respectively.

This is shown in **fig 62:**

[11] If the jet velocity is to be measured over 5 cm, the time for a 1000 m/s jet to traverse this distance is 50 μ seconds. The maximum permissable time error would be 5 μ seconds for a system accuracy of 10 % (if the distance was 100 % accurate). Similarly, if the time was 100 % accurate, the maximum permissable distance tolerance would be 0.5 mm. In reality the system accuracy is set by equation (8) -which considers the additive effect of the error in the two measurements.

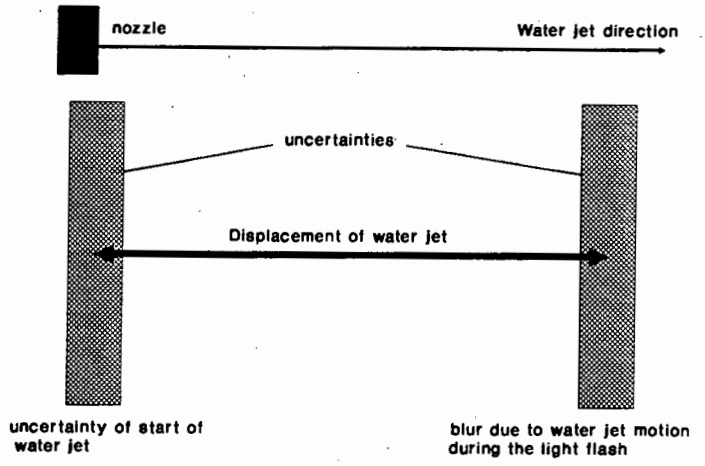

Figure 62: *Accuracy of water jet velocity*

High velocity water jets are affected by drag. This causes the jet to mushroom and decelerate soon after its emmision **[40,69]**. The measurement of the jet speed should therefore occur close to the nozzle (less than approximately 5 cm for nozzle diameters < 1 cm **[4]**).

8.2 Pressure measurement within the cavity

There are three possible techniques for the measurement of the weak shock wave pressure distribution in the cavity : Schlieren methods, interferometric approaches and pressure measurement by probes situated directly in the cavity.

8.2.1 Schlieren Systems

Schlieren systems show variations in the optical path length of light passing through transparent objects by causing the path length differences to appear as irradiance variations - density changes as being either darker or lighter grades on the image **[70,71]**.

Schlieren systems require a perpendicular transparent path through the object. Gustafsson **[15]** achieved this by replacing the outer covering plates of the water jet with optically ground glass plates. Two additional covering plates and a silicone sealing gasket ensured correct placement of the plates. This system required the electrode holders to be glued onto the glass plates (since no holes could be drilled in the glass). In addition, the cone duct and nozzle could not

be inserted. Thus cavity weak shock wave focusing could only be observed for a simplified condition.

Colour Schlieren

Relative pressures, compressions and rarefaction can be visualised using colour Schlieren systems. If there is a gradient in refractive index in one direction (either a compression or a rarefaction), this would appear as a different colour to a gradient in the other direction. The spectral colour bands have been used by some researchers to obtain quantitative pressure results. However, this technique is complex and the validity of quantitative Schlieren results is questionable [72].

8.2.2 Interferometric approach

Interferometric systems give a measure of density in terms of the change in optical path. This can be converted to pressure i.e. quantitative pressure results can be obtained [73]. Interferometric systems have been used to obtain quantitative pressure distributions in liquid shock cavities [87].

Interferometric measurements in the cavity are limited simplified generator systems[12] (the same simplified water jet system required for Schlieren work must also be used). These systems are expensive and require accurate optical alignment. Such techniques are beyond the scope (and budget) of this thesis.

8.2.3 Pressure probes

The development of the Lithotripters (Chapter 1) initiated a number of research projects into the physics of shock wave focusing in water. Part of that research resulted in the development of shock pressure probes suitable for water shock wave measurement[13] [8].

Müller and Platte [75,76] have designed a 1.2 mm diameter PVDF needle hydrophone. It has a bandwidth of 10 MHz and pressures up to 30 MPa can be measured. The probe is in commercial production : IMOTEC GmbH [77].

---

[12] Unpublished work using inetrferometric techniques have been used to study the deformation of the elliptical cavity walls [74]

[13] These probes require high mechanical strengths to withstand the shock pressures, risetimes of the order of nanoseconds and spacial compactness to enable the measurement of pressures 'at a point'

Other PVDF membrane hydrophones have been constructed [78] with higher bandwidths (20 MHz). However, these devices do not have the spacial resolution of the needle hydrophone.

A more recent advancement is the use of an acousto-optic fibre [78,79] The variation in the refractive index of the liquid at the front end of the fibre is measured. Similar bandwidths and spatial resolutions to the needle hydrophone have been achieved. However, at this stage the sensitivities are very low (0.8 mV/MPa).

These devices are not altogether suitable for pressure measurement within the cavity. Measurement will require a probe to be placed at different points in the cavity. In spite of the small spacial size of some of the probes (for instance the needle hydrophone), the dimensions of the probe relative to the cavity are relatively large. In addition the shock wave process has been shown (**Chapters 5** and 7) to be complex. All points of the cavity are traversed by two component shock waves. Measurement would result in the probe perturbing one or both of these components - perturbing the focusing process.

8.2.4 Conclusions

Pressure measurement within the cavity using pressure probes is not possible without perturbing the shock wave focusing process. Schlieren techniques give qualitative results and have been published for a simplified elliptical cavity generator in [15,17]. Quantitative results can be obtained using an interferometric approach. However, measurements are only possible if the elliptical cavity generator is a simplified system with two glass covering plates and no cone duct arrangement. These systems are complex and expensive. Thus the measurement of pressures within the cavity is not possible in the scope of this work.

8.3 Water jet measurement techniques

Techniques for the measurement of water jet slug velocity can be divided into photographic techniques and electro-optics techniques. Photographic techniques use specialised cameras, optical configurations, special light sources or a combination of these. The electro-optic approach uses two photodiode-LED pairs at a known spacing, and measures the delay between beam interruptions to calculate the speed of the opaque jet.

8.3.1 High speed photography

The velocity of the water jet can be calculated if the water jet slug's displacement between multiple frames (at a known rate) is recorded. Special cameras using a continuous bright light source have been designed. Framing rates of 24 frames per second can be attained with the conventional cine-camera (16 mm) [69]. High speed photography requires framing rates of the order of 500 f/s. Various high speed cameras have been designed [69] : rotating mirror, rotating prism and image converter cameras have been used in high speed physical experiments including water drop erosion, impact experiments, ballistics, fracture of plastic materials and explosions [4,5,69].

These techniques all require expensive, application specific equipment and usually require large amounts of film to be exposed for a single sequence.

8.3.2 High speed photography using short duration light sources

Water jet slug velocity can be measured by a conventional camera with an open shutter and a short duration flash [2]. The flash can either be repetitive or a single flash at a known delay from the initiation of the water jet. The former produces multiple exposures at a known rate. The latter will produce a single exposure of the water jet.

Duration of the flash

Light sources of short duration and high intensities are required to 'freeze' the event. If the water jet emerging from the nozzle is of the order of 100 m/s (100 000 mm/s) and the flash lamp has a duration of 10 μ seconds, the jet will have moved 1 mm during the time of the flash. This results in blur on the film. This blur is further amplified by any optical magnification used in the photography.

Continuous water jet photography systems can use special image compensating techniques to reduce this effect [2]. However, the photography of transient events relies on short duration light sources. A number of short duration light sources are available ranging from the Fisher nanolight[14] 10 ns spark source [80,81,82,83] to Xenon tubes (of the order 10 μ seconds) [84,85]. The cost of former system is prohibitively large for this thesis.

---

[14] The Fisher Nanolight is manufactured by Impulsephisik GmbH and has been used in in a wide range of Schlieren and high speed photography experiments.

Multiple flash sources

Velocity measurement using multiple exposures requires a number of short duration flashes at a high repetition rate (to ensure that the displacement of the water jet slug between exposures is small). The progression of a single water jet slug is then multiple exposed on an open shutter camera.

A number of short duration repetitive sources have been designed : multiple spark gaps and the pulsed laser. These sources are all characterised by their high cost (in the region of R300 000). Thus multiple flash sources are beyond the scope of this thesis.

Speed measurement by 100 Hz multiple exposure

An application of the multiple flash technique is to use the repetitive or strobe mode of commercial Xenon flash tubes [85] - typical xenon tubes can be flashed from 1 to 100 Hz.

This repetitive flash could be used to produce a multiple exposure (at 100 Hz) of the jet. This is shown in fig 63:

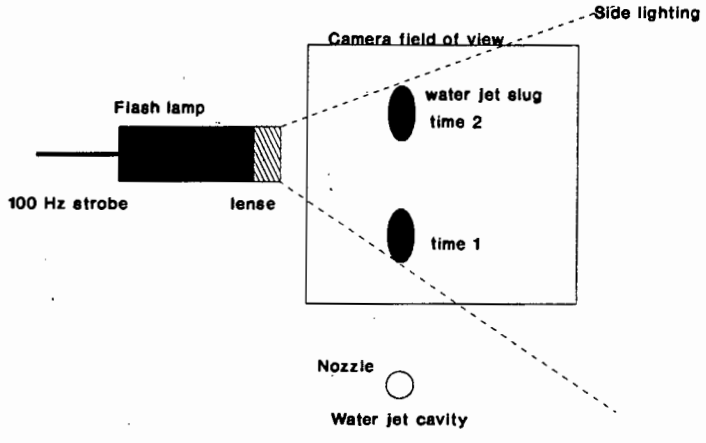

Figure 63 : *Water jet velocity measurement by 100 Hz flash*

The water jet is side lit to prevent continuous exposure of the film. The time between flashes at 100 Hz is 10 milliseconds. This restricts this method to small

velocities or large fields of view.

Speed measurement by the distance travelled during a known delay

If the time of water jet emission is known, a single exposure at a known delay using an open shutter and a triggered flash can be used to measure the water jet velocity. The displacement of the slug is measured on the film.

A suitable single flash system for the water jet prototype is shown in **fig 64** :

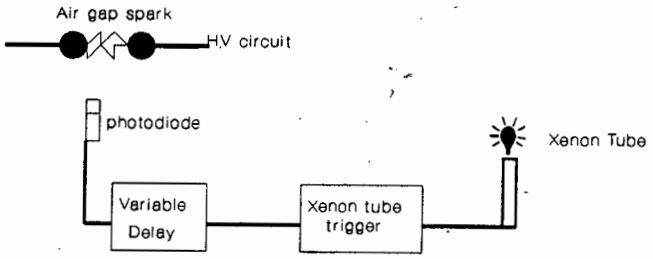

Figure 64 : ***Velocity measurement by a single flash at a known delay***

A photodiode is used to pick up the light emission from the air spark gap breakdown[15]. This triggers a delay (in microseconds) which in turn triggers the Xenon tube. The circuit operation and circuit diagrams for this system are given in **Appendix K**.

This technique requires the start time to be known accurately. In this case the system is triggered by the air gap spark. **Chapter 6** has shown that there is a variable delay before the water gap breaks down. Experimental results (chapter 9) show that this delay and consequent error is less than 50 μ seconds.

---

[15] In practice, a fiber optic cable is used as a 'light pipe' to the photodiode. This allows the photodiode, and delay circuitry to be located some distance from the air gap switch. Interference due to the air gap breakdown and HV discharge circuit disrupts the electronics.

8.3.3 Electro-optical technique

An electro-optical velocity measurement technique is an alternative to photographic techniques. Two photo diodes and LEDs are aligned perpendicular to the path of the water jet. The first at the nozzle and the second a small distance away from the nozzle. The light rays will be interrupted by the semi-opaque water jet slug as it is emitted from the nozzle and again when it passes through the second diode-LED pair. The delay between the water jet passing the first diode and reaching the second diode can be clocked and accurately measured **[86]**. The response times of the photo diodes are relatively fast (of the order of a few μ seconds). This is shown in **fig 65** :

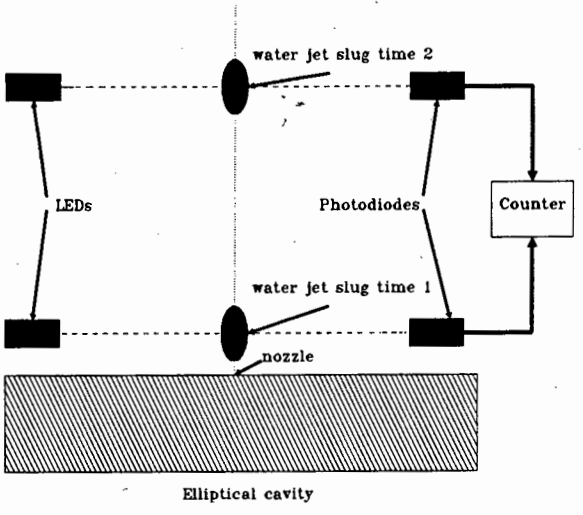

Figure 65: ***Electro-optic water jet velocity measurement system***

This technique is unsuitable for small diameter water jets - the photodiodes would then be required to be very close to the nozzle and the jet path. High voltage interference close to the prototype water jet cavity requires electronic devices to be situated at large[16] distances from the high voltage circuit.

[16] Experimental results showed that if a Faraday cage was used arround the air gap switch, electronics (in shielded enclosures) could operated unaffected by HV discharges at distances greater than 1 m from the HV circuit.

8.3.4 The choice of a velocity measurement system

A number of techniques are suitable for water jet slug velocity measurement. Multiple flash short duration light sources, special high speed cameras and ultra-short duration light sources (under 1 μs) are prohibitively expensive.

Velocity measurement using strobe techniques and electro-optical techniques are not suited to small diameter water jets. Prototype nozzle sizes (**Chapter 6**) are small - thus these techniques are not suited to this work.

Economic considerations have led to the choice of a Xenon tube (approximate duration 5 μ seconds) for use in a velocity measurement using a short duration flash at a known delay. The system can be triggered off the air gap switch or the breakdown between the electrodes in the cavity. The Xenon tube and power supply data are presented in **Appendix M.**

8.4 Water jet slug photography

Velocity measurement using a single short duration flash can use a number of different photographic setups : the subject (water jet), light source and camera can be positioned for different effects.

8.4.1 Silhouette photography

The most efficient system is to collimate the light from the Xenon tube and image this on the film. This ensures that all the light from the source is exposed on the film. The subject (water jet) appears as an opaque (dark) form on the film. This technique is also known as shadowgraph photography.

The camera should be located as close as possible to the subject (resolution). The collimation of the parallel light in a shadowgraph system limits this distance to the focal length of the collimating lens or mirror used. An alternative to this system is to use the modified shadowgraph system shown in **fig 66** :

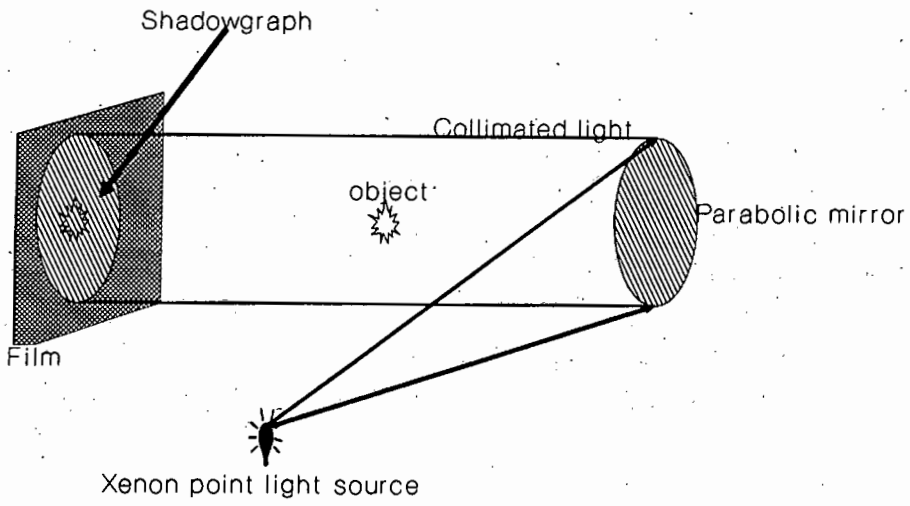

Figure 66 : *Modified shadowgraph system using only 1 collimating mirror*

The light from the Xenon tube is collimated and passes through the subject. This system is less efficient than a complete shadowgraph system. However, the camera and subject can be located in close proximity. Exposure calculations are presented in **Appendix P.**

8.4.2 Front lighting

An alternative to silhouette photography is to illuminate the water jet from a position close to the camera - front lighting. Thus water jet profile and detail can be viewed. The disadvantage of this system is that it is inefficient with only the reflected light from the subject and surround reaching the camera. Exposure calculations for this configuration are given in the following section.

8.4.3 Exposure calculations

When using open shutter flash photography, a useful guide to initial exposure aperture and flash-subject distances is the 'guide factor'(DA) **[84]**. A calculation for this DA is given in **Appendix P** for an open shutter camera with an aperture of f 1.4 , the Hamamatsu Xenon flash light source and a high speed black and white film (3200 ASA). The guide factor is the product of the camera lens aperture A, and the distance (in feet) D from the flash lamp to the subject.

The calculation shows that the DA is 0.377 for this configuration. Thus the light source must be situated at least 8 cm from the subject (water jet) for full

The height of a target of known mass is measured after a vertical impact. The potential energy E_P is related to the target momentum by :

$$E_P = mgh = E_K = \frac{1}{2}mv^2$$
$$p = mv$$

substituting we get :

$$p = \sqrt{2\frac{E_p}{m}}$$

If the system is assumed to be a 1 dimensional[17] conservative system i.e. no viscous losses and ideal collisions are assumed, the momentum of the water jet is equal to the target momentum.

If the velocity of the water jet slug is known, the momentum of the water jet slug can also, to a first approximation, be given by the product of the velocity and the mass of the water jet. The mass of the water jet can be obtained by measuring the volume of the liquid missing from the cavity. This analysis assumes that all of the water emitted from the cavity is in the form a coherent slug - the total mass of which is used in the collision process.

8.6 Conclusions

Two aspects of the water jet slug are to be measured - the water jet velocity and the water jet energy. A suitable experimental technique for the measurement of water jet velocity was found to be a photographic system - a single flash at a known delay after the initiation of the jet. A suitable technique for the measurement of water; jet slug energy was found to be a ballistics approach where a target of known mass was displaced by the water jet.

[17] This implies that the momentum transfer is linear - angular acceleration of the target is neglected

CHAPTER 9 :

EXPERIMENTAL RESULTS

This chapter presents the results of tests performed on the prototype water jet generator and discharge circuit. The primary objective of this testing was to assess the generator's performance and hence its suitability as a force mechanism in an ejection system. Requirements for the ejection system have been discussed in **Chapters** 1 and 2. Suitable experimental techniques have been reviewed in the previous chapter. That chapter concluded that the measurement of the water jet velocity and energy should be performed using a single flash modified shadowgraph photographic system and a ballistics system respectively.

Chapter 4 has shown that the transfer of energy to the liquid and the shape and characteristics of the initial shock wave are determined by the operation of the electrical circuit. This chapter examines circuit quantities during the discharge. Unknown circuit elements are measured, calculated and compared to the theoretical optimum.

9.1 Test Objectives

The objectives of this chapter are :

- To determine whether the elliptically focused water jet concept works.
- To experiment with different prototype dimensions.
- To compare the results of these permutations to the theoretical simulations of **Chapter 7.**
- To measure the electrical qualities during discharge and assess the circuit performance.
- To assess the system's suitability as a force mechanism for ejection purposes.

9.2 Testing of the prototype

The testing of the prototype was divided into three sections :

9.2.1 Discharge circuit analysis

Electrical circuit analysis - the voltage and the current during discharge were measured using specially designed probes. These measurements allowed the

inductance of the circuit elements to be calculated and the physics of the discharge process to be studied. The discharge circuit with and without a liquid gap was studied.

9.2.2 Water jet slug velocity

The velocity of the water jet slug was measured using approximate maximum jet slug height measurements and using photographic techniques (discussed in **Chapter 8**). The velocity of the water jets for different cone-nozzle combinations was measured.

9.2.3 Water jet energy and momentum

The water jet energy or momentum was calculated using two techniques : firstly measuring the amount of water missing from the cavity after discharge and the water jet velocity, and secondly by measuring the energy imparted to a target of known mass. The results of these tests are presented in section **9.8** for different cone / nozzle combinations and different circuit values.

9.3 Electrical discharge circuit measurement

9.3.1 Testing of circuit components

Testing of the air gap switch

Initial experiments used the circuit shown in **fig 69**. Different capacitors[18] were discharged across the air gap. This enabled the breakdown voltage of the airgaps for different gap lengths to be measured. The calibration of the 12.6 mm air gap is shown in **Appendix N**.

The spark gap jitter was expected to be less than 1% of the total discharge time **[5]**. The jitter on the experimental system was found to be virtually unmeasurable. Two typical voltage curves (measured by the TEK HV probe) for the sphere gaps are shown in **fig 68** :

[18] Capacitors were tested to their rated voltage (with suitable current limiting protection) before use in discharge experiments.

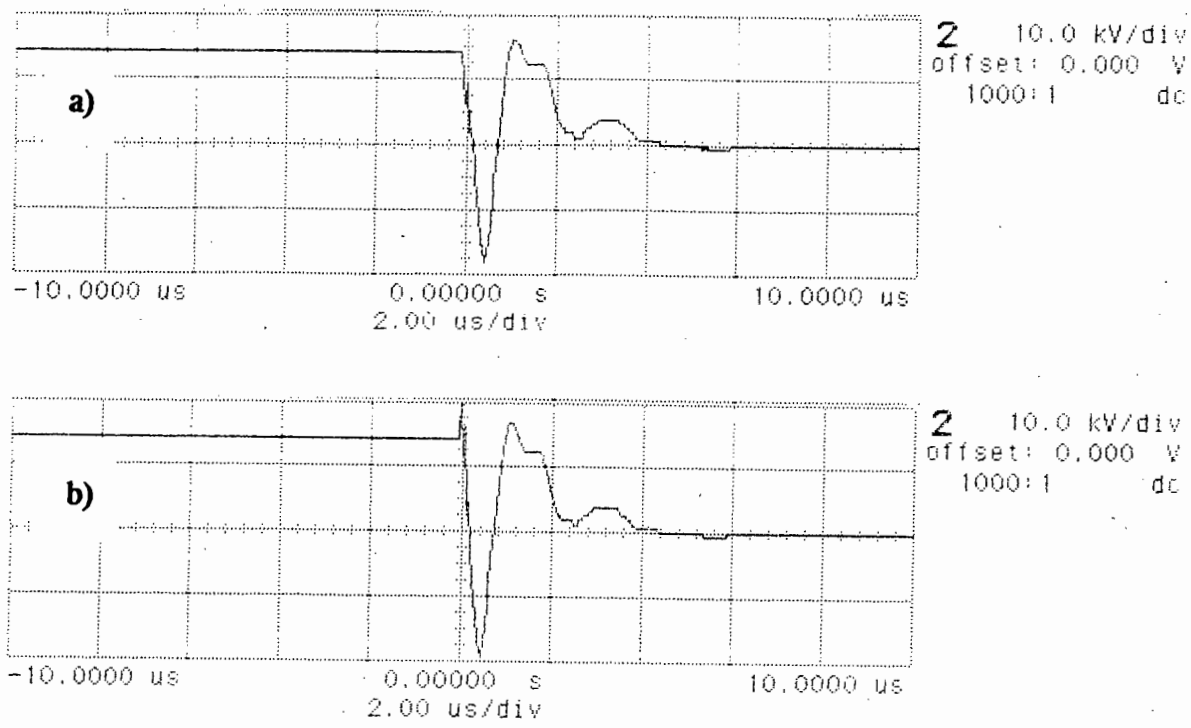

Figure 68 : ***Voltage across air gaps during breakdown a) no jitter b) small amount of jitter at the start of switching.***

The first voltage distribution shows no signs of oscillation. The second shows a very small oscillation at the start of switching - due to the spark gap jitter.

9.3.2 Measurement systems

Measurement of the voltage and current during the discharge requires special probes with fast rise times (under 1 μ second). High voltages and large peak currents during the discharge require probes designed to withstand large stresses.

High voltage measurement

The high voltage measurement was performed by a TEK 6502 HV DC measurement probe. This probe is a specially constructed resistive voltage divider. The resistances have been constructed with minimum inductance and a fluorocarbon dielectric. Voltage transients up to 40 kV with a rise time of less than 4 ns (ie. a 75 MHz bandwidth) can be measured **[88]**. The probe is a 1000 : 1 probe and is connected to a memory oscilloscope.

The resistance between the water gap electrodes does not remain constant throughout the discharge. This is due to the change in plasma channel width during the discharge (**Chapter 4**). Thus measurement of the voltage change across the water spark gap is not sufficient to infer the resultant current in the circuit (ie. by using Ohm's law).

The current must then be measured directly. This is done by means of the current shunt probe.

Current shunt probe

A low inductance resistance can be used to measure currents with short rise-times. A special shunt was constructed for this project. This probe has a bandwidth of 15 MHz and a resistance of 960 μ Ω. Thus the probe is an approximate 1000 : 1 (Amp to Volt) probe.

The current shunt resistance construction is shown in **Appendix** V.

9.4 Discharge without water gap

9.4.1 Measurement of the capacitor and circuit inductance

The inductance of the capacitors[19] and leads can be calculated from the frequency of the current oscillation during discharge. The discharge circuit is shown in **fig 69** :

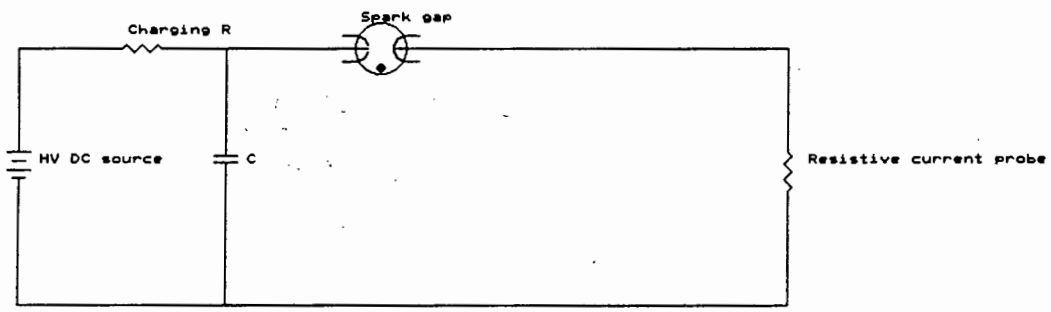

Figure 69: ***Discharge circuit schematic for the measurement of circuit inductance***

[19] Four, 60 kV, 0.04 μF capacitors could be connected in parallel to form a capacitor bank.

The capacitors are charged by the HV source (**Chapter 4**). The air gap breaks down and the capacitors are discharged to earth through the current measurement probe (**Appendix V**).

The resultant current variation - measured by the current probe and an HP 100 MHz digital oscilloscope - is shown in **fig 70** :

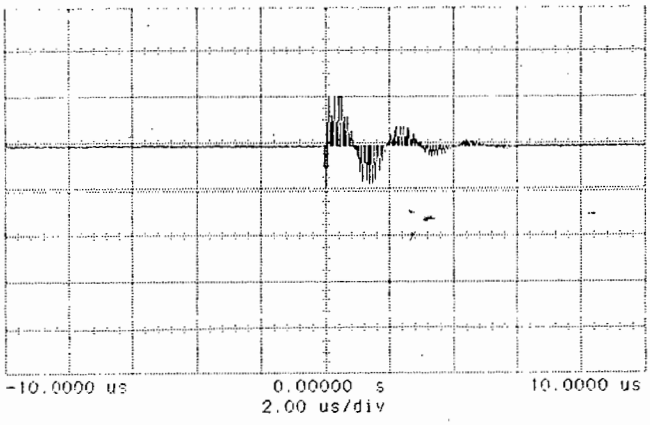

Figure 70: ***Current vs. time for C = 0.08 μF, V = 15 kV i.e. 2 capacitors***

The horizontal time-base is 2 μ seconds / div and the vertical scale is 2 kAmps / div. The current is oscillatory i.e. : the discharge circuit is underdamped.

The inductance of the circuit is calculated from (**Chapter 4**) :

$$T = \frac{1}{f} = 2\Pi\sqrt{LC} \qquad (9)$$
$$\tau = \Pi\sqrt{LC}$$

The current distributions and calculation of inductance is given in **Appendix R**. A summary of these calculations is shown in the following table :

Circuit Configuration	τ (μ seconds)	Inductance (μ H)
1 capacitor	0.8	1.6
2 capacitors	1.0	1.27
3 capacitors	1.2	1.22
4 capacitors	1.2	1.24

The calculated value of inductance includes the capacitor self-inductance[20] and the inductance of the leads of the circuit. The inductance of the circuit configuration is seen to drop with increasing parallel capacitor elements with the exception of four capacitors in parallel - here the inductance of the leads (longer lengths were required) dominate.

9.4.2 Measurement of the resistance of the leads

The total resistance of the leads and connections was measured to be approximately 0.3 Ω. This value included the value of the current shunt resistance[21] (1 milli Ω).

9.5 Discharge with a water gap

A water cavity with electrodes was introduced as a series element in the circuit of **fig 69**. Discharges were observed for different capacitors, gap lengths and applied voltages. The water cavity system that was used in these initial experiments is shown in **fig 71** :

[20] Commercial discharge capacitors (0.0005 μF - 0.1 μF) have advertised self-inductances of 0.01-0.1 μF. Thus the capacitors used in this work have comparatively large inductances.

[21] The shunt was left in the circuit during all discharge experiments.

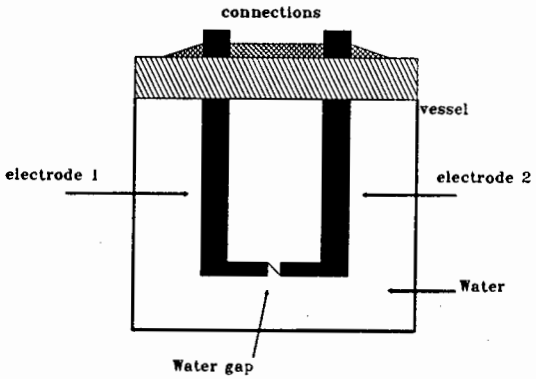

Figure 71: ***Experimental system for water gap discharges***

The water gap was shown to be a non-linear element in the circuit. Quiet or ionic discharges were observed for some discharges.

9.5.1 The water spark gap

The voltage across the water spark gap during a discharge is shown in **fig 72 :**

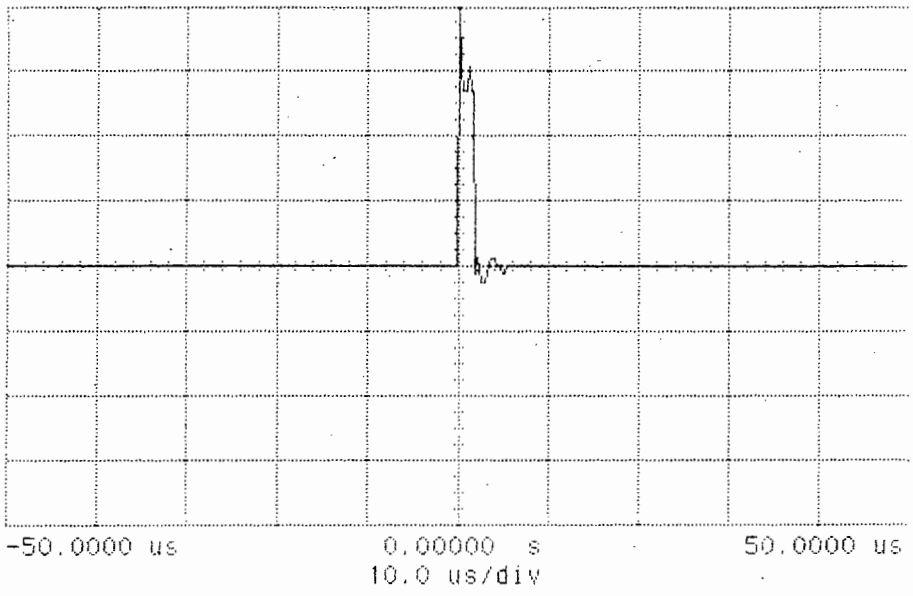

Figure 72 : *Voltage across a water spark gap during a discharge*

The vertical scale is 10 kV/div. The voltage across the gaps increases to the voltage of the capacitors almost instantaneously after air gap breakdown. The voltage is constant for a time (delay) before breakdown in the liquid starts to occur. The delay can be from a few μ seconds (shown in fig 72) to several tens of μ seconds. The latter is shown in fig 73 :

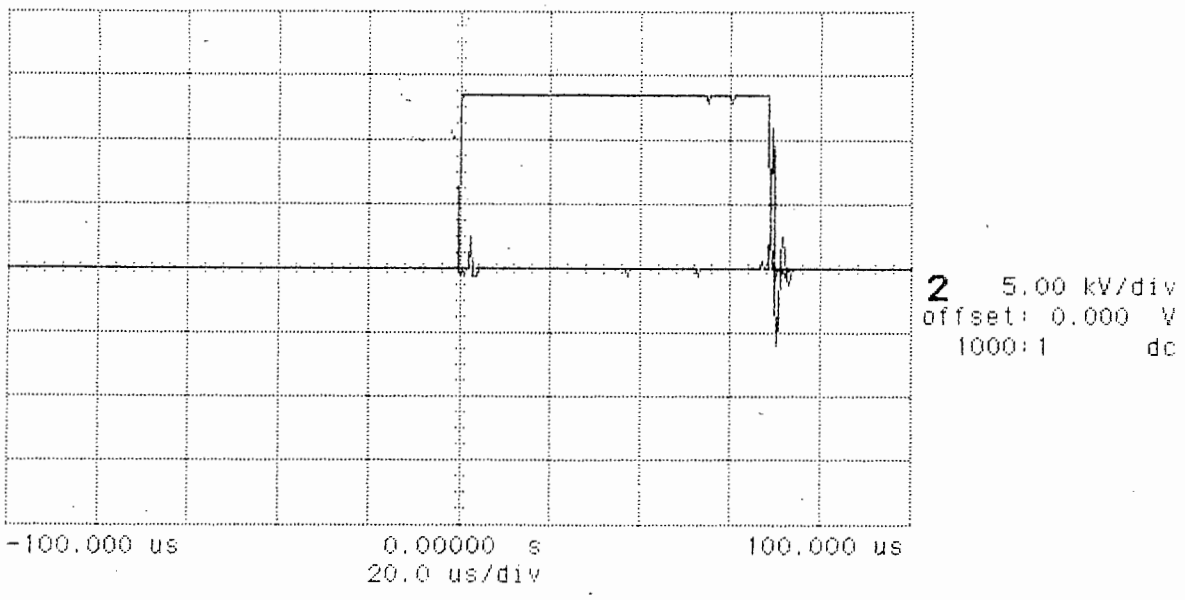

Figure 73 : *Voltage across water gap during discharge showing long delay before breakdown*

The variation in the delay is discussed in section **9.5.3** and calculated in **Appendix Q**.

After water gap breakdown, the voltage across the water gap decreases rapidly. At the same time a considerable rise in current takes place. This is shown in **fig 74** :

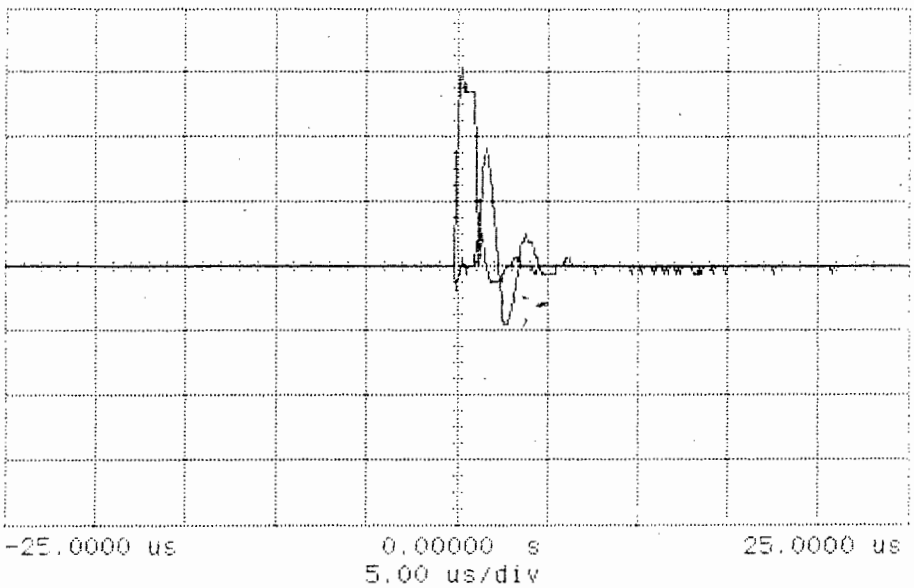

Figure 74 : ***Current through and voltage across a water gap during discharge - C = 0.08 μF, V = 15 kV, breakdown length 3 mm***

The current in the circuit is oscillatory. The frequency of oscillation is lower in this circuit than in the circuit shown in **fig 70** without the water gap - the inductance of the circuit has increased (equation (9)).

9.5.2 Quiet discharges

'Quiet discharges' were observed for some values of water gap length, water conductivity and electrical field strength. Quiet discharges are discharges without the formation of the spark channel. They are the result of the time delay before breakdown being so long that the voltage across the channel has decreased below the minimum required for water gap breakdown and the capacitor charge leaking away. The voltage across and current through a water gap during a quiet discharge is shown in **fig 75** :

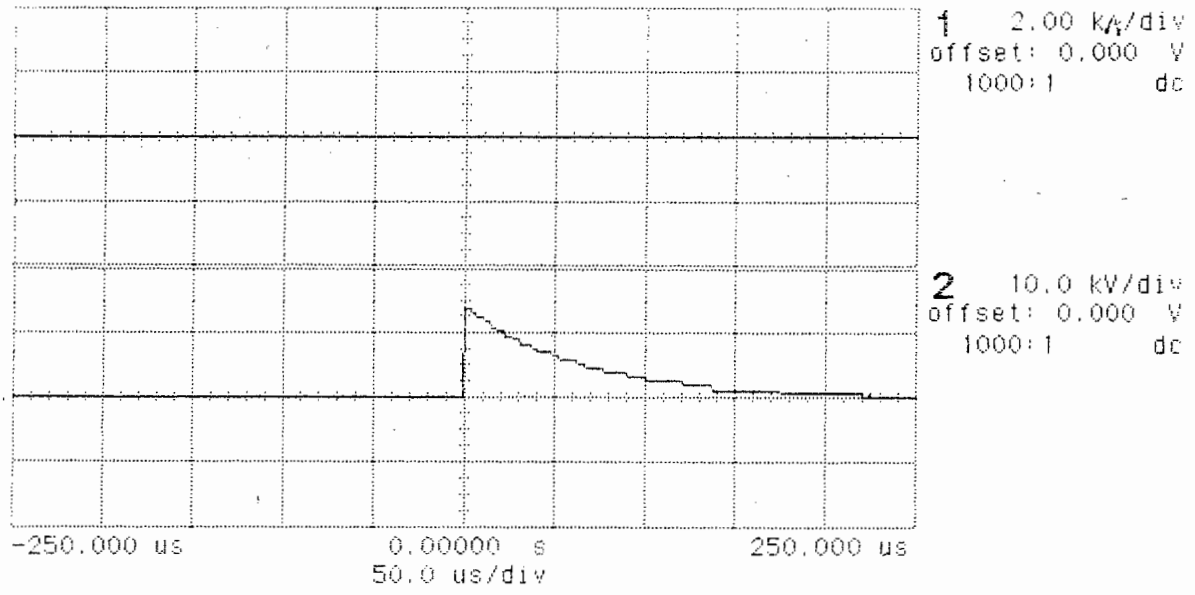

Figure 75 : *Voltage and current during a quiet discharge*

This effect only occurs for field strengths comparable to the breakdown strength of the water used (the breakdown strength of water is 10 kV/cm) or high conductivity liquids[22]. The former effects the field distribution and the latter effects the ionic resistance. The effect is also statistically variant i.e. it can be observed in some but not all discharges.

9.5.3 Variation in the delay before water gap breakdown

The time to breakdown or streamer formation is directly related to the field strength across the water gap. It is also related to the conductivity of the liquid. Since the water jet cavity was constructed out of tool steel, the conductivity of the water increases as the cavity walls oxidise. The resultant delay before breakdown increases. **Appendix Q** calculated the delay to breakdown to be on average 2.65 μ seconds for V = 14 kV, C = 0.08 μF and gap length = 3 mm. After 20 minutes of testing this average had increased to 20.45 μ seconds. No quiet discharges occured for this configuration.

[22] De-ionised, de-mineralised water was used in all prototype experiments - this ensured that the conductivity of the liquid (initially) was low.

9.6 Discharge in the prototype

The current distribution of a discharge in the cavity of the prototype generator is shown in fig 76 :

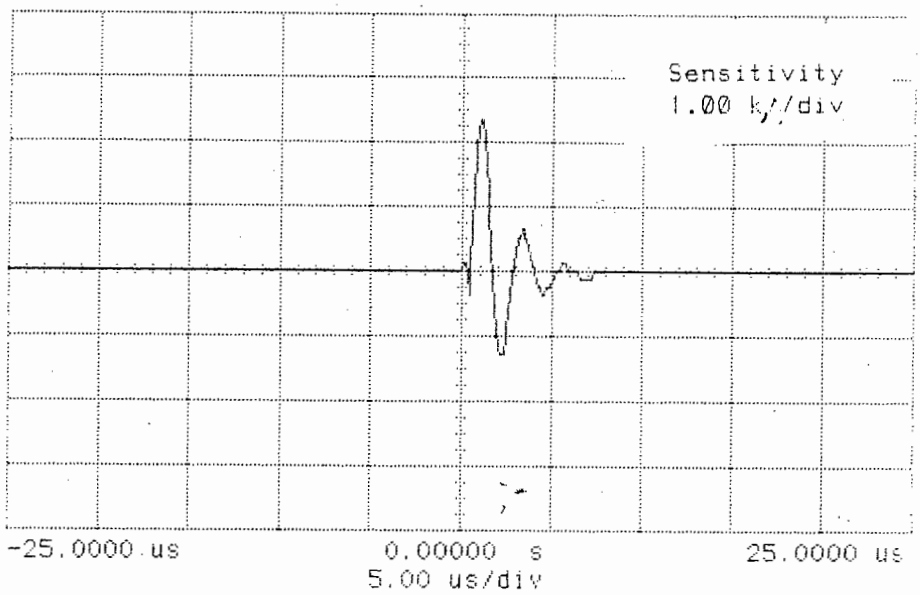

Figure 76 : *Current through prototype generator water gap during discharge - V = 14kV, C = 0.08 μF and water gap length = 3 mm*

This shows the current has a peak of approximately 2 kA and that the discharge circuit is underdamped.

9.6.1 Inductance of the prototype system

The circuit used two capacitors in parallel i.e. total capacitance = 0.08 μF. The inductance of these capacitors and of the circuit without the water gap has been calculated to be 1.27 μ H. The circuit including the water gap has a half period τ = 1.3 μ seconds. Thus the total inductance of the circuit and the water gap is (equation (9)) = 2.14 μ H. The inductance due to the water gap and leads to the water gap is :

$$L_{prototype} = L_{circuit\ with\ water\ gap} - L_{circuit\ without\ water\ gap}$$

Thus : $L_{prototype}$ = 2.14 - 1.27
= 0.87 μ H.

9.6.2 Resistance of the water gap

The resistance of the water gap will determine the circuit damping. **Chapter 4** has discussed the effect of this parameter on the circuit performance. The measurement of the water gap resistance is not immediately apparent since the voltage and current across the gap are highly non-linear. However, examination of the Laplacian analysis of **Appendix E** , shows that the maximum current in the discharge is given by :

$$
\begin{aligned}
I_{max} &= \frac{V e^{-\alpha t_{max}}}{L \omega_n} \\
\omega_n &= \frac{1}{\sqrt{LC}} \\
\alpha &= \frac{R}{2L}
\end{aligned}
\qquad (10)
$$

Where :

t_{max} = the time to the first current peak
I_{max} = maximum current peak

Hence the water gap resistance can be approximately calculated from the current distribution.

Water gap resistance measurements

Appendix W calculates the resistance of a number of water gaps during discharge. The circuit values were C = 0.08 μF, V = 14 kV, L = 2.14 μH:

Water gap length (mm)	Water gap resistance (Ω)
2	1.2
3	1.9
3.6	2.17

Thus the water gap resistance is seen to increase with increasing gap length.

9.6.3 Circuit damping

The circuit damping is given by :

$$\xi = \frac{1}{2}R\sqrt{\frac{C}{L}}$$

Thus the damping for the water gaps are :

- water gap length = 2 mm
  $\xi = 0.11$
- water gap length = 3 mm
  $\xi = 0.2$
- water gap length = 3.6 mm
  $\xi = 0.21$

Thus the circuit is underdamped.

Critical damping

The optimum power transfer in a RLC circuit will occur for damping values that lie between 0.5 and critically damped (**Chapter 4**). The required resistance for critical damping is given by :

$$R = 2\sqrt{\frac{L}{C}}$$

Thus the resistance of the water gap should be R = 10.3 Ω for critical damping in the circuit.

9.6.4 Discharge circuit operation

The electrical discharge circuit was found to be an underdamped RLC circuit. The inductance of the prototype system and circuit was measured to be 2.14 μH.

The resistance in the circuit was measured and calculated. This resistance was found to be very low (of the order 1 to 2 Ω). Thus the damping factor ,ξ , was calculated to be 0.1 - 0.2 i.e. very underdamped. Since the circuit is well below

the optimum critically damped condition the power transfer from the circuit to the water gap resistance is poor.

The resistance required for critical damping is very high. The maximum water gap resistance is limited by the maximum distance between electrodes which is approximately 4 mm - higher voltages must then be used to ensure that the electric field strength is high enough to ensure rapid breakdown in the liquid.

The inductance of the circuit is relatively high. This value can be reduced by using shorter leads and special designs (discussed in **Appendix S**). If this value is reduced, the resistance required for critical damping would be reduced. The damping factor would also start to approach the theoretical optimum of 0.5 - 1.

9.7 Measurement of the water jet velocity

9.7.1 Water jet height measurements

As a first approximation water jet speeds can be approximated by the maximum height h_{max} that the jet slug attains.

$$v_{jet}^2 = 2\, g h_{max}$$

For the parameters : C = 0.08 μF, V = 15 kV, water gap length = 3 mm and the prototype cavity combination : large nozzle / regular cone (**Chapter 6**), the maximum height of the water jet slug was measured to be approximately 6 m. Thus the velocity of this jet is approximately = 11 m/s.

This analysis excludes the effect of air resistance - the velocity (close to the nozzle) will be greater when measured close to the nozzle. A more accurate measure of this velocity is the method presented in section **9.7.2**.

Measurements for the other cone nozzle combinations are shown in **Appendix T**.

9.7.2 Water jet high speed photography

The photographic system used to measure the water jet velocity is shown in **fig 64** and **fig 66** of **Chapter 8**. This system has a delay triggered by the air spark gap. The delay is set in microseconds to milliseconds. The delay triggers the short duration Xenon flash lamp. The dislacement of the water jet is read from

the photograph. The velocity of this jet is then :

$$V_{jet} = \frac{jet\ displacement}{t_{set\ delay} - t_{start\ of\ jet}}$$

Section **9.5** has shown that there is a delay before the water gap breaks down. As has been shown in **Chapter 8**, any uncertainties in the displacement or the time measurement introduce errors into the measurement system. This delay has been calculated to be on average 2 μ seconds. The jet velocities that will be encountered are relativly low - thus the measurement times are of the order of milliseconds. Consequently, the error introduced by triggering using the air spark gap[23] is neglible.

Calculated jet velocities

The jet velocities obtained from this system are shown in the following table.

Circuit values were V = 14 kV, C = 0.08 μF and the gap length was = 3 mm. The start of the jet is taken to be approximately 100 μ seconds. The combination used throughout was the regular cone / medium nozzle.

displacement (cm)	delay ms	jet velocity m/s
1.5	1	17
2	1	22
2.6	1	30

9.7.3 Water jet slug propagation

The propagation of a single water jet slug is shown in the series of photographs shown in **fig 77 - 79** :

[23] The error can be reduced by triggering the process from the liquid gap breakdown directly. Thi ..an be done using a fiber optic cable, mounted flush against the wall of the cavity. This ible would receive the light emmitted from the liquid gap breakdown. This technique w not attempted in this project.

Figure 77 : ***Propagation of a water jet slug (delay 1 ms)***

This photograph shows the water jet as it is emitted from the nozzle. The water jet 3 ms after the air gap has closed is shown in fig 78 :

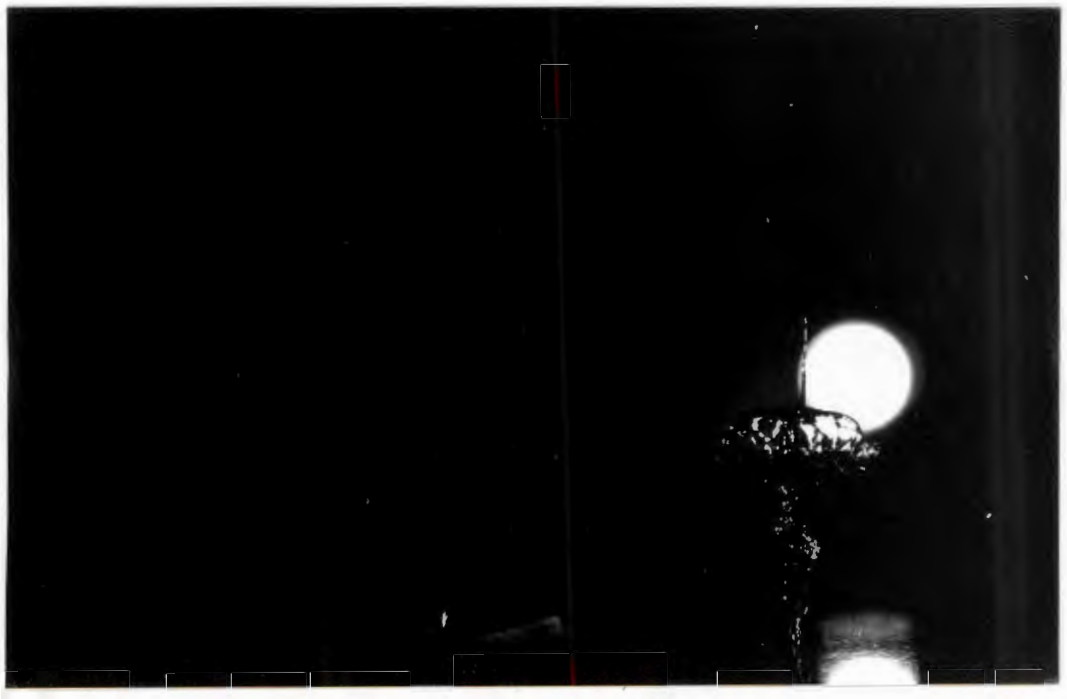

Figure 78 : *Water jet (delay 3 ms)*

Water jet at 5 milliseconds : fig 79 :

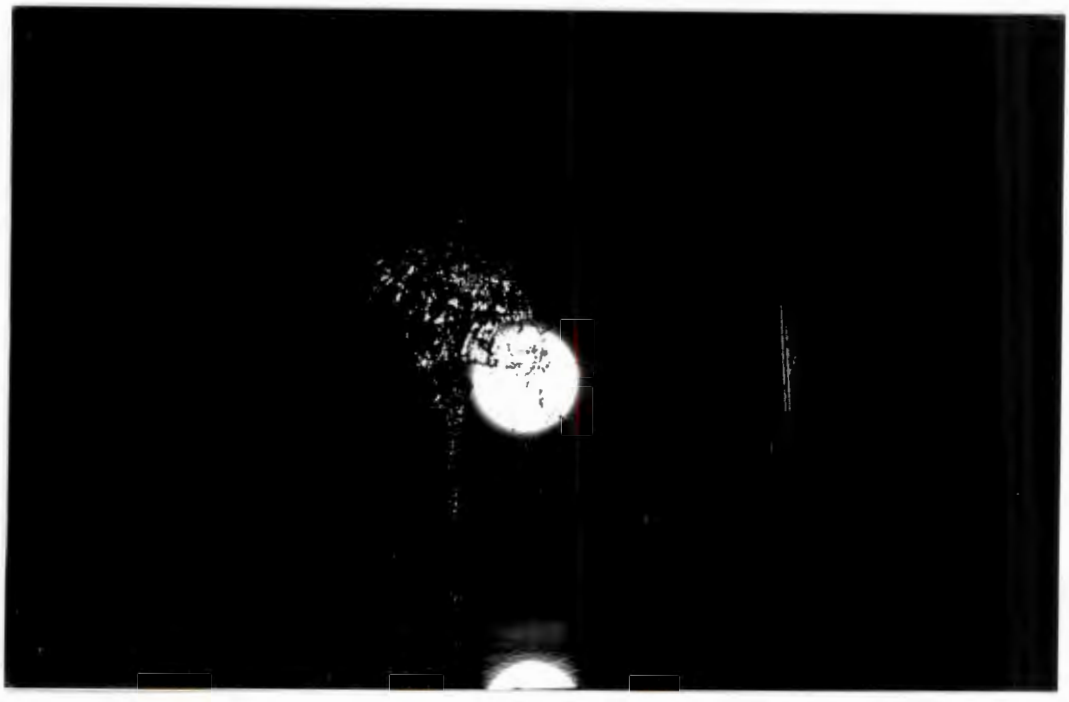

Figure 79 : *Water jet at 5 ms.*

The water jet slug has a mushroom shaped front - approximate diameter 1.5 - 2 cm. This mushroom as a small leader jet pointing in the direction of propagation. Some of the photographs (also shown in **Appendix Y**) show instabilities and breakup even at short distances from the nozzle - these are assumed to be due to the sub-optimum nozzle designes used in this project. All photographs are for different events - thus the propagation of an individual jet slug is not studied. The difference in profile between the jets is apparent.

Effect of adding a detergent

A small amount of detergent (TEPOL) was added to the water in the cavity to reduce the meniscus forces in the nozzle and to reduce the possibility of bubbles forming in the cavity. The conductivity of the water was raised. This would result in a greater ionic current before water gap breakdown. This effect could induce more quiet discharges. However, no effects[24] were experimentally observed.

[24] Leach and Walker **[89]** found that detergents improved water jet performance.

9.8 Water jet energy and momentum measurements

A more direct measure of the water jets performance is to measure the maximum height a target of known mass, impacted vertically by the water jet, reaches - the ballistics measurement system. Tests using this technique are described in section **9.8.2**.

9.8.1 Volume of water missing from the cavity

The momentum of the water jet can be approximated by the mass of the water jet multiplied by the velocity of the water jet. The velocity of the water jet has been calculated in the previous section. The volume of water missing from the cavity due to one discharge is assumed to be equal to the volume of water emitted as a water slug. This volume can be taken as first approximation to be the mass of the water jet slug.

The water missing after a discharge from the medium nozzle / regular cone was found to be approximately 0.2 ml i.e. : $m_{water\ jet} = 0.2$ g. If the water jet velocity is taken to be approximately 30 m/s, the water jet momentum is : 0.006 kg/m/s. This is smaller than the required momentum of 0.067 kg/m/s (**Chapter 1**) for deflection.

The amount of liquid missing from the cavity was difficult to measure - the approach was inaccurate for small nozzles. However a general trend was for the volume or mass of the water jet slugs to increase with increasing nozzle volume. A more accurate measure of the water jet momentum was obtained using the ballistics technique.

9.8.2 Water jet slug energy

A plastic cone target of mass 1.06 g was placed over the nozzle. The nozzle then emits a jet which strikes the inner section of the cone. The maximum height h is read visually from a meter rule - shown in **fig 67:** of **Chapter 8**.

Assumptions

This system assumes : the water jet - target collision is an ideal collision, air resistance on the target can be neglected and that the water jet slug impacts the centre of the target cone (i.e. the cone has no angular momentum).

University of Cape Town

Target cone propagation

The vertical displacement of the target cone is shown in the sequence of photographs shown in **fig 80** :

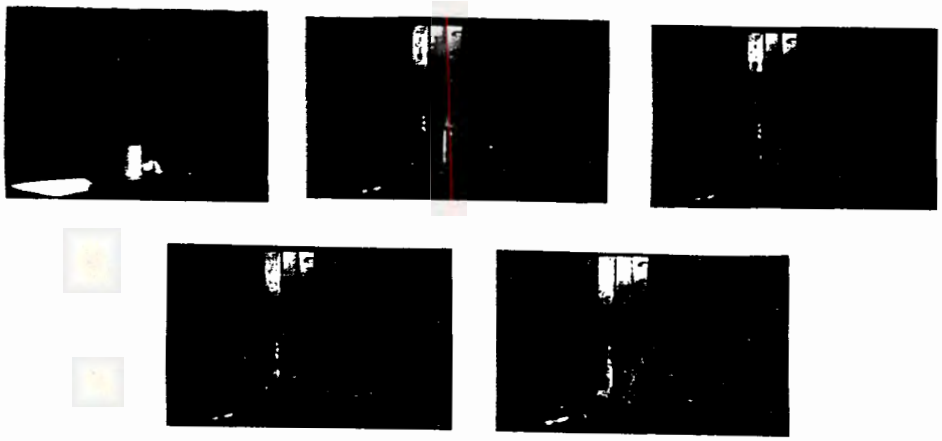

Figure 80 : *Target cone vertical displacement sequence. Photographs are 1 ms per frame (different events)*

The photographs show the cone at different times after air-gap discharge. The photographs are for separate events. The time between photographs is 1 ms.

Results

The maximum height of the target was recorded for all the cone - nozzle combinations.

Detailed results are presented in **Appendix U:** . The average and maximum target height for the different cone-nozzle combinations are shown in **table II:**

Table II

Cone-nozzle Combination	Max Height [cm]	Ave Height [cm]
large nozzle / regular cone	100	66
medium nozzle / regular cone	100	74
small nozzle / regular cone	7	4.7
large nozzle / low cone	43	32
medium nozzle / low cone	68	53
small nozzle / low cone	1	-
large nozzle / flat insert	66	45
medium nozzle / flat insert	80	61
small nozzle / flat insert	1	-

The combination with the highest average target height is the medium nozzle / regular cone combination.

The energy imparted to the target is given by :

$$E = m_{target} g h = \frac{1}{2} m_{target} v_{target}^2$$

Thus the approximate maximum energy imparted to the cone target is (maximum height = 1 m) 0.01 J

Efficiency of the generator

Thus the maximum water jet energy is approximately : E = 0.01 J.

The electrical circuit energy is given by ($0.5\ CV^2$). Since V = 14 kV, and C = 0.08 μF, the electrical energy is : 7.8 J.

Thus the efficiency of the generator is :

$$Efficiency = \frac{E_{target}}{E_{electrical}}$$
$$= \frac{0.01}{7.8}$$
$$= 0.001 = 0.1\,\%$$

9.9 Discussion

Two areas in this project have been experimentally investigated : the electric discharge circuit operation and the performance of a prototype of the elliptically focused water jet generator.

9.9.1 Electrical circuit operation

The circuit was found to be an underdamped system. The water gap resistance is much smaller than that required for critical damping. Two methods were considered for the improvement of this situation : the first involved the lengthening of the water spark gap. This was found to increase the gap resistance and thus the damping factor - however, the maximum gap length was limited by practical cavity height limitations and no marked improvement was found. The second method proposes a reduction in the circuit inductance. This requires special low inductance capacitors, stripline conductors and a small physical configuration. These methods are discussed further in **Appendix S** , and were not attempted in this project.

9.9.2 Water jet energy dependence on cone / nozzle combination

The combination with highest jet energy was found to be the medium nozzle / regular cone combination. The theoretical simulations of **Chapter 7**, predicted that this combination would have a the maximum back pressure and pulse length. **Chapter 7** also predicted that the low cone combinations would be inferior to the regular cone combinations - this is verified in the water jet energy experiments.

Table II: also shows that in each of the cone combinations, the medium nozzle in each case outperforms the large nozzle. This indicates that the energy in the water jet shows the same trend when different cones are used.

A factor that may seem surprising is the relatively good performance of the flat cone insert combinations. This combination will have no disruption (due to the

University of Cape Town

cone) during focusing. The resultant pressure at the second focus of the ellipse would therefore be the strongest in this case (theoretically infinite). Diffraction effects account for some of the shock energy being transmitted into the nozzle and therefore causing a water jet slug.

The nozzle size has shown been shown to be have some effect on the jet. The inertia of the water in the nozzle as well as the back pressure probably plays a part in the resultant jet energy. Nozzle outlet diameters and the angle of nozzle constriction are different between nozzles. Leach and Walker [89] showed that these factors are important in nozzle design. No conclusions on nozzle optimisation can be reached from these experiments. Further work is required in this area.

9.9.3 Water jet velocities

The water jet velocities were measured and found to be relatively low - of the order 30 m/s.

9.9.4 Prototype performance

The prototype system was found to have an efficiency of only 0.1 %. **Chapter 4**, calculated that the system must have a minimum efficiency of at least 1 % if only 100 J of electrical energy was used. The efficiency of the system must therefore be improved before it can be considered for ejector application.

Two areas require some optimisation. The first is the electrical circuit. As has been discussed, the circuit is severely underdamped. Better damping will be achieved if the circuit inductance is reduced. The second area is the cone nozzle interaction. As has been shown, the water jet dependence on the combination used is essential to the production of the water jet.

CHAPTER 10 :

CONCLUSIONS AND RECOMMENDATIONS

This project has investigated acoustically based force mechanisms. In particular an elliptically focused shock wave, transient water jet generator has been investigated. Factors effecting the design of this device and a theoretical analysis of aspects of its operation have been performed. Simulation confirmed and extended this work. Experimental tests on a prototype generator gave a measure of the performance of water jet generator systems. The systems suitability as an ejection mechanism could thus be assessed.

10.1 Project summary

A kinematic analysis of an ideal ejector system has shown that the deflection of a target of mass 50 g by 15^o from its trajectory requires approximately 70 N acting for 1 ms. The momentum product required for target deflection (assuming ideal collision between target and force mechanism) was found to be 0.067 Kg.m/s.

Acoustics has been reviewed as a source of force for ejection purposes. A number of techniques were reviewed. All linear acoustic techniques were shown to produce extremely small forces. Thus these techniques were found to be unsuitable for ejection purposes.

Non-linear acoustic phenomena were also investigated. The force on a sphere due to a plane shock wave in air for different values of shock wave Mach number were calculated. The magnitudes of the calculated forces for moderate to strong shocks were found to be sufficient for ejection purposes. However, the production, containment and focusing of shock waves in air was found to be complex. The non-linearities of the medium (air) introduce complex reflection (including Mach reflection), self-focusing and non analytical effects. The design of shock wave focusing systems in air is thus extremely complex. Thus air shock wave forces were found to be unsuitable for use in ejection systems.

An alternative medium for the production and generation of the ejection mechanism was investigated. A water jet was found to be an effective ejection mechanism. A transient water jet system using a shock wave in a cavity was found to be a suitable system. This system was not limited by the mechanical

inertias of any moving parts. A suitable method for the generation of the shock wave was found to be a HV capacitor discharge.

The properties of the HV discharge circuit were theoretically and experimentally investigated. The circuit was found to be an RLC underdamped circuit. The circuit current and voltage were measured during discharges. The circuit component inductance and water gap resistance were calculated using these measurements. The occurrence of 'quiet discharges` was predicted and measured. The water gap length dependence on resistance was shown experimentally.

The transfer of electrical energy to a weak shock wave in the liquid was investigated theoretically. The pressure at the spark channel boundary during the discharge for the prototype circuit was calculated to be : P = 30 kBar.

An elliptical cavity for the optimal transfer of energy from the plasma channel to the water jet has been investigated. The cavity was designed to be a cylindrically symmetric cavity with the electrode pair at one focus and a focusing duct and nozzle at the second focus.

The wave propagation and focusing in an elliptical cavity was reviewed. The pressure in the converging wave was found to be non-uniform. The energy in the converging wave is concentrated at small angles of θ (i.e. on the ellipse axis).

Parameters effecting the focusing process were examined theoretically and a set of design guidelines was developed - the design criteria for a prototype elliptically focused water jet generator.

Lateral waves (wall modes ahead of the converging weak shock wave in the liquid), were found to be eliminated for cavities of small eccentricity. This corresponded to 'flat' or 'circular' elliptical cavities. Cavities with small eccentricities have focal points in close proximity. The focal length was also shown to effect the focusing process. The area of initial shock wave disrupted on the first pass and the propagation distance (and therefore shock decay) were determined by this parameter. For this reason cavities of larger eccentricity were required. A compromise of eccentricity e = 0.5 was chosen for the prototype cavity.

The cavity height was chosen to ensure cylindrical shock wave propagation from the electrodes of the spark gap. Since the voltages were restricted to voltages below 20 kV, the maximum water gap length was 2 mm . A cavity height of

5 mm was chosen.

The prototype was constructed with removable cone and nozzle inserts.

Theoretical simulation of the focusing process in the cavity was performed using a finite difference analysis package. Focal point to focal point weak shock wave propagation was simulated and found to closely correlate to theoretical predictions.

The cone duct nozzle interaction was simulated. A simplification of this process was simulated. Nozzle back pressures were recorded for different cone / nozzle combinations. The highest back pressure was for the medium nozzle / regular cone combination.

Testing of the prototype generator concentrated on two areas : the measurement of the water jet energy (using a ballistics approach), and the measurement of the water jet velocity (using high speed photographic techniques). The former involved the vertical displacement of a target cone of known mass. Different cone / nozzle combinations and circuit configurations were used in these tests.

The velocity of the water jet was measured by the use of a short duration flash and an open shutter. The flash occurred at a preset delay after the air-gap breakdown. The distance travelled by the jet in the time to the flash gave the velocity of the water jet. It was noted that the breakdown in the liquid gap could occur several tens of microseconds after the air gap breakdown - thus introducing an error in the velocity measurement. This delay was found to depend on the electric field strength and conductivity of the liquid. Gap lengths and duration of tests were chosen such that this delay was on average 2 μ seconds - thus this error could be ignored.

10.2 Prototype performance

10.2.1 Discharge circuit operation

The discharge circuit operation was found to effect the transfer of energy from the circuit to the shock wave. The pressure of the shock wave was found to be directly related to the circuit energy, current pulse duration and current pulse rise time. The circuit was found to be an underdamped RLC circuit.

The rise time of the circuit depends on the time constant of the discharge. This is given by $(LC)^{0.5}$. The capacitance is set by energy requirements. Thus it was concluded that the circuit inductance must be minimized.

The optimum circuit conditions for maximum power transfer to the water gap were found to be for values of ξ in the range 0.5 - 1. The latter corresponds to the critically damped condition where no oscillation occurs. The water gap resistance was found to increase with gap length. Thus the water gap length could be set to ensure critical damping.

The inductance of the prototype system was measured to be 2.14 μH. The water gap resistance required for the prototype circuit was then calculated to be of the order 10 Ω. The maximum water gap length was 3.6 mm. The maximum water gap resistance was calculated to be 2.17 Ω. Thus the prototype circuit operation was well underdamped. The damping factor was calculated to be 0.21. Thus the circuit was found to be sub-optimum. Improvement of this situation was only possible if the circuit inductance was reduced. Methods for the reduction of circuit inductance were presented. Higher voltages and capacitances with less self inductance, constructed in a coaxial arrangement were required.

10.2.2 Water jet performance

The concept of the elliptical shock wave focused water jet generator has been shown to work. The performance of the device was found to depend on a large number of electrical and physical parameters. The optimisation of the device therefore requires attention to all of these parameters.

The water jet system was found to have a low efficiency - 0.1 %. Water jet slug velocities were measured to be approximately 30 m/s. Water jet energies were found to vary with circuit configuration and cone / nozzle combination. The effect of cone / nozzle combination was found to correlate well with the theoretical simulations.

The energy of the water jet slug was found to be relatively low $\approx$ 0.01 J and water jet momentums of 0.006 kg/m/s. These values are below those values required for ejection : 0.067 kg/m/s. Thus the water jet prototype system cannot be used in its present form as an ejection mechanism for material handling.

Water jet performance was shown to depend strongly on gap length and nozzle size. The effect of different cone reflectors on jet energies was less severe. The flat cone insert (no cone) was found to perform surprisingly well. This was thought to be due to fact that there is no disruption by the cone area during focusing for this combination - leading to high second focus pressures.

10.3 Water jet generator application in an ejection system

The minimum efficiency (using an electrical circuit with a maximum energy of 32 J) was calculated to be 1 %. The measured efficiency of the device was found to be below this value. Thus the largest range of desired particles will not be deflected sufficiently with this device. In its present form the prototype blast strength is unsuitable for ejection purposes (**Chapter 1**)

The ejector blast width of the system was shown (photographs) to be very small. The blast duration is short. The water jet slug is short (approximately 2 cm travelling at 30 m/s). Thus the system can be used to discriminate between individual particles.

The response time of the prototype ejector system is determined by the HV switching. Experimental work used an untriggered air spark gap. Thus no measurements of the switching response time could be made. The response time of the device is rapid - the time for the shock to reach the nozzle is less than 100 μ seconds. The water jet has been shown to reach the ejector spacing distance (4 cm) in less than 5 milliseconds. Thus response times an order of magnitude better that existing systems are possible with this system.

The operation of the prototype system was shown to be sub-optimum. The optimisation of the electrical circuit (lower circuit inductance) and the use of higher energy levels (higher voltage) will probably result in more efficient systems. The design of an optimised nozzle and cone combination would also together with an efficient circuit produce nozzle pressure and water jet velocities far in excess of that obtained in this work.

The transient water jet has been shown to be a suitable ejection force mechanism (provided blst strengths can be improved). Practical systems will be limited by the fact that the system is a high voltage system. The design of the charging systems for a high repetition rate requires further work. The use of HV discharge systems in an industrial environment, especially with the HV circuit directly coupled to the water, introduces a safety hazard - possibly limiting the industrial application of a device of this nature.

10.4 Recommendations

- Reduce the circuit inductance
- Increase the circuit energy (0.5 CV^2) by increasing the voltage
- Theoretically investigate the cone nozzle interaction
- Investigate optimum pulsed nozzle design

- Construct the cavity from a non-corrosive materials such as Brass or Nickel plating.
- Investigate the use of alternate shock wave energy sources

Alternate methods for the production of a water jet

- EMAS

One of the drawbacks of the discussed work is that the discharges occur in a conducting medium - thus causing a safety hazard. Similar problems were found in lithotripter development. A second generation of shock wave sources; the electromagnetic shock wave tube (**Chapter** 1) have been developed to avoid this problem. The use of EMAS as a method for the production shock waves for water jet application should be investigated.

- Different focusing systems

There are a number of alternative shock wave focusing systems that should be investigated :

Converging pipe

The elliptical cavity can be replaced by a converging pipe. The electrical circuit and water electrodes of the elliptical generator can be used. Unpublished jet speeds using this technique are in the region of 1000 m/s **[18]**.

Other methods

The shock pulse can also be focused by acoustic lenses, by a spheroid shaped disk, by a paraboloid reflector, and by phasing a number of small EMAS units.

REFERENCES

[1] Neve, R. S. , **Particle deflection using air jets** , Trans. Inst. MC , Vol 7 , No. 1 , Jan/March 1985.

[2] Taylor, J. J. , Hoyt, J. W. ,**Water Jet Photography - Techniques and methods** , Experiments in fluids, Vol 1 , pp. 113-120, 1983.

[3] Glenn, L. A. , **The mechanics of the impulsive water cannon**, Computers and fluids, Vol 3 pp. 197-215, 1975.

[4] Field, J. E. , Lesser, M. B. , **On the mechanics of high speed liquid jets**, Proc. R. Soc. London, A 357, pp. 143-162, 1977.

[5] Frungel F. B. , **High speed pulse technology Vol I** , Academic Press, pp 555 , 1965.

[6] Bjorno, L. , **A comparison between measured pressure waves in water arising from electrical discharges and detonation of small amounts of chemical explosives** , Trans. of the ASME, Journal of engineering for industry, Paper No. 69-unit 1., pp. 1-8 ,1968.

[7] Carley-Macauly, K. W. , **Electrohydrolic Crushing** , Chemical and Process engineering, Sept. 1968, pp 87-96.

[8] Reichenberger, H. , **Lithotripter systems** , Proceedings of the IEEE, Vol. 76, No. 9, September 1988.

[9] Folberth, W. , **A universal lithotripter for interdisciplinary use : the Siemens "Lithostar Plus"**, Scandinavian journal of urology and nephrology supplementum 122, Exctracorporeal shock wave lithotripsy - medical, technical, economic and policy implications, Ed. Per Carlsson and H. Tiselius, Linköping 1989.

[10] **Jet cutting and cleaning bibliography, fluid mechanics of jets** , water jet abstracts, 1989.

[11] Dornier Systems Gmbh, **The Dornier Kidney Lithotripter**, product advertisement.

[12] Riehle, R. A. Ed. , associate ed. Newman, R. C. , **Principles of extracorporeal shock wave lithotripsy**, Churchill Livingstone , NY. 1987.

[13] Eisenmenger, W. , **Elektromagnetische erzeugung von eben druckstossen in flussigkeiten**, Acoustica, Vol 12, pp.185-202 , 1962.

[14] Reichenberger, H., Naser, G , **Electromagnetic acoustic source for extracorporeal generation of shock waves in lithotripsy** , Siemens Forsch. -u. Entwickl.-Ber. Bd. 15 (1986) Nr. 4.

[15] Gustafsson G. , **Experiments on shock wave focusing in an elliptical cavity**, J. Appl Physics , 61(11), 1 June 1987.

[16] Gustafsson G. , **Focusing of weak shock waves in a slightly elliptical cavity** , Journal of Sound and Vibration, 116(1), pp 137-148 , 1987.

[17] Gustafsson G. , **Propagation of weak shock waves in an elliptical cavity** , Doctoral Thesis , Tekhiska Hogskolan I Lulea , Division of fluid Mechanics , 1985.

[18] Private communication with Dr. G. Gustafsson (31 October 1989).

[19] Meriam J. L. , **Dynamics engineering mechanics (vol 2, SI version)** , Wiley, 1980.

[20] Beyer R. T., **Radiation pressure : the history of a mislabled tensor** , Journal of the Acoustical Society of America , 63(4) , Apr 1978.

[21] Rooney J. A. , Nyborg W. L. , **Acoustic radiation pressure in a travelling plane wave** , American Journal of physics, Vol. 40 , pp 1825-1830 , 1972.

[22] Stapper M. , **Acoustic wave propagation II** , Acoustica Vol. 39, p111, 1978.

[23] Beissner K, **Acoustic radiation pressure in the near field** , Journal of sound and vibration, 93(4) , pp 537-548, 1984.

[24] Beyer, R. T. , **Nonlinear acoustics** , US Navy press, 1972.

[25] Landau L. D. , Lifshitz E. M. , **Fluid Mechanics (2^{nd} Ed.), Course on theoretical physics, Volume 6** , Pergamon Press , p61, 1987.

[26] Apfel R. E. , **Technical notes and research briefs acoustic levitation for studying liquids and biological materials** , Journal of the Acoustical Society of America , 70(2) , 1981.

[27] Research and Development , **Space acoustic ultrasound goes into orbit** , Ultrasonics, p3 , Jan 1975

[28] King L. V. , **On the acoustic radiation pressure on spheres**, Proceedings of the Royal Society of London , A147 , pp 212-240, 1934.

[29] Putterman S. et al , **Acoustic levitation and the Boltzman Ehrenfest principle**, Journal of the Acoustical Society of America , 85(1) , 1988.

[30] Whymark R. R., **Acoustic field positioning for containerless processing** , Ultrasonics, p 251. , Nov 1985.

[31] Patent Note, **Improved acoustic levitation apparatus** (43.20.KS), Journal of the Acoustical Society of America , 70(2) , Aug 1981.

[32] Wach P. , Holzer F. , Leitgeb N., Schuy S. , **On the theory of acoustic radiation force and its application in ultrasonic power measurements** , Acoustica , Vol. 49 , p55 , 1981.

[33] Zieniuk J. , Chivers R. C. , **Measurement of ultrasonic exposure with radiation force and thermal methods** , Ultrasonics , p 161 , July 1976.

[34] Hasegawa, T , **Acoustic Radiation force on a solid elastic sphere** , Journal of the Acoustical Society of America , 46(5 part 2) 1969 p 1139, 65(1) 1979 p 32 p 41, 58 (3) 1975 p 581, 61(6) 1977 p 1445, 63(6) 1978 p 1733, 67(3) 1980 p 770, 69(4) 1981 p 937.

[35] Anson L. W. , Chivers R. C. , Stockdale H. , **The calculation of Y_P for suspended sphere radiometer targets** , Acoustica , Vol. 48 , p302 , 1981.

[36] Courant, R. , Friedrichs, K. O. , **Supersonic flow and shock waves** , Interscience, 1948.

[37] Lyakhov, V. N., Potapov, V. M. , **Force action of a shock wave on a sphere or cylinder in numerical and physical experiments** , Fluid dynamics (USSR), Vol 20(6), pp 946-951, 1985.

[38] Lesser, M. B. , **Analytic solutions of liquid-drop impact problems**, Proc.

R. Soc. Lond. , A 377, pp 289-308 , 1981.

[39] Lesser, M. B. , Field, J. E. , **The impact of compressible liquids**, Am. Rev. Fluid Mech., Vol 15, pp 97-122, 1983.

[40] Bowden, F. P. , Brunton, J. H., **Damage to solids by liquid impact at supersonic speeds**, Nature, 29 March pp 873-875, 1958.

[41] Kuwahara, M. , Takayama, K. et al , **Underwater shock wave focusing for application to extracorporeal** , Proceedings of the Internation Conference on shock waves, Experimental methods, pp 641-647, 1989.

[42] Russel, D. A., **Shock dynamics of noninvasive fracturing of kidney stones**, Proceedings of the 15th Int. Sym. on shock waves, Stanford. 1985.

[43] Frungel, F. , **High speed pulse technology Volume III**, Academic press, 1970.

[44] Wright, W. M., McKittrick, J. L. , **Diffraction of spark produced acoustic impulses**, Am. J. of Physics, 35, pp 124-128, 1967.

[45] Wright, W. M., Medendorp, N. W. , **Acoustic radiation from a finite line source with N-wave excitation**, J. of the Ac. Soc. Am., Vol 43, pp 966-971, 1968.

[46] Kuffel, E., Zaengl, W. S. , **High Voltage Engineering Fundamentals**, Pergamon Press, 1986.

[47] Kind, D. , **High Voltage laboratory technique** , 1984.

[48] Carley-Macauly, K. W., Hitchon, M. A., Maroudas, N. G. , **Energy consumption in electrohydraulic crushing** , Trans. Instn Chem. Engineers, Vol 44, pp T395-T404, 1966.

[49] Martin, E. A., **Experimental Investigation of a high density, high pressure, arc plasma**, J. of Applied physics, Vol 31, No. 3 , pp 255-267, 1960.

[50] Roi, N. A. , Frolov, D. P. , **On the electroacoustical efficiency of a spark discharge in water**, Soviet Physics Doklady, 3 , pp 118-121, 1958.

[51] Graneau P. , **AlphaTorque Forces** , Electronics and Wireless World, pp 556-559, June 1989.

[52] Zingermann, A. S. **Soviet phys. tech. phys.** , 1 , 2454, 1957.

[53] Kvortsov, Yu V. S. , Komel'kov, V. S. , Kuznetsov, N. M. , **Expansion of a spark channel in a liquid**, Soviet Physics, Technical physics, 5(10), pp 1100-1112, 1961.

[54] Frungel F. B. , **High speed pulse technology Vol I** , Academic Press, pp 477 , 1965.

[55] Frungel F. B. , **Zum mechanischen wirkungsgrad von flussigheitsfunkten**, Optik, Vol. 3, pp 124-127, 1948.

[56] Giancoli, D. C. , **General physics**, Prentice Hall, 1984.

[57] Salas, S. L. , Hille, E. , **Calculus one and several variables Part 1 3ed**, Wiley, 1978, pp. 381-382.

[58] Muller, M. , **Experimentelle Untersuchungen zur fokussierung spharisher stobwellen in wasser durch tiefe ellipsoide reflectoren**, Acoustica, Vol 66. , pp 258-265, 1988.

[59] Whitham, G. B. , **Linear and non linear waves**, Wiley, 1974.

[60] Kinsler, L. E. , Frey, A. R., Coppens, A. B., Sanders, J. V., **Fundamentals of acoustics 3rd edition**, Wiley, 1982.

[61] Whitham, G. B. , **Linear and non linear waves**, Wiley, pp 235-239, 1974.

[62] Siemens, **Handbook for electrical engineers**

[63] Autodyne II, Instruction manual, ALE, Lagrange and Euler tutorials.

[64] Prof. B. Skews, **Discussion** , Mechanical Engineering school, Wits , July 1990.

[65] Oliver, H., Gröning, H. , **Two dimensional shock focusing and diffraction in air and water**, 15th Int. Syp. on shock tubes and waves, Berkeley, 1985.

[66] Muller M , **Experimental investigations on focusing of weak shock waves in water by shallow ellipsoidal reflectors** , Acoustica , Vol 64. , pp 86-93, 1987.

[67] Sommerfield, M. , Muller, M. , **Experimental and numerical studies of shock wave focusing in water**, Experiments in fluids, No. 6, pp. 209-216, 1988.

[68] **Fluid Dynamics Vol 2**, 2.3 Visualisation by means of light deflection, pp 361-374.

[69] Field, J. E. , **High speed photography** , Contemp. Physics, Vol 24, No. 5, pp 439-459, 1983.

[70] Bronson, N. R. , **An inexpensive schlieren apparatus**, Ultrasonics, pp 67-70, Jan 1969.

[71] **Experiments in optics**, A21 , pp 123-129,

[72] **Schlieren Photography** , Eastman Kodak Company, pp 3-19, 1960.

[73] **Fluid Dynamics Vol 2**, 2.4 Interferometry, pp 374-392.

[74] Private communication with Dr. G. Gustafsson (19 Jan. 1990).

[75] Muller, M., Platte, M, **Einsatz einer breitbandigen piezodrucksonde auf PVDF-basis zur untersuchung konvergierender stobwellen in wasser**, Acoustca, Vol. 58, pp 215-222, 1985.

[76] Platte, M. , **Polyvinyldiflouride needle hydrophone for ultrasonic applications**, Ultrasonics, May 1985.

[77] IMOTEC GmbH, Paulinenstrasse 136, 5102, Würselen, **Piezoelektrischer Miniatur-druckaufnehmer**, Technical data sheet.

[78] Granz, B. , Holzapfel, R. , Köhler, G. , **Measurement of shock waves in the focus of a lithotripter**, Ultrasonics symposium, pp 991-994, 1989.

[79] Antonov, S. N. , Rechevskii, E. B., **Fibre-optic acoustic transducer**, Soviet Phys. Acoustics, 35(5), Sept-October, 1989.

[80] Fischer, H. , **Micromillisecond light source with increased brightness**, J. of the Optical Soc. of America, Vol. 51 , No. 5, 1961.

[81] Fischer, H. , **Simple micromillisecond light source with extreme brightness**, J. of the Optical Soc. of America, Vol. 47 , No. 11, 1957.

[82] Fisher, H. , **Impulsphysik GmbH : Nanolight - nanosecond flash lamps** , Data sheet, Postfach 13 49 , D-2000 Schenefeld, Hamburg.

[83] Miyashiro, S. , Grönig, H. , **Low-jitter reliable nanosecond spark source for optical short duration experiments**, Experiments in Fluids, 3, pp 71-75, 1985.

[84] Edgerton, F. , **Electronic flash strobe**, MIT university press, 1970.

[85] Hamamatsu : Technical data sheet, **Super quiet xenon flash tubes - flash mode**, Technical data sheet No. T-107.

[86] Horowitz, P. , Hill, W. , **Art of electronics**, Cambridge university press 1980.

[87] Nishida, M. , Nakagawa, T. , Saito, T. , Sommerfeld, M. **Interaction of weak shock waves reflected on concave walls**, Shock tubes and waves symp., pp 211-217 , Berkeley , 1985.

[88] Tektronics, **TEK products catalogue**, 1989.

[89] Leach, S. J. , Walker, G. L. , **The application of a high speed liquid jets to cutting**, Phil Trans Rolyal Soc of London, 260A, pp 295-308, 1966.

[90] Hasegawa, T. , et al , **Acoustic radiation force on a rigid sphere in the near field of a circular piston vibrator**, J. Ac. Sic. Am. , 88(3) , September 1990.

[91] Rehbinder, G. , **Investigation of water jet pulses generated by an impact piston device**, Applied scientific Research, 40, pp 7-37, 1983.

[92] Sturtevant, B. , Kulkarny, V. A. , **The focussing of weak shock waves**, J. Fluid mechanics, Vol. 73, part 4, pp 651-671, 1976.

[93] Cramer, M. S. , **Three dimensional effects on the focussing of weak shock waves** , J. Sound and Vibration, 90 (1), pp 25-28, 1983.

[94] Schwendeman, D. W. , Whitham, G. B. , **On converging shock waves**, Proc of the R. Soc London, A413, pp 297-311, 1987.

[95] Obermeier, F. , **On the propagation of weak and moderately strong curved shock waves** , J. Fluid Mech. , 129, pp 123-126, 1983.

[96] Skews, B. W. , **Diffraction and reflection of weak shock waves,** Proceedings of the Acoustics Today conference, SAAI, Durban , Natal 1989, pp 88-93.

[97] Gröning, H. , **Shock wave focusing phenomena,** Proceeding of Shock tubes and waves symp., Berkeley , 1985.

[98] Wright, W. M. , **Propagation in air of N waves produced by sparks,** J. Ac. Soc. of America, 73(6), pp 1948-1955, June 1983.

[99] Atkins, M. D. , Skews, B. W. , **Interaction of a weak shock wave with and acoustic foam** , Proceedings of the Acoustics Today conference, SAAI, Durban, Natal 1989, pp 94-99.

[100] Douglas, J. F. , et al, **Fluid mechanics,** Pitman , 1984.

[101] Beazley, M. , **Core business studies : statistics** , 1983.

APPENDICES

A : Frictionless horizontal plane motion
B : Projectile kinematic derivation
C : Redefinition of the angle of deflection
D : Shock wave force on a target sphere
E : Laplacian analysis of RLC circuit
F : HV switching techniques
G : Ellipse parameters
H : Elliptical cavity prototype technical drawing
I : Autodyne elliptical cavity simulations
J : Autodyne cone duct / nozzle interaction simulations
K : Delay circuit and Xenon flash tube driver
L : Gustafsson reference [15]
M : Hamamatsu Xenon flash tube and OEM power supply data
N : HV sphere gap calibration
O : Pulsed water jet operation
P : Calculation of the aperture for high speed photography
Q : Time delay before liquid gap breakdown
R : Calculation of the inductance of the discharge circuit
S : Reducing the circuit inductance
T : Schlieren systems
U : Water jet slug energy experiments
V : Resistive current probe
W : Water gap resistance measurements
X : Water jet maximum height
Y : Water jet propagation

APPENDIX A :

Derivation of frictionless horizontal plane motion

This appendix derives the relation between the applied external deflection force F_D acting for a time t_D on a particle of mass m, travelling on a frictionless horizontal plane. This is shown in Chapter 2, **fig 6** in the body of this thesis.

Assumptions

- Gravity is neglected.
- The deflection force is assumed to act only in the X direction (i.e. it has no Y component).
- The subscripts x and y refer to the relative planes.
- Point motion and action can be assumed.

Kinematic analysis

By the equations of motion :

$$X_D = U_X t + \frac{1}{2} a_X t^2$$
$$= \frac{1}{2} a_X t^2$$

but since :

$$F_D = m a_X$$

then :

$$S_X = \frac{t^2 F_D}{2m}$$

similarly :

$$S_Y = u_y t + \frac{1}{2} a_y t^2$$
$$= u_y t$$

with the angle of deflection then given by :

$$\tan\zeta = \frac{X_D}{Y_D}$$
$$= \frac{F_D t_D}{2mu}$$

APPENDIX B:

Projectile kinematic derivation

This section covers the complete derivation of projectile motion under the influence of gravity, initial conditions, and an external time-limited deflection force. An integral analysis in rectangular co-ordinates is performed using Newtonian kinematics.

The three stages of analysis are shown in **fig 8 , fig 10 and fig 12** of Chapter 2. The assumptions of **Chapter 2** are used in this analysis.

a) Particle motion before ejection

The motion of a particle projectile with an initial velocity **u** is shown in fig 8 of **Chapter 2**:
This analysis covers the motion of the particle up to point E.

Since air resistance is neglected :

$$a_X = 0$$
$$a_Y = -g$$

The kinematic relations are then :

$$\int_{s_1}^{s_2} ds = \int_{t_1}^{t_2} v\,dt$$
$$\int_{v_1}^{v_2} dv = \int_{t_1}^{t_2} a\,dt$$
$$\int_{v_1}^{v_2} v\,dv = \int_{s_1}^{s_2} a\,ds$$

Substituting the parameters of **fig 8** into these relations, the equation of motion of the projectile is obtained :

$$x = u.t.\cos\theta$$

$$y = u.t.\sin(\theta) - \frac{1}{2}.g.t^2$$

and the horizontal and vertical component velocities :

$$V_x = u.\cos(\theta)$$

$$V_y = u.\sin(\theta) - g.t$$

Eliminating t between x and y, the equation of the path of the projectile is obtained.

$$y = x\tan\theta - \frac{gx^2}{2u^2}\sec^2\theta$$

The slope of the path (gradient) at any point is given by the differential of this equation :

$$M_1 = \frac{dy}{dx} = \tan(\theta) - \frac{g.x}{u^2}.\sec^2(\theta)$$

This equations shows that the path of the projectile is parabolic.

b) Particle motion under the action of F_D

Forces acting on the particle

The diagram of forces acting on the target particle is shown in **fig 9** of Chapter 2 :

Then by Newton II :

$$F_X = F_D.\cos(\gamma) = ma_X$$

$$F_Y = F_D.\cos(\gamma) - m.g = ma_Y$$

Thus

$$a_X = \frac{F_D.\cos(\gamma)}{m}$$

$$a_Y = \frac{F_D.\sin(\gamma) - m.g}{m}$$

Thus the acceleration of the target particle due to the deflecting force is known in rectangular co-ordinates.

Motion of the target under the action of F_D

Transforming the horizontal co-ordinates and using the initial conditions from section **a)**. The motion of the projectile under the action of F_D is shown in **fig 10** of Chapter 2.

The time from the start of the ejection process is represented by t'. All superscripts ' indicate the co-ordinate system has been transformed from (0,0) to (s_E,h_E).

The velocity and displacement of the target particle is given by :

Substituting for v_y from the previous section a), the target particle vertical velocity component is given by:

$$dv_y' = a_y' dt'$$

$$\int_{v_y}^{v_y'} dv = \int_0^{t'} dt'$$

$$v_y - v_y = \int_0^{t'} \frac{F_d \sin\gamma - mg}{m} dt$$

$$V_Y' = \frac{F_D.\sin(\gamma) - mg}{m}.t' + u.\sin(\theta) - g.t_E$$

similarly :

$$\int_{v_x}^{v_x'} dv_x' = \int_0^{t'} a_x dt$$

$$= \int_0^{t'} \frac{F_D \cos\gamma}{m} + v_x$$

Substituting for v_x from section a) :

$$V_X' = \frac{F_D.t'.\cos(\gamma)}{m} + u.\cos(\theta)$$

The displacements are given by :

$$dx' = v_x' \, dt$$

$$x' = \int_0^{t'} [\frac{F_D t' \cos\gamma}{m} + u\cos\theta] dt'$$

then :

$$x' = u.t'.\cos(\theta) + \frac{F_D.t^2.\cos(\gamma)}{2.m}$$

Similarly the vertical displacement is given by :

$$dy' = v_y' dt'$$

$$y' = \int_0^{t'} ([\frac{F_D \sin\gamma - mg}{m}] t' - gt_E + u\sin\theta) \, dt'$$

and :

$$y' = \frac{F_D.\sin(\gamma) - m.gt^2}{2.m} - g.t_E.t' + u.t'.\sin(\theta)$$

The tangent of the deflected path

The gradient of the deflected path can be described by :

$$m_2 = \frac{dy'}{dx'} = \frac{\frac{dy'}{dt'}}{\frac{dx'}{dt'}} = \frac{V_y'}{V_x'}$$

The tangent of the deflected path is then :

$$m_2 = \frac{\frac{F_D.\sin(\gamma)-m.g}{m}.t' + u.\sin(\theta) - g.t_E}{\frac{F_D.t_D.\cos(\gamma)}{m} + u.\cos(\theta)}$$

Thus the slope of the path of the target particle undergoing deflection is known.

c) Particle motion after the ejection process

The motion of the particle after the ejection force has ceased will be projectile motion with initial velocity conditions given by section b). The path of the projectile is shown in **fig 12 :** of Chapter 2.

The co-ordinates are transformed to centre on the point where the path of the target under the action of the ejection force ceased. Double '' superscripts are given to parameters using this co-ordinate transformation.

Thus :

$$x'' = x + x'$$
$$y'' = y + y'$$
$$t'' = t + t'$$

Since the ejection force is no longer operating :

$$F_D = 0$$
$$a_x'' = 0$$
$$a_y'' = -g$$

Thus the equations of motion of the system are given by :

$$\int_{v_y'}^{v_y''} dv_y'' = \int_0^{t''} a_y'' dt''$$

$$v_y'' - v_y' = \int_0^{t''} -g\, dt'' = -t''g$$

$$v_y'' = v_y' - t''g$$

Where v_y refers to the vertical velocity of section b).

Similarly :

$$\int_{v_x'}^{v_x''} dv_x'' = \int_0^{t''} a_x'' dt$$

$$v_x'' - v_x' = 0$$

$$v_x'' = v_x' = \frac{F_D \cos\gamma t_D'}{m} + u\cos\theta$$

and :

$$dx'' = v_x'' dt$$

$$x'' = \int_0^{t''} \frac{F_D \cos\gamma t_D'}{m} + u\cos\theta \; dt$$

$$= \frac{F_D \cos\gamma\, t_D' t''}{m} + ut''\cos\theta$$

and :

These equations can be used to check that the deflected particle propagates clear of the undeflected path. They can also be used in the design of the ejector

$$dy'' = V_y'' dt$$

$$y'' = \int_0^{t''} [(F_D \sin\gamma - mg)\frac{t_D'}{m} + u\sin\theta - gt_E - gt''] \, dt$$

$$= \frac{(F_D \sin\gamma - mg)t_D' t''}{m} + ut''\sin\theta - gt''t_E - \frac{gt^{2''}}{2}$$

configuration - ejection mechanism, conveyer belt and hopper (waste and desired particle) location.

APPENDIX C:

Redefinition of the angle of deflection (geometrical approach)

The angle of deflection is defined as the angle between the tangents m_1 and m_2:

This is shown in **fig C1** and **fig C2** :

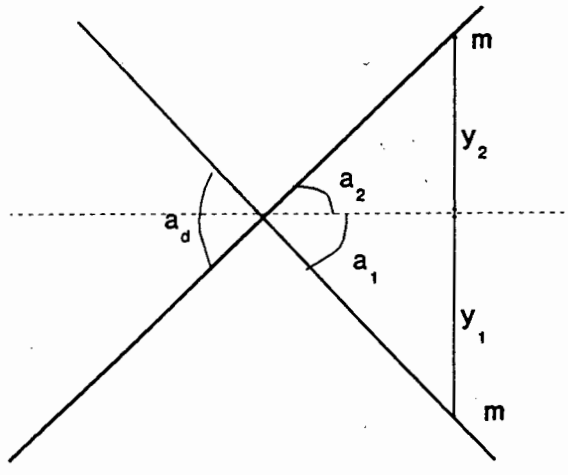

fig C1: *Definition of the angle of deflection in terms of the gradients of the deflected and undeflected slopes : first case*

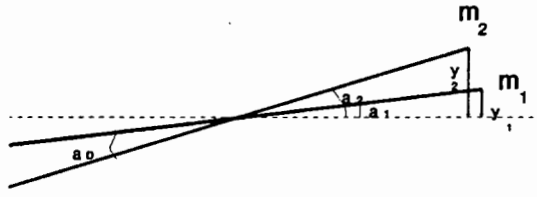

fig C2: *Definition of the angle of deflection : second case*

The angle of deflection is defined in terms of the tangents m1 and m2 in figures C1 and C2. The angle of deflection can be written as :

$$\begin{aligned} a_d &= a_1 - a\,2 \\ &= \arctan y_2 - \arctan y_1 \\ &= \arctan m_2 - \arctan m_1 \end{aligned}$$

$$\begin{aligned} \tan a_d &= \tan(a_2 - a_1) \\ &= \frac{\tan a_2 - \tan a_1}{1 + \tan a_1 \tan a_2} \end{aligned}$$

The deflection angle in terms of the tangents of the deflected and undeflected paths is thus given by :

$$\tan(\zeta) = \frac{m_2 - m_1}{1 + m_2 . m_1}$$

APPENDIX D:

Shock wave force on a target sphere

A theoretical derivation of the force on a sphere due to a shock wave has been presented in [37]. Two forces were found : the first is the volume compression force on the sphere and the second is the force on the sphere in the direction of the shock wave. It is the second force that is of interest when considering shock waves as a source of force for ejection purposes.

This force will be given by surface integral of the pressure acting on the surface of the sphere. [37]. This is shown in the following equation :

$$F = \int_{\sigma} P_w \cos\theta \, d\sigma$$

Where :

$$d\sigma = 2\pi R^2 \sin\theta \, d\theta = \textit{surface element}$$

and : P_w = pressure acting on the surface of the body
R = radius of the sphere

The system is shown in **fig D1** :

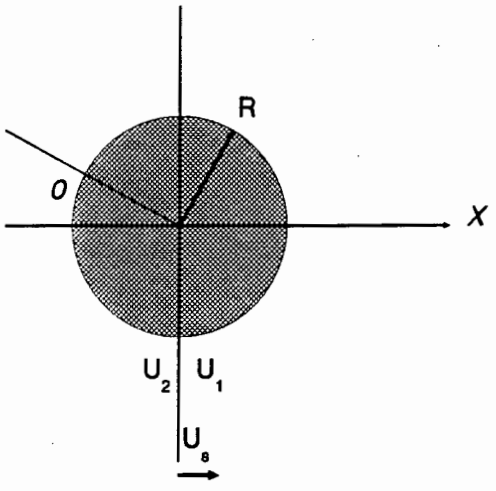

Fig D1 : *Shock wave acting on a sphere*

If the medium can be considered as being an inviscid, non-conducting ideal gas, the shock wave action on a body is described by the geometry of the body and two dimensionless parameters :

The specific heat ratio : $\gamma = 1.4$ for a diatomic gas [36].
The pressure ratio : P_{21}

The pressure ratio is the ratio of the pressure before the shock front to the pressure after the front.

These parameters can also be written as the Mach Number :

$$M_s = \sqrt{1 + \frac{(P_{21} - 1)}{\mu}}$$

$$\mu = \frac{2\gamma}{\gamma + 1}$$

The normalised force due to a shock wave is plotted in fig D2 for normalised dimensionless time. The calculation procedure used was a second order finite difference system with a third order smoothing operator [37].

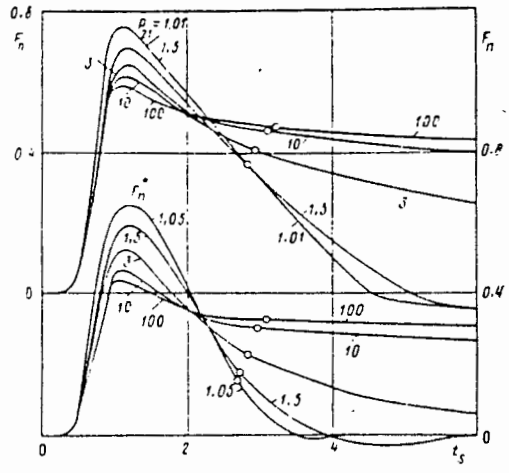

Fig D2 : *Axial force on a cylinder (top curve) and a sphere (lower curve)*

The normalised force is given by :

$$F_n = \frac{F}{(P_n - P_1)\sigma_x}$$
$$\sigma_x = \pi R^2$$

The normalised pressure is given by :

$$P_n = \left(\frac{(2\nu + 1)P_{21} - \nu}{1 + \nu P_{21}}\right)P_2$$
$$\nu = \frac{\gamma - 1}{\gamma + 1} = 0.166$$

Pressure P_1 is 1 Bar , or 100 kPa. The time is dimensionless :

$$t_S = \frac{tu_S}{R}$$

Where R is the radius of the sphere and u_S is the velocity of the shock wave.

If a sphere of radius 16 mm is chosen, $\sigma_x = 0.0008$

The following table shows the calculation procedure and intermediate results. The calculation starts on the left of the table and proceeds allong each row until the force on the sphere has been calculated.

P_{21}	P_2 bar	Ms	Pn	Fn*	F
1.05	1.05	1.02	1.05 P2	0.6	4.9
1.5	1.5	1.2	1.46 P2	0.5	48
3	3	1.65	2.55 P2	0.45	240
10	100	2.95	4.9 P2	0.425	1649

Fn^* is obtained from diagram D2.

APPENDIX E:

Laplacian analysis of the RLC discharge circuit

E.1 Charging RC circuit

The charging circuit is a series RC circuit. This circuit is equivalent to the circuit before discharge. The resistance in the circuit is a series current limiting resistance.

The current in this circuit will decrease as the capacitor attains the final voltage.

$$e = \frac{1}{c}\int i\,dt$$
$$= V - iR$$

This is a differential equation with a solution :

$$i = I_o e^{-\alpha t}$$

Where I_o and α are constants determined by the initial conditions of the circuit.

Thus :

$$\alpha = \frac{1}{RC}$$
$$I_o = \frac{V}{R}$$

$$i = \frac{V}{R} e^{-\frac{t}{RC}}$$

E.1.1 Energy lost in the charging resistor

The instantaneous power in the charging resistor is : $i^2 R$

The total energy lost during the charging cycle is :

$$w = \int_{t=0}^{t=\infty} i^2 R dt \qquad [watts.seconds]$$

$$since : i = \frac{V}{R} e^{-\alpha t}$$

$$w = V^2 \frac{C}{2}$$

E.1.2 Efficiency of a DC charging system

The above equation for the energy lost in the charging resistor shows that this energy is the same as that stored in the capacitor. Thus the maximum efficiency of the charging system is 50 %. The efficiency will be less than this value if the charging cycle is not completed **[84]**.

E.2 Discharge circuit analysis

The discharge circuit used for the creation of shock waves in the water is shown in **fig E.1** :

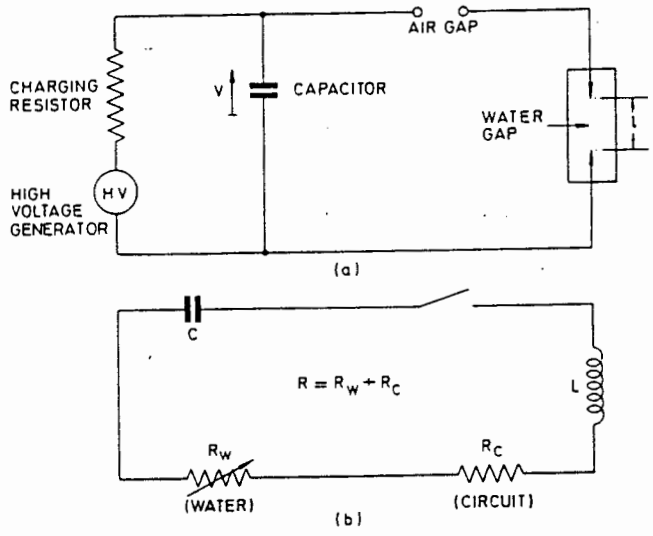

fig E1 : ***RLC discharge circuit for the production of shock waves in water***

This appendix derives the current, optimum power release in the water gap, the maximum current, and the maximum instantanious power.

E.2.1 Laplacian analysis of circuit

The circuit resistance is made up of two components : that due to the circuit (leads, connections and components) and that due to the water gap plasma channel (as described in **Chapter 4**, this is assumed constant).

$$R = R_{circuit} + R_W$$

Theory

Assume the capacitor is charged to a voltage V_c

Then by Kirchoff's voltage law :

$$
\begin{aligned}
0 &= V_c + V_1 + V_r \\
V_1 &= L\frac{di}{dt} \\
V_r &= i(t)R \\
V_c &= \frac{1}{C}\int i(t)
\end{aligned}
$$

Substituting and taking the Laplace transform :

$$
\begin{aligned}
0 &= sLI(s) + RI(s) + \frac{1}{sC}I(s) - \frac{V_c}{s} \\
&= (sL + R + \frac{1}{sC})I(s) - \frac{V_c}{s}
\end{aligned}
$$

Therefore :

$$
\begin{aligned}
I(s) &= \frac{V_c}{L}\frac{1}{(s^2 + \frac{R}{2L} + \frac{1}{LC})} \\
&= \frac{V_c}{L}\frac{1}{(s - a)(s - b)}
\end{aligned}
$$

where :

$$
\begin{aligned}
a &= -\frac{R}{2L} + \sqrt{(\frac{R^2}{2L}) - \frac{1}{LC}} \\
b &= -\frac{R}{2L} - \sqrt{(\frac{R^2}{2L}) - \frac{1}{LC}}
\end{aligned}
$$

There are three possible solutions to I(s): a solution with ringing (underdamped solution), a critically damped solution and an overdamped solution.

For the underdamped (ringing) or the critically damped condition :

$$\frac{1}{LC} \geq \left(\frac{R}{2L}\right)^2$$

Critical damping will achieved if :

$$\xi = \frac{1}{2}R\sqrt{\frac{C}{L}}$$
$$= 1$$

Thus if the inductance elements and capacitive elements are fixed for a given circuit, critical damping can be achieved if the circuit resistance is equal to :

$$R_{critical} = 2\sqrt{\frac{L}{C}}$$

The circuit resistance will be made up of the water gap resistance and the circuit resistance. The latter can be expected to be small (resistance of leads) if large diameter conductors are used. The circuit power dissipation will thus be mainly in the water gap resistance.

The way in which the power release in the resistance varies with the parameter ξ is shown in **fig 21** of Chapter 4.

This diagram shows that the most concentrated release of power in the initial peak occurs for values of ξ in the range 0.5 to 1.

Since the resistance of the water gap is difficult to set exactly equal to the critical resistance required for critical damping (the water gap resistance also changes throughout the discharge as the plasma channel width changes), the solution most probable is the underdamped solution :

Let :

$$\alpha = \frac{R}{2L}$$

$$\beta = \sqrt{\left(\frac{R}{2L}\right)^2 - \frac{1}{LC}}$$

Then since **6** will be immaginary :

$$\beta = j\omega_n$$

$$= j\sqrt{\frac{1}{LC} - \frac{R^2}{2L}}$$

Substituting this value in laplacian solution and taking the inverse Laplace transform :

$$i(t) = \frac{V_c}{L}\frac{(e^{bt} - e^{at})}{(b - a)}$$

$$= -\frac{V_c}{\omega_n L}e^{-\alpha t}\frac{(e^{j\omega_n} - e^{-j\omega_n})}{-2j}$$

$$= \frac{V_c e^{-\alpha t}}{L\omega_n}\sin(\omega_n t)$$

The current vs. time curve is thus shown in **fig E2** :

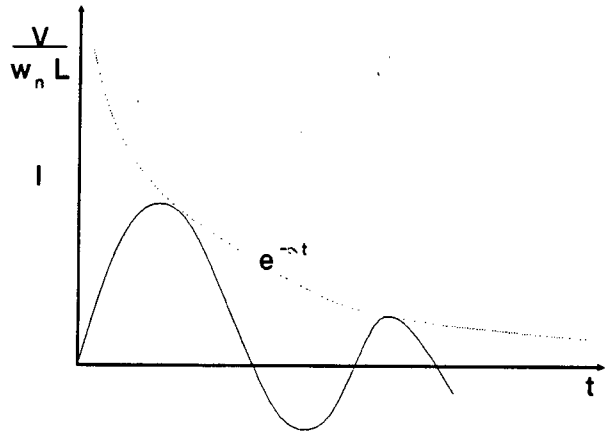

fig E2 : *Current response of a series RLC circuit*

T h e
Maximum Current

The equation of i(t) is differentiated and set to zero.

$$i(t) = \frac{V_c e^{\alpha t}}{\omega_n L}\sin(\omega_n t)$$

$$\frac{di(t)}{dt} = 0$$

$$= \frac{V_c}{\omega_n L}(-\alpha e - \alpha t \sin(\omega_n t) + e^{-\alpha t}\cos(\omega_n t)\,\omega_n$$

Thus :

$$\alpha \sin\omega_n t = \omega_n \cos\omega_n t$$

$$\tan\omega_n t = \frac{\omega_n}{\alpha}$$

$$t_{max} = \frac{1}{\omega_n} \tan^{-1}\left(\frac{\omega_n}{\alpha}\right)$$

substituting :

$$i_{max} = \frac{V_c}{\omega_n L} e^{-\alpha t_{max}}$$

If the natural frequency of the system is approximately the resonant frequency (i.e. the system is nearly critically damped) :

$$\omega_n = \sqrt{\left(\frac{1}{C} - \left(\frac{R}{2L}\right)^2\right)} \approx \omega_o = \frac{1}{\sqrt{LC}}$$

Then :

$$\omega_n \approx \omega_o = \frac{1}{\sqrt{LC}}$$

$$i_{max} = V_c\sqrt{\frac{C}{L}}\, e-\alpha t_{max}$$

Maximum instantaneous power

The maximum instantaneous power dissipated in the circuit is given by :

$$P = (i_{max})^2 R$$
$$= R(V_c\sqrt{\frac{C}{L}}\, e^{-\alpha t_{max}})^2$$
$$= \frac{RV_c^2 C}{L}\, e^{-2\alpha t_{max}}$$

APPENDIX F:

HV Switching Techniques

F.1 Selection of a suitable switching technique

The selection of a suitable HV switching technique is based on the following criteria [5]:

- Nature of the switched voltage [V]: Whether oscillatory, periodic or impulse.
- The rated voltage [V]
- The discharge energy [J]
- The peak current [A]
- The total coulombs in the capacitor discharge [Q]
- The amount of noise or jitter permitted during switching

The switching requirements for the discharge circuit for the elliptical water jet generator are thus :

Charging voltage of the capacitor 10 to 25 kV. The circuit is a RLC discharge circuit that is underdamped - i.e. oscillatory. Maximum energy in the discharge will be about 32 J (V= 20 kV, C = 0.16 μF). The maximum charge (Q = CV) will be 0.0032 A/s. Thus the peak current for a discharge of 2 μ seconds will be about : 1.6 kA (I = Q/t).

Jitter on the switch will introduce permutations in the power release in the gap. This could effect the resultant shock profile. Thus a switching technique with jitter far less than the pulse duration is required.

F.2 Review of switching techniques

F.2.1 Thyratrons

Thyratrons can eliminate unwanted oscillations in the discharge circuit by cutting off the current at the first pass through zero. There are two types of thyratron - those with heated cathodes and those with cold cathodes. Although the latter does not require any external circuitry (for the heating of the cathode) they are limited by fairly low maximum reverse voltages (a few kilovolts) and maximum peak cathode emission currents (approximately 0.2 A maximum). These thyratron also have a delay between the ignition spark and the discharge emission proper thus limiting the starting precision.

Hot-cathode thyratrons require additional circuitry but can have typical reverse voltages and maximum peak emission currents of 5 kV and 100 A respectively **[5]**. Some thyratrons can have higher reverse voltages eg. AEG SIS/40i : 20 kV and 10 A. Hot cathode thyratrons have very fast ignition times requiring very little energy to initiate breakdown (10^5 seconds between ignition pulse and main pulse). In special cases hydrogen thyratrons can be used to switch voltages of up to 50 kV and with peak currents of 2000 A.

F.2.2 Ignitron

Ignitrons have no emission current until an ignition pulse forms an electron emitting spot on the cathode. These devices can take high currents (10 kA) but cannot withstand high reverse voltages (< 3 kV) unless special glass chambers are used (20 kV). Ignitrons also have the property that they extinguish if the cathode goes negative in voltage **[5]**.

F.2.3 Spark Gaps

Spark gaps are historically the earliest type of switching means. Usually spark gaps consist of sphere gaps in air - though other gasses (eg. nitrogen) can be used. The breakdown voltage or breakdown distance in this case depends on the diameter of the spheres, the distance between the spheres and the pressure of the gas. The resistance of the spark gap is given by Toepler's formula **[5,46,47]** :

$$R_F = \frac{k\,l}{Q}$$

Where : $k = 0.8\ 10^{-3}$ for air
l = the length of the spark gap
Q = the number of amps / s transmitted through the spark.

Typically the value of R_F is small ; 20 milli Ω. Thus spark gaps dissipate very little energy. R_F for the circuit used in the discharge experiment ($Q = 0.0012$, $l = 4.5$ mm) was typically of the order 3 milli Ω.

It is difficult to initiate spark breakdown. Usually the voltage is raised until spark-over occurs. However, this process will have some statistical time lag associated with it due to the statistical randomness of the time for a spark leader to form. Movable spark gaps (one sphere is motorised towards the other) can give timing accuracies of ± 5 μ seconds. Jitter on the spark switching is approximately 1 % of the spark duration time [5].

F.2.4 Vacuum switch

The distance between the electrodes of a switch can be made very small if the switch is operated in a vacuum (breakdown voltage is inversely proportional to pressure) [46]. Thus the path that the electrodes have to travel to make contact can be very small, and if the contacts are closed rapidly, the switching process will be rapid. Prearcing and jitter will be minimised.

Vacuum switches can carry large currents - the GEC 24 kV breaker has a peak current carrying capacity of 8 kA. The switch requires a mechanical actuator to close the contacts. A solenoid with a piston can be used for this purpose.

F.3 Conclusions

Only heated thyratrons can be used for this application. These devices are very expensive and therefore are not viable for this project. Ignitrons and spark gaps have jitter. Ignitrons will be expensive since only specially constructed glass ignitrons are suitable for this project.

Vacuum switches provide suitable HV switching with minimal jitter. Since the switching is actuated by a transducer all measurement systems can be triggered

by this event. Vacuum switches are however, expensive.

Spark gaps are the simplest switching technique. Although spark gaps only break down once the voltage across the spheres exceeds the breakdown voltage and distance, prototype experimentation does not require the switching to occur at a predefined instant. Instead this thesis requires a switching technique that facilitates testing of the water jet device performance. A water jet in an actual ejector system environment would have to be designed with a switching technique that allows accurate predetermined, externally triggered switching. A vacuum tube or a triggered spark gap should be used in this case.

Thus, for the purposes of this thesis project, the spark gap is chosen as the switching mechanism for the high voltage discharge circuit.

APPENDIX G:

Ellipse Parameters

An ellipse is shown in **fig G1** :

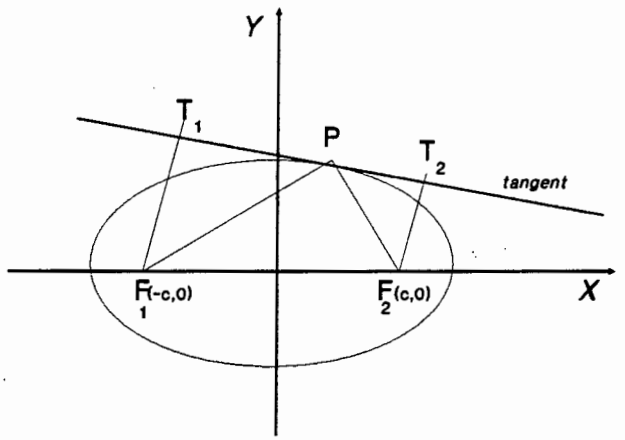

Fig G1 : ***Ellipse parameters***

G.1 Equation of the ellipse

$$\frac{x^2}{a^2} + \frac{y^2}{b^2} = 1$$

The intercepts with the vertical and horizontal axes are :

a = x intercept = (1/2) major axis
b = y intercept = (1/2) minor axis

The relationship between the focal chord and the minor and major axes is :

$C^2 = a^2 - b^2$

The eccentricity e is given by :

$$e = C/a$$

G.2 Ellipse focusing properties :

Differentiation of the ellipse equation w.r.t. x gives :

$$\frac{2x}{a^2} + \frac{2y}{b^2}\frac{dy}{dx} = 0$$

$$\frac{dy}{dx} = -\frac{b^2x}{a^2y}$$

The slope at the point (x_o,y_o) is :

$$m = -\frac{b^2x_0}{a^2y_0}$$

with a tangent line :

$$y - y_0 = -\frac{b^2x_0}{a^2y_0}(x - x_0)$$

$$(b^2x_0)x + (a^2y_0)y - a^2b^2 = 0$$

A property of the ellipse is that a ray originating at one focus will converge to the other focus. This can be proven by showing that at each point P of the ellipse (**fig F1**), the focal radii F_1P and F_2P make eqaul angles with the tangent. This can be proved by showing that the triangles PT_1F_1 and PT_2F_2 are similar triangles **[57]**.

i.e. :

$$\frac{d(T_1,F_1)}{d(F_1,P)} = \frac{d(T_2,F_2)}{d(F_2,P)}$$

$$\frac{|-b^2x_0c - a^2b^2|}{\sqrt{(x_0+c)^2+y_0^2}} = \frac{|b^2x_0c - a^2b^2|}{\sqrt{(x_0-c)^2+y_0^2}}$$

or rearranging :

$$\frac{x_0^2}{a^2} + \frac{y_0^2}{b^2} = 1$$

Thus the points at which the triangles are similar correspond to the point of an ellipse.

G.3 Volume of an elliptical cavity

The volume of the elliptical cavity is given by the area of an ellipse multiplied by the cavity height h. Thus :

$$Volume_{elliptical\ cavity} \approx \pi\ ab\ .\ h$$

Where a and b are the full major and Minor axes of the ellipse respectively. Thus the volume for the prototype elliptical cavity was : 34 ml

APPENDIX H:

Elliptical cavity prototype technical drawing

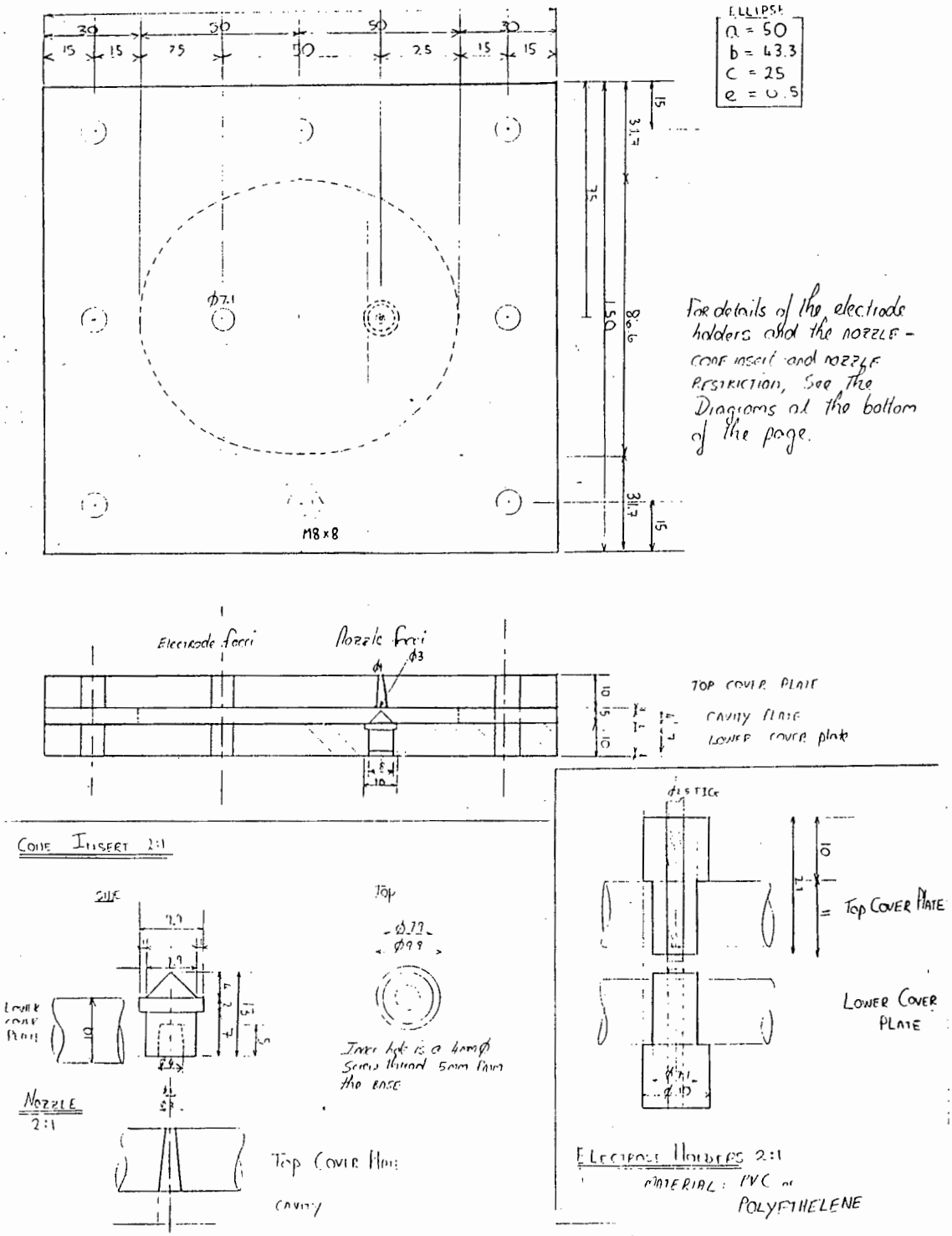

APPENDIX I:

Autodyne elliptical cavity simulations

This appendix presents the simulations of the elliptical cavity using the Autodyne finite difference package (**Chapter 7**).

I.1 Half ellipse simulations

This section shows simulations using only the top half of the ellipse. This corresponded to two quadrants of the ellipse. Simulations used a triangular pressure pulse as the shock source. The start of the pulse was a time 0, peak at 2 and tail at 4 microseconds. The peak pulse amplitue was 200 Bar.

Rigid boundary conditions were imposed on the walls of the ellipse and on the X axis. The latter was required to contain the water (i.e. stop a component flow across the X axis). The equation of state used was the linear equation of state for water.

The ellipse co-ordinates used are the same as that of the prototype elliptical cavity :

a = 50 mm
b = 43.3
e = 0.5

This simulation shows the focusing process from the first focal point of an ellipse to the second focal point. The process is assumed to be symmetric about the X-axis.

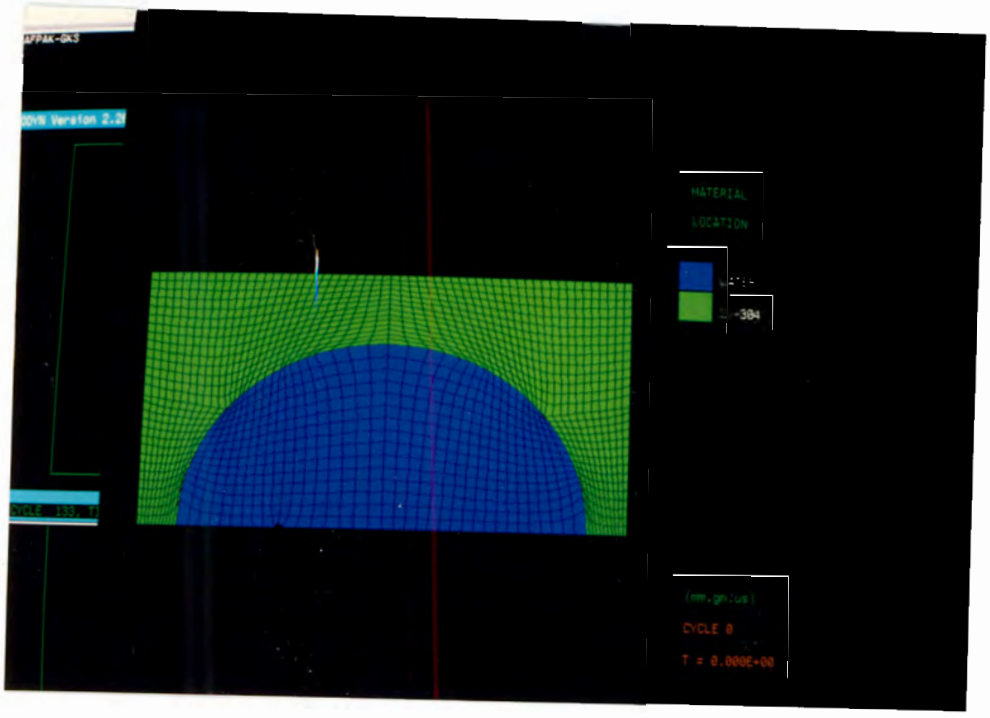

Fig I1 : ***Material and Lagrangian grid used in the 1/2 ellipse simulations***

Fig I1 shows the material and the Lagrangian (finite difference) grid. The focal point is 25 mm to each side of the center of the ellipse. The first focal point has a pertubation (1 mm by 1 mm) which is a free surface. This surface has the initial pressure boundary condition imposed on it. The resultant free surface oscillation effects will correspond closely with the real system where the high pressure plasma gas borders on the liquid. However, the real boundary condition would be a semi-circle - this boundary is shown as a polygon.

The grid is a rectangle mapped to the ellipse boundary.

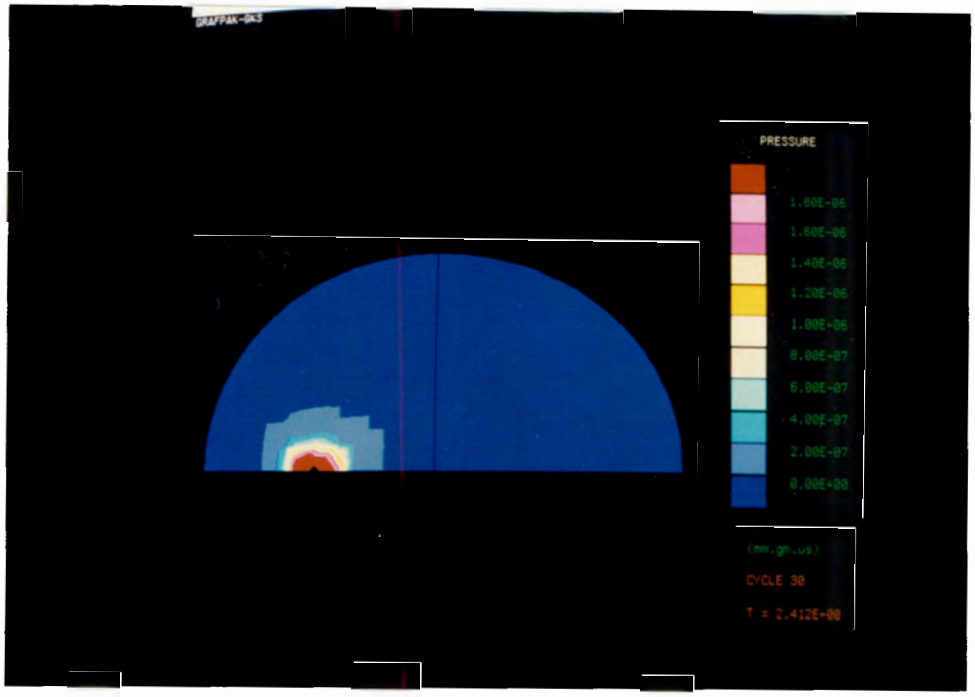

Fig I2 : *Half ellipse focussing 2.4 μ seconds after discharge*

Fig I2 shows the shock at 2.4 microseconds. The weak shock is expanding spherically.

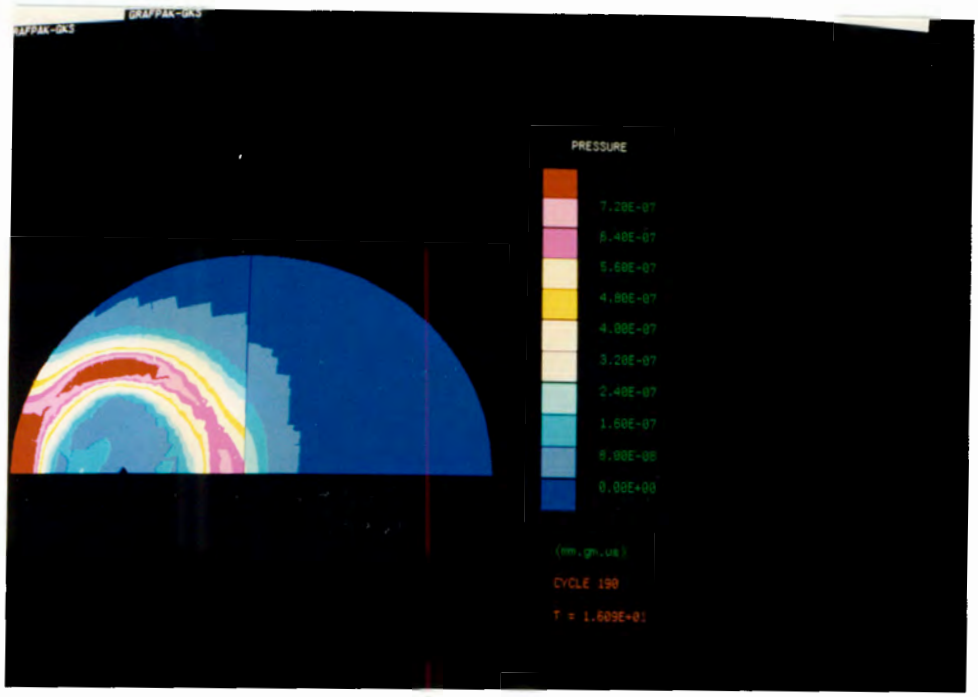

Fig I3 : *Weak shock wave at 16 μ seconds from discharge, undergoing reflection from the wall*

Fig I3 shows the shock at first reflection from the first boundary. This occurred at time 16 microseconds.

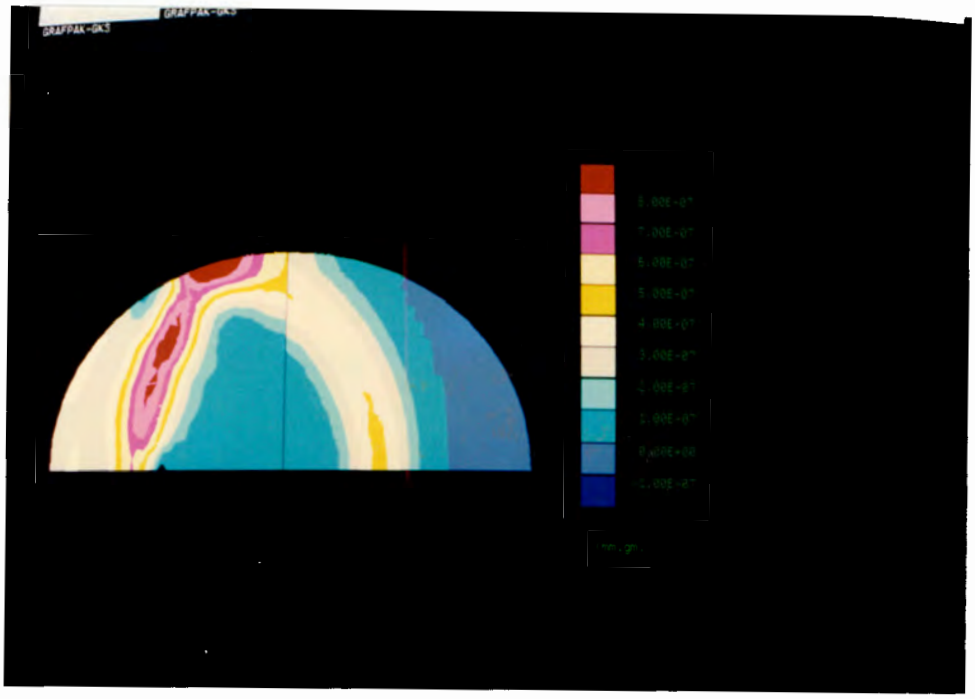

Fig I4 : *Weak shock wave at 32 μ seconds form discharge*

Fig I4 shows the wave propagating towards the second focal point. Note that there are two components to the wave ; a convex component ahead of a concave wave which has completed reflection from the cavity wall (rigid). The concave component is converging and strengthening on the second focus. The convex component is expanding and dissipating - it will reflect off the rear cavity wall after crossing (as it expands) through the second focus.

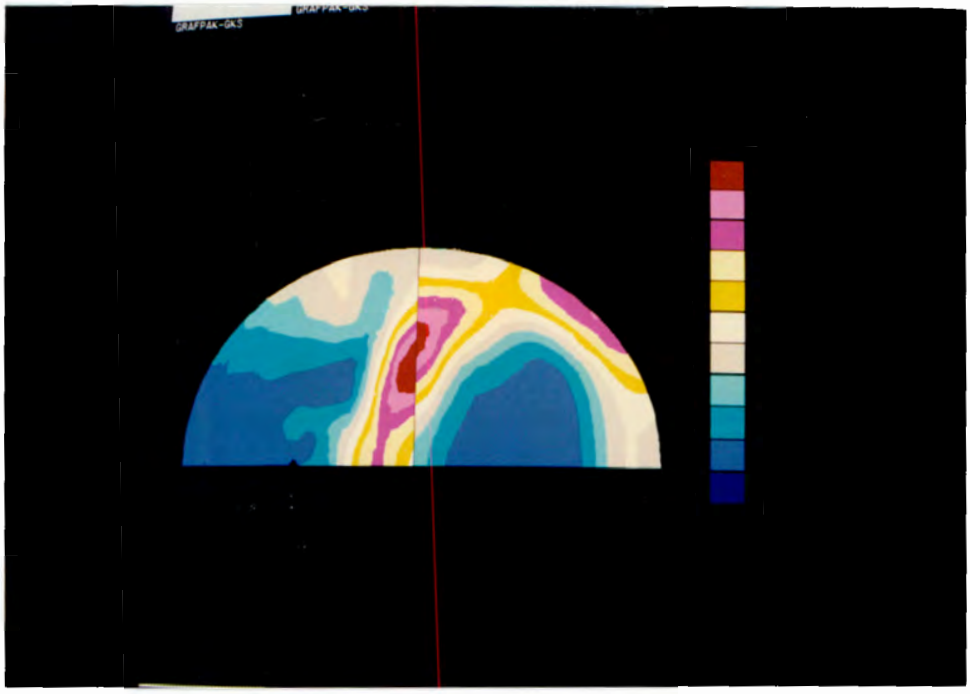

Fig I5 : *Weak shock wave at 49 μ seconds*

Fig I5 shows reflection of the initial convex wavefront from the far wall at time 49 microseconds.

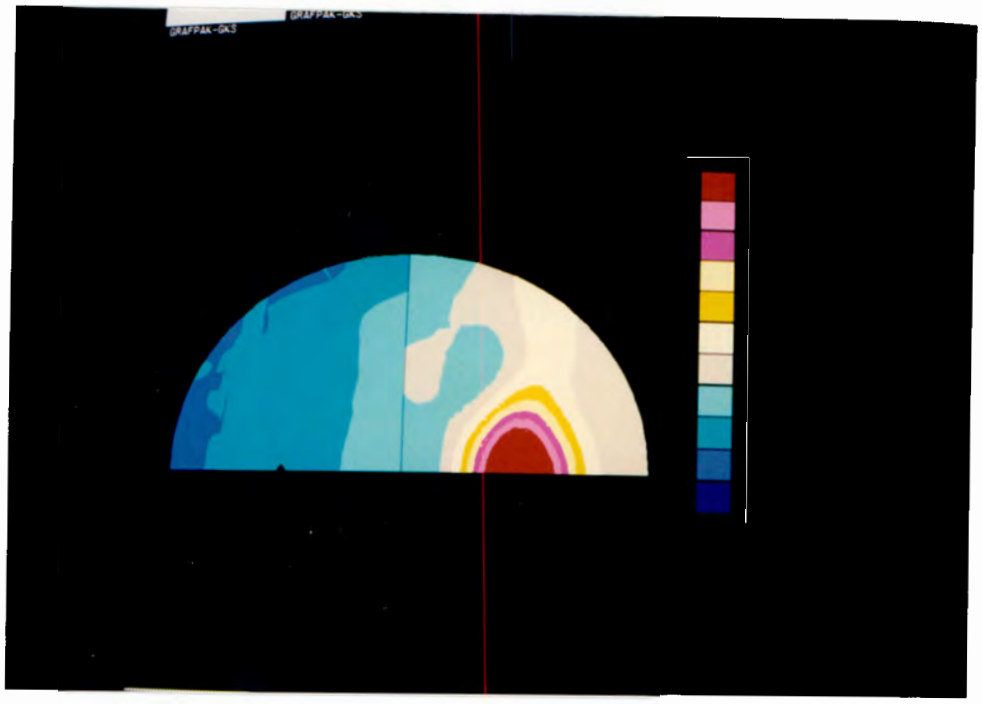

Fig I6 : *Weak shock wave at 67 μ seconds from the discharge. Convergence to the second focal point is shown.*

Fig I6 shows the pressure contour of the weak shock wave focussed to the second focal point. This has occurred at 66.6 μ seconds. Since the waves have travelled 75 mm it shows that the shock is a weak shock travelling at approximately the acoustic sound speed.

Fig I7 : *Target pressure location points*

Fig I7 shows the location of the target pressure record points. These points record the pressure time history of the simulation.

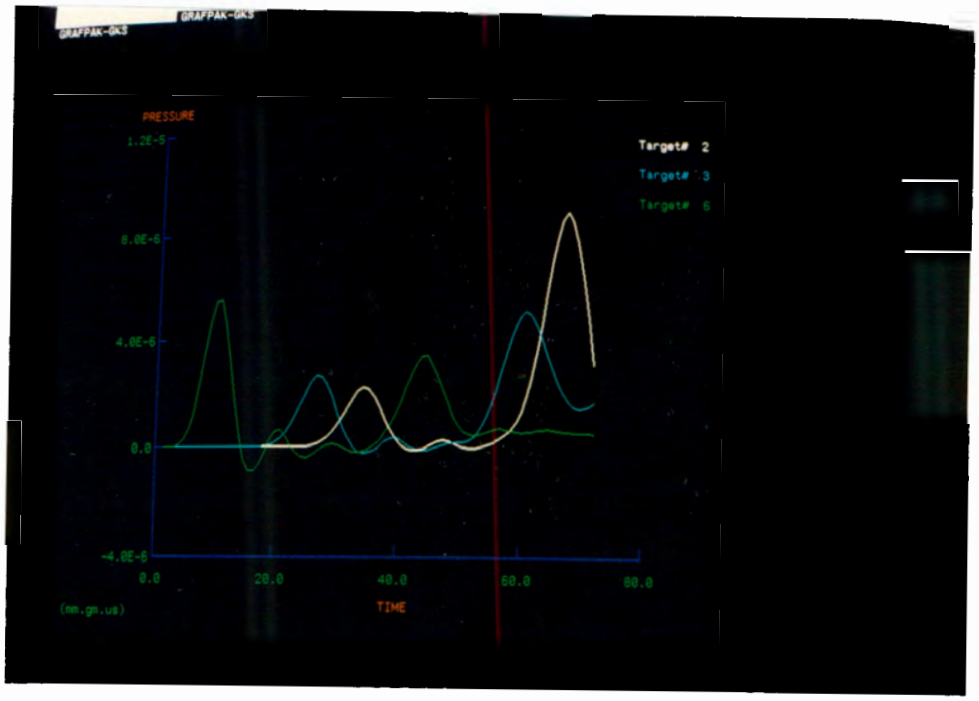

Fig I8 : ***Pressure vs. time for target points shown in fig I7***

Fig I8 shows the pressure time history for the target points 2,6,and 3 shown in **fig I7**. These points are on the focal chord of the ellipse. Point 6 shows an initial peak due to the expanding convex wave and a peak (at approximately 45 μ seconds) due to the converging concave wave. This second component is seen to be less than the initial wave. This is a result of the longer propagation distance travelled by this wave. Point 3 shows an initial peak due to the expansion wave. The magnitude of this wave is less than the initial peak of target 6. Target 3 is located further from the first focus - thus the dissipation is greater. Tartget 3 shows a peak at approximately 60 μ seconds. This is the weak shock wvae converging on the second focus. Target 2 shows the pressure recorded at the second focal point of the ellipse. This pressure contour history is discussed in Chapter 7.

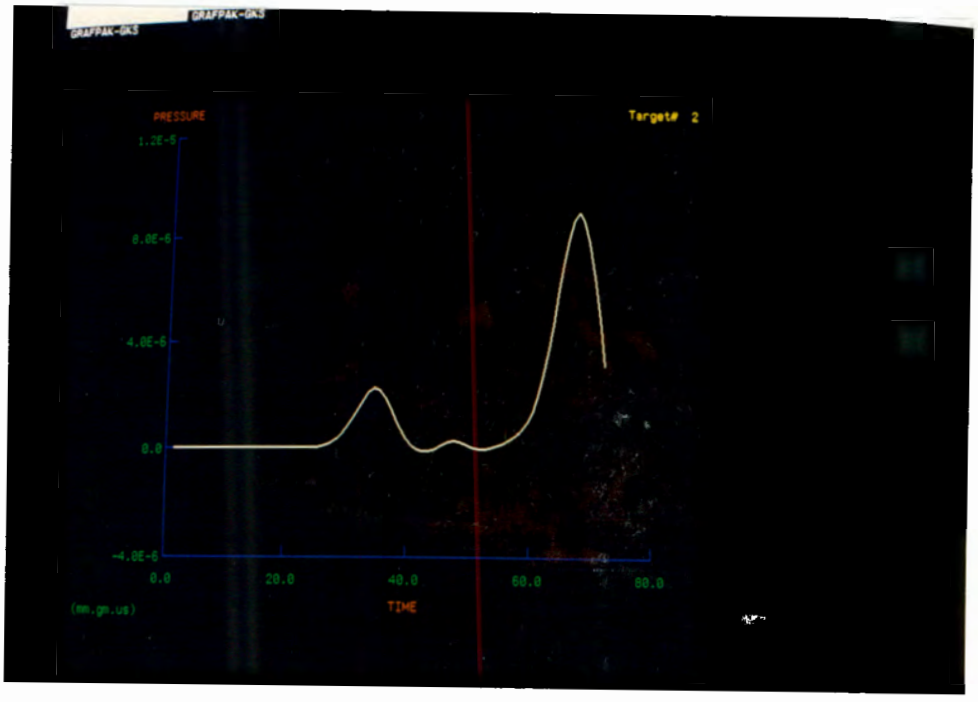

Fig I9 : *Pressure history recorded at target point 2 (second focus of ellipse)*

The pressure recorded at the second focal point of the ellipse is shown in **fig I9**. The first peak occurs at time 33 microseconds corresponding to the first pass of the shock before reflection from the back wall. Full focus i ng occurs at 66 μ seconds.

The magnification factor (ratio of focussed wave to the first wave) is about 6.

I2 Full ellipse focusing

The particle velocity of the full ellipse near focusing showing the streaming effect of the source (at the first focus) is shown in **fig I10**:

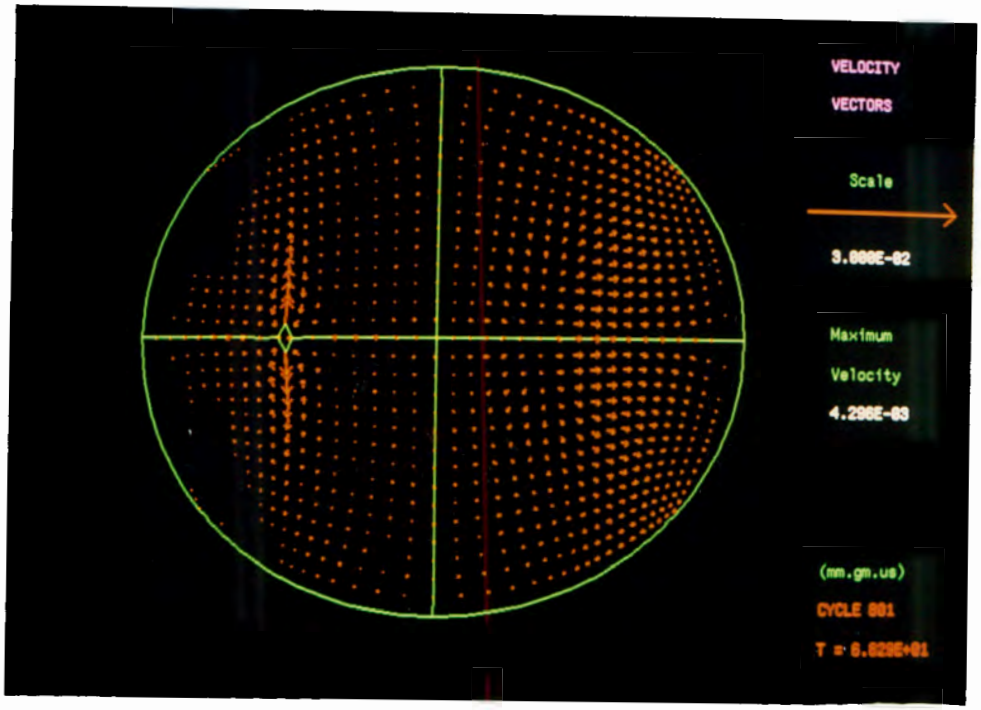

Fig I10 : *Full ellipse particle velocity*

The grid used in full ellipse focusing was a Lagrangian grid with four sub-spaces - each corresponding to a quadrant. These quadrants are rectangles mapped to the curved surface of the ellipse. The abnormality in the velocity profile is a result of numerical errors.

APPENDIX J :

Autodyne cone duct / nozzle simulations

J1 Grid and material locations

The material and grid locations for the cone / nozzle interactions are shown in this section. The shock reflection and pressure measurements for these combinations are shown in Chapter 7.

The first combination was the regular cone - small nozzle combination. The material layout for this combination is shown in **Fig J1 :**

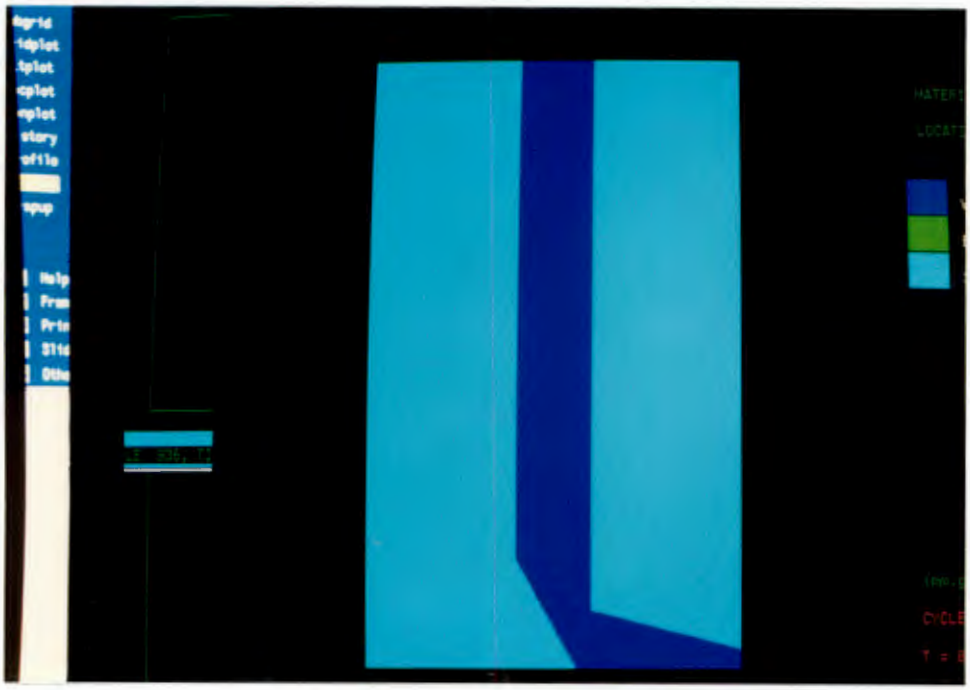

Fig J1 : *Material layout for the regular cone - small nozzle combination*

The material layout for the low cone - small nozzle combination is shown in **fig J2 :**

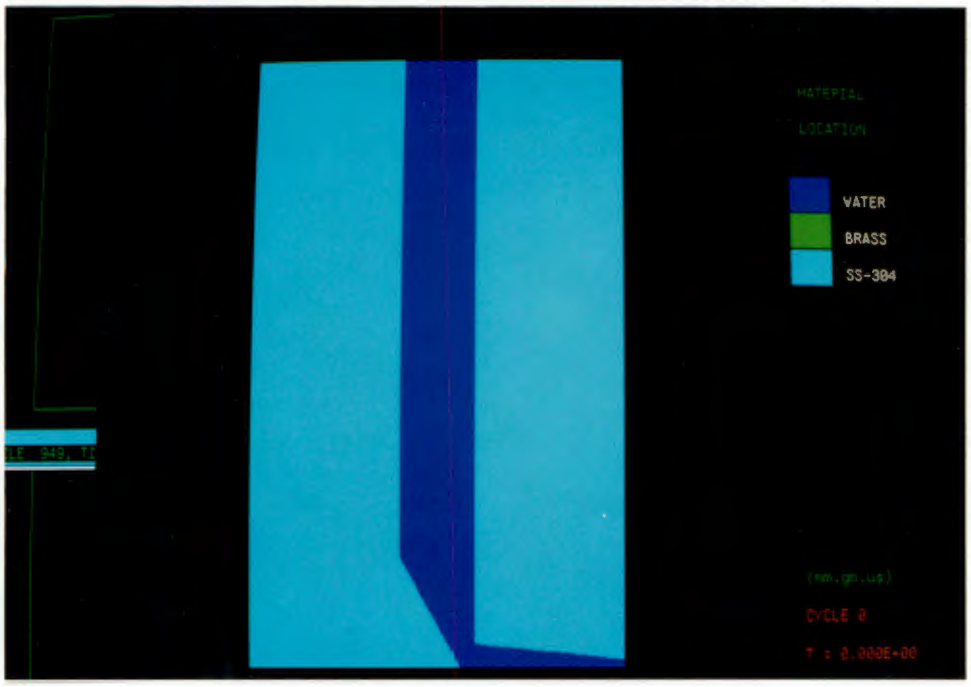

Fig J2 : ***Material layout for the low cone and small nozzle combination***

The final material layout for the low cone - medium nozzle combination is shown in fig J3 :

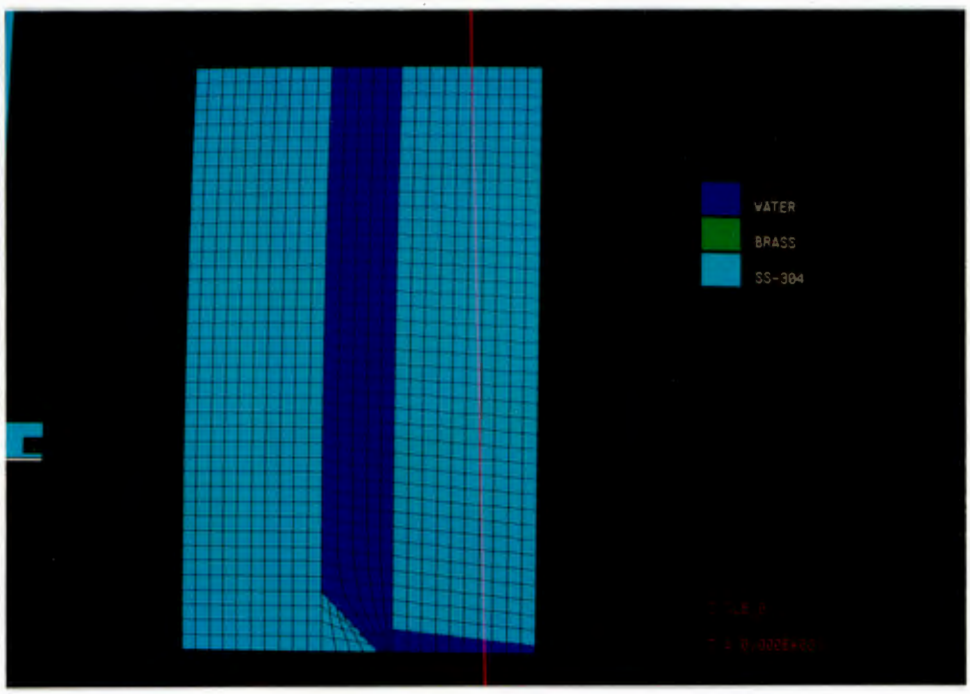

Fig J3 : *Material layout for low cone - medium nozzle combination*

APPENDIX K:

Delay circuit and Xenon tube driver

Chapter 8 reviews technologies suitable for the measurement of pressure in the cavity prototype and water jet slug velocity. It concluded that pressure measurement was beyond the scope of this thesis, but that water jet velocities could be measured photographically if a short duration light flash and delay were used. A Hamamatsu Xenon tube (duration 15 microseconds) and OEM power supply were found to be a suitable short duration light source - **Appendix M**.

A variable delay unit and trigger system are described in this appendix. They are designed to trigger the xenon tube at the at a preset delayed time (the water jet occurs several microseconds after the electrical discharge).

K.1) Trigger circuit

The electrical discharge can be used to trigger the delay unit. Peak currents in the order of several KiloAmps make it possible to use inductive coils to sense the current. However, such systems have slow rise times. The shunt resistance can also be used since it produces a voltage pulse at discharge. The magnitude of this pulse would differ for different circuit energies: The flash circuit would also then be directly electrically coupled to the discharge circuit leading to the possibility of multiple earths occurring in the circuit.

The trigger mechanism chosen (shown in **fig K1**), uses the light output of the spark gap switch to cause a photodiode to conduct. A comparator is set via a potentiometer such that the unit triggers at the correct threshold. Thus the electrical spark will produce a trigger pulse (0 to Vcc) that is used to start the delay unit.

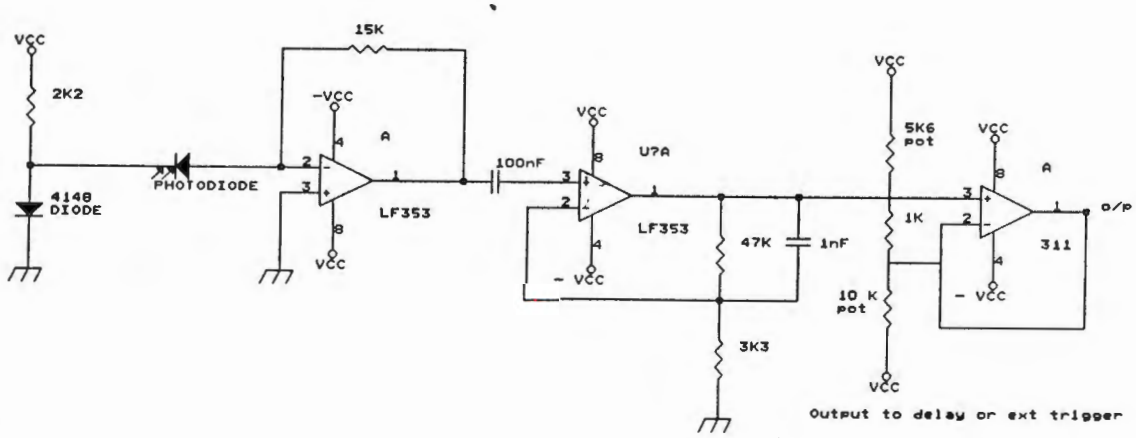

Fig K1 : *Trigger circuit*

K.2) The delay unit

The rising edge of either a test switch or the trigger circuit described in the previous section is used to clock a D-latch, this pulse is then synchronized to the clock frequency and sends a pulse which is used to start four decrimental decade counters (they are preset to initial values by four BCD thumbwheel switches). Once the counters have counted synchronously down to zero, an underflow output on the MSB counter is used to trigger a monostable circuit. This monostable produces a 5 V, 1.2 millisecond pulse which is sufficient to drive the thyratron of the OEM Xenon power supply. The counters on completion also

reset the D-latches.

The counters can be set to decrement in 1 microsecond, 100 nanosecond, and 10 microsecond intervals by changing the clock frequency from 1 MHz, to 10 MHz, and 100 kHz respectively.

The circuit is shown in fig K2 :

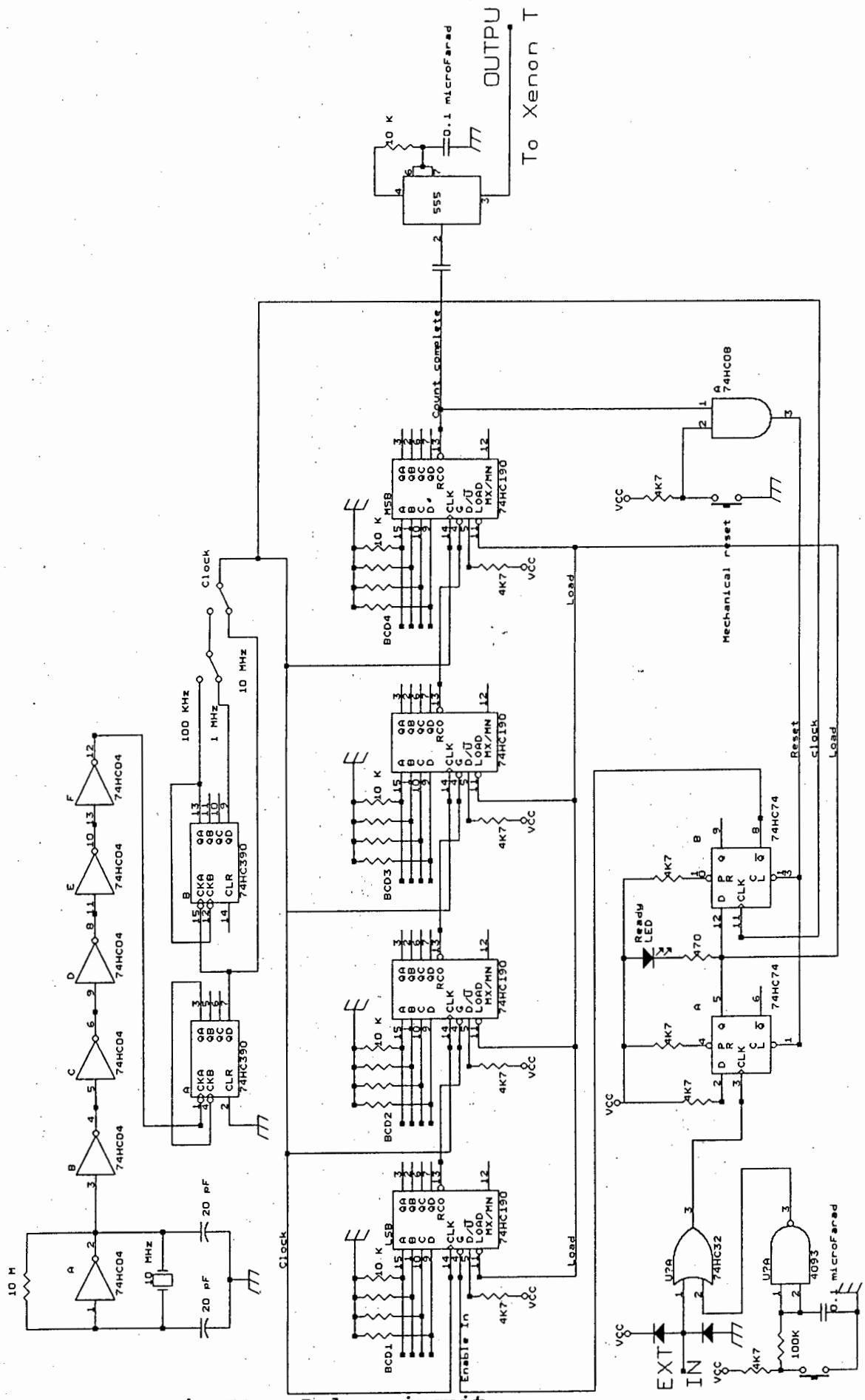

Fig K2 : ***Delay circuit***

K.3 Complete trigger unit

The trigger unit is also designed to give an external trigger output pulse. This pulse is used as an external trigger input to the memory scope. The current and voltage measurement during discharge are triggered using this system.

Light flash delay testing

Testing of the delay and trigger circuit while in operation was accomplished by the use of a second photodiode trigger system (same circuit as shown in **fig K1**). A fiber optic cable taken from the Xenon flash tube (light pipe) to this circuit and photodiode allowed the measurement of the light pulse to be displayed on a memoryu scope. The external trigger output from the circuit was used to trigger the scope. The resultant delay before the light flash occured could be read from the display timebase and validated with the delay set on the counters.

A typical response is shown in **fig K3**:

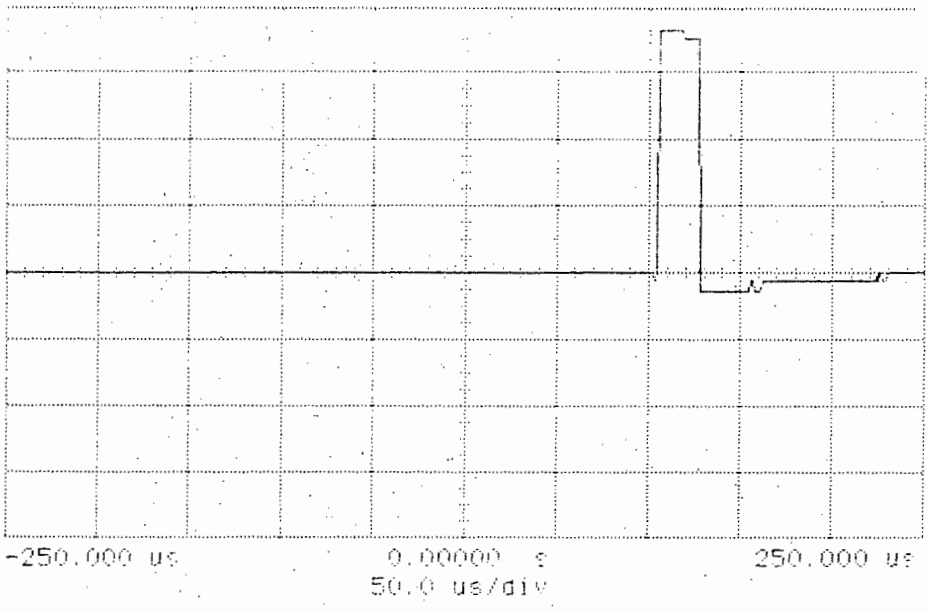

Fig K3 : *Response of test circuit to the Xenon flash*

The delay on the counter was set to 100 μ seconds. **fig K3** shows that the actual delay is slightly longer than this value. This is due to the propagation delays in the two trigger circuits. The pulse duration of shown in the figure is due to the Schmitt trigger of the circuit and is not an accurate measure of the flash lamp response or duration. The advertised duration of the Hamamatsu Xenon lamp is less than 10 μ seconds.

APPENDIX L:

Gustaffson reference [15]

Experiments on shock-wave focusing in an elliptical cavity

Göran Gustafsson[a)]
Department of Mechanical Engineering, Luleå University of Technology, S-951 87 Luleå, Sweden

(Received 6 June 1986; accepted for publication 2 February 1987)

Experimental work on reflection and focusing of weak cylindrical shock waves in a liquid-filled elliptical cavity is presented. The shocks are generated at one focus of the cavity by electrical discharges, and converge at the other focus after reflection in the cavity wall. High-speed photographs of the resulting wave system, which appears to be considerably more complex than the corresponding one in air, are shown and discussed. The results are of interest in the design of a transient water-jet generator, which utilizes the energy in the converging shock wave to produce a fast liquid jet.

Focused and converging shock waves provide a means for obtaining high pressures and temperatures at a specific point in time and space. Over the years many researchers have worked on different aspects of the problem (see for example Refs. 1–3). This communication presents results from focusing experiments with spark-induced weak shock (acoustic) waves in a water-filled elliptical cavity.

The principle is shown in Fig. 1. An acoustic wave induced at one focus of an elliptical chamber will reflect off the walls and converge at the other focus with increasing ampli-

a) Present address: URT/LAB, SKF Norden, S-415 50 Göteborg, Sweden.

 0021-8979/87/115193-03$02.40 © 1987 American Institute of Physics

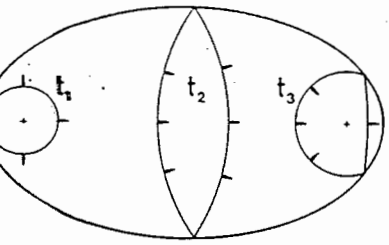

G. 1. Wave fronts from a discharge at the left focus of an elliptical mber at three different times, $t_1 < t_2 < t_3$.

de. The motivation for the present investigation is the pos-ble use of the technique for generation of transient high-eed water jets which can be used for cutting and cleaning rposes.

Figure 2 shows a cross-sectional view of the elliptical vity used in the experiments. It consists of five layers of flat el plates, and a glass plate, 10 mm thick, on each side of e 20-mm-thick center plate. The steel plates have elliptical les with lengths of the major and minor axes of 150 and 0 mm, respectively. The glass plates are sealed with silicon bber. The stack is held together by screws passing through les along the edges of the steel plates. A pair of flat-ended lindrical TIG (tungsten inert gas) electrodes, ∅ 2.4 mm, attached to the glass plates at one focus. The lead wires run ong the major axis of the ellipse and out of the cavity rough grooves in the center plate.

The cavity was filled with water and placed in a hlieren system. A "single-shot" discharge circuit with a pacitor of 0.6 μF and a dc source of 8 kV was connected to e electrodes. The gap between these was less than 1 mm. v using an intermittent light source (Fischer Nanolite)[4] onnected to a delay unit triggered by the discharge circuit, ctures of appearing waves were taken with an open-shutter mera.

Figures 3(a)–3(d) show photographs of the waves at ur different times after discharge. The complex pattern ppears to be very repeatable since every picture comes from different event. The almost circular-symmetric wave front VF) in Fig. 3(a) is the leading wave from the discharge. In is photograph, taken at 81 μs after discharge, its reflection om the cavity wall is just completed. It converges to zero

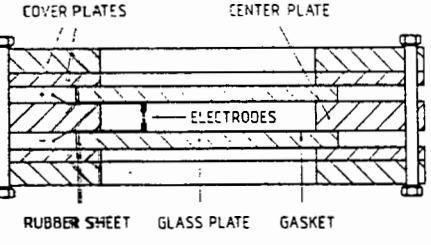

IG. 2. A cross-sectional view of experimental apparatus.

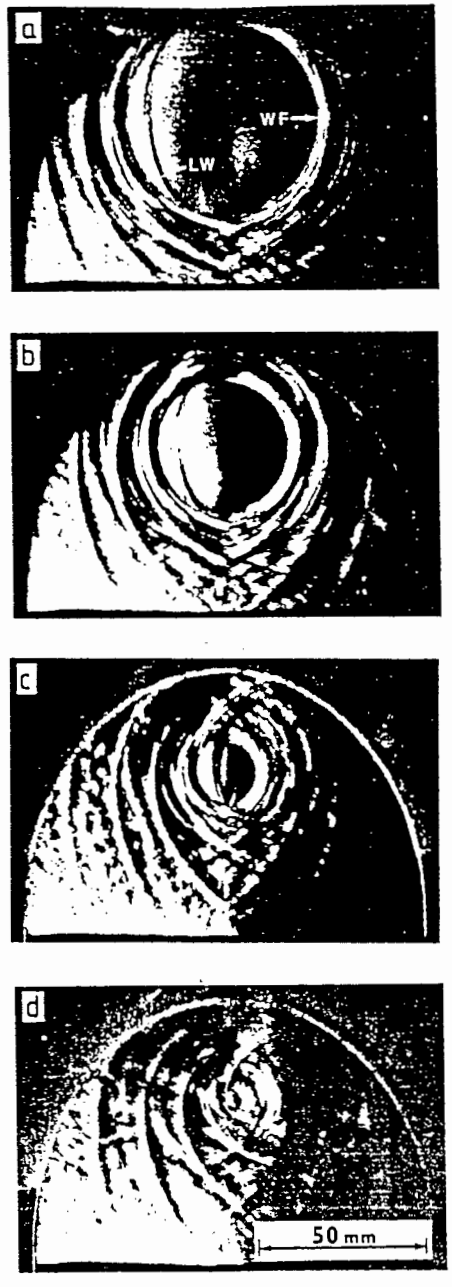

FIG. 3. High-speed photographs of the wave system in the elliptical cavity at (a) 81, (b) 87, (c) 93, and (d) 99 μs after discharge. WF is the leading reflected wave, and LW is the lateral wave induced by wave motion in the cavity wall.

radius in 100 μs, which shows that it travels with a speed of 1500 m/s and, hence, is approximately acoustic. Inside this wave is a lens-shaped lateral wave (LW), originating at the wall. This is induced by a wave mode in the wall which travels faster than the contact point between the incident and reflected shocks and the wall. This wave overtakes the contact point in the lower, hidden part of the ellipse and is caught up again at about 80 μs. A second lateral wave can also be identified, and is most clearly visible in the photographs taken at later times. Behind the primary wave is a set of almost equally spaced waves, and between them a large number of others that are apparently irregular. In pictures from the corresponding experiment carried out with an air-filled cavity these waves do not appear. Only the leading wave front is distinguished, and it seems to be unaffected by the presence of the electrodes and the electrical wires. The discrepancies between the two cases may be explained as a combination of two effects.

One is the oscillations in the electrical circuit during discharge, due to resonant behavior caused by the capacitive and inductive elements. Measurements with a storage oscilloscope showed a period of oscillation of approximately 6 μs regardless of whether the ellipse was filled with water or air. This indicates that the resonance is mainly dependent on the external electrical characteristics of the discharge circuit. The period was the same as the difference in time between the respective waves in water as shown in Figs. 3(a)–3(d). The oscillations thus may produce a series of shocks rather than just a single wave. From the pictures of the experiments with air the different shocks appear as one. This can be explained by the lower sound speed in air, which makes the distance between two consecutive shocks shorter.

The other phenomenon which is different in the two media is the occurrence of surface waves in the glass plates. This is due to the better impedance matching between the liquid medium and the plates, as the effect is more pronounced in the water-filled ellipse. The complex geometry and boundary conditions of the cavity and the glass side plates make it difficult to predict the resulting wave motion, however.

In connection with work on discharges in liquids, Germer *et al.*[5] detected a compression ring surrounding the electrodes, which disintegrates spontaneously by emitting shock waves through a zone of cavitation bubbles outside it. Since this phenomenon was not directly observed in the present experiments it is unclear if any of the appearing waves can be attributed to it.

For the objective in question, i.e., to produce one coherent wave, only the leading circular wave is desirable. Reflections from the side plates can be minimized by flush mounting the electrodes in them. The waves generated by the oscillations present a more serious problem since a fraction of the available energy is distributed over them. As discussed, the behavior of the discharge circuit seems to depend mainly on its external components, and by changing the electrical characteristics it might be possible to suppress the oscillations. The influence of geometry and material parameters on the surface waves in the side plates needs further investigation. The lateral wave can, in view of its relative weakness, probably be neglected as far as energy loss is concerned; but it might obstruct the focusing process since it arrives at the second focus before the reflected shock does. By using a cavity with a small eccentricity it can be avoided altogether.

Thanks are due to Professor Martin Lesser of the University of Pennsylvania for helpful discussions, and to Dr. John Field of the University of Cambridge, and Dr. Jan-Erik Ögren of the Luleå University of Technology for advice on the high-speed photography. Allan Holmgren is to be thanked for assistance with the electrical equipment. This work was supported by the National Swedish Board for Technical Development (STU).

[1] B. Sturtevant and V. A. Kulkarny, J. Fluid Mech. 73, 651 (1976).
[2] Frank Obermeier, J. Fluid Mech. 129, 123 (1983).
[3] W. D. Henshaw, N. F. Smyth, and D. W. Schwendeman, J. Fluid Mech. 171, 519 (1986).
[4] J. E. Field, Contemp. Phys. 24, 439 (1983).
[5] R. Germer, W. Schaaffs, and P. Krehl, in *Proceedings of the 11th International Congress on High Speed Photography*, edited by P. J. Rolls (Chapman and Hall, London, 1975), pp. 504–510.

APPENDIX M:

Hamamatsu Xenon flash tube and OEM power supply data

Super-Quiet Xenon Lamps - Flash Mode/UV to IR continuous spectrum

Hamamatsu flash mode Super-Quiet (SQ) Xenon Lamps were designed specially for use in photometric applications, and feature dramatically improved performance, having arc stability 5 times higher and service life 10 times longer than those of conventional lamps. Compared with continuous mode lamps, they are smaller, generate less heat and produce a particularly high-intensity continuous spectrum from ultraviolet to the visible region. They can be driven at a repetition rate of up to 100 Hz and are guaranteed to have life of more than 10^9 flashes.

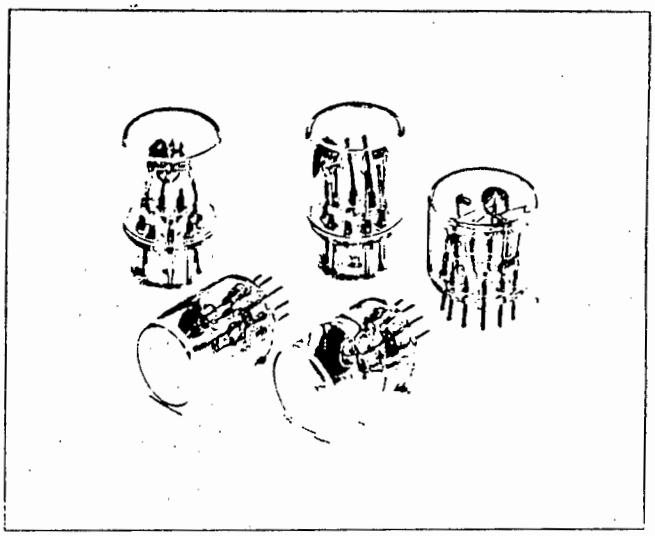

APPLICATIONS

- **Stroboscopes**
- **Chromatography**
- **Photoacoustic spectroscopy**
- **High-speed camera light source**
- **Medical instrumentation**
- **Photomask light source**
- **SO_2 analyzer**
- **Fluorospectrophotometer**
- **Color analyzer**

Type No.	Arc Size (mm)	Outline (P.9)	Window Material	Spectral Distribution (nm)	Supply Voltage (Vdc)	Trigger Voltage (kV)	Max. Average Power (W)	Max. Power Energy Per Flash (J/Flash)	Repetition Rate Max. (Hz)	Output Stability[A] Jitter[B] Typ. (ns)	Output Stability[A] Output[C] Fluctuation Max. (%)	Life[A] Min. (Number of flashes)
22mm Diameter Type												
L2467	8.0 x 1.5	A	Synthetic Silica	160~2000	700~1000	5~7	10	0.10	100	200	2.0	1×10^9
L2468			UV Glass	185~2000								
L2469			Borosilicate	240~2000								
L2415	3.0 x 1.5	B	Synthetic Silica	160~2000	700~1000	5~7	10	0.10	100	200	2.0	1×10^9
L2416			UV Glass	185~2000								
L2417			Borosilicate	240~2000								
L2439	1.5 x 1.5	C	Synthetic Silica	160~2000	700~1000	5~7	10	0.10	100	200	2.0	1×10^9
L2440			UV Glass	185~2000								
L2441			Borosilicate	240~2000								
26mm Diameter Type												
L2187	8.0 x 1.5	A	Synthetic Silica	160~2000	700~1000	5~7	15	0.15	100	200	2.0	1×10^9
L2188			UV Glass	185~2000								
L2189			Borosilicate	240~2000								
L2358	3.0 x 1.5	B	Synthetic Silica	160~2000	700~1000	5~7	15	0.15	100	200	2.0	1×10^9
L2359			UV Glass	185~2000								
L2360			Borosilicate	240~2000								
L2435	1.5 x 1.5	C	Synthetic Silica	160~2000	700~1000	5~7	15	0.15	100	200	2.0	1×10^9
L2436			UV Glass	185~2000								
L2437			Borosilicate	240~2000								

APPENDIX N :

HV Sphere gap callibration

Two 12.6 mm spheres were used as the air gap switch. The spheres were mounted in a glass vessel (with an open top), on movable pistons. The spheres were aligned head on.

Published sphere gap callibration results **[46,47]** are for spheres > 2 cm diameter. The breakdown voltage for different sphere gap spacing is shown in **table N1):**

Table N1

Sphere gap spacing [cm]	Breakdown Voltage [kV]
0.05	2.8
0.1	4.7
0.15	6.4
0.2	8.0
0.25	9.6
0.3	11.2
0.4	14.4
0.5	17.4
0.6	20.4
0.7	23.2
0.8	25.8

Small gaps are accurate for breakdown voltages lower than 30 KV (gaps are only reliable for gap spacings less than 0.5 D).

Using the 12.6 mm sphere gaps the following breakdown voltages were recorded (23^{o}, 679 mm Hg) **Table N2:**

Table N2

Gap spacing [mm]	Breakdown Voltage [kV]
2.5	9.5
3.0	11.3
4.0	13.1
5.0	18.3
6.0	20.2

The breakdown voltages are comparable to those found in **table N1** even though the spheres used in these results are smaller. The increase in breakdown strength of this system can be attributed to the close proximity of the glass walls to the spheres in this system. Kuffel **[46]** gives the criteria for standard measurement of sphere gap breakdown. These requirements state that there should be no obstacles in the viscinity of the gaps and that the measurements should be taken at standard atmospheric conditions.

APPENDIX O:

Pulsed water jet operation

O1 Shock wave reflection method

The transient water jet produced by the water jet generator is the result of a shock wave impinging on the free surface at the nozzle - air interface. This method is termed the shock reflection method.

The shock wave pressure profile at the second focus has been analyzed and found to be a function of angle from the second focal point. This analysis has excluded the effect of the cone reflecting surface on the focusing process and resultant pressure. An analysis of this process would be complex - and probably only possible using numerical techniques. Thus the pressure profile at the base of the nozzle is unknown - but probably a function of time, r' and cavity height.

O2 Analysis of nozzle equations

As a first approximation, the complex initiation of the pressure in the nozzle is ignored. A plane wave is assumed to propagate down this nozzle. The relationship between pressure velocity and elevation will be given by Bernoulli's equation - provided that the pulse length can (for a short time) be considered continuous **[100]**. The total energy entering the nozzle can be assumed to equal the energy out of the nozzle (jet) - conservation of energy principle **[100]**. The constriction in the nozzle will cause the pressure in the nozzle to increase with distance down the nozzle. The effect of gravity is assumed to be neglible. Thus the relationship in the nozzle can be written as **[91]** :

$$\phi + \frac{u^2}{2} + \int^{\rho} \frac{dp}{\rho} = const$$

Where u is the velocity of the liquid in the nozzle, p is the pressure in the liquid and ρ is the density of the liquid. The velocity function ϕ is given by :

$$\phi = \int^{\delta} \frac{\partial u}{\partial t} d\delta$$

Where δ is the normalised distance from the base of the nozzle (towards the nozzle opening).

Substituting and integrating δ from 0 to 1 yields **[91]** :

$$\int_0^1 \frac{\dot{u}}{u} d\delta + \frac{u^2}{2} + \int_p^0 \frac{dp}{\rho} = 0$$

If the mean value theorem of integral calculus is applied - an effective length l_e of the nozzle (<1) can be defined such that :

$$l_e \frac{\dot{v}}{v} + \frac{v^2}{2} + \int_p^0 \frac{dp}{\rho} = 0 \qquad \text{(O1)}$$

Where v is the velocity at the exit of the nozzle. It the nozzle is an ideal uniform tapered nozzle, the effective length is given by :

$$l_e = \left(\frac{d_{out\ diameter}}{d_{inner\ diameter}}\right) l$$

Where l is the length of the nozzle.

The difficulty in solving equation (O1) is finding p(t) - the pressure w.r.t. time at the nozzle base. An analytical solution of this aspect is beyond the scope of this work.

O3 Factors influencing the performance of the nozzle

Equation (O1) shows the relationship between the pressure and velocity in nozzles - the higher the pressure, the faster the jet velocity (provided the fluid can still be considered as incompressible). Thus the greater the pressure at the base of the nozzle, the greater the nozzle velocity.

The nozzle diameters i.e. the outer diameter and the angle of constriction of the nozzle together with the nozzle length, also play a part in determining the nozzle performance (as seen in equation (O1)). These factors have been experimentally inverstigated by Leach and Walker **[89]**.

The momentum product of the water jet is determined by the mass of the water jet slug and the velocity. The factors influencing the velocity have been outlined above. The water jet pulse length is determined by the duration of the pressure pulse p(t). This has been found in the simulations of **Chapter 7** to vary with different cone shapes.

When faster jets are used (100's of m/s) it becomes very difficult to design jets that are still coherent (i.e. one slug). Factors effecting the stability are jet turbulence effects, wall finish and compression effects in the nozzle. High speed nozzles are usually exponential **[3,4]** or fluted **[89]**.

APPENDIX P:

Calculation of initial aperture for high speed photography

The guide factor DA. described in **[84]** allows the aperture for a single flash lamp lighting system to be determined. The guide factor is the product of the distance D (in feet) from the flash lamp to subject and A, the lens aperture.

Assumptions :

- That the flash lamp and camera are fairly close to each other and are approximately the same distance from the subject.
- That the subject distance from the camera is at least 10 times the focal length of the lens.

The guide factor is then defined as :

$$DA = \sqrt{BCPS \frac{s}{c}}$$

Where : s is the ASA film speed, c is a constant between 15 and 25, BCPS is the beam candela second output of the flash lamp given by :

$$BCPS = (\frac{CE^2}{2}) nM$$

Where : n is the efficiency of the lamp in CP per Watt. C = the capacitance in Farads of the energy storage system and E is the voltage of the capacitor of the Xenon power supply. M is the reflection factor of the lamp in its housing compared with the light output of the lamp alone.

The Hamamatsu flash lamp and OEM power supply have the following values:

C = 0.1 μ Farad

E = 1 kV
energy per shot = 0.15 J

Relative luminous radiant intensity at this energy = 20 %
resultant calculated efficiency = 0.00133 Cd/W

Thus :

$$BCPS = 666.7\ 10^{-6}$$

If a film speed of 3200 ASA is used, the guide factor is then : DA = 0.377

If the aperture of the camera is set to f 1.4, the distance from the subject to the flash lamp is then :

D = 0.27 feet = 0.08 m = 8 cm

Thus for correct exposure, the Xenon tube should be located next to the camera 8 cm from the subject (water jet).

Shadow graph exposure calculations

The available light from a point source at some distance from the subject is given by :

$$\textit{Exposure available at the source} = \frac{CPS}{D^2}$$

$$= \frac{\textit{cdseconds o/p of source}}{\textit{distance } [m]^2}$$

Since CPS = 666.7×10^{-6} , the exposure available at the film from the Xenon tube at 3 meters from the camera is : 74 μ Cd s/m^2

This is a very small value **[84]**. Thus high speed film (3200 ASA) and long development times must be used.

APPENDIX Q:

Time delay before liquid gap breakdown

Chapter 4 has discussed the physics of a plasma discharge in water. After air gap switching, it was found that the water gap does not break-down immediately - there is a variable delay before breakdown in the liquid.

Q1 Delay circuit triggering

The delay circuit described in Chapter 8 uses the air gap switching as the trigger for the delay process. As has been described, this switching does not necessarily correspond to liquid breakdown. Since the delay circuit and photographic methods are required to be timed from the water gap breakdown, the delay to breakdown should be minimised so that the error in the delay is minimised.

Q2 Measurement of the delay before breakdown

Measurement of the delay before breakdown for d^Xxferent discharges was performed. It was found that the delay before breakdown increased with increasing gap width and also in the case of the elliptical cavity prototype ; increased with water time in the cavity. The latter was a result of the conductivity of the cavity increasing due to the oxidation of the cavity walls with time.

The delay to breakdown was measured using either the voltage probe (across the water gap) or the current shunt resistance and a HP digital oscilloscope. The scope was triggered by the air gap switch. The delay before current oscillation or voltage breakdown was the delay before breakdown.

Q3 Variation in breakdown times

The water gap length used in all experiments was l = 3 mm. The circuit values were V = 14 kV, C = 0.08 μF. Two time periods were considered : 0 - 20 minutes and greater than 20 minutes :

Time 0 - 20 minutes

86 samples were taken. The average delay to breakdown was 2.65 μ seconds. The standard deviation was 4.73 and the maximum and minimum values (of delay) were 25 and 0 respectivly.

Time > 20 minutes

58 samples were taken. The average delay to breakdown was now 20.45 μ seconds with a standard deviation of 22. The maximum and minimum delays read were 100 and 0 microseconds respectively.

These results show that if the testing period is less than 20 minutes increase in conductivity of the liquid in the cavity is negligible. The percentage error introduced by triggering off the air gap switch and not the water gap breakdown is also negligible (since delay times of the order of 100's of microseconds were used).

APPENDIX R:

Calculation of the inductance of the discharge circuit

The inductance of the capacitors and circuit configuration was calculated from the current oscillation during discharge. The capacitors were t^Xxs charged to the breakdown voltage of the air gap. At breakdown, the energy of the capacitors was discharged to earth through the circuit configuration (leads, connectors). This discharge circuit is equivalent to an RLC discharge circuit and has been analyzed in Chapter 4.

R.1 Calculation of inductance

If the half period of the current oscillation is measured and the capacitance of the bank is known, the inductance of the capacitors and circuit configuration is given by :

$$\tau = \pi\sqrt{LC}$$

R.2 One capacitor

The current distribution during the discharge is shown in fig R1:

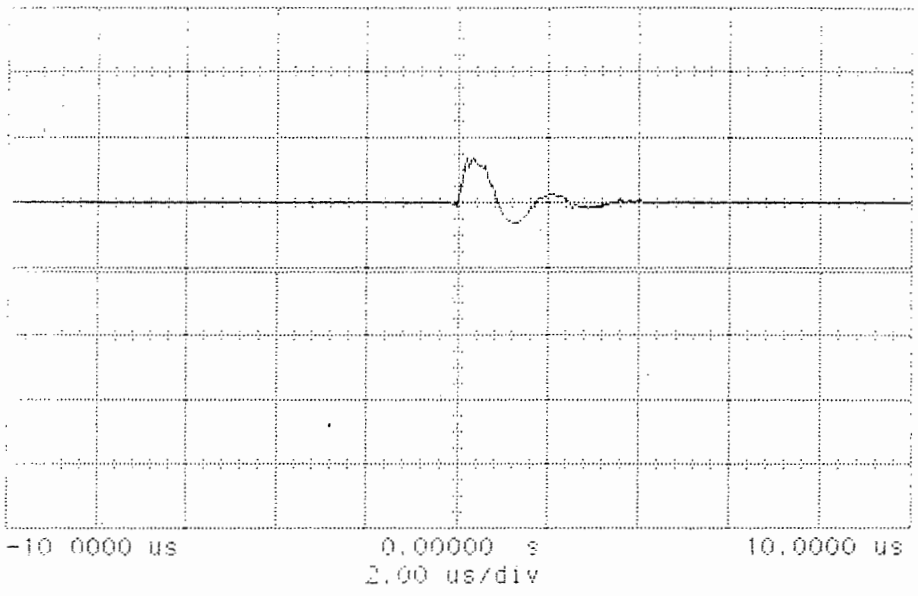

Fig R1 : *Current distribution for single capacitor discharge*

This shows that the time for the half cycle of the current is :

$\tau = 0.8\ \mu$ seconds.

Thus the oscillation frequency is :

$f = 625$ kHz

The capacitance of a single capacitor is 0.04 μ F. Thus the inductance of the circuit and capacitor is :

$L = 1.6\ \mu$ H

R.3 Two capacitors

The current distribution during the dischar^Xx is shown in **fig 70 (Chapter 9):**

This shows that the time for the half cycle of the current is :

$\tau = 1\ \mu$ seconds.

Thus the oscillation frequency is :

$f = 500$ kHz

The capacitance is 0.08 μ F. Thus the inductance of the circuit and capacitor is :

$$L = 1.27\ \mu H$$

R.4 Three capacitors

The current distribution during the discharge is shown in **fig R2:**

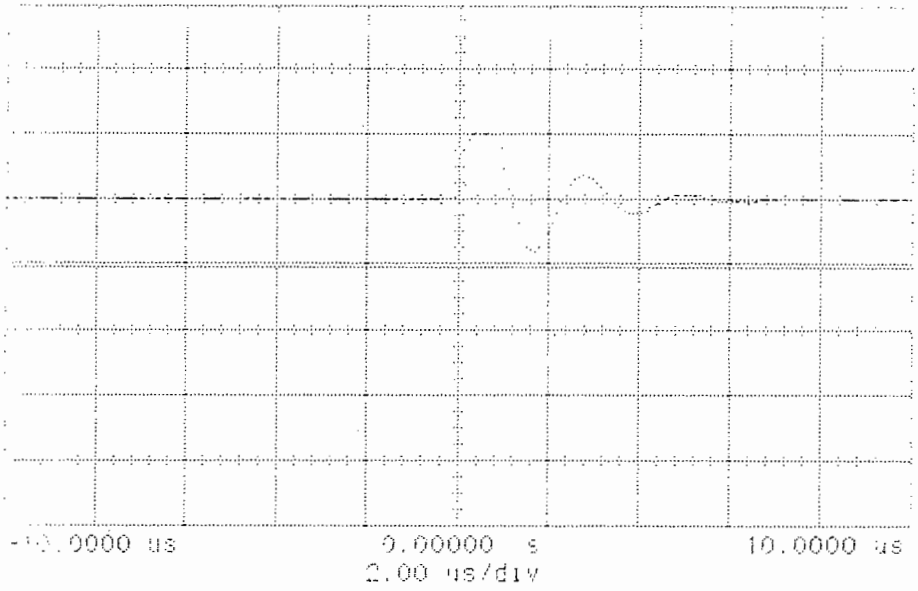

Fig R2 : Current distribution for a capacitor discharge C = 0.12 μF

This shows that the time for the half cycle of the current is :

$$\tau = 1.2\ \mu \text{ seconds.}$$

Thus the oscillation frequency is :

$$f = 42\ \text{kHz}$$

The capacitance is 0.12 μ F. Thus the inductance of the circuit and capacitor is:

$$L = 1.22\ \mu H$$

R.5 Four capacitors

The current distribution during the discharge is shown in **fig R4:**

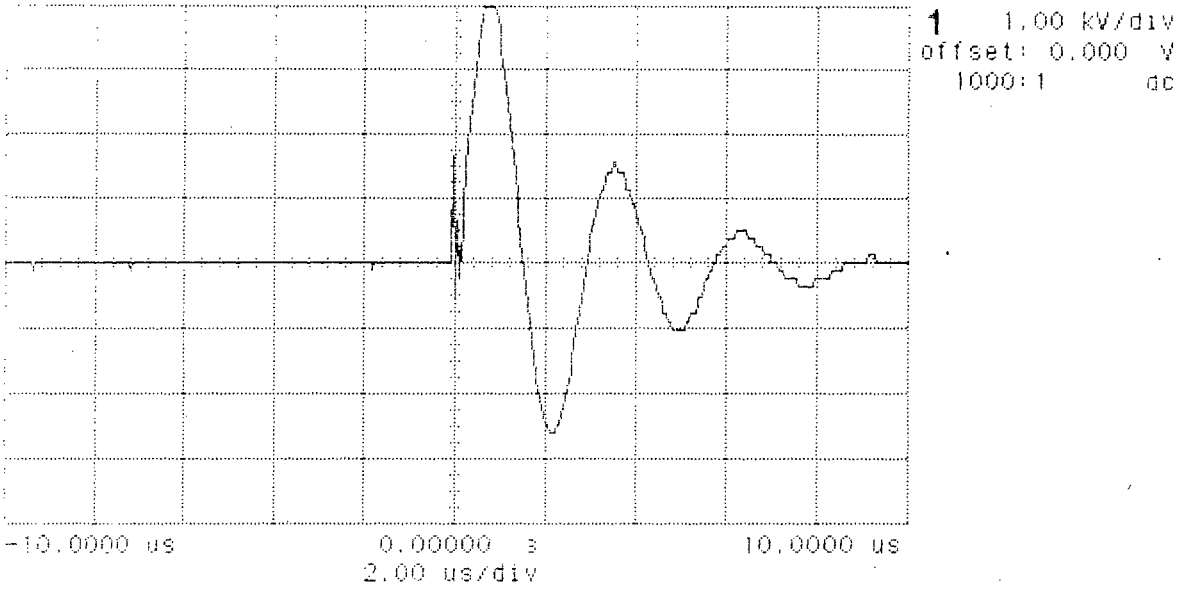

Fig R4 : *Current distribution for capacitor discharge C = 0.16 μF*

This shows that the time for the half cycle of the current is :

$\tau = 1.4\ \mu$ seconds.

Thus the oscillation frequency is :

f = 360 kHz

The capacitance is 0.16 μ F. Thus the inductance of the circuit and capacitor is:

L = 1.24 μ H

APPENDIX S:

Reducing the circuit inductance

High voltage work requires physically large components because of the insulation criterion. Thus they will have inherent inductance as a result of their size.

If multiple capacitors are to be used, they can be arranged in a symmetrical circular array around an air gap switch.
If only one capacitor is used, the connecting leads must be short parallel strips (to reduce the skin effect). Loops in the leads must be avoided.

S.1 The electrical circuit system

In some cases the air gap switch can be made integral with the capacitor. This significantly reduces the inductance.

A proposed water jet cavity system that is designed to be integral with the electric discharge circuit is shown in fig S1:

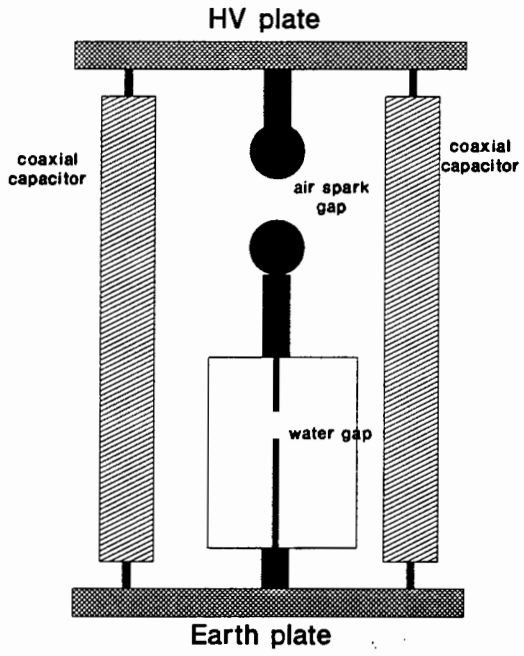

Fig S1 : ***Proposed minimum inductance water jet cavity and electrical circuit system***

This system has the advantage that the whole process is shielded. This will minimise interference effects.

S.2 Special capacitors

Certain capacitors have been specially designed to have low values of inductance. The Fischer capacitor (used in the Fischer Nanolight light source) consists of a number of coaxial cables connected in parallel at the ends (ie. a toroidal capacitor). These capacitors have inductances under 0.004 micro Henries [4].

APPENDIX T:

Schlieren systems

T1 Sclieren systems

A typical Schlieren system is shown in **fig T1:**

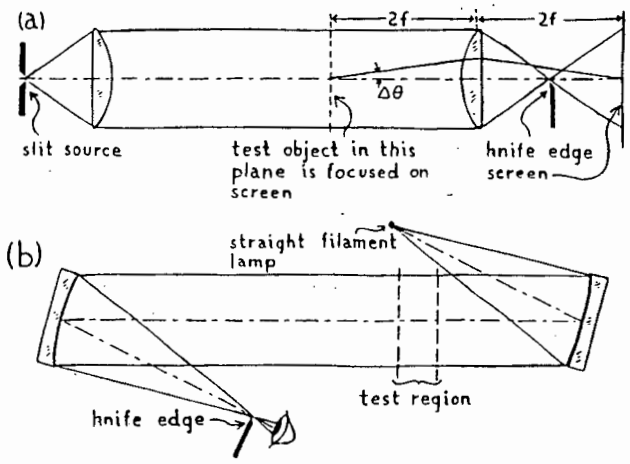

Fig T1 : ***Schlieren measurement system a) using collimating lenses b) the Z-type system using parabolic mirrors***

T2 Schlieren operation

Light from a small source is condensed onto a slit (point source). The light is collimated and passes through the object. The collimated light is then imaged by a second lens. An image of the slit source is formed by this second lens at an opaque stop. If the object is perfectly flat, homogenous and transparent, the

source image will be totally blocked by the stop. Imperfections or density changes will introduce deflections in the rays causing them to miss the stop and appear as bright or dark regions in the image [71,72].

The amount of deflection will depend on the gradient of the optical path length through the object in the plane perpendicular to the system axis. The stop is also known as the knife edge [72].

T3 Requirements

In practice the Z type (shown in fig 63) Schlieren system is used. This eliminates the requirement for high quality collimating lenses. Instead columnating parabolic mirrors can be used (which are easier to construct) [72].

APPENDIX U:

Water jet slug energy experiments

The energy in the water jet slug was measured using the system shown in **fig 67** of Chapter 8. This involved the measurement of the maximum height reached by a target cone of mass 1.06 g. Measurements were performed for different gap lengths, circuit capacitances and cone nozzle / combinations.

U1 Cone / nozzle combinations

The circuit values were : V = 14 kV, C = 0.08 μF. The gap length was set to be 3 mm.

Large nozzle / regular cone

24 samples were taken. The mean height was 66 cm, the standard deviation 12.8, and the maximum and minimum heights 1 m and 50 cm respectively. The covariance of these results was 0.19.

Medium nozzle / regular cone

11 samples were taken. The mean height was 74 cm, the standard deviation 11.7, and the maximum and minimum heights 1 m and 60 cm respectively. The covariance of these results was 0.15.

Small nozzle / regular cone

13 samples were taken. The mean height was 4.69 cm, the standard deviation 1.25, and the maximum and minimum heights 7 cm and 3 cm respectively. The covariance of these results was 0.266.

Large nozzle / low cone

17 samples were taken. The mean height was 32 cm, the standard deviation 6.3, and the maximum and minimum heights 43 cm and 20 cm respectively. The covariance of these results was 0.197.

Medium nozzle / low cone

17 samples were taken. The mean height was 53 cm, the standard deviation 6.5, and the maximum and minimum heights 68 cm and 45 cm respectively. The covariance of these results was 0.12.

Small nozzle / low cone

No measurable deflection occured.

Large nozzle / flat insert

21 samples were taken. The mean height was 45 cm, the standard deviation 9.75, and the maximum and minimum heights 66 cm and 30 cm respectively. The covariance of these results was 0.21.

Medium nozzle / flat insert

21 samples were taken. The mean height was 61 cm, the standard deviation 10.9, and the maximum and minimum heights 80 cm and 40 cm respectively. The covariance of these results was 0.18.

Small nozzle / flat insert

No measurable deflection occured.

Discussion

The coefficient of variation can be used to compare distributions if they are in the same units **[101]**. This factor shows that there was some variation between readings, but all experiments showed a similar spread. This was the result of experimental variables. The cone target could not be placed accurately over the centre of the nozzle. Hence some of the water jet energy goes into angular momentum in the target.

D2 Gap width variation

The water gap width was shortened to 2 mm. The electrical circuit parameters remained the same. The cone / nozzle combination used was the large nozzle / regular cone combination.

18 samples were taken. The average height was 22, the standard deviation 4 and the maximum and minimum heights 28 and 14 cm respectively.

These results show that if the water gap is shortened, the water gap resistance decreases and hence the power released in the water gap is decreased - leading to a weaker shock.

D3 Capacitance variation

The capacitance of the circuit was increased to 0.16 μF. The water gap length was 2.5 mm and the breakdown voltage 14 kV. The combination used was the medium nozzle / regular cone combination.

10 samples were taken. The mean was found to be 48 cm, the standard deviation 15 and the maximum and minimum heights 80 and 29 respectively.

Although the energy has increased, the mean value is lower than that measured previously (D1). The inductance of the circuit is slightly less than that used in the previous circuits. Chapter 4 and 9 have shown that this will lead to more efficient circuit operation. However, it is noted that the water gap length is smaller and this effect (i.e. reduced energy in the gap) is assumed to dominate the performance in this case.

APPENDIX V:

Resistive current probe

V.1 Measurement of transient current in a HV discharge circuit

The current can be measured using current transformers, Rogowski coils or resistance shunts [47]. The first two are unsuitable for the measurement of rapidly varying, short duration currents.

V2 Current measuring resistive shunt

A current measuring shunt resistance can be constructed to measure currents with short rise-times. A suitable coaxial shunt is shown in **fig V1** (after Kind [47]):

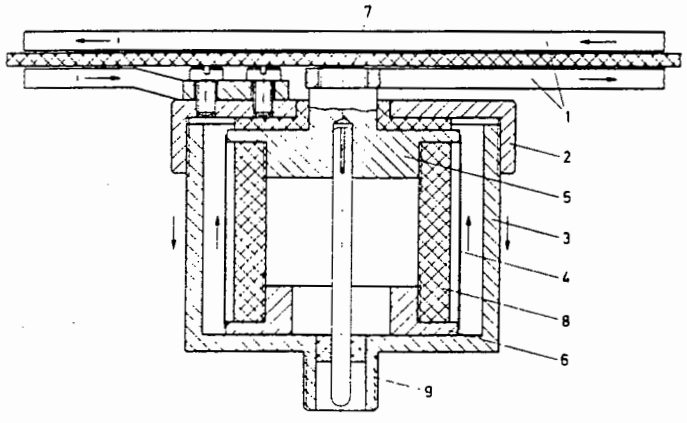

Fig. 3.12-5 Coaxial measuring resistance in the path of a strip conductor

1 Strip conductor	5 and 6 Contact discs
2 Fixing ring	7 Threaded connector
3 Screening chamber	8 Insulating distance ring
4 Resistance element	9 Connector terminal

Fig V1 : *Coaxial design for a resistance shunt*

This design has a very low inductance and hence a wide bandwidth.

APPENDIX W :

Water gap resistance measurements

The water gap resistance is calculated using the method presented in Chapter 9 section 9.6.2.

The current trace of **fig 76** Chapter 9, used a circuit with a water gap length of 2 mm. The breakdown voltage was V = 14 kV and the circuit capacitance C = 0.08 μF. Thus the resistance for this water gap length was calculated to be 1.2 Ω.

The current trace for the above circuit with a 3 mm water gap length is shown in **fig W1** :

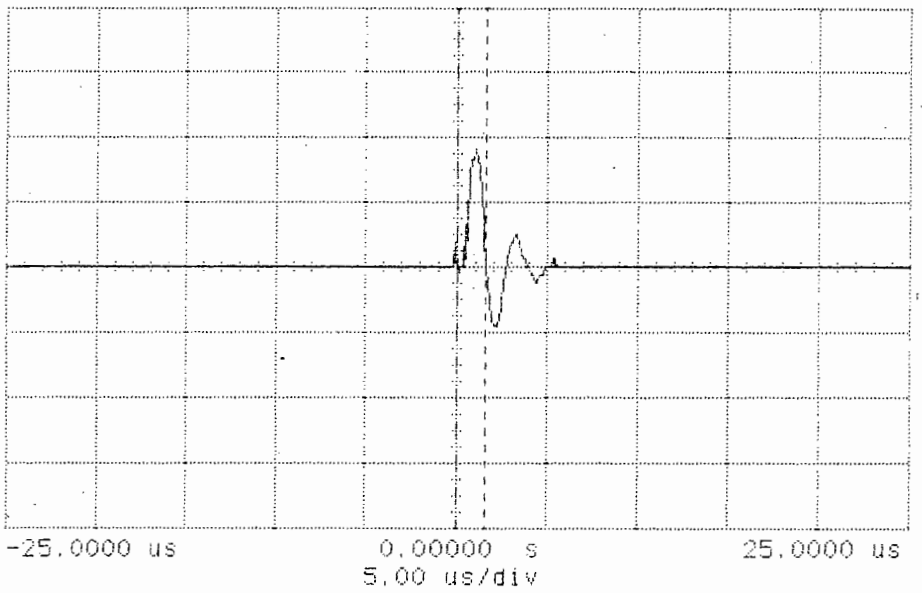

Fig W1 : *Current distribution for a 3 mm water gap*

The resistance is then calculated to be 1.9 Ω.

The current trace resulting from a 3.6 mm gap is shown in **fig W2** :

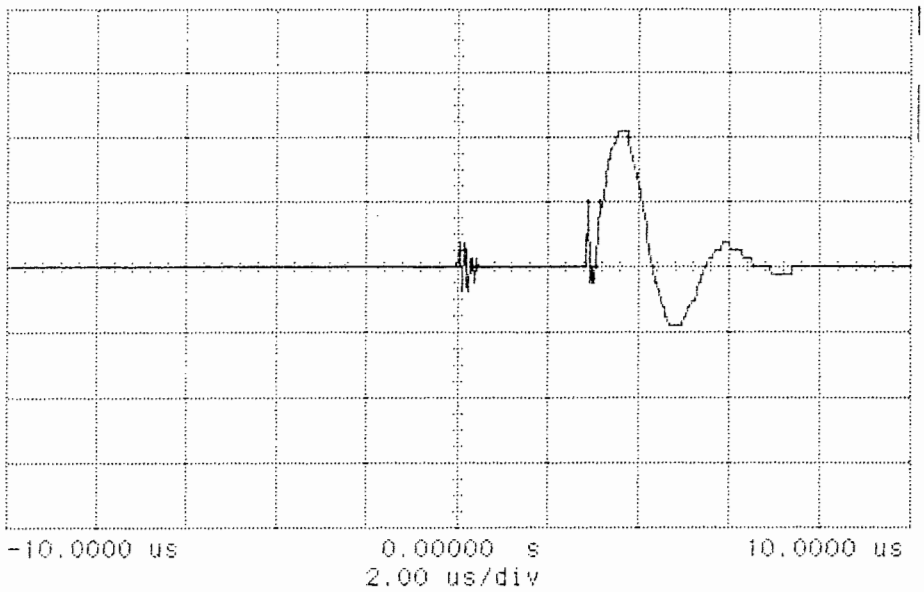

Fig W2 : ***Current trace resulting from a 3.6 mm gap***

The resistance of this gap is then calculated to be 2.17 Ω.

APPENDIX X :

Water jet maximum height

The maximum height that the water jet droplets were approximately measured by firing the water jet vertically and visually reading the maximum altitude reached by the droplets. The electrical circuit used V = 14 kV and C = 0.08 μF and gap length = 3 mm. The initial velocity was calculated using the approach discussed in section 9.7.1. The maximum height and calculated initial velocities are shown :

regular cone / large nozzle	:	6 m ie. 11 m/s
regular cone / medium nozzle	:	6.5 m ie. 11.4 m/s
regular cone / small nozzle	:	3 m ie. 8 m/s
low cone / large nozzle	:	5 m ie. 10 m/s
low cone / medium nozzle	:	5 m ie. 10 m/s
low cone / small nozzle	:	2.5 m ie. 7 m/s
flat insert / large nozzle	:	3 m ie. 8 m/s
flat insert / medium nozzle	:	4 m ie. 9 m/s
flat insert / small nozzle	:	2.5 m ie. 7 m/s

The trend is approximately the same as that shown in the energy of the jet vs. nozzle combination (**Chapter 9**). The small nozzle is seen to have a very low velocity for all cone combinations. The analysis of **Appendix O** predicts that the jet velocity will increase if smaller nozzles are used. However, the pressure at the nozzle base will be less for a small nozzle diameter ie. not all the energy will be reflected down the nozzle - some will be reflected back into the cavity. The design of the nozzle must consider the total percentage of energy at the second focus transmitted to the nozzle.

APPENDIX Y :

Water jet propagation

The propagation of the water jet slug is presented.

Figure 32 : *1 milli second*

Figure 33 : *3 milli seconds*

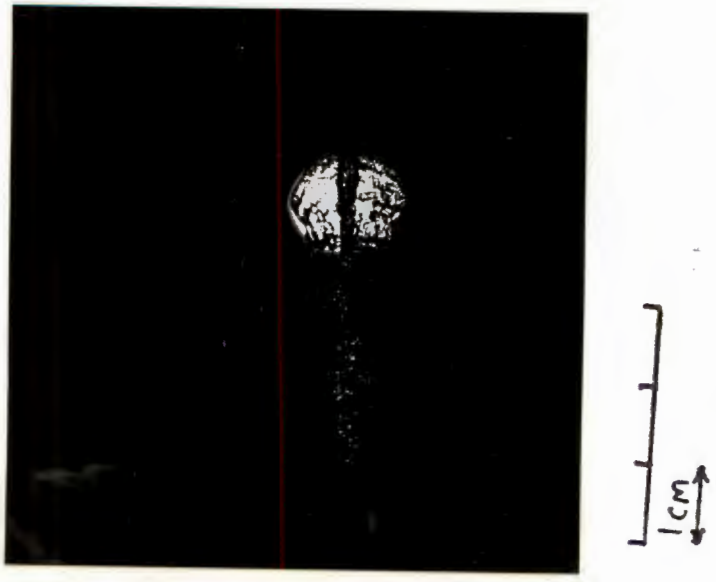

Figure 34 : *4 milli seconds*

Figure 35 : *5 milli seconds*

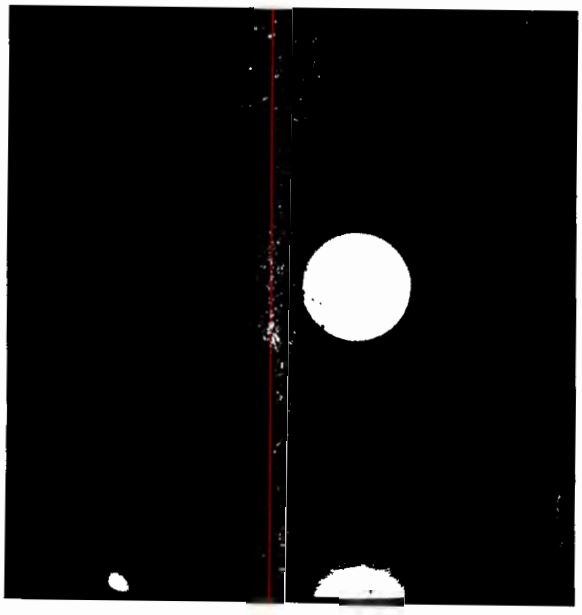

Figure 36 : *6 milli seconds*

The water jet slug at different times is shown. At 1 and 3 microsecond the mushroom shape of the slug can clearly be seen. The photograph at 4 microseconds shows a similar shape. These three photograhs are separate events. Thus the filling conditions (level in the nozzle) must have been similar in these cases. The water jet at five and 6 microseconds shows a different less coherent jet. This is assumed to be the result of nozzle instabilities and the filling conditions varying.